DOCTORAL DISSERTATION SERIES
Publication No.: 11,303

AUTHOR: Robert Eugene Keith, Ph. D., 1955
University of Michigan

TITLE: AN INVESTIGATION OF INTERGRANULAR OXIDATION IN SOME STAINLESS STEELS

University Microfilms, Ann Arbor, Michigan

AN INVESTIGATION OF INTERGRANULAR OXIDATION IN SOME STAINLESS STEELS

by

Robert Eugene Keith

A dissertation submitted in partial fulfillment
of the requirements for the degree of
Doctor of Philosophy in the
University of Michigan
1954

Doctoral Committee:

Professor Clarence A. Siebert, Chairman
Professor Lawrence O. Brockway
Associate Professor Maurice J. Sinnott
Professor Lars Thomassen
Associate Professor Lawrence H. Van Vlack

ABSTRACT

AN INVESTIGATION OF INTERGRANULAR OXIDATION IN SOME STAINLESS STEELS

by Robert E. Keith

Stainless steels are among a number of types of alloys which are known to be subject to preferential attack at grain boundaries under oxidizing conditions. The purpose of this investigation was to study the effects of time, temperature, and minor changes in alloy composition upon the severity of intergranular oxidation brought about by exposure at temperature to dry air under flow conditions, and to determine whether the compositions of intergranular oxides differed appreciably from surface oxides.

Specimens of eight heats of type 310 (25 Cr - 20 Ni) and one heat of type 309 (25 Cr - 12 Ni) stainless steels, the latter being stabilized with Nb, were oxidized for times between 10 and 100 hr at temperatures between 1600° and 2000°F. A metallographic method was devised to measure quantitatively the severity of intergranular oxidation in tested specimens. X-ray powder patterns were made of external scales from selected specimens. Intergranular oxides were analyzed by means of a technique of successive etches coupled with reflection electron diffraction measurements.

It was found that intergranular oxidation in the stainless steels investigated increased in severity with both time and temperature of exposure to oxidizing conditions. No differences in severity of intergranular attack were attributable to differences in compositions of the alloys. External scales were found to consist, in general, of two phases: a rhombohedral sesquioxide phase identified as Cr_2O_3, Fe_2O_3, or a solid solution of the two; and a high-parameter (8.42 kX) spinel phase most probably $MnCr_2O_4$. In a few instances, a low-parameter (about 8.37 kX) spinel phase was also observed. At alloy Mn contents of less than one to one and one-half percent, the high-parameter spinel phase was not found in more than trace amounts. The same

phases found in the external scales were also found in the intergranular oxides, but the precision of the electron diffraction method was not sufficiently great to permit closer identification than merely as being spinel or rhombohedral phases having lattice parameters somewhere within the expected ranges. The effect of the existence of a preferred orientation in the alloy prior to exposure was found to be that the severity of intergranular oxidation was reduced but at the expense of accelerated surface oxidation.

The mechanism of intergranular oxidation is believed to be essentially an intergranular diffusion mechanism complicated by compound formation. Preferential attack is observed at grain boundaries because of the nature of the grain boundary itself, involving as it does a widened lattice interval, and thus creating an easier diffusion path than the grains themselves offer. Oxides eventually form in exposed grain boundaries because the boundaries also act as areas of concentration of easily oxidizable alloying elements. The presence of these grain boundary oxides is believed to result in more rapid grain boundary diffusion of O than would otherwise be the case. A further requirement for intergranular oxidation to take place is that the external scale must be one which is formed to an appreciable extent by anionic transport, for otherwise it would be difficult to maintain the concentration of O ions at the metal-oxide interface necessary for intergranular diffusion.

DEDICATED
to
My Wife and my Parents,
without whose assistance and encouragement
this dissertation would not have been possible.

PREFACE

The author wishes to take this opportunity to acknowledge with gratitude the contributions of several groups and individuals to the carrying out of this research. Particular thanks is due to Professor Siebert, who served as chairman of the Doctoral Committee, for the many instances in which he gave wise counsel throughout the program. Thanks also to the members of the Doctoral Committee, each of whom actively interested himself in this project and each of whom contributed significantly towards its execution. The General Electric Company and the United States Steel Company supplied the material used in the investigation, for which the author is grateful. The very important contributions toward the interpretation and understanding of the x-ray data made by Drs. H. J. Yearian and J. F. Radavich of the Department of Physics of Purdue University is much appreciated. Without the loyal and painstaking work of the student assistants employed in connection with the experimental work, L. H. DeSmyter, M. T. Kuo, H. M. Ferrari, J. C. Tobin, H. B. Probst, R. Sanford, H. Hsu, and H. Levinstein, the experimental program could never have been carried out in a reasonable time. The author is much indebted to these assistants. Discussions from time to time with various members of the Staffs of the Departments of Chemical and Metallurgical Engineering and Production Engineering and with various other students were of great value to the author. The cooperation of the group in the Chemistry Department working under Professor Brockway is gratefully

acknowledged, especially the contributions made by Dr. W. C. Bigelow toward setting up a suitable procedure for electron diffraction.

This research was carried out as part of a research project sponsored by the U. S. Air Force under Contract No. AF 33(616)-353 initiated under Research and Development Order No. 615-13, "High Temperature Alloys". The project was administered by the Engineering Research Institute of the University of Michigan. The author wishes to express his appreciation to both the Air Force and the Engineering Research Institute for their very basic contributions to the furtherance of this investigation.

TABLE OF CONTENTS

		Page
	LIST OF TABLES	vi
	LIST OF ILLUSTRATIONS	vii
I.	INTRODUCTION	1
II.	STATEMENT OF PROBLEM	3
III.	SURVEY OF LITERATURE	7
	External Scaling	7
	Internal Oxidation	17
	Intergranular Oxidation	18
	Effect of Relative Grain Orientation on Intergranular Oxidation	22
IV.	EXPERIMENTAL INVESTIGATION	24
	Oxidation Equipment	24
	Specimen Preparation	26
	Oxidation Equipment Operation	26
	Evaluation of Specimens	28
	Evaluation of Oxide Scales	34
	Interface Movements	36
	Electron Diffraction	38
V.	RESULTS AND DISCUSSIONS	42
	Oxidation Tests	42
	Interface Movement Measurements	48
	Visual and Magnetic Examination	51
	Metallographic Examination	56
	Effect of Preferred Orientation	64
	Analysis of Oxides	67
VI.	SUMMARY AND CONCLUSIONS	80
VII.	BIBLIOGRAPHY	83

LIST OF TABLES

Table		Page
1	Composition of Stainless Steel Stock, Weight Percent	86
2	Explanation of Symbols Used in Oxidation Data Tabulations	87
3	Results of Oxidation Tests, Type 309 + Nb Alloy	88
4	Results of Oxidation Tests, Type 310 Alloy, Heat 64177	89
5	Results of Oxidation Tests, Type 310 Alloy, Heat 64270	90
6	Results of Oxidation Tests, Type 310 Alloy, Heat X11306	91
7	Results of Oxidation Tests, Type 310 Alloy, Heat X11338	91
8	Results of Oxidation Tests, Type 310 Alloy, Heat X27258	92
9	Results of Oxidation Tests, Type 310 Alloy, Heat X45558	92
10	Results of Oxidation Tests, Type 310 Alloy, Heat X46063	93
11	Results of Oxidation Tests, Type 310 Alloy, Heat X46572	93
12	Oxide-Metal Interface Movement in 100 Hours Calculated from Weight Loss Measurements	94
13	Results of Metallographic Analysis	95-96
14	Heats of Formation of Oxides at Room Temperature	97
15	Some Properties of Oxides of Metals Occurring in Stainless Steels	98-99
16	Variation in Scale Composition on Replicate Specimens of Stainless Steels	100-102
17	Analyses of Intergranular Oxides of Stainless Steels Obtained by Electron Diffraction	103-108

LIST OF ILLUSTRATIONS

Figure		Page
1	Photomicrograph. Type 309 + Nb Alloy, As Received	109
2	Photomicrograph. Type 310 Alloy, Heat 64177, As Received	109
3	Photomicrograph. Type 310 Alloy, Heat 64270, As Received	109
4	Photomicrograph. Type 310 Alloy, Heat X11306, As Received	109
5	Photomicrograph. Type 310 Alloy, Heat X11338, As Received	110
6	Photomicrograph. Type 310 Alloy, Heat X27258, As Received	110
7	Photomicrograph. Type 310 Alloy, Heat X45558, As Received	110
8	Photomicrograph. Type 310 Alloy, Heat X46063, As Received	110
9	Photomicrograph. Type 310 Alloy, Heat X46572, As Received	111
10	Photomicrograph. Grain Boundary Network, Type 310 Alloy, Heat 64177, As Received	111
11	Photomicrograph. Grain Boundary. Type 310 Alloy, Heat X45558, As Received	111
12	Photomicrograph. Cross Section. Type 310 Alloy, Heat 64177, As Received	111
13	Photomicrograph. Cross Section. Type 310 Alloy, Heat X11338, As Received	112
14	Line Drawing. Schematic Drawing of Oxidation Equipment	113
15	Photograph. Specimens and Ceramic Holders	114
16	Photograph. Bending Die and Specimens	114
17	Graph. Penetration vs. Depth Below Surface. Type 309 + Nb Alloy. Run 5	115

LIST OF ILLUSTRATIONS (Continued)

Figure		Page
18	Graph. Penetration vs. Depth Below Surface. Type 310 Alloy, Heat 64177. Run 5	116
19	Graph. Penetration vs. Depth Below Surface. Type 310 Alloy, Heat 64270. Run 5	117
20	Graph. Penetration vs. Depth Below Surface. Type 309 + Nb Alloy. Run 6	118
21	Graph. Penetration vs. Depth Below Surface. Type 310 Alloy, Heat 64177. Run 6	119
22	Graph. Penetration vs. Depth Below Surface. Type 310 Alloy, Heat 64270. Run 6	120
23	Graph. Penetration vs. Depth Below Surface. Type 309 + Nb Alloy. Run 8	121
24	Graph. Penetration vs. Depth Below Surface. Type 310 Alloy, Heat 64177. Run 8	122
25	Graph. Penetration vs. Depth Below Surface Type 310 Alloy, Heat 64270. Run 8	123
26	Graph. Penetration vs. Depth Below Surface. Type 309 + Nb Alloy. Run 9. Straight Section.	124
27	Graph. Penetration vs. Depth Below Surface. Type 310 Alloy, Heat 64177. Run 9. Straight Section	125
28	Graph. Penetration vs. Depth Below Surface. Type 310 Alloy, Heat 64270. Run 9. Straight Section	126
29	Graph. Penetration vs. Depth Below Surface. Type 309 + Nb Alloy. Run 9. Curved Section	127
30	Graph. Penetration vs. Depth Below Surface. Type 310 Alloy, Heat 64177. Run 9. Curved Section	128
31	Graph. Penetration vs. Depth Below Surface. Type 310 Alloy, Heat 64270. Run 9. Curved Section	129
32	Graph. Penetration vs. Depth Below Surface. Type 309 + Nb Alloy. Run 10	130
33	Graph. Penetration vs. Depth Below Surface. Type 310 Alloy, Heat 64177. Run 10	131

LIST OF ILLUSTRATIONS (Continued)

Figure		Page
34	Graph. Penetration vs. Depth Below Surface. Type 310 Alloy, Heat 64270. Run 10	132
35	Graph. Penetration vs. Depth Below Surface. Type 309 + Nb Alloy. Runs 11 and 27	133
36	Graph. Penetration vs. Depth Below Surface. Type 310 Alloy, Heat 64177. Runs 11 and 27	134
37	Graph. Penetration vs. Depth Below Surface. Type 310 Alloy, Heat 64270. Runs 11 and 27	135
38	Graph. Penetration vs. Depth Below Surface. Type 309 + Nb Alloy. Runs 12 and 26	136
39	Graph. Penetration vs. Depth Below Surface. Type 310 Alloy, Heat 64177. Runs 12 and 26.	137
40	Graph. Penetration vs. Depth Below Surface. Type 310 Alloy, Heat 64270. Runs 12 and 26	138
41	Graph. Penetration vs. Depth Below Surface. Type 309 + Nb Alloy. Run 13	139
42	Graph. Penetration vs. Depth Below Surface. Type 310 Alloy, Heat 64177. Run 13	140
43	Graph. Penetration vs. Depth Below Surface. Type 310 Alloy, Heat 64270. Run 13	141
44	Graph. Penetration vs. Depth Below Surface. Type 309 + Nb Alloy. Run 14	142
45	Graph. Penetration vs. Depth Below Surface. Type 310 Alloy, Heat 64177. Run 14	143
46	Graph. Penetration vs. Depth Below Surface. Type 310 Alloy, Heat 64270. Run 14	144
47	Graph. Penetration vs. Depth Below Surface. Type 309 + Nb Alloy. Run 15	145
48	Graph. Penetration vs. Depth Below Surface. Type 310 Alloy, Heat 64177. Run 15	146
49	Graph. Penetration vs. Depth Below Surface. Type 310 Alloy, Heat 64270. Run 15	147
50	Graph. Penetration vs. Depth Below Surface. Type 310 Alloy, Heat X11306. Runs 16 and 28	148
51	Graph. Penetration vs. Depth Below Surface. Type 310 Alloy, Heat X11338. Runs 16 and 28	149

LIST OF ILLUSTRATIONS (Continued)

Figure		Page
52	Graph. Penetration vs. Depth Below Surface. Type 310 Alloy, Heat X27258. Runs 16 and 28	150
53	Graph. Penetration vs. Depth Below Surface. Type 310 Alloy, Heat X45558. Runs 17 and 28	151
54	Graph. Penetration vs. Depth Below Surface. Type 310 Alloy, Heat X46063. Runs 17 and 28	152
55	Graph. Penetration vs. Depth Below Surface. Type 310 Alloy, Heat X46572. Runs 17 and 28	153
56	Graph. Penetration vs. Depth Below Surface. Type 310 Alloy, Heat X11306. Runs 21 and 27	154
57	Graph. Penetration vs. Depth Below Surface. Type 310 Alloy, Heat X11338. Runs 21 and 27	155
58	Graph. Penetration vs. Depth Below Surface. Type 310 Alloy, Heat X27258. Runs 21 and 27	156
59	Graph. Penetration vs. Depth Below Surface. Type 310 Alloy, Heat X45558. Runs 22 and 26	157
60	Graph. Penetration vs. Depth Below Surface. Type 310 Alloy, Heat X46063. Runs 22 and 26	158
61	Graph. Penetration vs. Depth Below Surface. Type 310 Alloy, Heat X46572. Runs 22 and 26	159
62	Graph. Penetration vs. Depth Below Surface. Type 310 Alloy, Heat X45558. Runs 23 and 27	160
63	Graph. Penetration vs. Depth Below Surface. Type 310 Alloy, Heat X46063. Runs 23 and 27	161
64	Graph. Penetration vs. Depth Below Surface. Type 310 Alloy, Heat X46572. Runs 23 and 27	162
65	Graph. Penetration vs. Depth Below Surface. Type 310 Alloy, Heat X11306. Runs 24 and 26	163
66	Graph. Penetration vs. Depth Below Surface. Type 310 Alloy, Heat X11338. Runs 24 and 26	164
67	Graph. Penetration vs. Depth Below Surface. Type 310 Alloy, Heat X27258. Runs 24 and 26	165
68	Graph. Summary Penetration Frequency Curves. Type 309 + Nb Alloy. 100 Hours Duration. Effect of Air Velocity and Humidity	166

LIST OF ILLUSTRATIONS (Continued)

Figure		Page
69	Graph. Summary Penetration Depth Curves. Type 309 + Nb Alloy. 100 Hours Duration. Effect of Air Velocity and Humidity	167
70	Graph. Summary Penetration Frequency and Depth Curves. Type 309 + Nb Alloy. Effect of Cold Work. 100 Hours Duration	168
71	Graph. Summary Penetration Frequency Curves. Type 309 + Nb Alloy. Effect of Time	169
72	Graph. Summary Penetration Depth Curves. Type 309 + Nb Alloy. Effect of Time	170
73	Graph. Summary Penetration Frequency Curves. Type 310 Alloy, Heat 64177. 100 Hours Duration. Effect of Air Velocity and Humidity	171
74	Graph. Summary Penetration Depth Curves. Type 310 Alloy, Heat 64177. 100 Hours Duration. Effect of Air Velocity and Humidity	172
75	Graph. Summary Penetration Frequency and Depth Curves. Type 310 Alloy, Heat 64177. Effect of Cold Work. 100 Hours Duration	173
76	Graph. Summary Penetration Frequency Curves. Type 310 Alloy, Heat 64177. Effect of Time	174
77	Graph. Summary Penetration Depth Curves. Type 310 Alloy, Heat 64177. Effect of Time	175
78	Graph. Summary Penetration Frequency Curves. Type 310 Alloy, Heat 64270. 100 Hours Duration. Effect of Air Velocity and Humidity	176
79	Graph. Summary Penetration Depth Curves. Type 310 Alloy, Heat 64270. 100 Hours Duration. Effect of Air Velocity and Humidity	177
80	Graph. Summary Penetration Frequency and Depth Curves Type 310 Alloy, Heat 64270. Effect of Cold Work. 100 Hours Duration	178
81	Graph. Summary Penetration Frequency Curves. Type 310 Alloy, Heat 64270. Effect of Time	179
82	Graph. Summary Penetration Depth Curves. Type 310 Alloy, Heat 64270. Effect of Time	180
83	Graph. Summary Penetration Frequency Curves. Type 310 Alloy, Heat X11306. Effect of Time	181

LIST OF ILLUSTRATIONS (Continued)

Figure		Page
84	Graph. Summary Penetration Depth Curves. Type 310 Alloy, Heat X11306. Effect of Time	182
85	Graph. Summary Penetration Frequency Curves. Type 310 Alloy, Heat X11338. Effect of Time	183
86	Graph. Summary Penetration Depth Curves. Type 310 Alloy, Heat X11338. Effect of Time	184
87	Graph. Summary Penetration Frequency Curves. Type 310 Alloy, Heat X27258. Effect of Time	185
88	Graph. Summary Penetration Depth Curves. Type 310 Alloy, Heat X27258. Effect of Time	186
89	Graph. Summary Penetration Frequency Curves. Type 310 Alloy, Heat X45558. Effect of Time	187
90	Graph. Summary Penetration Depth Curves. Type 310 Alloy, Heat X45558. Effect of Time	188
91	Graph. Summary Penetration Frequency Curves. Type 310 Alloy, Heat X46063. Effect of Time	189
92	Graph. Summary Penetration Depth Curves. Type 310 Alloy, Heat X46063. Effect of Time	190
93	Graph. Summary Penetration Frequency Curves. Type 310 Alloy, Heat X46572. Effect of Time	191
94	Graph. Summary Penetration Depth Curves. Type 310 Alloy, Heat X46572. Effect of Time	192
95	Photomicrograph. Type I Penetration. Web from Surface	193
96	Photomicrograph. Type II Penetration. Web from Pits	193
97	Photomicrograph. Type III Penetration. Rough Web	193
98	Photomicrograph. Type IV Penetration. Smooth Fissures	193
99	Photomicrograph. Type V Penetration. Developed Web	194
100	Photomicrograph. Type VI Penetration. Coalesced Web	194
101	Photomicrograph. Grain Boundaries Before Testing. Type 310 Alloy, Heat 64270, As Received	194

LIST OF ILLUSTRATIONS (Continued)

Figure		Page
102	Photomicrograph. Penetration and Grain Structure. Type 310 Alloy, Heat 64270, 1700°F and 100 hr	194
103	Photomicrograph. Penetration and Precipitation. Type 310 Alloy, Heat X11306, 1600°F and 100 hr	195
104	Photomicrograph. Penetration and Precipitation. Type 310 Alloy, Heat X11306, 1900°F and 100 hr	195
105	Photomicrograph. Penetration and Precipitation. Type 310 Alloy, Heat X11306. 2000°F and 100 hr	195
106	Photomicrograph. Penetration and Precipitation. Type 310 Alloy, Heat X11306. 2000°F and 10 hr	195
107	Photomicrograph. Developed Web Penetration. Type 310 Alloy, Heat X11338. 1900°F and 100 hr	196
108	Photomicrograph. Developed Web Penetration. Type 310 Alloy, Heat X11338. 1900°F and 100 hr	196
109	Photomicrograph. Oxide-filled Pits. Type 310 Alloy, Heat X45558. 2000°F and 100 hr	196
110	Photomicrograph. Delta Ferrite. Type 309 + Nb Alloy. 1700°F and 100 hr	196
111	Photomicrograph. Sigma Phase or Chromium Nitrides. Type 310 Alloy, Heat X27258. 1600°F and 100 hr	197
112	Photomicrograph. Delta Ferrite near Edge. Type 309 + Nb Alloy. 1700°F and 100 hr	197
113	Photomicrograph. Sigma Phase or Chromium Nitrides near Edge. Type 310 Alloy, Heat X27258. 1600°F and 100 hr	197
114	Photomicrograph. Surface Layer. Type 310 Alloy, Heat X27258. 1900°F and 10 hr	197
115	Photomicrograph. Concentration Gradients. Type 310 Alloy, Heat X45558. As Received	198
116	Photomicrograph. Carbide Precipitation Bands. Type 310 Alloy, Heat X45558. 1600°F and 10 hr	198

Figure		Page
117	Photomicrograph. Carbide Precipitation Bands. Type 310 Alloy, Heat X45558. 1600°F and 10 hr	198
118	Photomicrograph. Carbide Bands and Grain Refinement. Type 310 Alloy, Heat X45558. 1600°F and 100 hr	198
119	Graph. Penetration vs. Depth Below Surface. Type 310 Alloy, Heat X11338. Variability	199
120	Graph. Penetration vs. Depth Below Surface. Type 310 Alloy, Heat X45558. Variability	200
121	Graph. Variability of Mean Penetration Frequency and Depth. Type 310 Alloy, Heats X11338 and X45558	201
122	Graph. Penetration vs. Depth Below Surface. Type 310 Alloy, Heat 31372. As-Received. Effect of Preferred Orientation	202
123	Graph. Penetration vs. Depth Below Surface. Type 310 Alloy, Heat 31372. Cold-Worked 97% and Annealed. Effect of Preferred Orientation	203
124	Graph. Summary Penetration Frequency Curves. Type 310 Alloy, Heat 31372. Effect of Preferred Orientation	204
125	Graph. Summary Penetration Depth Curves. Type 310 Alloy, Heat 31372. Effect of Preferred Orientation	205
126	Photograph. X-Ray Transmission Pattern. Type 310 Alloy, Heat 31372. Cold-reduced 97% in Thickness	206
127	Photograph. X-Ray Transmission Pattern. Type 310 Alloy, Heat 31372. Cold-reduced 97% in Thickness and Annealed in Argon at 2000°F for 5-1/2 hr	206
128	Typical Electron Diffraction Pattern of Rhombohedral Phase	206
129	Typical Electron Diffraction Pattern of Spinel Phase. Some Rhombohedral Phase also present	206
130	Metallographic Appearance of Typical Oxidized Specimen. Surface Unetched	207
131	Metallographic Appearance of Typical Oxidized Specimen Surface after 4 min. Electr. Etch. 0.0004 in. Removed	207

LIST OF ILLUSTRATIONS (Continued)

Figure		Page
132	Metallographic Appearance of Typical Oxidized Specimen Surface after 10 min. Electr. Etch. 0.0004 in. Removed	207
133	Metallographic Appearance of Typical Oxidized Specimen Surface after 12 min. Electr. Etch. 0.0011 in. Removed	207
134	Graph. X-Ray Diffraction Patterns of Typical Scale Components, Cr Radiation	208

AN INVESTIGATION OF INTERGRANULAR OXIDATION IN SOME STAINLESS STEELS

by

Robert E. Keith

I. INTRODUCTION

When a metal is exposed to oxygen or to an oxidizing medium, the usual result is the formation of a more or less continuous and adherent layer of oxide on the exposed metal surface. In general, with increasing time and/or temperature of exposure to the oxidizing medium, this oxide scale, which may be quite complex in its physical and chemical makeup, tends to increase in amount, becoming thicker at the expense of the underlying metal. This results in a progressive movement of the interface between the metal and the oxide layer toward the center of the metallic body. With some alloys, however, in addition to this progressive type of oxidation, there is also oxidation occurring in the metal ahead of the metal-oxide interface. This latter type of oxidation has been variously known as internal oxidation or as subscale formation. Internal oxidation may be further subdivided into cases in which the oxide occurs in a fine dispersion throughout the metal layer just beneath the metal-oxide interface, and cases in which the oxidation takes place

principally in grain boundaries. In this latter type, the surface metal grains retain something like their original appearance even though they may become completely surrounded by a network of grain-boundary oxide. It is this last type of oxidation with which this investigation is concerned.

The results of certain experiments conducted in connection with this investigation will be presented and assessed, and the conditions under which intergranular oxidation may be expected to take place will be set forth in the light of this investigation and the researches of previous workers in the field of oxidation of metals.

II. STATEMENT OF PROBLEM

Although intergranular oxidation of metals and alloys has been observed in the past, little systematic work has been done to determine the factors which influence its occurrence. The objectives of this investigation were to make such a systematic study for a typical alloy and to determine the laws governing intergranular oxidation within the framework of the theories of oxidation which have been proposed to date, extending or modifying these theories as necessary to account for the experimental results.

Experience in the field of metallic oxidation indicates that intergranular oxidation could be affected at least by the variables of time, temperature, initial condition of the metal surface, composition of the metal, nature of the oxidizing medium, application of external stress, and possibly by the state of internal strain in the metal. On a more fundamental plane, a basic factor controlling intergranular oxidation should be the relative grain orientations on either side of the grain boundary in question. The present research included all of these variables except the initial condition of the metal surface and the nature of the oxidizing medium.

A stainless steel was selected for use in the experimental program because stainless steels are known to be subject to intergranular oxidation and because there was some prior evidence that conclusions concerning the mechanism of intergranular oxidation drawn on the basis of one stainless steel composition could likely be extended with relatively

minor modifications to include the whole wide range of stainless steel compositions. The particular type of steel selected is known as type 310 stainless steel, and has a nominal composition of 25 weight per cent Cr and 20 weight per cent Ni. Specimens were obtained from eight different heats of type 310 alloy. Six of these were furnished through the courtesy of the United States Steel Company and were selected in such a manner that their range of variation in contents of the elements Cr, Ni, C, Mn, Si, S, and P was as large as possible within the commercial specification limits for the type 310 composition.

The six commercial heats were very likely made according to the usual practice employed by the United States Steel Company, although no specific data were available on these particular heats. This practice consists of melting in an electric furnace under an oxidizing slag, during which operation the C is lowered to below the desired level; slagging off; introducing a reducing slag; making final adjustments of C, Cr, and Ni compositions; tapping; and pouring into ingot molds. No special deoxidizing is done because, although the O level is high relative to an intentionally killed steel, there is no rimming action because of the high Cr content. Ingots to be formed into sheets are conditioned and hot-rolled to the form of slabs about 3 in. thick at temperatures between 2050° and 2100°F. The slabs are conditioned again and hot-rolled to thicknesses between 1/4 and 1/2 in., in which form they are known as sheet bars. The sheet bars are again conditioned and hot-rolled to thicknesses somewhat greater than the desired

final thicknesses. The sheets are then annealed at 1975°F and water quenched. Next the sheets are given a NaH descale and a HNO_3-HF pickle. The sheets are then cold-rolled almost to size, a reduction of 18 per cent for sheets of the thickness used in this investigation. The sheets are then given another 1975°F anneal and water quench, NaH descale, and a wash pickle. Following these operations, the sheets are roller leveled, stretcher leveled, and sheared to size.

The other two heats of type 310 alloy (heats 64177 and 64270) were special heats having substantially different compositions from the other six heats. Also included in the investigation as being representative of even larger compositional variation were specimens from one heat of type 309 alloy (25 weight per cent Cr, 12 weight per cent Ni) stabilized with an addition of Nb. These last three heats were obtained through the courtesy of the General Electric Company. Chemical compositions of the nine heats are presented in Table 1. Photomicrographs of the as-received materials are presented in Figures 1 through 9. All of the specimens were in the form of sheet, and ranged from 0.04 to 0.06 in. in thickness. The surfaces were smooth and bright in the as-received conditions (United States Steel heats had a standard 2D finish), and no further treatment was given to the surfaces other than to clean them just prior to oxidation.

It will be noticed from Figures 1 through 9 that there is considerable difference in appearance among the different heats. There was also considerable difference in their etching characteristics. Upon metallographic examination at high

magnification, it was found that the differences resulted from the presence of a grain boundary carbide network in heats 64177, 64270, X11338, and X46572. A photomicrograph of this network appears in Figure 10, and an example of a grain boundary of a heat in which no grain boundary network was present is shown in Figure 11 by way of contrast.

Each heat of alloy stock was also examined in cross section in the as-received condition in order to ascertain the subsurface condition. It was found that of all the heats, only heat 64177 showed subsurface defects. These defects took the form of already-existing intergranular oxide penetration, an example of which is shown in Figure 12. For comparison, Figure 13 shows an example of a good surface from one of the other heats. It was later found that there had been considerable difficulty in the mill processing of heat 64177, which doubtless accounts for the presence of the intergranular penetration.

The experimental program adopted consisted of exposing specimens to dry, moving air at temperatures between 1600° and 2000°F for times up to 100 hr. The resulting severity of intergranular attack was determined metallographically for each specimen. Oxide scales from representative specimens were analyzed by x-ray diffraction techniques, and analyses of the intergramular oxides were made by electron diffraction. Visual appearances of the specimens and scales were noted, and magnetic tests were made on both specimens and scales. Data were evaluated and interpreted in terms of a proposed mechanism of intergranular oxidation.

III. SURVEY OF LITERATURE

External Scaling

The basis of modern theoretical developments in the field of metallic oxidation is the theory of semiconductors largely developed by Wagner in a series of publications in the years since 1933. Wagner's theory applies to thick scales in which diffusion through the scale is the controlling factor. The theory presupposes that semiconducting oxides have a number of possible defect structures consisting of "ion defects" and "electron defects". From theoretical deductions, Wagner and others have been able to determine the types of defect structures present in a fairly wide selection of oxides. This has largely been done either by predicting what effects additions of small quantities of oxides of metals of higher or lower valence would have on the electrical conductivity of the oxide in question, or by predicting the dependence of electrical conductivity of the oxide on the oxygen pressure. Measurements of cation and anion transport numbers, the fraction of the electric current carried by cations and by anions, respectively, have been made on some oxides. Thus for some of the more common oxides, a fairly complete picture exists of their kinetics and mechanisms of formation. An excellent critical summary of Wagner's theory is given in the recent and very comprehensive monograph by Kubaschewski and Hopkins (1).

Wagner's theory in its present stage of development applies only for pure metals, and it has been pointed out (2)

that the parabolic weight gain-vs.-time relationship, which is predicted by his theory and which is characteristic of almost all scaling processes of pure or nearly pure metals which are controlled by diffusion through the scale, cannot be expected to hold precisely for alloys. Nevertheless, it has been possible to make some predictions for alloy systems based on Wagner's theory, insofar as the development of oxidation-resistant alloys is concerned. Two possibilities are outlined for such development. First, a metal of fairly high melting point should be selected as the basis metal, and the type of defect structure of its stable oxide or oxides likely to form should be ascertained. Alloying elements soluble in the oxides can then be selected in such a manner as to decrease the number of oxide lattice defects. An example of this approach is the improvement in the oxidation resistance of Zn resulting from additions of small amounts of Al. A second approach is to attempt to cause the formation of the protective oxide of an alloying element having a low-conductivity oxide and being more easily oxidizable than the basis metal. This alloying element must be added in sufficient concentration to form a thin, continuous layer of its oxide at the metal surface. It is characteristic in such cases that the oxide of the basis metal will form a layer outside the layer of oxide of the alloying element, but at a rate controlled by the cationic diffusion rate of the basis metal through the inner oxide layer. The improved oxidation resistance of Fe-Al alloys relative to pure Fe, for example, is due to the formation of a thin,

continuous, compact film of Al_2O_3 on the metal surface early in the oxidation process. It might be mentioned here that it is sometimes possible to preoxidize an alloy for a short time at a low oxygen pressure, thus obtaining only the thin protective alloying element oxide without any of the basis metal oxide (3). The addition of an alloying element which is more noble than the basis metal has been found to have surprisingly little effect on the oxidation resistance of the alloy. The nobler element tends to concentrate in the metal layer just below the metal-oxide interface, diffusing ahead of the scale, but since most metal-through-metal diffusion rates are of about the same order of magnitude, the layer of nobler alloying element does not offer serious hindrance to the passage of basis metal ions which subsequently react with oxygen.

It should be borne in mind that the above discussion applies to thick scales, in which the assumption can be made that the electron concentration is uniform throughout the thickness of the scale. The mechanism of the formation of thin films, however, must differ considerably from the scaling mechanism, because it has been observed experimentally that films are subject to different growth laws from those laws governing the formation of thick scales. Film growth laws having asymptotic, logarithmic, and cubic forms, as well as parabolic forms having different rate constants from those of subsequently-formed scales, have been observed. Furthermore, the effects of temperature on film formation rates are very unpredictable, while most true scales have an Arrhenius-type temperature dependence (4), at least in simple systems. A fairly

satisfactory theory of thin film formation has been proposed by Cabrera and Mott (5). This theory is based on the existence of a strong electric field across the film, which arises from the close proximity of positive metal ions and negative oxygen ions which are adsorbed on the surface of the film. The electric field, rather than concentration gradients, is believed to be responsible for the migration of metal and oxygen ions and subsequent growth of the film to sufficient thickness for the Wagner theory to apply.

Two very interesting papers consider the effects taking place in a metal itself as a result of the operation of an oxidation mechanism involving transport of cations through the scale from the metal-oxide interface to the oxide surface (6, 7). Such a mechanism must create a lattice vacancy in the metal for each cation diffusing. It is pointed out that groups of these vacancies will tend to come together at certain points along the metal-oxide interface, leading, it is postulated, to the formation of "blisters" or of areas of nonadherent scale. The existence of these vacancies and the consequent formation of areas of nonadherent scale on the specimen surface is a necessary characteristic of any scale forming by cation transport. It is not meant to imply that all cases of formation of nonadherent scales are the result of a cation transport mechanism of scale formation, for certainly the metal-oxide volume ratio, sometimes known as the Pilling-Bedworth ratio, is a major factor in scale adherence, as are relative thermal expansion coefficients and gas evolution.

A large volume of experimental work has been done on the scaling processes of a number of pure metals and alloys, and some general principles governing the formation of oxides on the surface of binary alloys have been established. It seems reasonable to consider the entire range of composition of a general binary alloy in three subdivisions: 1) at the noble metal end of the system, where only the oxide of the more noble metal is present, although the less noble metal may be dissolved in it; 2) at the less noble metal end of the system, where only the oxide of the less noble metal is present, possibly containing some of the more noble metal in solution; and 3) in the intermediate range of composition, where either heterogeneous oxide layers or double oxides, such as spinels, may be formed. Theoretical predictions have been made concerning the compositional extent of these three regions (8, 9), which have been fairly satisfactorily verified experimentally. Judging from these predictions, it seems likely that complex alloys in which even the minor alloying elements occur in as high percentages as they do in stainless steels would fall in the third, or intermediate, range. Experimental studies on stainless steels show that at least one spinel and a rhombohedral oxide solid solution are present in the scales occurring on this type material.

Beginning detailed discussion with the oxidation of pure Fe, it has been shown that when Fe is exposed to oxygen, three distinct layers of oxide are formed, the innermost layer consisting of the lowest oxide, FeO; the intermediate layer consisting of Fe_3O_4; and the outermost layer consisting of the

highest oxide, Fe_2O_3 (7, 10, 11). Recent studies by Davies, Simnad, and Birchenall (10), using marker techniques, have revealed the mechanism of formation of these three oxides. It was found that FeO forms almost entirely by Fe transport, Fe_2O_3 almost entirely by O transport, and Fe_3O_4 about 80 per cent by Fe transport and 20 per cent by O transport. Such a picture fits in well with the dynamic concept of an oxidation process which would result in the formation of the three observed oxide layers. A further point is that in these oxides, and indeed in just about all oxides in dynamic equilibrium with their metals, there may be rather large deviations from stoichiometric compositions. It is these deviations which allow the formation of the concentration gradients which provide the driving force for diffusion.

For Fe-Cr-Ni alloys, the external scales have been shown to consist of a face-centered cubic phase and a rhombohedral phase. The cubic phase has been variously identified as being Fe_3O_4, $FeCr_2O_4$, $NiCr_2O_4$, or $MnCr_2O_4$ (12, 13, 14). All of these spinels have rather similar lattice parameters. The rhombohedral phase has been shown to consist of α-Fe_2O_3, Cr_2O_3, or a solid solution of these two oxides. The α-Fe_2O_3-Cr_2O_3 system consists of a single solid solution area with lattice parameters which change slightly over the composition range. The absence of NiO as a major scale component is at first glance unexpected, considering the amount of Ni present in the alloy. Identification of NiO by diffraction techniques when in the presence of the spinel phase is difficult, however, owing to the fact that NiO, having

almost an NaCl type of face-centered cubic structure, has a lattice parameter (4.176 kX) of half that of the possible spinels in the scales (which range between 8.299 and 8.502 kX). Therefore, the NiO lines coincide with some of the spinel lines. Investigators who have coupled X-ray investigations with chemical analyses of their scales, however, (15, 16), have shown that Ni is indeed present in the scales only in very small amounts, usually of the order of a per cent. One group of investigators has reported a layer of NiO at the metal-oxide interface (17). Furthermore, in the case of Fe-Ni alloys, in which the Fe oxidizes preferentially, there is a tendency for islands of Ni-rich metal to be entrapped in the deeper portion of the scale (18, 19, 20), although there is almost no Ni in the outer scale layers. Apparently no such entrapment takes place in the stainless steels. When the problem of Ni is studied a little more deeply, it develops that of all of the elements occurring in stainless steels, both major and minor components, Ni and Cu are the only ones which are more noble than the Fe basis metal. It is therefore thermodynamically reasonable to expect that NiO should be among the last oxides to form, and that, for relatively short times of oxidation, at least, the Ni should be able to diffuse back into the metal ahead of the advancing oxide front. The driving force for this diffusion would have to be the increased concentration of Ni at the metal-oxide interface resulting from the preferential oxidation of the other components. At some late stage in the oxidation, as the other component metals begin to be exhausted, the equilibrium oxygen pressure at the metal-oxide

interface would rise sufficiently to allow the stable formation of NiO. This would account for the above-noted observation of NiO at the interface. In the case of the Fe-Ni alloys, in which the oxidation rate is considerably faster than in the stainless steels, there is apparently not sufficient time for the Ni to back-diffuse, and it is therefore entrapped in the scale.

The time sequence in which the various alloy components of the Cr-Ni stainless steels oxidize is of interest. In the stainless steels, as in alloy systems in general, those cations will tend to oxidize first which have the highest thermodynamic activity. From the standpoint of the mass action law, those oxides will tend to form first which have the lowest dissociation pressure. If one constructs a table of enthalpies of formation of the usually-occurring oxides of the cations composing stainless steel (see Table 14), one finds that the cations, ranked in order of descending heats of formation of their oxides are: Si, C (to CO_2), Mn, Cr, P, Fe (to Fe_3O_4), Fe (to FeO), Ni, Fe (to Fe_2O_3), and S. Experimental observations on the oxidation of some of these elements in stainless steels (C, P, and S) are difficult to make, but data available in the literature (21, 22) indicate that C, Si, and Cr oxidize preferentially to the Fe basis metal.

The distribution of the various oxides in the scale layers, however, bears no direct relation to the order of oxidation. It has been shown (16, 23) that there may be large differences between the concentration of a given

element in the alloy and its concentration in the scale. In the case of a binary alloy in which oxides of both the more noble and the less noble metal form, the general rule is that a layer of the less noble metal oxide first forms at the metal-oxide interface, and subsequently a layer of the more noble metal oxide forms at the air-oxide interface (1).

All of these observations indicate that the scaling process in the stainless steels is a complicated one, involving simultaneous inward diffusion of some ions, notably O and Ni, and outward diffusion of other ions, among them C, Cr, Fe, Mn, and Si. Other ions, such as P and S, have not been studied in detail, but presumably have little effect on the oxidation process if they are held to the very small concentrations (of the order of 0.01 per cent) in which they usually occur in common grades of steels.

The oxidation resistance of the Cr-Ni stainless steels has long been attributed to the formation of a protective oxide. The requirements for a protective oxide have been established qualitatively. These requirements are: 1) the oxide layer must be coherent with the matrix and of a high degree of perfection, i.e., there must be freedom from cracks, pores, and other alternate diffusion paths; 2) the diffusion rates of both anions and cations through the oxide must be small; and 3) no low-melting oxide eutectics should be formed. The requirement of low diffusion rates is equivalent to a requirement that the oxide have a low electrical conductivity, since electron transport is necessarily concomitant with ionic transport in order that electrical neutrality be maintained.

In the case of stainless steels, there has been a difference of opinion as to which of the oxides in the scales is responsible for the oxidation resistance of these alloys. It was long believed that the single protective oxide on stainless steels was Cr_2O_3, and it is certain that Cr does have a highly beneficial effect on oxidation resistance. The spinel phase, however, may also be a major factor in oxidation resistance (12, 24, 25, 26). Although little experimental work has been done on spinels, it appears that the conductivities of spinels are usually less than those of their component oxides in the pure state. It has been shown that yet a third compound, SiO_2, may also play an important role in oxidation resistance of the stainless steels. Preece, et al., (18) observed an SiO_2-rich film at the metal-oxide interface in 4 per cent Si steels oxidized in sulfur-free furnace atmospheres. Gulbransen and McMillan (27) have reported the existence of a thin layer of SiO_2 at the metal-oxide interface of heat-resistant alloys of the 80Ni-20Cr type, and it was known for some years previously that Si improves the life of this class of alloys. Radavich (28) has reported a similar layer on stainless steels. Apparently the reasons that this layer has not been reported earlier are that it is too thin to be metallographically observed in cross-section (8000 A. or less, capable of showing interference colors), and that it is situated at the metal-oxide interface, which might cause it to be lost or overlooked during scale removal. Perhaps this latter reason accounts for Bandel's failure to find Si in the scales of the Fe-base, Cr-Ni-Si alloys he studied (22).

From a conductivity standpoint, SiO_2 should be very desirable, since it has a conductivity five orders of magnitude smaller than that of Cr_2O_3 (1). At the present stage of knowledge, the oxidation resistance of stainless steels cannot be ascribed definitely to any one of the three oxides: Cr_2O_3, the spinel phase, or SiO_2. In fact, all three oxides very likely contribute to the oxidation resistance, perhaps more or less equally. Warr (29) and Boren (30) used the presence of both the spinel phase and Cr_2O_3, which almost always occur together, as their criteria for a protective scale. McCullough, Fontana, and Beck (16) reported that, on Cr steel and 18Cr-8Ni steel, oxidation resistance was high as long as the spinel layer remained intact. They found that after prolonged exposure, the spinel layer ruptured. An oxide consisting largely of Fe_2O_3 was then found to form at the points of rupture of the spinel, and the oxidation resistance of the steel was partly lost.

Internal Oxidation

The formation of a layer of alloying metal oxide particles in the region below the metal-oxide interface in Cu-base and Ag-base alloys, where Cu and Ag were the nobler metals, has been noted by several investigators (31, 32, 33). Perhaps the most systematic study of this "subscale" layer has been the work of Rhines (31) on Cu-base alloys. Several of Rhines' observations are pertinent to the present investigation and will be discussed in some detail. It was found that the depth of the subscale was a direct function of temperature and time of oxidation; that the number of individual

oxide particles per unit volume of subscale decreased with increasing temperature and decreasing oxide stability, the individual particles becoming larger; that at lower temperatures of oxidation, the subscale particles tended to concentrate at grain boundaries, while at higher temperatures, the distribution of particles tended to be random; that the depth attained by the subscale varied as an inverse function of the amount of alloying element, no subscales being formed when the concentration of alloying element exceeded about 1 or 2 per cent. In the case of ternary Cu-base alloys, it is possible to form two superimposed subscales, one of each of the two alloying elements. Rhines lays down four necessary conditions for subscale formation: 1) a solubility of oxygen in the alloy; 2) the ability of oxygen to diffuse at an appreciable rate into the alloy; 3) the possibility of formation by the alloying element of an oxide more stable than the oxide of the base metal; and 4) a relatively low solubility of the oxide in the base metal.

Intergranular Oxidation

As intimated from the results of Rhines described in the previous section, intergranular oxidation may be considered as being a special case of low-temperature internal oxidation. A temperature that is "low" for one alloy system, however, may be "high" for another system.

Intergranular oxidation has been reported for Fe-Ni alloys as early as 1929 in the classic article of Pfeil on metallic oxidation (19). Similar observations have been

reported subsequently by various investigators for this system (18, 20). Apparently in Fe-Ni alloys, oxidation proceeds sufficiently rapidly at grain boundaries so that islands of metal are surrounded by the advancing scale and subsequently become enriched in Ni by preferential oxidation of the Fe.

In the Cr-Ni alloys such as those commonly used as electrical heating elements, and having compositions close to 80 per cent Cr and 20 per cent Ni, a form of intergranular oxidation known as "green rot" has long been known. In this type of attack, there is preferential oxidation of the Cr, principally in the grain boundaries, forming the green oxide, Cr_2O_3. Subsequent intergranular fracture of the weakened metal exposes this oxide; hence the picturesque name. Recent investigations of Spooner, Thomas, and Thomassen (34) have shown that green rot tends to occur under conditions of low oxygen pressure. Essentially, the low oxygen pressure results in a decrease in the overall rate of oxidation, thus allowing time for the establishment of some degree of thermodynamic equilibrium in the system. Since NiO is a less stable oxide than Cr_2O_3, the reaction

$$NiO + Cr \text{ (in alloy)} \longrightarrow Ni + Cr_2O_3$$

tends to take place.

In 1936, Baeyertz (21), in a metallographic study of the oxidation process in steels ranging from plain carbon steels up through 18-8 stainless steel, showed the presence of intergranular oxidation products in all of the steels, and in the case of stainless steel, identified the products as being vitreous silicates and a Cr_2O_3-rich phase.

Fisher (35) has developed a mathematical treatment for an idealized case of grain boundary diffusion (The same equation can be applied to surface diffusion also.) and has shown that in diffusion experiments, lack of dependence of the diffusion rate on grain size is not a valid indication that the grain boundary diffusion coefficient and the matrix diffusion coefficient are equal. The ratio of the boundary coefficient to the matrix coefficient may easily be several powers of 10. Fisher's model consists of a bicrystal having a plane grain boundary normal to the free surface. A layer of the element M to be diffused is assumed to be located on the free surface. The assumption is made that the grain boundary diffusion coefficient of M is greater than its volume diffusion coefficient. A coordinate system is set up such that x lies in the free surface and perpendicular to the grain boundary, and y is perpendicular to the free surface and lies in the plane of the grain boundary. The visualization of the diffusion process is then that M diffuses to a greater depth in the y direction in the grain boundary than in the grains themselves because of the larger grain boundary diffusion coefficient. Simultaneously, M from the grain boundary will tend to diffuse out into the grains below the level of the M diffused into the grains from the surface. This mechanism will result in isoconcentration contours having a cusped shape, the cusp occurring at the grain boundary and pointing away from the free surface. An example of this sort of appearance is shown in Figure 114. Making the further assumptions (a) that the grain boundary is a zone of uniform width δ ; (b) lateral

diffusion into the grains occurs normal to the grain boundary; (c) the amount of M in the boundary region is negligible compared with the amount lost by lateral diffusion; (d) with respect to lateral diffusion the concentration within the boundary region is constant at its final value for the entire time of diffusion t; (e) $\partial C/\partial t = 0$ in the boundary at time t. Making these assumptions, an expression can be derived for the concentration of laterally diffusing material in the vicinity of the grain boundary. This equation is as follows:

$$C = C_o \exp\left[-(4 D_v/\pi t)^{1/4} y/(\delta D_{gb})^{1/2}\right] \operatorname{erfc}\left[x/2(D_v t)^{1/2}\right] \quad (1)$$

where C and C_o are general and surface M concentrations, respectively; D_v and D_{gb} are the volume and grain boundary diffusion coefficients, t is the diffusion time, δ is the width of the grain boundary, and x and y are the previously defined coordinates.

LeClaire (36), by differentiating equation (1) considering x and y variables, has obtained an interesting result:

$$D_{gb}/D_v = \left[2(\pi D_v t)^{1/2} \cot^2 \varphi\right]/\delta \quad (2)$$

where φ is the half-vertex angle of the cusp of an isoconcentration contour; or, expressed mathematically, φ is (dy/dx) at x = 0. There is a fallacy in this differentiation,

since the grain boundary, in which x is here taken to be equal to zero, was previously assumed to have a width in the positive x direction amounting to $\delta/2$, and Fisher's equation does not apply within the grain boundary itself. Technically, then, the derivative at x = 0 has no meaning. Actually, δ is usually taken as being about 5 A., which is practically zero in comparison to the distances involved in the diffusion.

Using LeClaire's equation, if in a physical case one measures φ, knows D_v from diffusion data, and assumes a value for δ, one can solve directly for D_{gb} for that grain boundary.

Effect of Relative Grain Orientation on Intergranular Oxidation

The problem of intergranular oxidation is a specific case of the problem of grain boundary diffusion, complicated by compound formation. There have recently been two investigations published concerned with grain boundary diffusion of Ag in Cu and grain boundary self-diffusion in Ag dependence upon the relative orientation difference between the two grains on either side of the grain boundary. Achter and Smoluchowski's study (37) showed that the grain boundary diffusion constant was essentially that of the matrix for grains whose relative orientations differed by less than approximately 17° measured in a plane perpendicular to the grain boundary and the external surface. For orientation differences greater than 17°, the grain boundary diffusivity increased rapidly to a maximum at 45°, returning to the matrix diffusivity level for orientation differences greater than

about 73°. According to Hoffman and Turnbull (38), the grain boundary diffusion coefficient increases to its maximum value very rapidly and for very small differences in orientation.

Snoek (39), in an effort to obtain a material having a constant magnetic permeability, attempted to form an oxide envelope around the grains of a sheet of Fe-Ni alloy having a strongly developed cube texture. It was found that oxygen could not be made to go down the grain boundaries of this material, although it would diffuse along the grain boundaries of a specimen of unoriented sheet stock.

In experiments concerned with the effect of cold work on oxidation of pure Fe and pure Cu, Benard (40) found that cold work up to 80 per cent reduction in cross section resulted in a linear increase in the oxidation rate, measured as weight gain per unit area, such that the oxidation rate at 1562°F for Fe reduced 80 per cent was about 1.5 times that of material having no cold work. Benard also noticed differing rates of oxide growth on different metal grains depending upon their orientation with respect to the surface.

IV. EXPERIMENTAL INVESTIGATION

Oxidation Equipment

The oxidation equipment used in the investigation consisted of four tube-type laboratory furnaces. A schematic drawing of such a furnace with its associated air and power supply is shown in Figure 14. Air at approximately 90 psig passes through a porous Al_2O_3 filter to remove any entrained oil, sediment, or other foreign matter. The air then passes through a pressure-reducing valve and then through two drying towers, the first filled with activated alumina and the second filled with phosphorus pentoxide. A valve is provided to bleed off a sample of the dried air for a dewpoint determination at suitable time intervals, using a General Electric Model 5993823G4 Dew Point Indicator. The air is delivered to a manifold from which four side streams are withdrawn, one to each of the four horizontal tube furnaces. Flow to each furnace is controlled by a needle valve, and is metered by a flowmeter of the rotameter type in conjunction with a manometer. The air is then delivered to one end of a 2-in. sillimanite tube in the furnace. This tube is concentric with a similar, but shorter, 3-in. sillimanite tube in the furnace. The chromel heating wire is wound about the latter tube and imbedded in alundum cement. There is a 5-in. layer of vermiculite insulation contained in an aluminum shell around the heating coils. The furnace draws approximately 12 amperes at 220 volts. The 2-in. tube is packed for approximately one-third its length with broken pieces of ceramic, the purpose of which is to provide a large surface area to preheat the

incoming air. A thermocouple well extends into the furnace as close as possible to the location of the specimens, which are in the center portion of the 2-in. tube and are supported on ceramic fixtures consisting of combustion carbon-analysis boats with their covers cemented in an inverted position (Figure 15). The uniform temperature zone of the furnace, in which as many as three of these boats are placed, is approximately 8 in. long. The temperature is controlled by means of a Foxboro controller with the control thermocouple imbedded in the furnace windings.

Considerable difficulty was encountered in the early part of the program from an inability to maintain a sufficiently low dew point throughout a 100-hr. run using only the alumina dryer. Although the form of alumina used contained a cobalt salt intended to indicate by a color change when the alumina became useless, it was found that the alumina ceased to adsorb an appreciable amount of moisture long before the color change took place. Furthermore, the alumina dryer alone was seldom capable of producing air with a dew point lower than -20°F, whereas it was felt that a dew point of -40°F would have been more desirable. Accordingly, a stainless steel vessel was constructed to hold alternate layers of phosphorus pentoxide and glass wool. This dryer was connected in series following the alumina dryer between runs 13 and 14. The alumina was replaced with regenerated material every 100 hr.; the phosphorus pentoxide dryer, once filled, lasted over 1500 hr. without attention. At that time, it was opened and the contents were replaced, although from their

appearance it was not necessary. With this combination of dryers, it was possible to maintain a dew point of -35° to -40°F consistently.

Specimen Preparation

Rectangles 1/2 x 1 in. were first scribed on the sheet stock. Single small punch marks were then placed on one side of the sheet in one corner of each rectangle, thus permanently identifying the sides of the specimens relative to the original sheet. The specimens were then cut from the sheet using a shear. Shearing was found to be superior to bandsawing because it resulted in a neater edge and also gave fewer scratches on the faces of the specimens, which were tested without further surface treatment other than cleaning. Specimens were given code numbers which identified their original positions in the sheets. These numbers were recorded on the individual envelopes in which the specimens were stored, no markers being placed on the specimens themselves.

Oxidation Equipment Operation

Before starting an oxidation run, the furnaces were brought to temperature and the air was allowed to flow through them for a period of 2 - 4 hr. to establish thermal equilibrium. An air flow rate of 30 ft/min at the furnace temperature was selected as standard. This air velocity was sufficiently great to deliver oxygen to the specimen surfaces faster than it could take part in the oxidation reaction, and thus assured that the oxidation resulting on the surfaces of the specimens would be truly representative of the kinetics of the oxidation process

as limited by the scale diffusion reactions. Usually, one furnace was operated at each of the temperatures 1600°, 1700°, 1800°, and 1900°F, and one specimen of each of three heats was assigned to each furnace at random. In the later runs, in which all the furnaces were operated at 2000°F, specimens from all nine heats, including some duplicates, could be run simultaneously. Prior to charging, the specimens were cleaned with acetone and placed in the ceramic fixtures previously described and illustrated in Figure 15.

During the runs, readings of furnace temperatures, air flow rates, air pressure, and room temperature were taken twice a day. Barometer readings and dew point readings of the furnace air were taken once a day, and the furnace temperature controllers were balanced once a day. Runs were of 10, 30, and 100-hr. duration, except for one 50-hr. run and one 77-hr. run.

At the conclusions of the runs, the specimens were quenched into distilled water in stainless steel beakers, in order to avoid the loss of any scale, to arrest any phase transformations which might have taken place in the oxides on slower cooling, and to preserve the carbide distributions existing in the metal at the test temperatures. The contents of the beakers were then filtered through coarse filter paper and the solids on the paper were washed with acetone and then with ether to accelerate drying. After the filter papers had dried, their contents were brushed off and bottled. The total elapsed time between the quenching and the completion of the bottling operation was about 1 hr. Any loosely adhering scale

was gently scraped off the surface of the specimens with a surgical scalpel and was combined with the bottled scale.

Evaluation of Specimens

The visual appearances of the specimens were recorded, after which a lengthwise strip approximately 1/8 in. wide was cut from each specimen and discarded, in order to assure freedom from edge effects in the subsequent measurements. A 90° bend was then accurately put into each of the specimens perpendicular to the sawed edge using the specially designed die illustrated in Figure 16.

At this point, qualitative magnetic tests were made on the specimens. To make these tests, a specimen was placed on a glass plate resting on the bent portion, both "legs" extending upward. The specimen was then set in motion by a gentle tap, and, while it oscillated, an Alnico magnet was brought near, but not touching, the specimen and parallel to one of the flat faces. If there was no noticeable attractive effect or change in periodicity of the motion, the specimen was classified as "not detectably" magnetic. If the reverse was true, the specimen was allowed to come to rest and the magnet was again brought up parallel to a flat face. If the specimen moved violently so that the face touched the magnet, it was classified as "strongly" magnetic. If the specimen could be made to move slightly, although not sufficiently to touch the magnet, it was classified as having "medium" magnetism. If a specimen proved to belong to neither of these latter two classifications, it was recorded as being "weakly" magnetic in view of the magnetism shown in the first test,

when the specimen was already in motion. Obviously, this test is qualitative, and too much emphasis must not be placed on the classifications themselves. Their only importance is the fact that almost all the specimens showed increases in magnetism after oxidation, as will be discussed subsequently.

Following the magnetic tests, the specimens from each heat were mounted, several to the mount, in bakelite with the sawed sides exposed. An untested specimen, or control, was included in each mount in the majority of cases. Considerable experimentation was carried out before a satisfactory polishing technique was developed. The technique finally adopted consisted of grinding the sawed edge of each specimen smooth and beveling it very slightly before mounting. Rough polishing was done under water using 240-grit silicon carbide paper. Finer polishing was done using 400- and 600-grit silicon carbide papers, also wet, which were mounted on metallographic wheels. Final polishing was done on a low-nap metallographic wheel impregnated with 2-micron diamond paste. The resulting polish was not scratch-free, but it was adequate. It was not found to be possible at first to use such relatively soft abrasives as Gamal, Linde "B", or C-RO, to obtain a smoother surface, since with these abrasives the oxides and inclusions tended to tear out. A finer, 1/2-micron diamond polishing compound was also tried, but it proved excessively difficult to keep the wheel free from contamination, and its use was stopped. At the very end of the experimental program, it was found that a satisfactory

final polish could be obtained by using a large quantity of a thick paste of Linde "B" (levigated alumina) on a low-nap wheel.

All of the early specimens, and many of the later ones, were examined at 1000X in the unetched condition using bright field, dark field, and polarized illumination. The latter two contributed little to the investigation. Unusual areas were noted for future reference and/or photographed.

After polishing and metallographic examination, measurements were made of the extent of intergranular penetration, which was clearly visible in properly polished unetched specimens. To make these measurements, a desk microscope with a 4-mm objective lens, a travelling stage, and a Bausch and Lomb grain-size eyepiece was used. Magnification was approximately 500X. The edge of a specimen cross section was aligned with one edge of the square A.S.T.M. No. 6 grid of the eyepiece, and the entire straight portion of the specimen edge was traversed. The bent portion of the specimen was not read (except in Run 9). For convenience, scratches had been previously made on the polished surface to mark the beginnings of the bent portion of the specimen, and readings were made up to a scratch. Initial and final stage positions were recorded for each straight portion. All readings were begun at a distance of 1 mm from the corner of the specimen, to avoid edge effects. As a traverse was made, the number of intergranular fissures ending in each of the six rows of the grid parallel to the specimen edge was counted using a desk counter, and was

recorded. This same procedure was repeated for the other three straight portions of each specimen (both sides of both straight "legs"--a total of four).

During the course of the project, penetration measurements were made by five different technicians. Considerable pains were taken to see that satisfactory agreement was attained among the technicians reading the same specimens before they were allowed to proceed to specimens which had not yet been measured. Checks were made from time to time by having different technicians repeat a specimen counted by one of the other technicians. It was found that readings of the number of penetrations in a given surface made by different technicians usually agreed within about 5 per cent on all but the shallowest group of fissures, those between 0 and 0.00063 in. in depth. On these shallow penetrations, operator variability ran as high as 30 per cent. This lack of agreement in the shallow group is understandable when it is considered that many of the fissures in this group were of the order of 0.0002 in. or less in depth, the order of magnitude of the surface roughness. In addition, even slight polishing scratches and tears can produce effects likely to be mistaken for shallow penetration, especially in specimens in which there is little true penetration. For these reasons, too much confidence must not be placed in the actual numbers obtained for penetrations less than 0.00063 in. deep.

The figures for penetration in the four portions of a single specimen were added and divided by the total length traversed (from 1.1 to 1.4 in.) to put data from different

specimens on a comparative basis. The sizes of the squares of the eyepiece grid had been previously determined, by calibration with a stage micrometer, to be 0.00063 in. on a side. Using this calibration, a frequency-vs.-depth curve could be constructed for each specimen by plotting a bar chart and then drawing a smooth curve to fit the data. Curves constructed by this process appear in Figures 17 through 67. Theoretically, any curve obtained by this method would tend to be biased toward the shallow side, even if the counting were completely accurate, because the probability of any fissure's ending precisely at the plane of polish, and thus the probability of its being observed in its true depth, is quite small.

To condense the data further, it was decided to examine the behavior of two parameters of the frequency-vs.-depth curves. The parameters, N and X, are defined as follows:

$$N = \int_0^s n(s)\, ds \cong \sum_{i=1}^{7} n_i \qquad (3)$$

and

$$X = \frac{\int_0^s sn(s)\, ds}{N} \cong \frac{\sum_{i=1}^{7} a_i n_i}{N} , \qquad (4)$$

where n_i is the number of fissures per inch of specimen surface in the ith group, a_i is the midpoint of the ith group measured from the surface, and s is the depth coordinate. The data were taken in seven groups: the six levels of the grid and a seventh class, rarely occurring, consisting of fissures which extended past the sixth grid level and which were arbitrarily assigned a group midpoint one grid level

(0.00063 in.) beyond the sixth level. It can be seen that the parameter N is simply the total number of fissures per inch of all depths. The parameter X is a mean penetration depth; more precisely, X is the first moment of the penetration-vs.-depth curve with respect to the y-axis (or specimen surface) divided by the total number of fissures. Alternatively, X may be considered as being the depth coordinate of the centroid of the penetration-vs.-depth curve. Having obtained these two parameters for each specimen, the penetration data could be concisely summarized.

One word of caution is necessary, however, in the interpretation of the meaning of the X parameter. Referring to the summation form of Equation (4), it will be noted that it is impossible to have a value of X less than the midpoint of the first data group. Suppose, for example, that a specimen contains penetration fissures of the first group only. The quantity n_1 then becomes equal to N, and can be taken outside the summation sign, where it cancels with the N in the denominator, leaving only a_1, the first group midpoint. In the present case, the midpoint of the first group was 0.00032 in. Therefore, a number of the specimens are recorded as having X = 0.00032 in. in which the penetration was actually much less than this average depth. The 0.00032 in. is not a lower limit in the size of fissure detectable, but is, rather, a consequence of the group size selected. The question may legitimately be asked, why was not a smaller group size chosen? There are two answers to this question: first, that when these standards were set up, only a small fraction of the specimens had been

examined, and there was no way of knowing what sizes of penetration would be encountered later in the program; and, second, that any number of groups more than about six becomes excessively clumsy for an operator to use in obtaining data. In retrospect, it seems that the group size chosen was about ideal.

After penetration measurements had been completed, specimens were etched and again examined metallographically, photomicrographs being taken of significant areas. The usual procedure used for revealing the grain structure and carbide distribution in the specimens was an electrolytic etch in 10 per cent chromic acid. For the identification of metallic phases, viz., ferrite and sigma phase, a concentrated Murakami's reagent was used, which colors ferrite yellow and sigma blue (41).

Evaluation of Oxide Scales

The physical appearances of the oxides were recorded after they had been bottled. Magnetic tests were then run, which were somewhat similar to those on the specimens themselves. The magnet was placed in contact with the outside of a bottle containing an oxide sample at a point nearest the sample itself. The bottle and magnet were then rotated, without moving the magnet relative to the bottle, until the weight of the oxide overcame the attractive force of the magnet and the oxide dropped to the bottom of the bottle. Oxides which could not be attracted by the magnet at all were classified as "not detectably" magnetic. Oxides which dropped

back when the bottle wall was approximately 90° to the horizontal were classified as "weakly" magnetic. Oxides which were attracted by the magnet sufficiently to allow 180° rotation of the bottle, suspending them under the magnet, were classified as "medium" or "strongly" magnetic, the latter classification being used when oscillatory movement of the magnet outside the bottle produced pronounced movement of the oxide particles within the bottle. This test is even more qualitative than the tests of the metallic specimens, since it is influenced by the amount and density of the oxide, the oxide particle size, and the smoothness and cleanliness of the inside of the bottle. It is valuable, nevertheless, as an indication of the presence of appreciable quantities of magnetic components in the scales.

Following the visual and magnetic examinations, oxides were pulverized in an agate mortar and pestle, mixed with Duco cement, and rolled out into thin cylinders between two glass microscope slides while still plastic. The diameters of these cylindrical specimens were approximately 0.2 mm, and the cross sections were quite uniform. Specimens were mounted and centered in a 57.3-mm diameter Norelco x-ray powder camera, utilizing a Straumanis-mounted film. X-ray exposures were made on a Norelco water-cooled diffraction unit using V-filtered Cr $K\alpha$ radiation. A standard exposure time of 2 hrs. was selected, and all exposures were of this length except two, which required somewhat longer times. One series of four samples was run using a Norelco 114.6-mm camera, which required exposure time of 10 hrs. After the

films had been processed, traces were made of them on a Leeds and Northrup Knorr-Albers type of microphotometer. These traces were then measured using a ruler of adequate length. This method of measurement was used in preference to an optical comparator, first because it is believed to be more accurate, and second because it gives quantitative values for diffraction line peak intensities. Interplanar spacings were computed from the distances measured on the microphotometer traces in the same manner as they would have been from distances measured directly on the film, a film shrinkage correction being included. This technique is well-known, and will not be elaborated here. Comparison was then made with interplanar spacings of the compounds expected to be present, as made available by Yearian and Radavich (42).

Interface Movements

In reporting the penetration data, it would be desirable to refer the penetration depth always to the original metal surface. Early in the experimental work, attempts were made to measure the specimen thickness losses directly by mounting an untested specimen from the same heat and nearly the same location in the sheet stock along with the specimens from a given run. After polishing, several thickness measurements were made of each specimen with a travelling microscope, the object being to subtract these values from the thickness of the untested specimen. It was found, however, that the interface movement was of the order of magnitude of the experimental error and normal thickness variation in the sheet, so that it was not possible to obtain consistent results by this method.

Attempts were then made to carry out weight-loss measurements on specimens given the same oxidation cycle as the specimens used in the regular procedure. Specimens were weighed and their dimensions were measured before and after oxidation and after descaling treatment and brushing. The descaling treatment consisted of making the specimen the cathode in a 10 per cent H_2SO_4 electrolyte as described by Upthegrove and Murphy (43) and Siebert (44). A current of 10 amp was passed through each specimen for 1 min. The treatment was not successful in removing any but interference-film types of scale, although it is known to be very effective for the scales found on lower-alloy steels. In an effort to remove the scale further, the specimens were brushed with a rotary wire brush attached to a hand power tool. This treatment succeeded in removing all but the pit-type oxide deposits without removing any appreciable amount of metal. Density measurements were then made on specimens from each heat by measuring the loss of weight in water. Knowing the density and the weight loss, the movement of one metal-oxide interface could be calculated by the formula:

$$\Delta s = \frac{\Delta w}{(2ab - c)\, d} \qquad (5)$$

where Δs is the interface movement, Δw is the weight loss, a and b are the dimensions of the sheet faces of the specimen, c is a correction for the rounded corners of the specimen, and d is the density of the metal. The results of these interface measurements are presented in Table 12, and

are discussed more fully in the Results and Discussion Section. It should be noted here, however, that the interface movements were, as the early thickness measurements indicated, quite small. In view of the uncertainty in the interface movements arising from the small amounts of oxide remaining on the surfaces and from the roughness of the surfaces, it was decided to report the penetration data relative to the existing metal-oxide interfaces.

Electron Diffraction

In an effort to determine the nature of the intergranular compounds, a technique was developed for examining the subsurface regions of oxidized specimens by means of reflection electron diffraction, a method well suited for the study of solid surface layers. The procedure which was followed on previously oxidized specimens consisted of the following steps:

1) All of the external scale possible was removed by scraping, without actually disturbing the metal surface itself. The scale thus collected was powdered and analyzed by x-ray diffraction using the same technique described previously.
2) Thickness measurements were made on the specimen at two points on the surface. One of these points was later to be subject to etching action while the other was to be protected from etching by Scotch tape, and thus served as a reference standard for later thickness measurements. These measurements were made on a Pratt and Whitney supermicrometer

accurate to 0.0001 in. The assumption was made that the etching attack on the exposed underside of the specimen was essentially uniform.

3) An electron diffraction pattern was made of the specimen surface, using an RCA Type EMD-2 electron diffraction apparatus.

4) The specimen was electrolytically etched for from 15 to 30 sec. in a mixture of 10 per cent perchloric acid and 90 per cent glacial acetic acid at a temperature of 15°C and a current density of 6 amp/in^2. This etching treatment has the property of removing the metal without disturbing the intergranular compounds (45).

5) An electron diffraction pattern was made of the exposed compounds.

6) The exposed compounds were brushed off the surface using a rotary wire brush on a hand power tool. The brush did not damage the surface, and, in addition, was much less likely to cause contamination than was an abrasive compound. The Scotch tape covering the unetched portion of the specimen was then removed.

7) Thickness measurements were made of the etched and unetched portions of the specimen as described in Step 2. By appropriate subtractions, the amount of metal removed in the etching operation could then be determined. A fresh piece of Scotch tape was then applied to the unetched portion of the

surface, and Steps 4 through 7 were repeated as many times as necessary to reach the depth in the specimen where diffraction patterns from the intergranular compounds nc longer appeared.

The electron diffraction procedure outlined above made it possible to show any changes in the overall composition of the intergranular compounds resulting from oxidation as a function of their depth below the metal-oxide interface. For this part of the program, six heats were selected from the nine studied in the oxidation runs. These heats were: type 309 + Nb and type 310, heats 64177, 64270, X11306, X11338, and X27258. The other three type 310 heats were similar in their penetration characteristics to heat X27258, and the latter heat was taken as being representative of them also. In the case of the type 309 + Nb, and type 310, heats 64177 and 64270, specimens were studied following 100 hr. oxidation at 1600°, 1700°, 1800°, and 1900°F. For the heats X11306, X11338, and X27258, 2000°F specimens were studied in addition to the other four temperatures.

In connection with the electron diffraction studies, it should be mentioned that this method, although it is capable of use with extremely small amounts of materials and is especially useful for thin films, also has its limitations. The smallest uncertainty in interplanar spacing which can be expected using the reflection electron diffraction technique is about one percent. Since this uncertainty is of the same order as the change in interplanar spacing between the diffraction patterns of Fe_2O_3 and Cr_2O_3, and between

spinels having low and high lattice parameters, the electron diffraction studies can do little more in the present case than to indicate the presence or absence of the rhombohedral or cubic phases.

In evaluating the diffraction patterns obtained, the relative proportions of spinel and rhombohedral phases shown in individual patterns were indicated by specifying whether the patterns of specific phases were strong (S), medium (M), weak (W), very weak (VW), or very very weak (VVW) (see Table 17). In addition, a qualitative attempt was made to show the diminution of diffracted intensity from intergranular oxides on individual specimens accompanying successive etches by referring intensities to those obtained in patterns taken prior to etching. It must be borne in mind, however, that comparison of relative intensities obtained in different exposures can be misleading, since many factors related to exposure and specimen surface preparation and alignment can influence the intensity obtained in a given pattern, and these factors vary among exposures.

V. RESULTS AND DISCUSSION

Oxidation Tests

The technique by which the curves of number of intergranular cracks vs. depth below the oxide-metal interface were arrived at was explained in the preceding section. The curves obtained by this method appear in Figures 17 through 67. The basic type of penetration curve was found to be a curve which was called a "decay" type curve, monotonically decreasing to zero fissures per in. with increasing depth. With increasing time and/or temperature, the mean depth of this curve tended to increase and a maximum in the curve tended to develop and move toward greater depths. The explanation for this behavior is twofold. First, the number of grain boundary sites for oxygen penetration is finite, and as the process of oxidation continues, a state is reached where the existing penetration fissures have grown deep while relatively few new fissures are being formed. The second factor that tends to deplete the number of small fissures can be the progressive surface oxidation, which may overtake and absorb fissures which have been blocked in their further forward progress by encountering unfavorable grain orientations beneath the surface.

The behavior of the 1900°F penetration curve for type 310 alloy, heat X11338, Run 16 (100 hr), as shown in Figure 51, should be mentioned. This specimen showed some very deep penetration, photomicrographs of which appear in Figures 99, 107, and 108. A number of the fissures were of greater depth than

the six-row grid used in making the count of the fissures, and were recorded only as being beyond the grid. When the data were assembled, an arbitrary group interval equal to that of the six regular groups was assigned to these fissures. Since there was an appreciable number of the fissures, the resulting curve has an abnormal shape. If the deep fissures were subdivided into groups, the curve would no doubt be of normal shape. Since this particular specimen was the only instance in which the shape of the curve was affected by the excessively deep penetration, it was not considered worth while to alter the routine of measurement.

In each metallographic mount, one untested specimen was included as a control. Originally, it was planned to use this control specimen to obtain a value of the original thickness, from which thicknesses of the tested specimens were to have been subtracted to obtain thickness losses resulting from oxidation. This method proved to be impractical because of the small magnitude of the thickness losses, but it was found in the meantime that the control specimens gave an indication of the effect of surface roughness and of polishing on an otherwise undamaged surface. Surface irregularities gave rise to a background count of small artifacts on the control specimen which varied somewhat in different mounts from the same heat and was presumably indicative of the amount of error included in the fissure counts of the tested specimens. The fact that the penetration curves of some of the control specimens are of the same order of magnitude as the curves for some tested specimens reflects the uncertainty in the count of the

very small penetrations, as noted previously. It is to be observed that the control penetration curves almost always decay at a rate much faster than those of tested specimens, which results from the fact that only rarely was anything seen on a control specimen that would be interpreted as being a fissure extending as deep as the second grid level.

The maximum fissure depths, except for the one specimen from Heat X11338 previously referred to, were never found to be over 0.005 in. in depth, and usually were much less.

As is apparent from referring to Figures 17 through 67, an analysis of the intergranular penetration characteristics of the alloys which was based on the detailed shapes of the penetration curves themselves would be very difficult, both to prepare and to assimilate. Therefore, the two parameters N, the penetration frequency, and X, the mean penetration depth, as referred to in the previous section, were adopted. These parameters summarize the essential features of the penetration-vs.-depth curves. The behavior of these parameters with temperature is presented in Figures 68 through 94.

In several early runs (Nos. 5, 6, 8, 9, and 13), the air velocity through the furnaces was varied and the duration of the runs was held constant at 100 hr. These runs are summarized in Figures 68 and 69, 73 and 74, and 78 and 79 for the type 309 + Nb alloy and heats 64177 and 64270 of type 310 alloy, respectively. Since the humidity was also a variable in these runs, the results are inconclusive, and the penetration data are included only for the sake of completeness. Run 7, and also Run 25, were discarded because of temperature control difficulties during the oxidation period.

One run, No. 9, was carried out to determine the effect of cold work prior to exposure. The penetration results appear in Figures 70, 75, and 80. Cold work was introduced into the specimens by making a sharp angle bend in each specimen. After the specimens had been oxidized, quenched, mounted, and polished, penetration readings were made on the bent sections as well as the straight sections, the lengths of the bent sections being estimated by difference between the overall specimen length prior to testing and the measured lengths of the straight sections. These results showed that there were fewer penetration fissures in the cold-worked areas, but that the penetration present was somewhat more severe than that in the straight sections. There was no catastrophic effect of the cold work, most of the residual stress having relaxed before appreciable oxidation occurred. The case of a continuously applied stress during the oxidation period would be a different matter, however, and would likely lead to substantial increases in the penetration depth.

The effect of time on penetration for the type 309 + Nb, 64177, and 64270 alloys is presented in Figures 71 and 72, 76 and 77, and 81 and 82. In general, the penetration became deeper and the fissures more numerous with time, although there was considerable overlapping. There does not appear to be any marked difference in the number of fissures occurring in the three alloys, and, if there is any difference in the penetration depths, it would be that the depth in the type 309 + Nb alloy is slightly less than in the two type 310 alloys.

Figures 83 through 94 show the effect of time on the penetration in the remaining six heats of type 310 steel. Heat X11306 (Figures 83 and 84) showed severe penetration, both from the standpoint of number and depth of fissures. Of the other five heats, all showed penetration frequencies of the order of those of the type 309 + Nb, 64177, and 64270 heats. Except for the previously-mentioned 1900°F, 100-hr. specimen of heat X11338 (Figure 85), penetration depths were all somewhat lower than those found in the type 309 + Nb, 64177, and 64270 heats. Of the five heats, the penetration depth of heat X45558 was least by a narrow margin, with heat X46063 next best. This ranking is probably not significant, since the differences among these heats are of the order of the experimental error. It is also noteworthy that in the six alloys, the magnitudes of the penetration frequencies at a given temperature did not usually increase in the order of increasing oxidation times, whereas penetration depths did generally increase in such a manner. The values obtained for penetration depths appear to be more significant than the values for penetration frequency, since the depths are not as strongly influenced by the uncertainty in the count of the smallest fissures as are the frequencies. The definition of the mean depth, X, contains the factor a_1 (see Equation 4), which serves to bias X strongly in favor of deeper fissures, thus minimizing the effect of shallow ones.

The abnormal penetration found in the 1900°F, 100-hr specimen from heat X11338 was considered of sufficient importance to justify further work. Accordingly, a 100-hr

oxidation run at 1900°F was carried out using four specimens from heat X11338 and four specimens from heat X45558. One specimen from each heat was charged to each of the four furnaces. Following the usual quenching and specimen preparation procedure, penetration counts were made on these specimens, and the values of N and X were computed for each specimen. These values, along with those already obtained for this time and temperature in the previous runs (Figures 85, 86, 89, and 90) were averaged separately and standard deviations were computed. The results are presented graphically in Figures 119, 120, and 121. Several conclusions can be drawn from these results. First, heat X11338 shows a great deal of scatter at 1900°F. Presumably, its scatter at other temperatures is also large. Second, the abnormally deep penetration first found in Run 16 (Figure 86) falls on the high side of the range of variability established for this heat in the later run, and therefore should be thought of as being somewhat lower on the average. Third, the variabilities of N and X for heat X45558 reflect the inherently smaller variability of X with respect to N mentioned at the close of the last paragraph. The variability obtained for heat X45558 is believed to be the normally-encountered variability in measurements made on specimens from Runs 16 through 28. Variability was somewhat higher in the early runs, 5 through 15, partly due to inexperience in the counting technique and partly due to the lack of complete humidity control.

Interface Movement Measurements

Determination of the progress of the external oxidation process as measured by the advance of the metal-oxide interface would be desirable, since the measured depths of the intergranular fissures in each specimen relative to the final metal-oxide interface could then be made relative to the original metal surface by the addition of a figure representing the metal-oxide interface movement during the oxidation period. There are three reasonably straightforward methods of determining the interface movement, viz.: 1) direct comparison of the thicknesses of tested specimens with thicknesses of similar untested specimens; 2) measurement of the metal volume loss computed from density, initial specimen weight, and specimen weight following oxidation and descaling; and 3) measurement of weight gain of specimen and scale during testing and computation of the volume of metal necessary to cause this weight gain, which will be the volume of metal oxidized.

The first, and simplest, method was tried initially, but it was found that the thickness measurements obtained were not consistent because the thickness losses on testing were of the same order of magnitude as the normally-occurring thickness variations in the commercially-rolled sheet stock.

The second method was tried on a series of specimens oxidized for 100 hr. The detailed method by which these measurements were made was outlined in the previous section, and the measurements themselves are presented in Table 12. It will be noted that the computed interface movements for

specimens which were powdery gray black in appearance are in all cases abnormally small. The reason for this is the great tenacity of the powdery gray black type of scale, which, when not completely removed, caused the measured weight losses to be too small. For comparison, however, Warr (29) gives oxidation rates, in in./yr., for types 309 and 310 steels, gathered from the literature. These figures are as follows:

	Oxidation Rate			
	Type 309		Type 310	
Temp., °F	in./yr	in./100 hr	in./yr	in./100 hr
1600	0.004	5×10^{-5}	0.007	8×10^{-5}
1800	0.02	20 x	0.02	20 x
2000	0.05	60 x	0.03	30 x
2200	0.06	70 x	0.05	60 x

These figures are somewhat higher than those presented in Table 12, but are of the same order of magnitude. The major reason for the differences that exist is undoubtedly the inability to remove all the scale of the powdery gray black type. It should also be noted, however, that, since the time rate of oxidation of metals in general is not constant for a given single test, it is a dangerous practice to recompute oxidation rate figures given for one test period (e.g., a year) to another period (100 hr) as was done for this comparison. Likewise, it is dangerous to extrapolate short time oxidation rate data to longer times by reporting it in terms of a time period longer than the test. Still, Warr's figures are in the same range as those obtained in the present investigation, and both sets of figures confirm that the interface movement in types 309 and 310 stainless steels for oxidation

times up to 100 hr at temperatures below 2000-2200°F is quite small, amounting to less than 0.001 in.

The third mentioned technique for determining interface movement, the weight gain method, is one particularly adapted to pure metals or very simple alloy systems. To use this method, the chemical composition of the scale must be known to a high degree of accuracy, since it is necessary to compute the total weight of cations in the scale, which represents the amount of metal loss, from the weight gain, which represents the weight of the O taken up by the metal. Care must also be taken when using this method to be certain that no particles of scale are lost. In the present case, it would not have been possible to collect for analysis all of the oxides formed, since some of the scales were extremely adherent and some of the oxides were intergranular. Therefore, it would not have been possible to have obtained representative oxide chemical analyses for use in this method. For this reason, and considering also the small magnitudes of the interface movement as revealed by the weight loss techniques, no weight gain measurements were attempted.

Again, in view of the small magnitudes of the interface movements and the unreliability of interface movement measurements arising from inability to remove the scales completely in all cases, it was not deemed necessary or advisable to attempt to refer the penetration measurements to the original metal surface. Consequently, all penetration measurements were reported as they were made, relative to the final metal-oxide interface.

Visual and Magnetic Examination

The results of the visual and magnetic examination of both the specimens and the oxide scales are presented in Tables 3 through 11. A key to the abbreviations used is supplied in Table 2. Where more than one appearance is recorded for a specimen, the abbreviations are ranked in descending order of the proportion of the surface having that appearance. Great variations in the visual appearance of specimens and scales were observed, and a fuller description of the more or less arbitrary classifications adopted for their systematization is in order.

Porous gray black - This type of specimen surface appearance, when it constituted the majority of the specimen surface, was accomplished by small quantities of free scale loosened in quenching. Although it was possible to scrape some of the powdery oxide off the specimen, a tough, continuous, adherent layer always remained which could not be removed without damage to the underlying metal.

Porous gray black with orange substrate - If a specimen like that described above showed a red-orange color after scraping, it was given this classification. This color may have been partly due to Fe_2O_3, but this is not likely, considering the general rule that the basis metal oxide is usually found in the outer scale layer, and also that in some cases, at least, the color was due to the presence of an interference film beneath the powdery gray black scale. The x-ray results are inconclusive concerning the former possibility.

Shiny gray black - This appearance was not found as often as the powdery gray black and appeared to be associated with oxidation times of 30 hr. or less. The adherent scale causing this appearance was very thin and often discontinuous, showing smooth light gray areas beneath, and had almost a metallic sheen.

Black and scoriated - Occurrence of this appearance was unpredictable. Specimens having this appearance looked almost as though the oxide had once been liquid. The surfaces were checked, and individual segments of scale were plane and shiny. The scale was extremely dense, hard, and adherent.

Light gray - This type of appearance was associated with a loose, flaky scale which often came off entirely on quenching. The appearance of the underlying specimen was a very smooth light gray.

Light gray with interference colors - Specimens of the preceding basic appearance often showed orange, blue, or magenta interference films in swirling patterns.

Light gray with black pits - In some cases, the light gray surface was pitted, the pits containing an adherent gray-black material. Often the light gray areas around the pits showed interference colors.

Black Pits with light gray - This classification differs from the previous one in degree, the pits being the predominant feature.

Oxide appearances varied in color from metallic gray to dull black, and from fine powders to flakes sometimes almost as large as the specimen faces.

The magnetism of the specimens and the oxides varied from those with no detectable magnetism to one or two specimens in which the magnetism was sufficiently strong so that the specimens could be suspended from the magnet and a few oxide specimens which could be made to follow a magnet beneath the sheet of paper on which they rested in the same manner as iron filings. It was found that specimen magnetism was usually, though not always, concomitant with scale magnetism. There was no definite segregation of magnetic components in the one to the exclusion of the other. It should be remembered that the presence of ferromagnetism does not necessarily imply the presence of body-centered iron, per se, although δ-ferrite was observed metallographically in some of the magnetic specimens. As far as the specimens themselves are concerned, it was shown in the Literature Survey section that a concentration of Ni is to be expected in the surface metal layer during oxidation. Ni in the pure state is ferromagnetic at temperatures below about 660°F. As alloying elements are added to Ni, its Curie point drops. In the Ni-Cr system, for example, 7 wt per cent Cr is sufficient to bring the Curie point down to 50°F. Cr, though a major component of the alloy, is not likely to be found in large concentration in the Ni layer, however, because of its preferential oxidation characteristics. Fe, on the other hand, may be present in larger quantities, and in the Fe-Ni system the Curie point is between 650° and 1400°F over the entire composition range. Thus the diffusion gradients which must develop during the oxidation process can account for the observed ferromagnetism in the specimens.

It is more difficult to account for the scale magnetism in a satisfactory manner, especially since no Ni or other metallic phase was ever observed to have been entrapped in the scale. Of the possible oxides composing the scales, the only magnetic substances are certain of the spinels. The spinel unit cell contains eight molecules and can be considered as a face-centered cubic arrangement of O ions with the metal ions occupying certain vacant sites. In the O unit cell there are sixty-four vacant tetrahedral positions and thirty-two octahedral positions. The metal ions occupy a certain group of positions consisting of eight of the tetrahedral and sixteen of the octahedral positions. Barth and Posnjak (46) have established that the divalent and trivalent ions may be distributed among the twenty-four positions to be occupied in two distinct manners. In the "normal" spinel structure the eight divalent ions occupy the eight available tetrahedral positions and the sixteen trivalent ions are in the sixteen available octahedral positions. In the "inverse" spinel structure the eight tetrahedral positions are occupied by half of the sixteen trivalent ions, and the sixteen octahedral positions are occupied jointly by an equal number of divalent and trivalent ions.

Only spinels having the inverse type of structure are ferromagnetic. As Table 15 shows, of the possible spinels in the present study, only $NiFe_2O_4$ and Fe_3O_4 are strongly magnetic. $FeCr_2O_4$ and $MnFe_2O_4$ are sometimes observed to be weakly magnetic, but this magnetism probably results from impurities. $NiCr_2O_4$, $NiMn_2O_4$, and $MnCr_2O_4$ are not magnetic. As

Table 15 also shows, the lattice constants of the different spinels also differ slightly. Thus, it would seem at first glance that careful x-ray work could be used to identify the spinel phase and that at least a partial check on the x-ray results could be made on the basis of magnetism. Unfortunately, such is not the case. The reasons why x-ray evidence alone is insufficient to establish the spinel composition will be discussed in a following section dealing with the x-ray work carried out in the present program. There it will be pointed out that the same reasons also apply to the spinel magnetism as well. Magnetism cannot be made to serve as a qualitative analytical tool in study of the scales.

In Table 12 are recorded the specimen and oxide appearances of three duplicate runs the purpose of which was to obtain weight loss data. These runs duplicate Runs 15, 16, and 17, and comparison with descriptions from these runs shows that there is considerable variability in the specimen and oxide appearances and in magnetic characteristics, even in specimens which were as nearly as possible duplicates. Furthermore, there seems to be little correlation of specimen and oxide appearance and magnetism with time or temperature of oxidation, or with scale composition as revealed by x-ray analysis. Such variability seems to be the general rule in oxidation studies, and is perhaps the principal reason that there has not been more progress made in the field of oxidation research. The variability must result from fluctuation of variables which influence the oxidation process, some of which are as yet unrecognized. Among the known variables which contributed to

the variability in the present investigation are the surface condition and the elapsed time between removal of the hot specimen from the furnace and its reaching the water quenching medium. Quenching time varied between 1 and 7 sec.

Metallographic Examination

The results of the metallographic examination of the specimens following testing are presented in Table 13, and include, in addition to penetration appearance, the changes in microstructure which took place in the alloys during the oxidation period. For convenience in presenting the data, the metallographic appearances of the intergranular penetration encountered were classified in seven arbitrary groups. Examples of six of these groups appear in Figures 95 through 100. Type 0, which consisted of penetration fissures so small that they could not be definitely typed as belonging to any of the other six groups, was omitted. Referring to Table 13, the very shallow Type O penetration was found at low temperatures of oxidation, 1600°F and sometimes 1700°F, after 100-hr. exposure or less. At the other extreme, Type VI penetration (Figure 100) occurred at the highest temperature, 2000°F, and especially at times in excess of 30 hr. Type VI, "coalesced web" penetration, is characterized by a coalescence of the intergranular oxide into discrete particles spaced along the grain boundaries. This effect is probably the result of relatively high atomic mobility at the high temperature and the relative interfacial tension between the matrix and the intergranular material. At intermediate temperatures, there is considerable variation in the precise

appearance of the penetration. Some heats, notably heats 64177 and X46063, showed Type III penetration consistently, a rough-edged web. The other heats showed no specific trends, and there were no penetration characteristics that could be associated with composition.

Figures 101 and 102 show the change in appearance of the subsurface metal associated with penetration. In all of the heats except heat 64177, which showed penetration in the as-received condition (see Figures 12 and 13), the specimen surfaces were initially smooth, and etching (Figure 101) revealed the grain boundaries extending all the way to the surface. After oxidation, the etched structures resembled Figure 102. As far as could be seen, penetration took place along grain boundaries, but not along twin boundaries. A prominent characteristic was the occurrence of a layer in which no structure was revealed lying between the surface and a point beyond the ends of the visible penetration fissures. This layer gives the appearance of having an altered composition from that of the original alloy. The region is likely high in O content, within the solubility limit. The absence in the surface layer of the carbides which are visible further beneath the surface is an indication of decarburization accompanying the preferential oxidation of C. Furthermore, as has been previously mentioned, the surface metal layer must be Ni-rich, resulting from the inward diffusion of Ni away from the oxidation zone, which is an area of increased Ni activity by reason of oxidation of the other metallic elements. Noteworthy also is the solution of grain boundary

carbides well in advance of the intergranular oxide, indicative of O diffusion down the boundary and of the relatively high diffusion coefficient of C.

Figures 103 through 106 show the appearance of heat X11306 in the etched condition after oxidation. Heat X11306 behaved in a unique manner in two respects: its penetration was far greater, both in depth and number of fissures, than any of the other alloys; and its metallographic appearance differed from that of the other heats. Large quantities of precipitate which could be observed without etching appeared throughout the matrix following testing. It was also interesting to note that recognizable penetration fissures disappeared after 100 hr. at 2000°F, as shown in Figure 105, but were still present after 10 hr. at the same temperature and at all times up to 100 hr. at lower temperatures. This instance was the only one in the present investigation that could be construed as being at all analogous to Rhines' observation on Cu-base binaries that at higher temperatures, there is less tendency for preferential intergranular oxidation. Put another way, in some systems there is a certain temperature at which the volume diffusivity of the diffusing element, not necessarily O, becomes equal to the grain boundary diffusivity. Below this temperature, the grain boundary diffusivity is greater, and preferential intergranular diffusion is observed. Above this temperature, volume diffusivity is greater, and uniform volume diffusion is observed. Arguing from the standpoint of increased lattice spacing and atomic mobilities at higher temperatures and from the temperature

dependence of the volume and grain boundary diffusivities, one might expect to find no intergranular attack in general at very high temperatures. There are other factors in particular alloy systems, however, to be considered. The melting point, for instance, may be below the temperature at which the two diffusivities would become equal. In the case of oxidation of the type 310 stainless steels for times up to 100 hr., the present investigation has shown that preferential intergranular attack is still present at 2000°F. Therefore, any equivalence temperature between 0 volume and grain boundary diffusivity, if it exists at all, is at a still higher temperature in this system.

Figures 99, 107, and 108 show the metallographic appearance of the specimen from heat X11338 oxidized for 100 hr. at 1900°F. As was noted in the discussion of the penetration data, this specimen seemed to show abnormally deep penetration. This conclusion was verified by the data taken in the study of the variability among identical specimens, also mentioned in the discussion of the penetration data. Metallographic examination also showed that the penetration in this specimen was indeed abnormal. Examination of Table 13 shows that penetration on no other specimen was of this type. The width of the intergranular stringers was unique, as was the inclusion of metallic islands within them. Surface contamination of this particular heat cannot be ruled out as a possible cause of the abnormal penetration, because, as the variability run showed, the average penetration depth for several heat X11338 specimens tested under these conditions was 1.086×10^{-3} in., a value which

would fall in line with the penetration depth curve for heat X11338 shown in Figure 86. Thus, it may be that we are dealing here not with a case of abnormally deep penetration, but with a case of abnormally large variability, which might just as well have shown up in heat X11338 at any of the test temperatures. Possibly only the 1900°F-100-hr. point fell far enough on the high side of the range to bring it under closer scrutiny. It is clear, at any rate, that heat X11338 shows more variability in its penetration characteristics than the other heats. At this point it was decided to include specimens from heat X11338 in the electron diffraction program which was to be undertaken in an effort to identify the intergranular constituents.

In the specimen from heat X45558 tested for 100 hr. at 2000°F, several examples of a deep pit type of penetration were noted, as shown in Figure 109. This type of attack may represent points where grains have fallen out after having been completely encircled by oxide, the pits having later become filled with scale. This type of attack may be related to the fact that occasionally a sample of scale having the usual magnetic properties would contain several particles which were extremely magnetic. On several specimens the scales of which showed these particles, one or two pits of the order of 1/64-in. in diameter or less were plainly visible, and can be presumed to have been the original locations of the particles. The particles were removed from the scale samples before x-ray specimens were prepared. The reason for this disintegration

was most likely the occurrence of small surface imperfections in the sheet stock. This conclusion is borne out by the rarity of occurrence of disintegration.

Several other structural features were observed which it would be appropriate to note here, although it is not known whether they have any appreciable effect on the intergranular penetration. The first two of these are the occurrence of delta ferrite and a phase originally believed to be sigma phase. The temperatures at which these constituents were observed are tabulated in Table 13. Identification was made by means of Murakami's reagent, which, when used concentrated as described by Burgess and Forgeng (47), colors sigma light blue and ferrite yellow. Representative photomicrographs of the two constituents appear in Figures 110 through 113. The latter two figures show that these phases, like all the other structural features of the metal, tend not to occur in the region near the surface. One disturbing feature concerning the identification of sigma was the unusually high temperatures at which it seemingly appeared, for it is generally believed that sigma does not form in these alloys at temperatures above about 1800°F, although the blue-colored phase was observed in these specimens at 2000°F in some cases. It was later learned, however, that another group of investigators has shown that the phase originally identified as sigma phase may be a chromium nitride, CrN or Cr_2N, at least at the higher temperatures (48). These compounds appear blue the same as sigma phase when colored with Murakami's reagent. No features

of the observed penetration could be related to the presence of either delta ferrite, sigma phase, or nitrides.

Figure 114, taken using oblique light, shows in a striking manner the distinct metal layer mentioned previously. The increased thickness of the surface layer in the vicinity of a grain boundary is clearly visible, though the grain boundary itself, the carbides having dissolved, is not visible for some distance further back into the metal. This photomicrograph illustrates the greater magnitude of the grain boundary diffusion coefficient of O relative to the volume diffusion coefficient. Since LeClaire's differentiation of Fisher's equation (Equation 2) relates the vertex angle of an isoconcentration line, such as the one revealed by etching in Figure 114, to the ratio of the grain boundary diffusion coefficient to the volume diffusion coefficient (see Literature Survey section, page 21), it should be possible to obtain at least a rough estimate of the relative magnitudes of D_{gb} and D_v for this particular grain boundary. Measurement of the entire vertex angle of the cusp in Figure 114 gave a value of 67°, so φ was taken to be 33.5°. The grain boundary was assumed to be 5 A. thick, and the diffusion time was 10 hr. The temperature of diffusion was 1900°F. The best approximation of D_v that could be obtained was the value of 1×10^{-9} cm^2/sec, determined by Brower, Larsen, and Schenk (49) for diffusion of O in γ-Fe at 1100°C (2012°F). When these values are substituted in LeClaire's equation, the ratio D_{gb}/D_v comes out to be 1×10^8. This value compares well with a value of 8×10^5 reported by Barnes (50) for diffusion of Cu into Ni

at 1000°C. No further work along this line was carried out in the present investigation because such work was believed to lie outside the scope of the project as originally conceived.

When certain of the specimens were first etched in chromic acid, a structure was developed consisting of a number of long parallel stringers which appeared black under the microscope. Examination under oblique light at high magnification revealed that these stringers were troughs gouged in the metal surface by severe overetching. When the specimens were repolished and etched using a very low current density, a structure consisting of bands of carbide particles was revealed. Careful etching of the as-received heat X45558 and examination under oblique light showed the existence of depressions (Figure 115), accompanied by several pits along the depressions where particles had etched out. These depressions are interpreted as being concentration gradients in the matrix. Following exposure for 10 hr. at 1600°F, carbide particles had precipitated as shown in Figure 116, and the depressions no longer appeared on etching. Figures 117 and 118, taken at lower magnification, show that the bands of carbides were sometimes associated with a refinement in grain size, and sometimes not. It was observed that the bands tended to disappear, presumably by diffusion, with increasing time and/or temperature of heat treatment. Cross section specimens from all nine of the heats were examined to determine whether banding could be observed. A second series of cross section specimens at right angles to the first series was prepared and

examined, since it was believed that the stringers resulted from the hot-rolling operation in the mill, and would hence lie in the rolling direction. If the first series of cross section specimens had happened to be perpendicular to the rolling direction, there would have been no evidence of the stringers, but they should then have been revealed in the second series of specimens. Results of this examination appear in Table 13 under the heading "Banding". There is apparently no relation between the presence of the carbide bands and the grain boundary carbide network discovered in the initial examination of the heats. It is likely that the grain boundary networks, where they occur, are the result of one of the last stages of fabrication of the material, probably the anneal following hot-rolling, whereas the banding could probably be traced back to segregation in the original ingots. No penetration effects were observed that could be attributed to the presence of the carbide bands.

Effect of Preferred Orientation

From theoretical considerations, it seems likely that if it were possible to introduce a very strong preferred orientation into the stainless steel, a profound decrease in intergranular oxidation should result. The line of reasoning behind this argument is as follows: intergranular oxidation is apparently a manifestation of preferential diffusion of O along grain boundaries. From recent studies of grain boundary diffusion (37, 38, 39), it is known that the ratio of the grain boundary diffusion coefficient to the volume diffusion coefficient is strongly dependent upon the relative orientation

of the grains on either side of the boundary in question, this ratio decreasing to approximately unity for small angular misalignments between grains. The sine qua non of a strong preferred orientation is the existence of just such small angular misalignments among a majority of the grains of the metal. If, therefore, a thermally stable, strong preferred orientation could be introduced, intergranular oxidation should be significantly decreased in amount.

The requirement of thermal stability of the preferred orientation rules out the consideration of rolling textures, leaving only the possibility of recrystallization textures. Of the possible recrystallization textures which can occur, the well-known "cube" texture, which is formed in face-centered cubic metals under suitable conditions, is outstanding for its high degree of orientation. The cube, or (100) [001], texture, in those metals in which it can be caused to form, results from a high-temperature anneal following an extremely heavy cold-working operation. It is also known that in some cases the presence of small amounts of impurities, such as As in Cu, will prevent the formation of a cube texture.

It was decided to attempt to obtain a recrystallization texture in a type 310 stainless steel. For this purpose, some 1/2-in. thick sheet stock was obtained having the following analysis:

CHEMICAL ANALYSIS OF HEAT 31372

C	Mn	Si	P	S	Cr	Ni	Cu	Mo
0.08	1.84	0.72	0.031	0.018	24.60	20.45	0.25	0.43

An appropriate amount of this material was cold-rolled to a 97 per cent reduction in thickness, following which 1 x 1/2-in. specimens were sheared from the stock. These specimens were annealed at 2000°F for 5-1/2 hr. The anneal was carried out in a closed quartz tube in an atmosphere of dried argon. Once the technique of carrying out the anneal had been perfected, it was found to be possible to avoid completely any scale or film formation on the specimen surfaces.

For reference, specimens were prepared from the as-received stock of heat 31372 by splitting the stock lengthwise to 1/4-in. thickness. The material was then cold-reduced 10 per cent in order to obtain a surface comparable to the surfaces of the highly-reduced specimens. Specimens were cut to size, and were annealed along with the specimens of highly-reduced material.

A run was made at temperatures between 1600° and 2000°F for 100 hr., in which each furnace was at a different temperature and contained a cold-worked-and-annealed and a reference specimen. Following the run, the specimens were quenched, mounted, polished, and examined in the usual manner. The penetration-vs.-depth curves resulting from this examination are presented in Figures 122 and 123, and the penetration frequency and depth parameter curves appear in Figures 124 and 125. As the latter pair of figures shows, there was not a great deal of difference in penetration characteristics resulting from the two treatments. It does appear that at the higher temperatures the cold-worked-and-annealed material was superior by a small margin.

Forward-reflection Debye x-ray patterns were made of the material in the as-rolled and the rolled-and-annealed conditions. These patterns appear in Figures 126 and 127. A strong rolling texture was developed, but this texture failed to transform to a strong recrystallization texture on annealling. Recrystallization did take place during the anneal, however, as is evidenced by the discrete spots, and some degree of preferred orientation resulted.

It was noted that the cold-worked-and-annealed material possessed an extremely adherent scale, which appeared to be considerably thicker than the scales usually encountered. This effect has been observed by Benard (40) on Cu and Fe, viz., that there was an increase in the progressive oxidation rate accompanying the development of a preferred orientation. The effect appears to be related to oriented oxide growth.

It was decided not to undertake any extensive program in an effort to obtain a more pronounced texture in the stainless steel for two reasons. First, there was considerable doubt whether with the large number of different elements present in the commercial steel it would be possible to avoid inhibition of strong recrystallization texture formation; and, second, any improvement in oxidation characteristics resulting from suppression of the intergranular penetration would likely be more than offset by the increase in overall oxidation rate.

Analysis of Oxides

The methods emplcyed for the analysis of the scales and the intergranular oxides were limited to diffraction techniques.

The external scales were analyzed by x-ray diffraction, and the intergranular oxides were analyzed insofar as possible by reflection electron diffraction. The compositions of the external oxides of selected specimens from each heat of material are presented as part of Tables 3 through 11. The compositions of the intergranular oxides of six of the nine heats are presented in Table 17.

In interpreting the data concerned with the external scales, it is desirable to look first at the work of other investigators. A brief discussion of the present state of knowledge with regard to the scaling of stainless steels was presented in the Literature Survey section beginning on page 12. The recent work of Longo (14) sheds much light on this subject, and clears up a number of conflicting assertions in the literature as to the identity of the scale components. Longo has demonstrated very clearly the necessity for coupling chemical analysis with x-ray diffraction in any investigation aimed at obtaining definitive information concerning scale formation in alloy systems. X-ray diffraction does not in general give an unambiguous answer as to phase compositions, and the chemical analyses are necessary to eliminate incorrect compositions from consideration. On the other hand, chemical analyses themselves give no information regarding the number of phases present or their crystal structures.

Longo's work, which was a continuation of research begun by Warr (29) and Boren (30), was on Cr stainless steels. The phases present in scales formed on these steels, however, are the same as those formed on Cr-Ni stainless steels (12, 13)

and in general consist of a spinel phase and a rhombohedral phase, the latter being Cr_2O_3, α-Fe_2O_3, or a solid solution of the two. Warr, Boren, and Longo noted the presence of two distinct types of scale on their alloys. One scale, which they called Type A, was flaky and non-adherent, black to dark green in color, and was highly protective. The other, or Type B, scale was associated with conditions of rapid metal attack, and was grayish and adherent. It must be emphasized here that the type of test used by these investigators consisted of a single heating cycle. Whether the Type A scale would have proved superior in cyclic tests seems open to question. Longo's contribution consisted of determining the compositions and conditions of formation of these two types of scale. He found that the Type A scale consisted of Cr_2O_3, a high-parameter spinel which he definitely identified as being $MnCr_2O_4$, and sometimes Fe_2O_3. In those cases where Fe_2O_3 appeared, the amount of spinel was small. The Type B scale generally consisted of $Fe(Fe_{2-x}Cr_x)O_4$, $0 \leq x \leq 2$, which is a spinel of somewhat lower lattice parameter than $MnCr_2O_4$, together with FeO, Fe_2O_3, or both. The Type B scale contained considerably less Cr than the Type A scale, no Cr_2O_3 being present in the former. Longo found that high attack rates tended to result in layered scales, with the Cr becoming concentrated in the innermost layer. The Cr content of the low-parameter spinels increased with the Cr content of the alloys and generally increased with the temperature of oxidation. The Cr content of the total scale increased with the Cr content of the alloy and decreased with increasing temperature of oxidation.

Longo also considered the effect on the composition of the Type A scale of decreasing the Mn content of the alloy, and found that $MnCr_2O_4$, as might be expected, tended not to form at low Mn contents. Longo further showed that there was surface depletion of Mn with increasing time of oxidation.

Longo's work agrees with the results obtained by Yearian, Kortright, and Langenheim (51) regarding the lattice parameter-vs.-composition variation of $Fe(Fe_{2-x}Cr_x)O_4$ as x goes from zero to two. There are wide deviations from Vegard's Law in this system associated with changes from the inverse spinel structure (near $x = 0$) to the normal spinel structure (near $x = 2$). Over a considerable portion of the composition range, there is partial inversion of the spinel structure. The structural changes occurring in this system, $Fe(Fe_{2-x}Cr_x)O_4$, $0 \leq x \leq 2$, have the effect of making the composition a multi-valued function of the lattice parameter, thus making it very difficult, if not impossible, to evaluate x in a given physical case solely by means of lattice parameter measurements. The same structural changes that cause aberrations in the values of the lattice parameter also must result in similar effects in the values of magnetic permeability. Therefore, neither x-ray diffraction nor magnetic techniques can be relied upon as certain indications of the compositions of oxide specimens in which the presence of $Fe(Fe_{2-x}Cr_x)O_4$ is suspected.

The unusual variations in lattice parameter in the system $Fe(Fe_{2-x}Cr_x)O_4$, according to Yearian, Kortright, and Langenheim, are typical of what may be expected when one deals with a binary spinel system in which one of the terminal

spinels has an inverse structure and the other has a normal structure. If both terminal spinels are either normal or inverse, Vegard's Law holds. Thus, one would not expect the two high-parameter spinels which could conceivably occur on stainless steels, $MnCr_2O_4$ and $MnFe_2O_4$, both of which have normal structures, to show other than linear lattice parameter variation as Cr is replaced with Fe.

It has been noted (52) that some spinels which have normal structures may develop some inversion, with accompanying magnetism, when rapidly cooled, as was done in this investigation. In short, it must be concluded that presence or absence of ferromagnetism per se cannot be construed as being indicative of scale compositions.

Longo ascribed the oxidation resistance of the Cr stainless steels to the presence of Cr_2O_3 in the scales. In addition to his own experimental results in support of this conclusion, Longo was able to show that according to the data reported by McCullough, Fontana, and Beck (16), considerable Cr_2O_3 must have been present in their initial, highly oxidation-resistant scales, the protective nature of which the latter investigators attributed to the spinel phase.

It might be appropriate to point out here a theoretical prediction concerning the physical stability of spinel layers formed on the surfaces of stainless steels. This prediction is of special interest because it bears upon the experimental observations of McCullough, Fontana, and Beck, viz., that the spinel layers initially formed in the oxidation of 18-8 stainless steel (which layers Longo showed must also have contained

Cr_2O_3) tended to rupture after a relatively short time at temperature, resulting in a decrease in oxidation resistance and the formation of an Fe_2O_3-rich oxide at the points of rupture. When one examines the Pilling-Bedworth, or volume, ratios of the various possible oxides of the metals found in stainless steels (see Table 15), one finds that the volume ratios of the spinels tend to be quite high -- either about 3 or 6, depending on whether the trivalent or the divalent cation is considered. Pilling and Bedworth (53) showed that one requirement for an adherent scale on a metal surface was that its volume ratio with respect to an equivalent volume of underlying metal should be somewhat, but not a great deal, greater than unity. If the volume ratio is less than unity, the scale will be under a tensile stress which will ultimately cause rupture. If the volume ratio is very much greater than unity, the scale will eventually buckle as a result of accumulated compressive stresses. Considering the relatively high values of the volume ratios of spinels with respect to stainless steels, it seems unlikely that any scale layer containing spinel as the major component could remain continuous on these materials for oxidation times longer than several hours in air above 1600°F. The same is not the case for SiO_2, however. Although the volume ratio for SiO_2 in the form of β-cristobalite formed on stainless steel is about 4, the interference film thickness of what is believed to be SiO_2 on these materials would probably not permit the accumulation of sufficient stresses to cause buckling of the SiO_2 layer.

The results of x-ray analysis of the scales obtained as part of the present investigation confirm the work of Longo in many respects, as can be seen from Tables 3 through 11. A typical x-ray pattern is presented in Figure 134, along with appropriate pure-component patterns. The spinel pattern shown is that of Fe_3O_4, and above this pattern are shown the ranges of θ over which the spinel lines occur as the spinel lattice parameter changes from 8.299 kX ($NiCr_2O_4$) to 8.502 kX ($MnFe_2O_4$). Most of the scales obtained contained Cr_2O_3 and high-parameter spinel, and many of them also contained Fe_2O_3. In some cases, the Cr_2O_3 and/or Fe_2O_3 phases seemed to contain minor amounts of each other. The scales formed on two of the heats, 64177 and 64270 (Tables 4 and 5), did not in general show a spinel phase, but rather tended towards Cr_2O_3-Fe_2O_3 solid solution scales. This behavior can be explained by the fact that the Mn contents of these two heats were much lower than in the rest of the heats (see Table 1). This again is in accord with Longo's observations. Although the physical appearance of the Cr_2O_3-Fe_2O_3 solid solution scales on heats 64177 and 64270 was similar to that of the Type B scales reported by Longo for Cr stainless steels, apparently these were simply a degenerate form of the Type A scale having no spinel phase, because the attack rates did not appear to differ appreciably between heats 64177 and 64270 and the other heats. Further, FeO was never observed at any time, either in this investigation or in any other investigation of Cr-Ni stainless steels, so far as is known to this author. The existence of a low-parameter spinel phase, most likely

$Fe(Fe_{2-x}Cr_x)O_4$, was confirmed in a few cases. There is reason to believe that this low-parameter spinel made up an inner layer of the scale, since the low-parameter spinel did not appear in replicate specimens in some cases. Presumably, efforts to remove the scales for analysis were not as successful in these cases as in the cases in which low-parameter spinel was observed. It is significant that low-parameter spinel was often found in scales also containing Cr_2O_3 and high-parameter spinel. Thus, Type B scale cannot be said to exist in the Cr-Ni stainless steels as the separate and distinct type observed in the Cr stainless steels.

Considerable variability was encountered in the scale compositions, even in supposedly identical specimens. This variability is well illustrated by the representative results presented in Table 16. Specimens shown in this table were run under as nearly identical conditions as possible. In all cases, the dew point was kept near -40°F, the air velocity was kept at 30 ft/sec, temperatures were controlled to approximately ±5°F, and the oxidation times were all 100 hr, within 1 percent. As can be seen from Table 16, there was considerable variation in specimen and scale appearances as well as in the scale compositions. The differing adherence characteristic of the scales as it affects representative sampling is no doubt responsible for part of the scale composition variation, but the ultimate reason for the variation is more fundamental, and is probably connected with the initial surface condition. Although the surfaces of the specimens used in this investigation were quite satisfactory from a commercial

standpoint, there were probably minor variations present from specimen to specimen which were sufficient to alter the scale characteristics. Current thinking by outstanding workers in the field (54) is that minor surface contaminations and other variations are able to alter considerably the composition and mode of growth of the scale, creating differences between replicate specimens which may persist for hundreds of hours.

As far as the present investigation is concerned, one of its tacit objectives was to see whether variations in oxidation characteristics caused by normally-encountered surface variations were of major or of minor importance. From the data presented in Tables 3 through 11 and Table 16, it appears that sufficient variation in scale characteristics and composition is present so that differences resulting from time and temperature are obscured, but that, taken in toto, a fairly reliable picture of the usual scale compositions and physical characteristics of the materials in question becomes apparent. Scales ranged from gray to black in color, tended to show some magnetism in general, were never copiously produced in the same sense as scales on lower alloyed metals, and contained the previously-noted rhombohedral and spinel phases, the latter of which tended to be absent at low Mn contents in the steels.

One of the objectives of this investigation was to attempt to determine the nature of the intergranular material extending into the metal from the scale layer. It was desired to find the composition of this material and whether there were any significant differences between its composition and that of the external scale material. Just how this was to be done

experimentally was something of a problem, since the intergranular material was well dispersed and extremely thin. The method ultimately adopted was described in the Experimental Investigation section, page 38, and utilized reflection electron diffraction following successive etching treatments. Using this technique, it was possible to obtain data on the composition of the intergranular material as a function of depth below the metal-oxide interface. The results obtained by this method are presented in Table 17. Six heats of material were selected for examination -- type 309 + Nb, and type 310, heats 64177, 64270, X11306, X11338, and X27258. Specimens from the latter three heats were examined at all temperatures of oxidation, while the first three heats were examined only at the four lower temperatures. The program was restricted to an oxidation time of 100 hr.

As was noted previously, the accuracy obtainable with the reflection electron diffraction technique is of the order of 1 or 2 percent error in interplanar spacing, the same order as the changes in lattice parameters between Cr_2O_3 and Fe_2O_3 and between spinels having the highest and lowest possible lattice parameters. Therefore, the phases shown to be present in the electron diffraction patterns could be identified only as "rhombohedral" or "spinel". Examples of these two patterns are presented in Figures 128 and 129. Identification was made on the basis of the (220) spinel line and several rhombohedral lines, notably the (100), (110), (120), and (200) lines. It is of interest, in comparison with Figure 134, that the (100) rhombohedral line appears clearly on the electron diffraction

pattern, although it is never observed in the x-ray patterns, either in this investigation or by Yearian and Radavich (42). The appearance of the (100) line in the electron diffraction patterns could be due either to oriented oxide growth or to the fact that the low-angle structure factor for electrons is greater than for x-rays. The latter reason is the more likely, considering the probable randomness of the surface metal grain orientations.

The electron diffraction results showed that the same phases exist in the grain boundary fissures as were found in the external scales. In heats 64177 and 64270, the spinel phase was rarely observed. In the other five heats, both phases appeared, the spinel phase being especially prominent in the type 309 + Nb alloy, with its high Mn content (see Table 1). The relative proportions of the phases in a given specimen seemed to vary slightly with depth but the two patterns taken on each specimen at the same depth often showed similar variations. As nearly as can be determined, the intergranular material is identical to the material found in the external scale, and, indeed, is in general simply an inward extension of the external scale.

In order to be absolutely certain that the electron diffraction patterns obtained were not from reaction products between the metal and the etchant, a specimen was etched and allowed to dry without rinsing. The resulting electron diffraction pattern could be easily differentiated from those associated with the two oxide phases obtained by the routine process.

Figures 130 through 133 show the metallographic appearance of the specimen surfaces following successive etching treatments. The photomicrographs were taken using oblique light in order to show the oxides in relief more clearly. These photomicrographs show that electrolytic etching with 10 percent perchloric acid and 90 percent glacial acetic acid at 15°C does, indeed, result in preferential metal attack, leaving the intergranular oxide films intact and exposed. Figures 130 through 133 also illustrate something which was observed at the time etching was carried out; namely, that the first etching usually attacked the metal only at certain points where the path through the non-removable scale to the metal was relatively open. Further etching undercut the scale layer adjacent to these points, and in the subsequent brushing process, new metal surface was exposed. Ultimately, the scale layer could be completely removed by this process, but at the same time, much of the deeper intergranular material in the areas which etched initially was probably lost. Furthermore, patterns taken while appreciable amounts of scale remained on the surface probably are not representative of intergranular material at all, since the scale would serve to block the intergranular material from the electron beam. In some specimens, no difficulty was encountered with adhering scales, and even the first patterns obtained are representative of intergramular material.

It will be noted from Table 17, when compared with the appropriate penetration-vs.-depth curves, that the measured depths below which no oxide patterns were obtained were sometimes very much less than the maximum fissure depths observed

metallographically. In a few cases, apparent increases in thickness of the metal were observed on etching. There are two alternative conclusions that can be drawn from these facts; either the thickness measurements as made on the supermicrometer were not as reliable as they were believed to be, or the number of intergranular oxide areas in relief at the deeper levels was not sufficient to give an electron diffraction pattern. Considering the apparent thickness increases on some specimens and the sensitivity of the electron diffraction technique, the probability is that the measurements were not representative. Since the surfaces often became rather rough as a result of the etching treatment, it was difficult to devise a suitable means of making thickness measurements which would be accurate to 0.0001 inch and at the same time would be representative of the surface as a whole.

VI. SUMMARY AND CONCLUSIONS

1. The proposed mechanism of intergranular oxidation in type 310 stainless steel is as follows. Oxygen ions reaching the metal-oxide interface by anionic transport through the external scale tend to segregate preferentially at points where grain boundaries intersect the metal-oxide interface. This segregation is the result of the greater diffusion coefficients relative to the grains existing at grain boundaries. Grain boundary diffusion coefficients are larger than volume diffusion coefficients in general because the lattice disorder present at grain boundaries results in somewhat widened interatomic spacings at these points, thus allowing easier passage of diffusing ions than does the relatively perfect lattice within grains. The amount by which the grain boundary diffusion coefficient exceeds the volume diffusion coefficient in a given case depends upon the relative orientation of the grains on either side of the boundary. The more nearly these grains are in registry, the closer will be the grain boundary diffusion coefficient to the volume diffusion coefficient in value.

2. The grain boundaries also act as areas of concentration of odd-sized alloying elements, again because of the widened lattice intervals at grain boundaries, which permit a low-energy spatial configuration. Oxygen ions proceeding down the grain boundaries will tend to react with those alloying elements which are the most easily oxidizable to form oxides essentially like those oxides composing the external scales.

3. Once oxide has formed in a grain boundary, further oxygen ion diffusion past this oxide most likely takes place along the interfaces between the oxide film and the grains. Thus, presence of an oxide grain boundary film may be expected to increase intergranular oxidation, since the presence of oxide essentially provides two diffusion paths instead of one per grain boundary. Some oxygen ions react to form oxide while diffusing past the intergranular oxide film, as is evidenced by the observation that the width of intergranular oxide-filled fissures tends to increase with increasing severity of oxidizing conditions. Most of the intergranularly-diffusing oxygen continues deeper into the grain boundary, however, because the region near the surface is one in which easily-oxidizable alloying elements have been depleted in concentration.

4. The intergranular oxides formed are indistinguishable from the external oxides by reflection electron diffraction techniques, and consist of a rhombohedral sesquioxide phase composed of Cr_2O_3 and Fe_2O_3 and a cubic spinel phase, either $MnCr_2O_4$ or $Fe(Fe_{2-x}Cr_x)O_4$. In addition, minor amounts of all of the alloying elements are probably dissolved in these oxides. Nickel, the only alloying element less electronegative than the basis metal, tends to concentrate in the metal layer just below the surface, and contributes little to the oxidation resistance of the alloy.

5. The only pronounced effect on oxidation characteristics of variation of alloy contents within the ranges studied was the disappearance of the high-parameter spinel phase,

$MnCr_2O_4$, in the scales when the manganese content dropped below 1 to 1.5 percent. The disappearance of the high-parameter spinel phase was not associated with any increase in oxidation rates, as far as could be determined.

6. Over the ranges of times and temperatures examined in this investigation, temperatures between 1600° and 2000°F and times between 10 hr and 100 hr, intergranular oxidation in general increased with both time and temperature of oxidation.

7. The effect of preferred orientation is to cause a decrease in the intergranular oxidation, presumably because of the smaller orientation differences existing between adjacent grains. This improvement in intergranular oxidation characteristics is offset by an increase in the overall, or volume, oxidation rate, however.

BIBLIOGRAPHY

1. Kubaschewski, O. and Hopkins, B. E., Oxidation of Metals and Alloys, Academic Press (New York), 1953.

2. Heindlhofer, K. and Larsen, B. M., Trans. Amer. Soc. Steel Treat., 21 (1933) 865.

3. Price, L. E. and Thomas, G. J., J. Inst. Met., 63 (1938) 21, 29.

4. Lustman, B., Trans. Electrochem. Soc., 81 (1942) 359.

5. Cabrera, N. and Mott, N. F., Rep. Progr. Phys., 12 (1948-49) 163.

6. Dravnieks, A. and McDonald, H. J., Trans. Electrochem. Soc., 94 (1948) 139.

7. Dunnington, B. W., Beck, F. H., and Fontana, M. G., Corrosion, 8 (1952) 2.

8. Smirnov, A., Acta phys.-chim. U.R.S.S., 22 (1947) 162.

9. Hauffe, K., Z. Metallk., 42 (1951) 34.

10. Davies, M. H., Simnad, M. T., and Birchenall, C. E., J. Metals, 3 (1951) 889; Ibid., 5, (1953) 1250.

11. Paidassi, P., J. Metals, 4 (1952) 536.

12. Hickman, J. W. and Gulbransen, E. A., Trans. Amer. Inst. Met. Engrs., 171 (1947) 344.

13. Miyake, S., Sci. Pap. Inst. phys. chem. Res. Tokyo, 29 (1936) 167; 31 (1937) 161.

14. Longo, T. A., Master's Thesis, Dept. of Physics, Purdue Univ., 1953.

15. Yearian, H. J. and Radavich, J. F., Reports published under ONR Contract No. N7onr-39419.

16. McCullough, H. M., Fontana, M. G., and Beck, F. H., Trans. Amer. Soc. Metals, 43 (1951) 404.

17. Iitaka, I., Nakayama, T., and Sekiguchi, K., J. Sci. Res. Inst. Tokyo, 45 (1951) 57.

18. Preece, A., Richardson, G. T., Semister, E., and Cobb, J. W., in Special Report No. 24: Second Report of the Alloy Steels Research Committee, The Iron and Steel Institute (1939) 9-63.

19. Pfeil, L. B., J. Iron and Steel Inst., 119 (1929) 501; Ibid., 131 (1931) 237.

20. Benard, J. and Moreau, J., Rev. Met. 47 (1950) 317.

21. Baeyertz, M., Trans. Amer. Soc. Metals, 24 (1936) 420.

22. Bandel, G., Arch. Eisenhüttenw., 15 (1951) 271.

23. Rickett, R. L. and Wood, W. P., Trans. Amer. Soc. Steel Treat., 22 (1934) 347.

24. Iitaka, I. and Miyake, S., Nature, 137 (1936) 457.

25. Quarrell, A. G., Nature, 145 (1940) 821.

26. Arkharov, V. I., Bull. Acad. Sci. U.R.S.S., (1946) 127.

27. Gulbransen, E. A. and McMillan, W. R., Ind. Eng. Chem., 45 (1953) 1734.

28. Radavich, J. F., Doctor's Thesis, Dept. of Physics, Purdue Univ., 1953.

29. Warr, R. E., Master's Thesis, Dept. of Physics, Purdue Univ., 1951.

30. Boren, H. E., Jr., Master's Thesis, Dept. of Physics, Purdue Univ., 1950.

31. Rhines, F. N., Trans. Amer. Inst. Met. Engrs., 137 (1940) 246.

32. Smith, C. S., J. Inst. Met., 46 (1931) 49.

33. Chaston, J. C., J. Inst. Met., 71 (1945) 23.

34. Spooner, N., Thomas, J. M., and Thomassen, L., J. Metals, 5 (1953) 844.

35. Fisher, J. C., J. Appl. Phys., 22 (1951) 74.

36. Le Claire, A. D., Lond. Philos. Mag., 42 (1951) 468.

37. Achter, M. R. and Smoluchowski, R., J. Appl. Phys., 22 (1951) 1260; Phys. Rev., 83 (1951) 163; "Structure and Behavior of Grain Boundaries", in The Physics of Powder Metallurgy, McGraw-Hill (New York) 1951.

38. Turnbull, D. and Hoffman, R. E., Acta Met., 2 (1954) 419.

39. Snoek, J. L., Z. Metallk., 30 (1938) 94.

40. Benard, J., Metall. Ital., 42 (1950) 3.

41. Metals Hndbk., Publ. by Amer. Soc. Met. (Cleveland), 1948, p. 396.

42. Yearian, H. J. and Radavich, J. F. Private communication.

43. Upthegrove, C. and Murphy, D. W., Trans. Amer. Soc. Steel Treat., 21 (1933) 73.

44. Siebert, C. A., Trans. Amer. Soc. Metals, 27 (1939) 752.

45. Brockway, L. O. and Bigelow, W. C., "Development of Procedures for the Identification of Minor Phases in Heat Resistant Alloys by Electron Diffraction", Annual Summary Report on Project 2020, Eng. Res. Inst., Univ. of Mich., to Flight Research Laboratory (WCRRL), WADC, 15 Jan 1953.

46. Barth, T. F. W. and Posnjak, E., Z. Krist., 82 (1932) 325.

47. Burgess, C. O. and Forgeng, W. D., Trans. Amer. Inst. Met. Engrs., 131 (1938) 277.

48. Koshuba, W. J., Private communication.

49. Brower, T. E., Larsen, B. M., and Schenk, W. E., Trans. Amer. Inst. Met. Engrs., 61 (1934) 113.

50. Barnes, R. S., Metal Treatment and Drop Forging, 18 (1951) 531.

51. Yearian, H. J., Kortright, J. M., and Langenheim, R. H., J. Chem. Phys., 22 (1954) 1196.

52. Bozorth, R. M., Ferromagnetism, Van Nostrand (New York), 1951.

53. Pilling, N. B. and Bedworth, R. E., J. Inst. Met., 29 (1923) 529.

54. Mahla, E. M., Private communication.

TABLE 1

COMPOSITION OF STAINLESS STEEL STOCK, WEIGHT PERCENT

Heat No.	C	Ni	Cr	Si	Mn	P	S	Mo	Cu	Co	W	Nb
309 + Nb	0.08	15.39	22.64	0.46	2.31	0.012	0.008	-	-	-	-	0.82
64177	0.13	16.96	24.03	0.55	0.42	0.018	0.008	0.033	0.13	0.01	<0.01	-
64270	0.12	19.14	22.30	0.43	0.50	0.025	0.008	0.042	0.10	0.01	<0.01	-
X11306	0.07	20.33	25.48	0.78	1.41	0.023	0.013	-	-	-	-	-
X11338	0.085	20.08	24.28	0.83	1.53	0.029	0.029	0.14	0.25	-	-	-
X27258	0.073	20.81	24.64	0.75	1.58	0.025	0.008	0.15	0.30	-	-	-
X45558	0.069	21.56	24.71	0.58	1.54	0.025	0.011	0.12	0.27	-	-	-
X46063	0.059	20.67	24.28	0.31	1.57	0.024	0.014	0.12	0.25	-	-	-
X46572	0.089	19.48	24.35	0.67	1.60	0.021	0.022	0.14	0.34	-	-	-

TABLE 2

EXPLANATION OF SYMBOLS USED IN OXIDATION DATA TABULATIONS

SPECIMEN APPEARANCE:

PGB - Porous gray black
PGB w/ OS - Porous gray black with orange substrate
SGB - Shiny gray black
B and S - Black and scoriated
BP w/ LG - Black pits with light gray surface (mostly pits)
LG - Light gray surface
LG w/ BP - Light gray with black pits (mostly light gray)
LG w/ IC - Light gray with interference colors

MAGNETISM:

ND - Not detectable
W - Weak
M - Medium
S - Strong

OXIDE APPEARANCE:

Quantity:

N - None
S - Small amount
M - Medium amount
L - Large amount

Flake Size:

P - Powder
SF - Small flake (<1/32 in.)
MF - Medium flake (1/32 - 1/8 in.)
LF - Large flake (>1/8 in.)

Color:

G - Gray
B - Black
GB - Gray-black

OXIDE COMPOSITION:

S.S. xQ - Cr_2O_3- Fe_2O_3 solid solution with Q $\pm$ 10 atomic percent Cr_2O_3
HPS - High-parameter spinel
a = p - Lattice parameter of spinel in kX units
* - Lattice parameter determined from two-point extrapolation
Insuf. - Insufficient oxide for x-ray pattern
W - Weak pattern
M - Medium pattern
S - Strong pattern

TABLE 3

RESULTS OF OXIDATION TESTS, TYPE 309 + Nb ALLOY

0.08% C, 15.3% Ni, 22.64% Cr, 0.82% Nb, 0.46% Si, 2.31% Mn, 0.012% P, 0.008% S

Air Velocity, ft/min	Dew-point, °F	Penetration Curve, Fig. No.	Temp., °F	Specimen Appearance	Magnetism	No. of Fissures/in.	Mean Fissure Depth, in.x10^3	Oxide Scale Amount	Color	Flake Size	Magnetism	Composition (x-ray)
40	< -20	17	1600	LG w/ BP LG w/ IC	-	222.1	0.455	M	GB	SF	ND	-
			1700	PGB LG w/ IC	-	1011.1	0.692	L	G	LF	ND	-
			1800	PGB LG w/ IC	-	699.8	1.523	M	GB	LF	ND	-
			1900	LG w/ IC	-	719.0	1.700	L	B	MF	M	-
30	-	20	1600	LG w/ IC	-	96.0	0.332	M	GB	MF	ND	-
			1700	LG w/ IC	-	480.9	0.368	M	GB	LF	ND	-
			1800	LG w/ BP	-	723.5	0.403	S	GB	MF	M	-
			1900	PGB LG	-	869.1	1.307	S	GB	P	M	-
30	from +15 to +20	23	1600	LG w/ BP LG	-	435.9	0.371	M	B	P	ND	-
			1700	B and S	-	423.3	0.344	L	GB	MF	M	-
			1800	B and S PGB	-	321.6	0.486	L	GB	MF	M	-
			1900	LG w/ IC	-	386.8	1.117	L	GB	MF	M	-
						Straight Section						
30	from <-60 to -30	26	1600	PGB	-	611.4	0.544	S	GB	P	M	-
			1700	PGB LG	-	547.5	0.513	S	GB	P	M	-
			1800	LG w/ IC	-	837.8	0.936	S	GB	MF	M	-
			1900	LG	-	852.6	1.499	L	GB	MF	S	-
						Curved Section						
		29	1600	-	-	376.9	0.683	-	-	-	-	-
			1700	-	-	553.3	0.727	-	-	-	-	-
			1800	-	-	438.6	1.605	-	-	-	-	-
			1900	-	-	623.0	1.319	-	-	-	-	-
30	from -45 to +10	32	Control	-	-	280.6	0.343	-	-	-	-	-
			1600	BP w/ LG PGB	M	938.0	0.459	M	GB	P-SF	M	-
			1700	PGB LG w/ IC	M	772.2	0.774	L	GB	MF	ND	-
			1800	LG w/ IC	S	1016.0	0.369	L	GB	LF	M	-
			1900	LG w/ IC	S	859.6	0.572	L	G	LF	M	-
30	from -45 to -22	35	Control	-	-	1066.1	0.361	-	-	-	-	-
			1600	PGB LG w/ BP	-	862.4	0.408	S	B	P	ND	Insuf.
			1700	LG w/ BP PGB	-	1288.0	0.487	S	B	P-SF	M	Insuf.
			1800	LG w/ IC LG w/ BP	-	1023.4	0.455	L	GB	MF	S	Cr_2O_3(S) Fe_2O_3(M) HPS(W)
			1900	LG w/ IC LG w/ BP	-	1071.6	0.567	L	GB	MF	S	Cr_2O_3(S) Fe_2O_3(W) HPS(W) a=8.43*
30	from -22 to -16	38	Control	-	-	274.1	0.320	-	-	-	-	-
			1600	PGB LG w/IC	W	318.8	0.320	S	B	SF	W	Insuf.
			1700	PGB PGB	W	818.4	0.323	S	B	P	ND	Insuf. Cr_2O_3(S)
			1800	BP w/ LG LG	M	900.6	0.330	M	GB	P-SF	S	Fe_2O_3(M) HPS(M)
			1900	LG w/ BP PGB	M	719.6	0.365	M	B	P-SF	M	S.S.x30
40	from -30 to +20	41	Control	-	-	113.0	0.320	-	-	-	-	-
			1600	LG w/ IC BP w/ LG LG w/ BP	ND	785.4	0.336	L	B	SF	ND	-
			1700	PGB w/ OS SGB BP w/ LG LG w/ BP	M	831.4	0.336	L	G	MF	S	-
			1800	LG w/ IC LG w/ BP	M	778.3	0.580	L	G	LF	S	-
			1900	LG w/ IC	M	775.7	0.449	L	G	LF	S	-
30	from -45 to -35	44	Control	-	-	340.3	0.529	-	-	-	-	-
			1600	LG w/ BP B and S PGB	W	409.4	0.334	S	B	P	M	-
			1700	LG w/ BP PGB B and S	W	949.0	0.328	S	B	P	M	-
			1800	PGB B and S LG w/ IC BP w/ LG	W	1125.7	0.510	M	GB	P-SF	W	-
			1900	B and S PGB BP w/ LG	M	851.2	0.843	L	GB	P-SF	S	-
30	from -55 to -40	47	Control	-	-	146.6	0.339	-	-	-	-	-
			1600	LG w/ IC LG w/ BP	S	1218.6	0.372	L	B	LF	ND	Cr_2O_3(S) HPS(S)
			1700	BP w/ LG	M	1242.6	0.363	S	B	P	M	Cr_2O_3(S) Fe_2O_3(S) HPS(W)
			1800	LG w/ IC	S	475.2	0.529	L	G	LF	S	Cr_2O_3(S) Fe_2O_3(M) HPS(M) a=8.45*
			1900	LG w/ IC	M	504.5	0.496	L	G	LF	S	Cr_2O_3(S) Fe_2O_3(M) HPS(M) a=8.45*
30	-38	38	2000	PGB LG LG w/ IC	S	1456.2	0.562	M	GB	MF	S	-
30	from -46 to -38	35	2000	PGB w/ OS BP w/ LG PGB	M	1100.6	0.686	S	B	P	M	-

TABLE 4

RESULTS OF OXIDATION TESTS, TYPE 310 ALLOY, HEAT 64177

0.13% C, 16.96% Ni, 24.03% Cr, 0.55% Si, 0.42% Mn, 0.018% P, 0.008% S, 0.033% Mo, 0.13% Cu, 0.01% Co, <0.01% W

Run No.	Duration, hr	Air Velocity, ft/min	Dew-point, °F	Penetration Curve, Fig. No.	Temp., °F	Specimen Appearance	Specimen Magnetism	Specimen No. of Fissures/in.	Specimen Mean Fissure Depth, in.x10^3	Oxide Scale Amount	Oxide Scale Color	Oxide Scale Flake Size	Oxide Scale Magnetism	Oxide Scale Composition (x-ray)
4	100	40	<-20	18	1600	PGB	-	530.7	0.836	M	GB	P-SF	W	-
					1700	PGB	-	222.6	0.817	S	GB	P	S	-
					1800	PGB	-	130.9	0.650	M	GB	P-SF	ND	-
					1900	BP w/ LG	-	536.6	0.856	S	GB	P	ND	-
7	100	20	-	21	1600	PGB w/ OS	-	341.6	0.743	S	GB	P	ND	-
					1700	PGB w/ OS	-	451.5	0.730	S	GB	P	ND	-
					1800	PGB w/ OS	-	495.6	0.705	S	GB	P	W	-
					1900	PGB / LG	-	440.0	0.703	S	GB	P	ND	-
8	100	30	from +15 to +20	24	1600	PGB / LG w/ BP	-	438.4	0.749	S	GB	P	M	-
					1700	PGB / LG w/ BP	-	470.5	0.752	S	B	P	M	-
					1800	LG w/ BP / LG w/ IC	-	435.2	0.983	M	GB	MF	M	-
					1900		-	280.4	0.730	S	B	P	M	-
						Straight Section								
9	100	30	from <-60 to -30	27	1600	PGB	-	421.2	0.773	M	B	P	M	-
					1700	PGB	-	356.2	0.883	S	B	P	M	-
					1800	PGB	-	443.2	0.771	S	B	P	W	-
					1900	PGB	-	461.7	0.709	S	GB	P	M	-
						Curved Section								
				30	1600	-	-	194.5	1.032	-	-	-	-	-
					1700	-	-	205.5	0.725	-	-	-	-	-
					1800	-	-	227.6	0.931	-	-	-	-	-
					1900	-	-	180.2	0.825	-	-	-	-	-
10	50	30	from -45 to +10	33	Control	-	-	525.7	0.455	-	-	-	-	-
					1600	PGB / BP w/ LG	ND	589.0	0.770	S	B	P	ND	-
					1700	PGB / BP w/ LG	ND	675.6	0.697	S	B	P-SF	M	-
					1800	PGB / LG w/ IC	ND	662.9	0.740	M	GB	P-SF	S	-
					1900	BP w/ LG / PGB	ND	883.9	0.812	S	B	P	M	-
11	30	30	from -45 to -22	36	Control	-	-	460.2	0.547	-	-	-	-	-
					1600	BP w/ LG / PGB	-	757.0	0.548	S	B	P	ND	Insuf.
					1700	PGB / BP w/ LG	-	1004.2	0.556	S	B	P	M	Insuf.
					1800	BP w/ LG	-	666.4	0.341	S	B	P	ND	Insuf.
					1900	BP w/ LG	-	882.1	0.505	S	B	P	ND	Insuf.
12	10	30	from -22 to -16	39	Control	-	-	447.6	0.428	-	-	-	-	-
					1600	PGB w/ OS / LG	ND	490.9	0.563	S	B	SF	W	Insuf.
					1700	PGB / LG w/ BP / BP w/ LG	ND	548.5	0.531	S	B	P	M	Insuf.
					1800	LG w/ BP / LG w/ IC	ND	572.7	0.538	M	B	P-SF	S	S.S.x50(S) S.S.x25(W)
					1900	PGB / PGB / LG w/BP / LG w/ IC	ND	655.2	0.586	M	B	P-SF	S	Cr_2O_3 (S) Fe_2O_3 (M) HPS (M) a = 8.42Å
13	100	40	from -30 to +20	42	Control	-	-	608.3	0.468	-	-	-	-	-
					1600	PGB w/ OS / BP w/ LG	ND	1099.1	0.528	S	B	P	M	-
					1700	PGB w/ OS / BP w/ LG	ND	1076.6	0.547	S	B	P	M	-
					1800	PGB w/ OS / LG w/ IC	ND	991.5	0.787	M	GB	P-SF	M	-
					1900	PGB w/ OS / LG w/ BP	ND	1222.3	0.698	L	B	SF	M	-
14	77	30	from -45 to -35	45	Control	-	-	217.8	0.408	-	-	-	-	-
					1600	PGB / BP w/ LG	M	544.0	0.683	S	B	P	M	-
					1700	PGB / BP w/ LG	W	822.1	0.564	S	B	P	M	-
					1800	PGB / BP w/ LG	W	625.2	0.648	S	B	P	M	-
					1900	PGB / BP w/ LG / PGB	W	671.6	0.652	S	B	P	M	-
15	100	30	from -55 to -40	48	Control	-	-	634.6	0.537	-	-	-	-	-
					1600	PGB	M	895.6	0.710	S	B	P	M	Cr_2O_3 Insuf.
					1700	PGB	M	1147.5	0.802	S	B	P	M	S.S.x50
					1800	PGB / BP w/ LG	W	1275.0	0.842	S	B	P	M	S.S.x50
					1900	BP w/ LG	M	1283.9	0.766	M	B	P	M	-
22	10	30	-38	39	2000	PGB	M	980.2	0.606	S	B	F	M	-
23	50	30	from -46 to -38	36	2000	LG w/ IC B and S	S	1281.3	0.774	L	G	M	S	-

TABLE 5

RESULTS OF OXIDATION TESTS, TYPE 310 ALLOY, HEAT 64270

0.12% C, 19.14% Ni, 22.30% Cr, 0.43% Si, 0.50% Mn, 0.025% P, 0.008% S, 0.042% Mo, 0.10% Cu, 0.01% Co, < 0.01% W

Run No.	Duration, hr	Air Velocity, ft/min	Dew-point, °F	Penetration Curve, Fig. No.	Temp., °F	Specimen Appearance	Specimen Magnetism	Specimen No. of Fissures/in.	Specimen Mean Fissure Depth, in.x10^3	Oxide Scale Amount	Oxide Scale Color	Oxide Scale Flake Size	Oxide Scale Magnetism	Oxide Scale Composition (x-ray)
6	100	40	<-20	19	Control	-	-	56.2	0.508	-	-	-	-	-
					1600	PGB	-	269.4	0.605	S	B	P	ND	-
					1700	PGB LG LG w/IC	-	295.3	0.573	L	GB	P-SF	M	-
					1800	PGB LG w/IC	-	147.3	0.593	S	GB	P-SF	ND	-
					1900	LG w/BP	-	131.4	0.666	S	B	P	ND	-
4	100	20	-	22	1600	PGB w/OS	-	225.9	0.386	S	GB	P	W	-
					1700	PGB w/OS	-	370.4	0.439	S	GB	P-SF	S	-
					1800	PGB w/OS	-	323.8	1.127	S	GB	P	ND	-
					1900	PGB w/OS	-	223.3	1.063	S	GB	P	W	-
8	100	30	from +15 to + 20	25	1600	PGB	-	328.0	0.387	S	GB	P-SF	M	-
					1700	PGB	-	373.2	0.345	S	B	P	M	-
					1800	PGB	-	460.6	0.411	S	B	P	M	-
					1900	PGB LG w/BP PGB w/OS	-	232.0	0.416	S	B	P	M	-
								Straight Section						
3	100	30	from <-60 to -30	28	1600	PGB	-	216.0	0.370	S	GB	P	M	-
					1700	PGB	-	350.3	0.431	S	B	P	M	-
					1800	PGB	-	284.1	0.469	M	B	P	M	-
					1900	PGB	-	305.6	0.503	M	B	P	M	-
								Curved Section						
				31	1600	-	-	68.8	0.389	-	-	-	-	-
					1700	-	-	109.5	0.808	-	-	-	-	-
					1800	-	-	93.1	0.511	-	-	-	-	-
					1900	-	-	108.9	0.511	-	-	-	-	-
10	50	30	from -45 to +10	34	Control	-	-	442.3	0.336	-	-	-	-	-
					1600	PGB PGB	ND	500.4	0.390	S	B	P	S	-
					1700	BP w/LG LG w/IC	ND	445.4	0.482	M	B	P-SF	S	-
					1800	B and S BP w/LG	ND	604.7	0.808	L	B	P-SF	S	-
					1900	LG w/IC PGB	ND	784.3	0.615	L	B	P-SF	S	-
11	30	30	from -45 to -22	37	Control	-	-	106.0	0.351	-	-	-	-	-
					1600	PGB BP w/LG LG w/IC	-	533.4	0.332	S	B	P	M	Cr_2O_3
					1700	PGB LG w/IC	-	579.2	0.359	S	B	P-SF	M	Insuf.
					1800	PGB BP w/LG	-	597.0	0.485	S	B	P-SF	S	Insuf.
					1900	LG w/IC BP w/LG	-	791.3	0.777	M	B	P-SF	S	Insuf.
12	10	30	from -22 to -16	40	Control	-	-	242.4	0.324	-	-	-	-	-
					1600	PGB w/OS BP w/LG	W	457.9	0.345	S	B	P-SF	M	Insuf.
					1700	PGB BP w/LG	ND	453.3	0.373	S	B	P	W	Insuf.
					1800	PGB LG	ND	945.0	0.359	S	GB	SF	W	Insuf.
					1900	PGB LG	W	845.0	0.376	M	B	P-SF	M	S.S.x50
13	100	40	from -30 to +20	43	Control	-	-	380.0	0.328	-	-	-	-	-
					1600	PGB w/OS	ND	660.1	0.355	S	B	SF	M	-
					1700	PGB w/OS LG	ND	739.4	0.430	M	B	P	M	-
					1800	PGB w/OS B and S LG w/BP	ND	769.1	0.509	M	B	P	M	-
					1900	LG w/IC B and S PGB w/OS	W	967.5	0.603	L	B	P-SF	M	-
14	77	30	from -45 to -35	46	Control	-	-	361.9	0.323	-	-	-	-	-
					1600	PGB	W	940.2	0.369	S	B	P	M	-
					1700	PGB	M	986.4	0.362	S	B	P	M	-
					1800	PGB LG w/IC	W	870.2	0.499	S	B	P	M	-
					1900	PGB BP w/LG	ND	1104.1	0.426	S	B	P	M	-
15	100	30	from -55 to -40	49	Control	-	-	354.1	0.325	-	-	-	-	-
					1600	PGB	M	621.0	0.374	S	B	P	M	S.S.x50 Fe_2O_3(S)
					1700	LG LG B and S	S	752.0	0.784	L	B	M	S	LPS(M) X50(S)
					1800	PGB	M	927.9	0.508	S	B	P	M	LPS(W)
					1900	BP w/LG PGB	W	1154.7	0.512	M	B	P	W	S.S.x50(S) Fe_2O_3?(W)
16	10	30	-38	40	2000	PGB B and S	W	438.2	0.467	S	B	P	M	-
17	30	30	from -46 to -38	37	2000	BP w/LG PGB w/OS B and S	M	1411.8	0.794	S	B	P	S	-

TABLE 6

RESULTS OF OXIDATION TESTS, TYPE 310 ALLOY, HEAT A-1506

0.07% C, 20.33% Ni, 25.48% Cr, 0.78% Si, 1.41% Mn, 0.023% P, 0.013% S

Air Velocity, ft/min	Dew-point, °F	Penetration Curve, Fig. No.	Temp., °F	Specimen: Appearance	Specimen: Magnetism	Specimen: No. of Fissures/in.	Specimen: Mean Fissure Depth, in.x10³	Oxide Scale: Amount	Oxide Scale: Color	Oxide Scale: Flake Size	Oxide Scale: Magnetism	Oxide Scale: Composition (x-ray)
30	from -52 to -42	50	Control	-	-	318.0	0.326	-	-	-	-	-
			1600	LG w/ BP	S	1106.1	0.421	M	B	P-SF	ND	Cr_2O_3(S) Fe_2O_3(M) HPS (M
			1700	LG w/ BP	S	620.0	1.360	L	G	MF	ND	Cr_2O_3(S) S.S.x25(M) HPS (M) a=8.48*
			1800	LG w/ IC	W	631.6	1.631	L	G	LF	ND	Cr_2O_3(S) HPS (S) a=8.42
			1900	PGB w/ OS BP w/ LG B and S	W	1791.0	2.099	M	B	P	ND	HPS (S) a=8.42 Cr_2O_3(M)
30	from -50 to -42	56	Control	-	-	219.6	0.322	-	-	-	-	-
			1600	SGB	M	1393.3	0.407	S	B	P	M	Insuf.
			1700	LG w/ IC LG w/ BP	M	600.0	0.456	M	GB	SF	W	S.S.x75(S HPS (M
			1800	PGB w/ OS	M	1340.0	0.921	S	B	P	M	Cr_2O_3(S) HPS (M)
			1900	LG w/ BP LG w/ IC	M	1305.8	1.585	M	B	P-SF	ND	Cr_2O_3(S) HPS (M a=8.44*
30	from -52 to -44	65	Control	-	-	178.8	0.323	-	-	-	-	-
			1600	LG LG w/ BP PGB	M	548.0	0.343	M	B	P-SF	M	-
			1700	LG w/ IC LG w/ BP	W	667.5	0.641	M	GB	P-MF	M	-
			1800	LG w/ IC LG w/ BP	M	1031.2	0.839	M	B	P-SF	M	-
			1900	LG w/ IC LG w/ BP	M	1148.8	1.247	M	B	P-SF	W	-
30	-38	65	2000	PGB	M	2590.5	0.716	S	B	P	W	-
30	from -46 to -38	56	2000	BP w/ LG B and S	M	2589.7	0.998	M	B	P-SF	S	-
30	from -50 to -40	50	2000	BP w/ LG	M	2134.5	0.962	S	B	P	M	-

TABLE 7

RESULTS OF OXIDATION TESTS, TYPE 310 ALLOY, HEAT X11334

0.085% C, 20.08% Ni, 24.08% Cr, 0.83% Si, 1.53% Mn, 0.029% P, 0.029% S, 0.25% Cu, 0.14% Mo

Air Velocity, ft/min	Dew-point, °F	Penetration Curve, Fig. No.	Temp., °F	Specimen: Appearance	Specimen: Magnetism	Specimen: No. of Fissures/in.	Specimen: Mean Fissure Depth, in.x10³	Oxide Scale: Amount	Oxide Scale: Color	Oxide Scale: Flake Size	Oxide Scale: Magnetism	Oxide Scale: Composition (x-ray
30	from -52 to -42	51	Control	-	-	361.6	0.404	-	-	-	-	-
			1600	BP w/ LG PGB LG	M	592.1	0.581	M	GB	M	ND	S.S.x75(S HPS(M a=8.47*
			1700	LG w/ IC	M	363.5	0.392	L	G	MF	ND	S.S.x25(M S.S.x95(S HPS(M a=8.47*
			1800	LG w/ IC	M	202.9	0.523	L	G	MF	ND	S.S.x95(S HPS(M a=8.47*
			1900	B and S LG w/ BP LG w/ IC	M	1364.7	1.765	L	B	P-SF	ND M	S.S.x90(S HPS(M a=8.47
30	from -50 to -42	57	Control	-	-	378.5	0.325	-	-	-	-	-
			1600	SGB LG	W	845.1	0.524	S	B	P	M	Cr_2O_3(S HPS(M a=8.47*
			1700	SGB LG	M	1030.1	0.535	S	B	P	S	Cr_2O_3(S HPS(M
			1800	LG w/ IC LG w/ BP	M	1005.7	0.354	M	GB	MF	ND	Cr_2O_3(S HPS(S a=8.42*
			1900	LG w/ IC	M	728.2	0.857	M	GB	M	ND	Cr_2O_3(S) HPS(S a=8.44*
30	from -52 to -44	66	Control	-	-	762.7	0.344	-	-	-	-	-
			1600	SGB LG LG w/ IC	M	1163.1	0.365	S	B	P	M	-
			1700	SGB LG w/ IC LG w/ BP	M	1266.1	0.417	S	B	P-SF	M	-
			1800	SGB LG w/ IC BP w/ LG	M	1417.5	0.420	S	B	P-SF	M	-
			1900	LG w/ IC	M	1186.4	0.593	L	B	MF	W	-
30	-38	66	2000	LG w/ IC	S	699.2	0.734	L	GB	MF	S	-
30	from -46 to -38	57	2000	PGB w/ OS BP w/ LG	ND	1327.-	0.869	S	B	P	S	-
30	from -50 to -40	51	2000	BP w/ LG	M	1425.4	0.707	S	B	P	S	-

TABLE 8

RESULTS OF OXIDATION TESTS, TYPE 310 ALLOY, HEAT X27255

0.075% C, 20.81% Ni, 24.64% Cr, 0.75% Si, 1.58% Mn, 0.025% P, 0.008% S, 0.30% Cu, 0.15% Mo

Run No.	Duration, hr	Air Velocity, ft/min	Dew-point, °F	Penetration Curve, Fig. No.	Temp., °F	Specimen Appearance	Specimen Magnetism	Specimen No. of Fissures/in.	Specimen Mean Fissure Depth, in.x10³	Oxide Scale Amount	Oxide Scale Color	Oxide Scale Flake Size	Oxide Scale Magnetism	Oxide Scale Composition (x-ray)
[illegible]	[illegible]	30	from -52 to -42	52	Control	-	-	501.7	0.442	-	-	-	-	-
					1600	PGB BP w/ LG LG	M	1370.4	0.405	S	B	P	M	Cr_2O_3(S) Fe_2O_3(W) LPS(W)
					1700	LG w/ BP PGB w/ OS PGB	W	779.3	0.566	L	B	MF	ND	Cr_2O_3(S) HPS(M a=2.43*
					1800	PGB w/ OS BP w/ LG LG w/ BP LG w/ IC	W	1010.5	0.661	S	B	P-SF	ND M	Cr_2O_3(S) LPS(S)
					1900	LG w/ BP LG w/ IC BP w/ LG B and S LG	W	1235.4	0.665	M	G	P-SF	ND	X75(S) HPS(W) LPS(VW)?
[illegible]	[illegible]	30	from -50 to -42	58	Control	-	-	463.8	0.321	-	-	-	-	-
					1600	SGB PGB LG	W	301.5	0.321	S	B	P	M	Cr_2O_3(S) Fe_2O_3(M HPS(W)
					1700	SGB LG BP w/ LG	W	1203.5	0.320	S	B	P	M	Insuf.
					1800	PGB w/ OS LG w/ IC	W	900.9	0.384	S	B	P	M	X75 Fe_2O_3? HPS
					1900	LG PGB w/ OS B and S	M	894.1	0.527	S	B	P	M	S.S.X75(S Fe_2O_3(M
[illegible]	[illegible]	30	from -52 to -44	67	Control	-	-	985.8	0.329	-	-	-	-	-
					1600	SGB LG w/ IC PGB w/ OS	M	1214.8	0.347	S	B	P-SF	S	-
					1700	LG w/ BP LG w/ IC	ND	1300.0	0.384	S	B	P-SF	S	-
					1800	BP w/ LG LG w/ IC	W	1147.8	0.410	M	B	P-SF	W	-
					1900	LG w/ IC BP w/ LG	S	911.1	0.343	M	B	MF	W	-
[illegible]	[illegible]	30	-38	67	2000	PGB w/ OS PGB B and S	S	1269.7	0.526	M	GB	MF	S	-
	[illegible]	30	from -46 to -38	58	2000	BP w/ LG PGB w/ OS B and S	M	1214.8	0.500	S	B	P	S	-
[illegible]	[illegible]	30	from -50 to -40	52	2000	BP w/ LG B and S PGB w/ OS	W	956.2	0.645	S	B	P	S	-

TABLE 9

RESULTS OF OXIDATION TESTS, TYPE 310 ALLOY, HEAT X45555

0.069% C, 21.56% Ni, 24.71% Cr, 0.58% Si, 1.54% Mn, 0.025% P, 0.011% S, 0.27% Cu, 0.12% Mo

Run No.	Duration, hr	Air Velocity, ft/min	Dew-point, °F	Penetration Curve, Fig. No.	Temp., °F	Specimen Appearance	Specimen Magnetism	Specimen No. of Fissures/in.	Specimen Mean Fissure Depth, in.x10³	Oxide Scale Amount	Oxide Scale Color	Oxide Scale Flake Size	Oxide Scale Magnetism	Oxide Scale Composition (x-ray)
[illegible]	[illegible]	30	from -55 to -38	53	Control	-	-	955.0	0.352	-	-	-	-	-
					1600	PGB LG LG w/ IC	M	748.1	0.338	S	B	P	ND	Insuf.
					1700	PGB BP w/ LG LG w/ IC	M	1145.6	0.357	S	B	P	W	Insuf.
					1800	BP w/ LG PGB w/ OS	M	1303.3	0.486	S	B	P	S	Insuf.
					1900	PGB BP w/ LG LG w/ IC	M	1124.6	0.514	M	B	P	ND	HPS (S) a = 2.41 Cr_2O_3 (M)
[illegible]	[illegible]	30	from -46 to -42	59	Control	-	-	252.7	0.322	-	-	-	-	-
					1600	SGB LG w/ IC	W	450.0	0.320	S	B	P	M	Cr_2O_3 (S) Fe_2O_3 (M)
					1700	SGB PGB w/ OS LG w/ IC	M	1164.1	0.323	S	B	P	M	Insuf.
					1800	SGB PGB w/ OS	W	1137.6	0.334	S	B	P	M	Insuf.
					1900	PGB w/ OS LG w/ IC	M	943.8	0.367	S	B	P	M	Cr_2O_3 (S) HPS (M)
[illegible]	[illegible]	30	from -52 to -41	62	Control	-	-	854.9	0.320	-	-	-	-	-
					1600	SGB LG w/ IC	-	748.5	0.320	S	B	P	M	-
					1700	PGB w/ OS SGB LG w/ IC	-	878.4	0.334	S	B	P	M	-
					1800	PGB w/ OS SGB	-	662.3	0.370	S	B	P	M	-
					1900	BP w/ LG BP w/ LG PGB w/ OS	-	679.6	0.372	S	B	P	M	-
[illegible]	[illegible]	30	-38	59	2000	SGB	M	841.3	0.348	S	B	P	S	-
[illegible]	[illegible]	30	from -46 to -38	62	2000	BP w/ LG PGB	ND	672.9	0.490	S	B	P	M	-
[illegible]	[illegible]	30	from -50 to -40	53	2000	B and S BP w/ LG	M	1075.6	0.540	M	B	P-SF	S	-

TABLE 10

RESULTS OF OXIDATION TESTS, TYPE 310 ALLOY, HEAT X46063

0.059% C, 20.67% Ni, 24.28% Cr, 0.31% Si, 1.57% Mn, 0.024% P, 0.014% S, 0.25% Cu, 0.12% Mo

Run No.	Duration, hr	Air Velocity, ft/min	Dew-point, °F	Penetration Curve, Fig. No.	Temp., °F	Specimen Appearance	Specimen Magnetism	Specimen No. of Fissures/in.	Specimen Mean Fissure Depth, in.x10^3	Oxide Scale Amount	Oxide Scale Color	Oxide Scale Flake Size	Oxide Scale Magnetism	Oxide Scale Composition (x-ray)
17	100	30	from -55 to -38	54	Control	-	-	728.9	0.354	-	-	-	-	-
					1600	PGB LG w/BP LG	W	1010.0	0.360	S	B	P-SF	ND	Cr_2O_3(S) HPS(M)
					1700	BP w/ LG LG	W	1024.9	0.487	M	B	P-SF	ND	Cr_2O_3(S) HPS(M) a=8.42*
					1800	LG w/ IC LG w/ BP	W	1116.6	0.622	L	B	MF	ND	Cr_2O_3(S) HPS(M) a=8.46
					1900	LG w/ BP LG	W	806.7	0.582	L	B	MF	ND	Cr_2O_3(S) HPS(M) a=8.42*
24	10	30	from -46 to -42	60	Control	-	-	269.7	0.330	-	-	-	-	-
					1600	SGB PGB w/ OS LG w/ IC	M	555.2	0.332	S	B	P	M	Insuf.
					1700	SGB LG w/ IC LG w/ BP	M	565.1	0.321	S	B	P-SF	M	Cr_2O_3(S) Fe_2O_3(M)
					1800	SGB LG w/ IC	M	560.2	0.386	S	B	P	W	Cr_2O_3(S) HPS(M)
					1900	SGB LG w/ IC LG w/ BP PGB w/ OS	M	635.3	0.402	M	B	P-SF	W	Cr_2O_3(S) HPS(M) a=8.42*
23	30	30	from -52 to -41	63	Control	-	-	65.5	0.320	-	-	-	-	-
					1600	SGB LG w/ IC	W	194.9	0.334	S	B	P-SF	M	-
					1700	SGB LG w/ IC LG w/ BP	ND	287.3	0.354	M	B	P-SF	M	-
					1800	BP w/ LG PGB w/ OS LG w/ IC	W	425.0	0.393	M	B	P-SF	M	-
					1900	LG w/ IC SGB LG w/ BP	S	366.1	0.443	M	B	P-SF	S	-
25	10	30	-38	60	2000	LG w/ BP LG w/ IC	S	523.5	0.436	M	B	P-SF	M	-
27	30	30	from -46 to -38	63	2000	LG w/ IC PGB	W	1130.0	0.588	S	B	P	W	-
28	100	30	from -50 to -40	54	2000	BP w/ LG B and S	M	343.4	0.437	M	B	P-SF	S	-

TABLE 11

RESULTS OF OXIDATION TESTS, TYPE 310 ALLOY, HEAT X46572

0.089% C, 19.48% Ni, 24.35% Cr, 0.67% Si, 1.60% Mn, 0.021% P, 0.022% S, 0.34% Cu, 0.14% Mo

Run No.	Duration, hr	Air Velocity, ft/min	Dew-point, °F	Penetration Curve, Fig. No.	Temp., °F	Specimen Appearance	Specimen Magnetism	Specimen No. of Fissures/in.	Specimen Mean Fissure Depth, in.x10^3	Oxide Scale Amount	Oxide Scale Color	Oxide Scale Flake Size	Oxide Scale Magnetism	Oxide Scale Composition (x-ray)
17	100	30	from -55 to -38	55	Control	-	-	422.1	0.339	-	-	-	-	-
					1600	PGB LG w/ IC LG	W	520.1	0.358	M	B	P-SF	M	Cr_2O_3(S) HPS(M) a=8.43*
					1700	BP w/ LG PGB	M	781.3	0.361	M	B	P-SF	M	Cr_2O_3(S) HPS(M) a=8.43*
					1800	BP w/ LG LG w/ BP	W	686.4	0.631	M	B	P-SF	M	Cr_2O_3(S) HPS(M) a=8.42
					1900	B and S LG LG w/ IC LG w/ BP	M	1220.2	0.634	M	B	P-MF	S	HPS(S) a=8.46* S.S. x75(M) S.S. x25(M)
22	10	30	from -46 to -42	61	Control	-	-	145.0	0.330	-	-	-	-	-
					1600	SGB PGB w/ OS LG w/ BP	M	496.6	0.322	S	B	P	W	Insuf.
					1700	PGB w/ OS SGB LG w/ BP LG w/ IC	M	495.0	0.359	S	B	P	M	Cr_2O_3(S) HPS(M)
					1800	SGB LG w/ IC LG w/ BP PGB w/ OS	M	366.4	0.327	M	B	P-SF	M	Cr_2O_3(S) HPS(M) a=8.42*
					1900	LG w/ IC SGB LG w/ BP	M	488.3	0.405	M	B	M	W	Cr_2O_3(S) HPS(M) a=8.42*
23	30	30	from -52 to -41	64	Control	-	-	299.1	0.322	-	-	-	-	-
					1600	SGB PGB w/ OS LG w/ IC	-	630.7	0.323	S	B	P	M	-
					1700	SGB LG w/ IC PGB w/ OS BP w/ LG	-	611.1	0.346	S	B	P-SF	M	-
					1800	LG w/ IC BP w/ LG	-	571.7	0.442	M	B	P-SF	W	-
					1900	LG w/ IC BP w/ LG	-	432.2	0.608	M	B	P-SF	W	-
26	10	30	-38	61	2000	LG w/ IC PGB	S	1211.4	0.800	L	GB	MF	S	-
27	30	30	from -46 to -38	64	2000	PGB	M	1434.0	0.733	S	B	P	S	-
28	100	30	from -50 to -40	55	2000	B and S	M	1084.5	0.749	M	B	P-SF	S	-

TABLE 12

OXIDE-METAL INTERFACE MOVEMENT IN 100 HOURS CALCULATED FROM WEIGHT LOSS MEASUREMENTS

Run No.	Alloy	Measured Density, gm/cc	Temp., °F	Total Weight Loss, percent	Interface Movement, in.x10^5	Specimen Appearance	Oxide Scale			
							Amount	Color	Flake Size	Magnetism
2	309+Nb	7.94	Control	0.01	0.2	-	-	-	-	-
			1600	0.10	1.1	LG w/ BP BP w/ LG	S	B	P	M
			1700	0.79	9.2	BP w/ LG LG	M	GB	P-SF	M
			1800	1.32	14.8	LG LG w/ BP BP w/ LG LG w/ IC	M	G	MF	S
			1900	1.90	21.7	LG w/ IC LG w/ BP	L	G-GB	MF	S
2	64177	7.90	Control	0.01	0.1	-	-	-	-	-
			1600	-0.05	-0.8	PGB w/ OS	N	-	-	-
			1700	0.01	0.1	PGB w/ OS	S	B	P	M
			1800	0.08	1.2	BP w/ LG PGB w/ OS	S	B	P	M
			1900	0.02	0.3	PGB BP w/ LG	S	B	P	W
2	64270	7.93	Control	0.01	0.2	-	-	-	-	-
			1600	-0.04	-0.6	PGB w/ OS	N	-	-	-
			1700	-0.03	-0.4	PGB w/ OS	S	B	P	M
			1800	0.24	3.8	PGB w/ OS	S	B	P	M
			1900	0.08	1.3	PGB	S	B	P	M
1	X11306	7.83	Control	0.04	0.4	-	-	-	-	-
			1600	0.54	5.7	LG	M	GB	SF	M
			1700	0.99	10.3	LG w/ IC	L	G	MF	ND
			1800	0.74	7.4	LG w/ BP LG w/ IC	M	B	P	ND
			1900	1.94	20.5	LG LG w/ BP	M	B	P-SF	ND
2			2000	1.81	19.0	LG w/ IC LG w/ BP	M	GB	MF	M
1	X11338	7.90	Control	0.02	0.2	-	-	-	-	-
			1600	0.31	3.6	LG w/ IC LG w/ BP	M	B	MF	M
			1700	0.69	8.0	LG w/ IC	L	B	LF	W
			1800	1.12	12.8	LG w/ IC	L	GB	MF	ND
			1900	2.09	2.4	PGB w/ OS BP w/ LG LG	S	B	P-SF	M
2			2000	0.52	6.0	B and S BP w/ LG	S	B	P	S
2	X27258	7.89	Control	0.01	0.2	-	-	-	-	-
			1600	0.21	2.8	BP w/ LG LG w/ IC LG	M	B	P-SF	W
			1700	0.29	3.8	PGB w/ OS LG w/ BP BP w/ LG	S	B	P-SF	M
			1800	0.95	12.6	LG w/ IC BP w/ LG	L	B	MF	ND
			1900	0.33	4.4	PGB w/ OS LG BP w/ LG	S	B	P-SF	M
2			2000	0.12	1.6	PGB w/ OS B and S LG w/ BP	S	B	P	S
3	X46558	7.90	Control	0.00	0.0	-	-	-	-	-
			1600	-0.02	-0.2	PGB LG LG w/ IC	S	B	P	M
			1700	0.45	4.9	LG w/ IC BP w/ LG	M	B	P-SF	W
			1800	0.79	8.7	LG w/ IC PGB w/ OS	M	B	MF	ND
			1900	0.46	5.0	BP w/ LG LG PGB w/ OS	M	B	P	M
3			2000	0.14	1.6	BP w/ LG B and S	S	B	P	ND
3	X46063	7.93	Control	0.00	0.0	-	-	-	-	-
			1600	0.27	3.3	SGB LG w/ BP LG w/ IC	S	B	P-SF	M
			1700	0.51	6.2	LG w/ BP LG w/ IC	M	B	P-SF	W
			1800	1.23	15.2	LG w/ BP LG w/ IC	M	B	P-MF	W
			1900	2.23	26.6	LG w/ IC	M	GB	MF	ND
3	X46572	7.89	Control	0.01	0.2	-	-	-	-	-
			1600	0.14	1.8	SGB PGB LG	S	B	P-SF	W
			1700	0.48	6.2	LG w/ BP LG w/ IC	M	B	P-SF	W
			1800	1.10	14.6	LG w/ IC	L	GB	MF	ND
			1900	0.86	11.2	PGB PGB w/ OS	M	B	P-SF	M

TABLE 13

RESULTS OF METALLOGRAPHIC ANALYSIS

Alloy Type	100 hr Runs			30-hr Runs Chromic Acid Etch Results	100-hr Runs (Unless Otherwise Specified) Penetration Types (see Figs. 95-100)						hr
	Banding	σ Phase or Cr_xN	δ Ferrite		Control	1600°F	1700°F	1800°F	1900°F	2000°F	
309 + Nb	Not Detectable		1600°F 1700°F	No Detectable G.S. Change. Carbides Agglomerate.	S O	S IV	M IV	L IV	M II	M II M III	10 3
64177	Small Amt.	1600°F 1700°F 1800°F	1900°F S	G.S. Increase with Temp. Carbides Agglomerate. No Grains Visible at 2000°F.	F O	M III	M III	M III	M III	M III M III	10 80
64270	Not Detectable	2000°F		G.S. Increase with Temp. Carbides Agglomerate. No Grains Visible at 2000°F.	S O	O	M I	S II	S III	S III M VI	10 30
X11306	Small Amt.		1600°F 1700°F 1800°F 1900°F	No Detectable G.S. Change. No Grains Visible at 1800, 1900, 2000°F. Carbides Agglomerate.	S O	S IV	M III	M IV	See Figs. 103-106 for 1600°F and 1900°F and 2000°F		
X11338	Small Amt.	1600°F 1700°F 1800°F 1900°F		G.S. Increase with Temp. Carbides Agglomerate. No Grains Visible at 2000°F	S O	S IV	S IV	L I	L	M III M II S V	10 30 100

TABLE 13 (cont.)

Alloy Type	100 hr Runs: Banding	100 hr Runs: σ Phase or Cr_xN	100 hr Runs: δ Ferrite	30-hr Runs Chromic Acid Etch Results	100-hr Runs (Unless Otherwise Specified) Penetration Types (see Figs. 95-100): Control	1600°F	1700°F	1800°F	1900°F	2000°F	hr
X27258	Yes	1600°F		Band of Small Grains.	M O	S III	M III	M I	L I	S II	10
		1700°F		Increase G.S. with Temp.						M II	30
		1800°F		Carbides Agglomerate. No						L VI	100
		1900°F		General G.S. Change. No							
				Grains Visible at 2000°F.							
X45558	Yes		1600°F	Band of Small Grains In-	S O	O	S III	M II	S II	S VI	10
			1700°F	crease G.S. with Temp.						M VI	30
			1800°F							M VI	100
			1900°F	General G.S. Increase.							
X46063	Not Detectable		1800°F	No Detectable G.S. Change.	M O	O	S III	S III	M III	S VI	10
			1900°F	Carbides Agglomerate.						S VI	30
				No Grains Visible at 2000°F.						M VI	100
X46572	Yes	1800°F		No Detectable G.S. Change.	S O	S II	S I	S III	S III	M I	10
		1900°F		Carbides Agglomerate.						S III	30
										M VI	100

S = small penetrations
M = medium penetrations
L = large penetrations
F = fine penetrations

TABLE 14

HEATS OF FORMATION OF OXIDES AT ROOM TEMPERATURE

Basis: 1 gm. mol O_2

		$-\Delta H_f$, k cal/g mol O_2
1)	$Si + O_2 \longrightarrow SiO_2$	206.6 *
2)	$C + O_2 \longrightarrow CO_2$	194.4
3)	$2\ Mn + O_2 \longrightarrow 2\ Mn\ O$	185.0
4)	$4/3\ Cr + O_2 \longrightarrow 2/3\ Cr_2O_3$	180.0
5)	$4/5\ P + O_2 \longrightarrow 2/5\ P_2O_5$	146.7
6)	$3/2\ Fe + O_2 \longrightarrow 1/2\ Fe_3O_4$	146.6
7)	$2\ Fe + O_2 \longrightarrow 2\ FeO$	129.0
8)	$2\ Ni + O_2 \longrightarrow 2\ NiO$	116.8
9)	$4/3\ Fe + O_2 \longrightarrow 2/3\ Fe_2O_3$	104.0
10)	$S + O_2 \longrightarrow SO_2$	70.9

* Depends on crystalline form. Value selected is for β-cristobalite

TABLE 15

Some Properties of Oxides of Metals Occurring in Stainless Steels

Oxide	At.% O	Conductor Class	Structure	Lattice Constants, kX Units	Ferro-magnet-ism	Volume Ratio** From Molecular Volumes	Volume Ratio** From Lattice Constants
FeO	22.3	Metal Deficit	NaCl Cubic	a=4.28-4.30	None	1.72-1.81	1.72-1.78
α-Fe_2O_3	30.1	Metal Excess	Rhombohedral	a=5.419; α=55.28°	None	2.20	2.38
Cr_2O_3	31.6	*	Rhombohedral	a=5.348; α=55.11°	None	2.10	2.28
NiO	21.4	Metal Deficit	NaCl Cubic (approx.)	a=4.177	None	1.58	1.61
$NiCr_2O_4$	28.2	#	Norm. Spinel	a=8.299	None	3.10	3.16+
$NiFe_2O_4$	27.3	#	Inv. Spinel	a=8.324	Strong	3.25	3.18+
$FeCr_2O_4$	28.6	#	Norm. Spinel	a=8.359	None++	3.2-3.4	3.22+
$NiMn_2O_4$	27.5	#	Norm. Spinel	a=8.37	None	?	3.25+
$FeFe_2O_4$	27.6	#	Inv. Spinel	a=8.378	Strong	3.15	3.22+
$MnCr_2O_4$	28.7	#	Norm. Spinel	a=8.428	None	3.33	3.23+
$MnFe_2O_4$	27.8	#	Norm. Spinel	a=8.502	None++	3.34	3.38+
MnO	22.6	Metal Deficit	NaCl Cubic	a=4.435	None	1.90	1.91
SiO_2 (β-cristobalite)	53.3	?	Cubic	a=7.16	None	3.90	4.05

TABLE 15 (Continued)

Legend:

* May be metal deficit, transition, or intrinsic impurities semiconductor.

\# Mechanism of conductivity unknown, but metal excess conductivity reported for $ZnCr_2O_4$ and $MgFe_2O_4$.

** Spinel Volume Ratios are with respect to the trivalent cation. Volume Ratios with respect to the divalent cation are twice the tabular value.

\+ Taking a = 1/2 the crystallographic lattice constant.

++ May be weakly ferromagnetic when quenched.

TABLE 16

Variation in Scale Composition on Replicate Specimens of Stainless Steels

(For key to symbols, see Table 2)

Temp., °F	Run 16 Specimen Appear.	Run 16 Scale Appear. Amt.	Clr.	Flake	Magn.	Run 16 Scale Analysis	Run 18 Specimen Appear.	Run 18 Scale Appear. Amt.	Clr.	Flake	Magn.	Run 18 Scale Analysis	Run 35 Specimen Appear.	Run 35 Scale Appear. Amt.	Clr.	Flake	Magn.	Run 35 Scale Analysis
TYPE 310 ALLOY, HEAT X11306																		
1600	LG w/BP	M	B	P SF	ND	Cr_2O_3(S) Fe_2O_3(M) HPS (M)	LG	M	GB	SF	M	Cr_2O_3(S) Fe_2O_3(M) HPS (M)	SGB	S	B	?	W	Fe_2O_3(S) HPS (M)
1700	LG w/BP	L	G	MF	ND	Cr_2O_3(S) X25 (M) HPS (M)	LG w/IC	L	G	MF	ND	X75 (S) HPS (M)	SGB	S	B	?	W	Fe_2O_3(S) LPS (M)
1800	LG w/IC	L	G	LF	ND	Cr_2O_3(S) HPS (S)	LG w/BP LG w/IC	M	B	P	ND	Cr_2O_3(S) HPS (S)	PGB LG BP w/LG	L	B	?	S	Cr_2O_3(S) HPS (S)
1900	PGB w/OS BP w/LG B ∅ S	M	B	P	ND	HPS (S) Cr_2O_3 (S)	IG LG w/BP	M	B	P SF	ND	HPS (S) Cr_2O_3(M)	PGB w/OS BP w/LG	L	B	?	M	Cr_2O_3(S) HPS (S) LPS (W)
2000	-			-		-	-			-		-	B ∅ S	L	GB	P	S	X75 (S) LPS (S) HPS (M)

TABLE 16 (Continued)

Temp., °F	Run 16 Specimen Appear.	Run 16 Scale Appear. Amt.	Clr.	Flake	Magn.	Run 16 Scale Analysis	Run 18 Specimen Appear.	Run 18 Scale Appear. Amt.	Clr.	Flake	Magn.	Run 18 Scale Analysis	Run 35 Specimen Appear.	Run 35 Scale Appear. Amt.	Clr.	Flake	Magn.	Run 35 Scale Analysis
TYPE 310 ALLOY, HEAT X11338																		
1600	BP w/LG PGB LG	M	GB	MF	ND	X75 (S) Fe_2O_3(M) LPS (M)	LG w/BP LG w/IC	M	B	MF	M	Cr_2O_3(S) HPS (M)	SGB	L	B	?	W	Cr_2O_3(S) HPS (S)
1700	LG w/IC	L	G	MF	ND	X85 (S) HPS (M)	LG w/IC	L	B	LF	W	Cr_2O_3(S) HPS (M)	BP W/LG LG w/BP	M	B	?	S	Cr_2O_3(S) HPS (S) LPS (W)
1800	LG w/IC	L	G	MF	ND	X95 (S) HPS (M)	LG w/IC	L	GB	MF	ND	Cr_2O_3(S) HPS (M)	LG w/IC LG w/PB	L	B	?	S	Cr_2O_3(S) HPS (S) LPS (W)
1900	B Ø S LG w/BP LG w/IC	L	B	P SF	ND M	X90 (S) HPS (M)	PGB w/OS BP w/LG LG	S	B	P SF	M	X50 (S) HPS (M)	BP w/LG PGB	M	B	?	S	X25 (S) LPS (M)
2000	-	-				-	-			-		-	BP w/LG	M	GB	P	S	X25 (S) LPS (M)
TYPE 310 ALLOY, HEAT X27258																		
1600	PGB BP w/LG LG	S	B	P	M	Cr_2O_3(S) Fe_2O_3(M) LPS (W)?	BP w/LG LG w/IC LB	M	B	P SF	W	X75 (S) HPS (M)	PGB LG w/IC LG w/BP	M	B	?	S	Cr_2O_3(S) HPS (S)

TABLE 16 (Continued)

Temp., °F	Run 16 Specimen Appear.	Run 16 Scale Appear. Amt.	Clr.	Flake	Magn.	Run 16 Scale Analysis	Run 18 Specimen Appear.	Run 18 Scale Appear. Amt.	Clr.	Flake	Magn.	Run 18 Scale Analysis	Run 35 Specimen Appear.	Run 35 Scale Appear. Amt.	Clr.	Flake	Magn.	Run 35 Scale Analysis
1700	LG w/BP PGB w/OS PGB	L	B	MF	ND	Cr_2O_3(S) HPS (S)	PGB w/OS LG w/BP BP w/LG	S	B	P SF	M	Cr_2O_3(S) HPS (S)	BP w/LG PGB w/OS	M	B	?	S	X75 (S) HPS (S) LPS (S)
1800	LG w/BP BP w/LG PGB w/OS LG w/IC	S	B	P SF	ND M	Cr_2O_3(S) HPS (S)	LG w/IC	L	B	MF	ND	X75 (S) HPS (S)	PGB LG w/IC	M	B	?	S	Cr_2O_3(S) HPS (S) LPS (W)?
1900	LG w/BP LG w/IC BP w/LG B ϕ S LG	M	G	P SF	ND	X25 (S) HPS (W) LPS (W)	BP w/LG PGB w/OS LG	S	B	P SF	M	Cr_2O_3(S) HPS (M)	BP W/LG PGB w/OS LG w/IC	L	B	?	S	X50 (S) HPS (S)
2000	-			-		-	-			-		-	BP w/LG	M	GB	P	S	Cr_2O_3(S) HPS (S)

TABLE 17

ANALYSES OF INTERGRANULAR OXIDES OF STAINLESS STEELS OBTAINED BY ELECTRON DIFFRACTION

Etch	Oxidizing Temperature, °F									
	1600 Measured Analysis Depth, in.		1700 Measured Analysis Depth, in.		1800 Measured Analysis Depth, in.		1900 Measured Analysis Depth, in.		2000 Measured Analysis Depth, in.	
TYPE 309 + Nb ALLOY - Run 20										
Scale (X-ray)		Cr_2O_3(S) HPS (S)		Cr_2O_3(S) Fe_2O_3(S) HPS (W)		Cr_2O_3(S) Fe_2O_3(M) HPS (M)		Cr_2O_3(S) Fe_2O_3(M) HPS (M)		-
Surface	0	Sp (S) Rh (S)	0	Sp (S) Rh (S)	0	Sp (S) Rh (M)	0	Sp (S)		-
I	-	Sp (S) Rh (S)	-	Sp (S) Rh (S)	0.0002	Sp (S) Rh (M)	0.0004	Sp (S) Rh (VW)?		
II	-	$M_{23}C_6$?	-	Sp (S) Rh (S)	0.0002	Sp (S) Rh (M)	0.0006			
III			-	Sp (M) Rh (M)	0.0001	Sp (W) Rh (W)	0.0007	Sp (VW) Rh (VW)		
IV					0.0004	Sp (W) Rh (W)	0.0007	Sp (VVW) Rh (VW)		

HPS - High-parameter Spinel
LPS - Low-parameter Spinel
Sp - Spinel Phase
Rh - Rhombohedral Phase

TABLE 17 (Cont'd.)

Etch	Oxidizing Temperature, °F: 1600 Measured Analysis Depth, in.		1700 Measured Analysis Depth, in.		1800 Measured Analysis Depth, in.		1900 Measured Analysis Depth, in.		2000 Measured Analysis Depth, in.	
TYPE 310 ALLOY, HEAT 64177 - Run 20										
Scale (X-ray)		Cr_2O_3		Insuf.		X 50		X 50		-
Surface	0	Rh (S)	0	Rh (S)	0	Rh (S)	0	Rh (S)		-
I	-	Rh (S)	-	Rh (S)	-0.0003	Rh (S)	0.0000	Rh (S) Sp (VVW)?		
II	-	Rh (S)	-	Rh (S)	0.0000	Rh (S) Sp (VVW)?	-0.0003	Rh (S)		
III					-0.0001	Rh (W)	-0.0006	Rh (S)		
IV					-0.0003	No Pattern	-0.0007	Metal		

TABLE 17 (Cont'd.)

Etch	Oxidizing Temperature, °F									
	1600		1700		1800		1900		2000	
	Measured Depth, in.	Analysis	Measured Depth, in.	Analysis	Measured Depth, in.	Analysis	Measured Depth, in.	Analysis	Measured Depth, in.	Analysis
TYPE 310 ALLOY, HEAT 64270 - Run 20										
Scale (X-ray)		X 50		Fe_2O_3(S) LPS (M)		X 50 (S) LPS (W)		X 50 (S) Fe_2O_3(W)?		-
Surface	0	Rh (S)	0	Rh (S) Sp (VW)?	0	Rh (S)	0	Rh (S) Sp (VVW)		-
I			-0.0002	Rh (S)	0.0000	Rh (S)	0.0000	Rh (S) Sp (VVW)		
II			0.0000	Rh (W)	0.0004	Rh (S)	0.0001	Rh (S) Sp (VVW)?		
III			-0.0001	No Pattern	0.0006	Rh (M)	0.0003	Rh (M) Sp (VVW)?		
IV					0.0007	Metal	0.0001	Metal		

TABLE 17 (Cont'd.)

Etch	Oxidizing Temperature, °F									
	1600		1700		1800		1900		2000	
	Measured Depth, in.	Analysis	Measured Depth, in.	Analysis	Measured Depth, in.	Analysis	Measured Depth, in.	Analysis	Measured Depth, in.	Analysis
TYPE 310 ALLOY, HEAT X11306										
Scale (X-ray)		Fe_2O_3(S) HPS (M)		Fe_2O_3(S) LPS (M)		Cr_2O_3(S) HPS (S)		Cr_2O_3(S) HPS (S) LPS (W)		X 75 (S) LPS (S) HPS (M)
Surface	0	Sp (S) Rh (M)	0	Sp (S) Rh (M)	0	Sp (S) Rh (W)	0	Sp (S)	0	Sp (S) Rh (VW)?
I	0.0002	Sp (S) Rh (VW)?	0.0000	Sp (S) Rh (M)	0.0000	Contam.	0.0003	Sp (S)	0.0002	Sp (S) Rh (VW)?
II	0.0001	Sp (S)	0.0000	Sp (S) Rh (M)	0.0000	Sp (M) Rh (VW)?	0.0003	Sp (S) Rh (S)	-0.0001	Sp (W) Rh (VVW)?
III	0.0001	Sp (S)	0.0001	Sp (M) Rh (M)	0.0002	Sp (S) Rh (M)	0.0004	Sp (M) Rh (M)	-0.0002	Sp (VVW)? Rh (VW)
IV	0.0002	Metal	0.0001	Sp (M) Rh (M)	0.0000		0.0004	Sp (W) Rh (W)	-0.0003	Sp (VVVW) Rh (VVW)
V			0.0001	Sp (VVW) Rh (VVW)	0.0000	Sp (M) Rh (W)	0.0002	Sp (M) Rh (M)		
VI					0.0001	Sp (W) Rh (VW)?	0.0000	Sp (M) Rh (W)		
VII					0.0001	Sp (W) Rh (VW)?	0.0003	Sp (W) Rh (W)		
VIII					0.0001	Sp (VW) Rh (VVW)?	0.0007	Sp (VVW) Rh (VVW)?		

TABLE 17 (Cont'd.)

Etch	Oxidizing Temperature, °F									
	1600		1700		1800		1900		2000	
	Measured Depth, in.	Analysis	Measured Depth, in.	Analysis	Measured Depth, in.	Analysis	Measured Depth, in.	Analysis	Measured Depth, in.	Analysis
TYPE 310 ALLOY, HEAT X11338										
Scale (X-ray)		Cr_2O_3 (S) HPS (S)		Cr_2O_3 (S) HPS (S) LPS (W)		Cr_2O_3 (S) HPS (S) LPS (W)		X 25 (S) LPS (M)		X 25 (S) LPS (M)
Surface	0	Sp (S) Rh (S)	0	Sp (S) Rh (S)	0	Sp (S) Rh (W)	0	Sp (S)	0	Sp (S) Rh (VW)
I	0.0001	Sp (S) Rh (S)	0.0002	Sp (S) Rh (S)	0.0001	Contam.	0.0002	Sp (S)	0.0003	Sp (S) Rh (W)
II	0.0001	Sp (S) Rh (S)	0.0002	Sp (S) Rh (S)	0.0001	No Pattern	0.0002	Sp (S) Rh (S)	0.0003	Rh (M)
III	0.0001	Sp (W) Rh (M)	0.0003	Sp (M) Rh (VW)?	0.0004	No Pattern	0.0002	Sp (M) Rh (M)	0.0005	Sp (M) Rh (M)
IV	0.0001	No Pattern	0.0002	Sp (W) Rh (VVW)?			0.0004	Sp (S) Rh (S)	0.0004	Sp (M) Rh (M)
V							0.0002	Sp (M) Rh (M)	0.0004	Sp (VW) Rh (VW)
VI							0.0002	Sp (M) Rh (W)	0.0004	Sp (VW) Rh (VVW)?
VII							0.0002	Sp (M) Rh (W)		
VIII							0.0002	Sp (VVW) Rh (VVW)?		

TABLE 17 (Cont'd.)

Etch	Oxidizing Temperature, °F									
	1600		1700		1800		1900		2000	
	Measured Depth, in.	Analysis	Measured Depth, in.	Analysis	Measured Depth, in.	Analysis	Measured Depth, in.	Analysis	Measured Depth, in.	Analysis
TYPE 310 ALLOY, HEAT X27258										
Scale (X-ray)		Cr_2O_3(S) HPS (S)		X 75 (S) HPS (S) LPS (W)		Cr_2O_3(S) HPS (S) LPS (W)?		X 50 (S) HPS (S)		Cr_2O_3(S) HPS (S)
Surface	0	Sp (S) Rh (S)	0	Sp (S) Rh (M)	0	Sp (S) Rh (W)	0	Sp (S) Rh (W)?	0	Sp (S) Rh (W)
I	0.0000	Sp (S) Rh (M)	0.0002	Sp (S) Rh (M)	-0.0001	Sp (S) Rh (W)?	0.0001	Sp (S)	-0.0001	Sp (S) Rh (W)
II	0.0000	Sp (S) Rh (S)	0.0005	Sp (S) Rh (M)	0.0002	Sp (M) Rh (W)	0.0003	Sp (S) Rh (W)	0.0001	Sp (M) Rh (M)
III	0.0001	No Pattern	0.0006	Sp (S) Rh (M)	0.0005	Sp (S) Rh (M)	0.0006	Sp (S) Rh (S)	0.0000	Sp (VW) Rh (W)
IV	0.0002	No Pattern	0.0008	No Pattern	0.0005	Sp (S) Rh (M)	0.0005	Contam.	0.0001	Sp (VW) Rh (VW)
V			0.0007	No Pattern	0.0003	Sp (M) Rh (W)	0.0005	Sp (S) Rh (S)	0.0000	Sp (VW) Rh (VW)
VI					0.0004	Sp (W) Rh (VW)?	0.0007	No Pattern	-0.0001	Sp (VW) Rh (VVW)?
VII					0.0005	No Pattern				

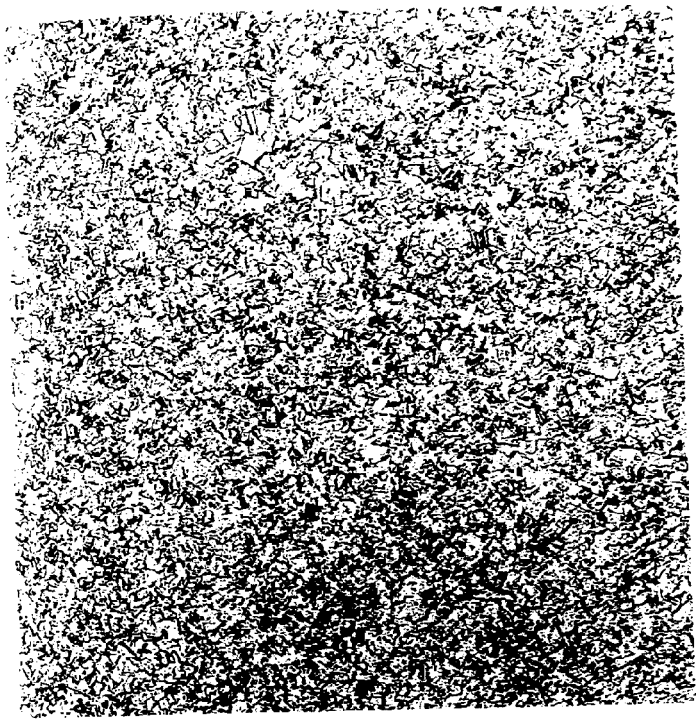

Fig. 1. Type 309+ Nb Alloy. As Received. 100x. Plane of Rolling. Etch: Electr. Chromic Acid.

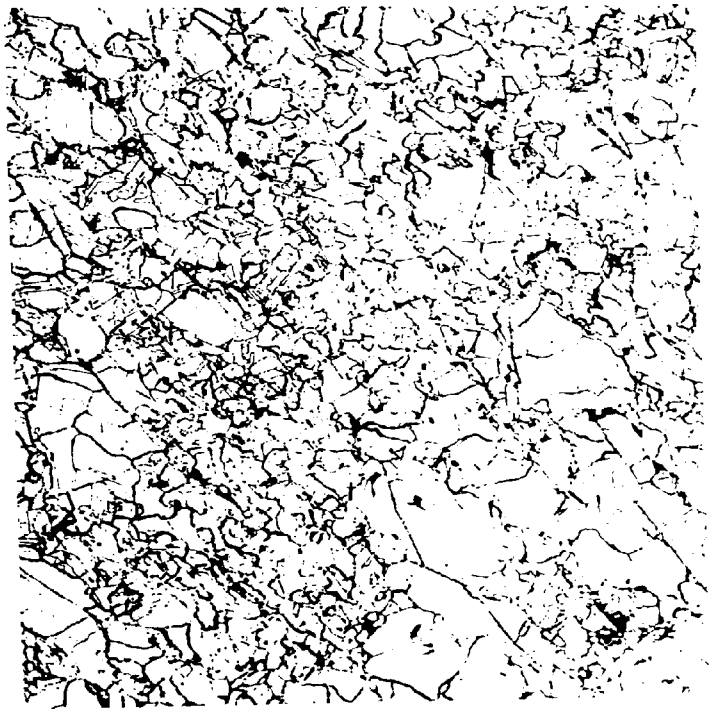

Fig. 2. Type 310 Alloy, Heat 64177. As Received. 100x. Plane of Rolling. Etch: Electr. Chromic Acid.

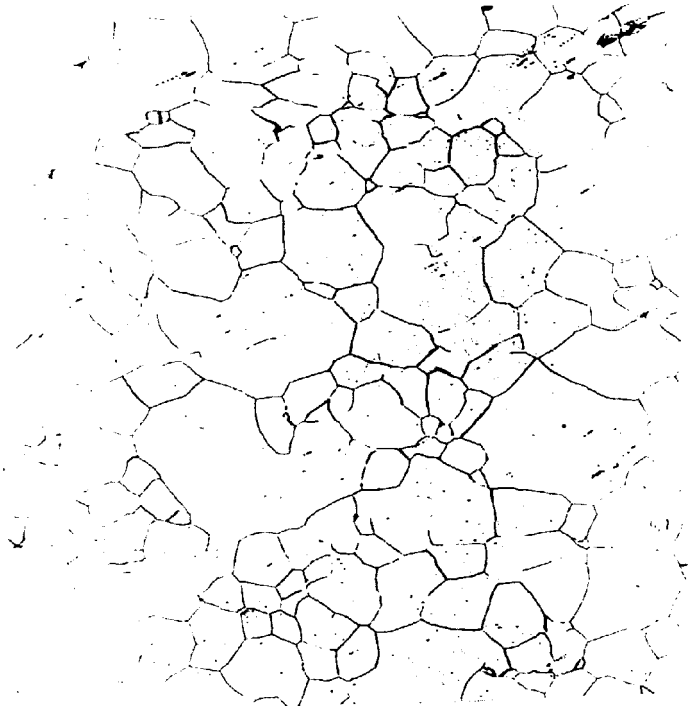

Fig. 3. Type 310 Alloy, Heat 64270. As Received. 100x. Plane of Rolling. Etch: Electr. Chromic Acid.

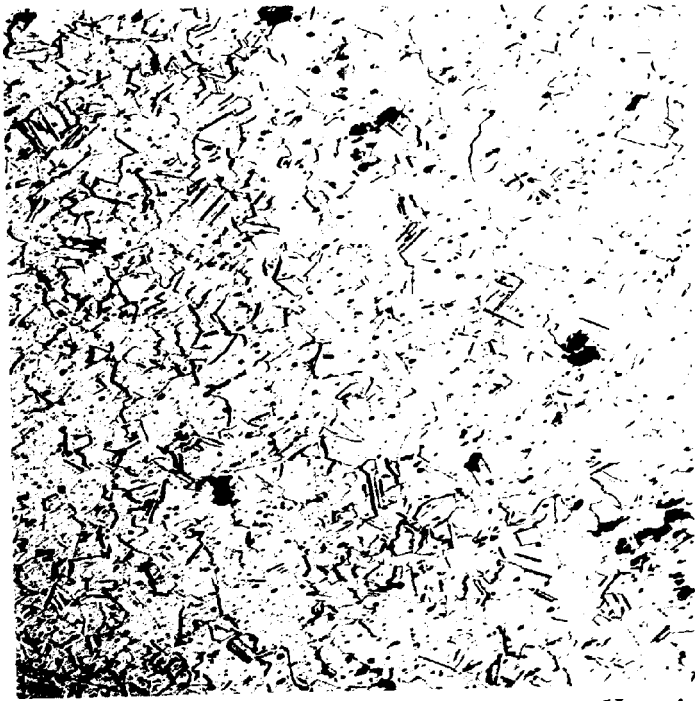

Fig. 4. Type 310 Alloy, Heat X 11306. As Received. 100x. Obl. Light. Plane of Rolling. Etch: Electr. 1:1:1 HCl, HNO_3, H_2O.

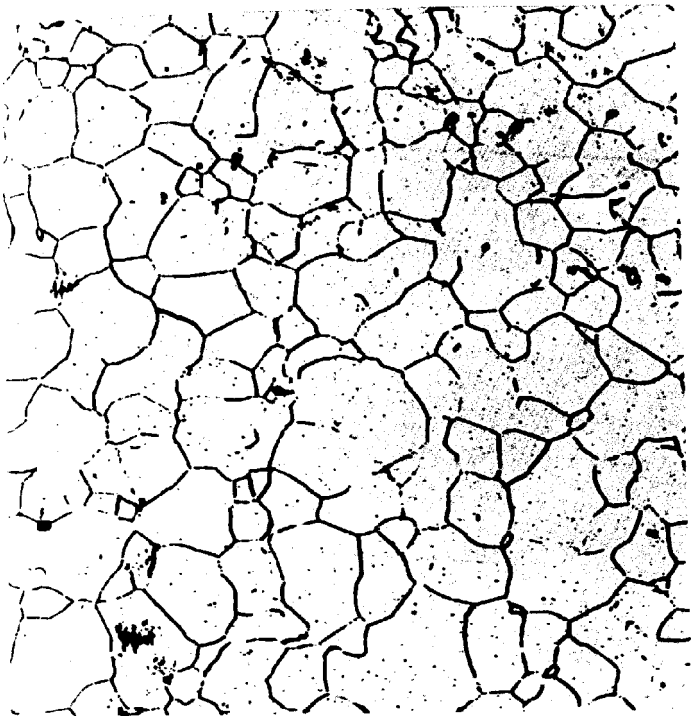

Fig. 5. Type 310 Alloy, Heat X 11338. As Received. 100x. Plane of Rolling. Etch: Electr. Chromic Acid.

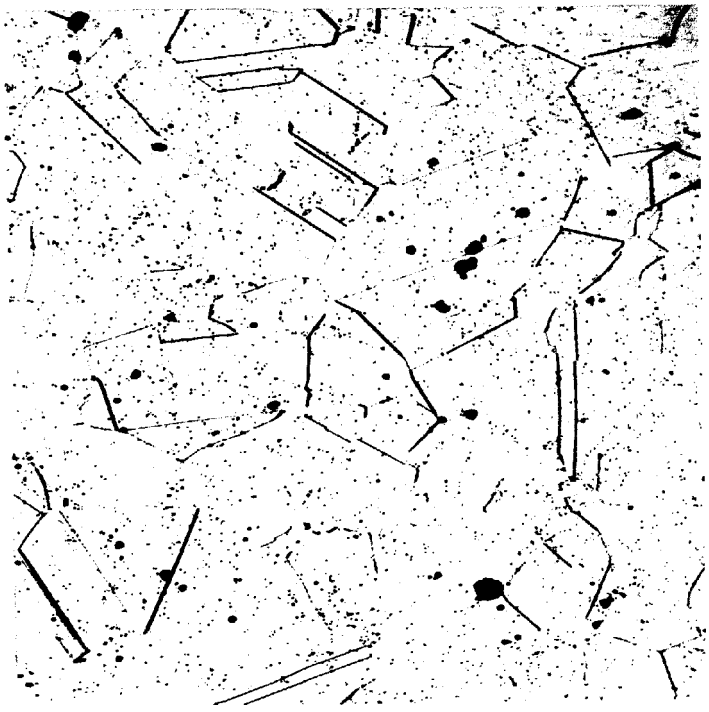

Fig. 6. Type 310 Alloy, Heat X 27258. As Received. 100x. Obl. Light. Plane of Rolling. Etch: Electr. 1:1:1 HCl, HNO_3, H_2O.

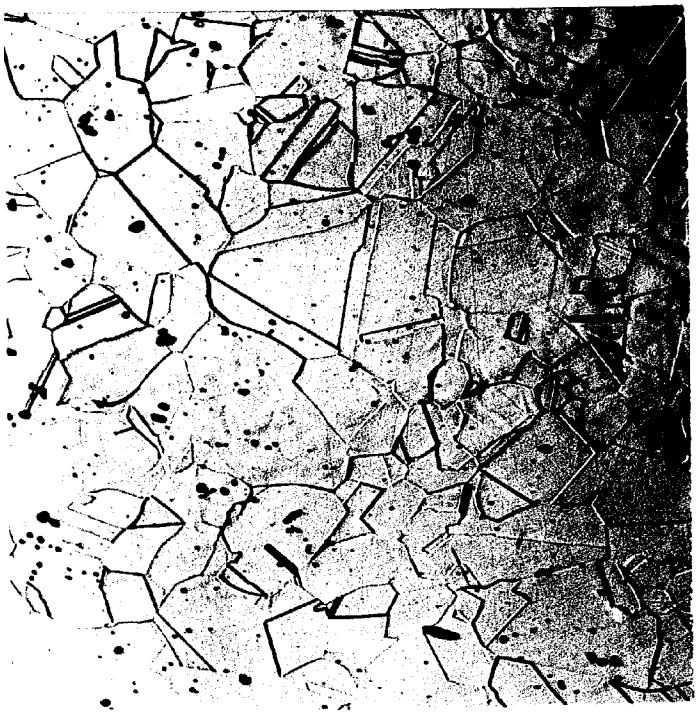

Fig. 7. Type 310 Alloy, Heat X 45558. As Received. 100x. Obl. Light. Plane of Rolling. Etch: Electr. 1:1:1 HCl, HNO_3, H_2O.

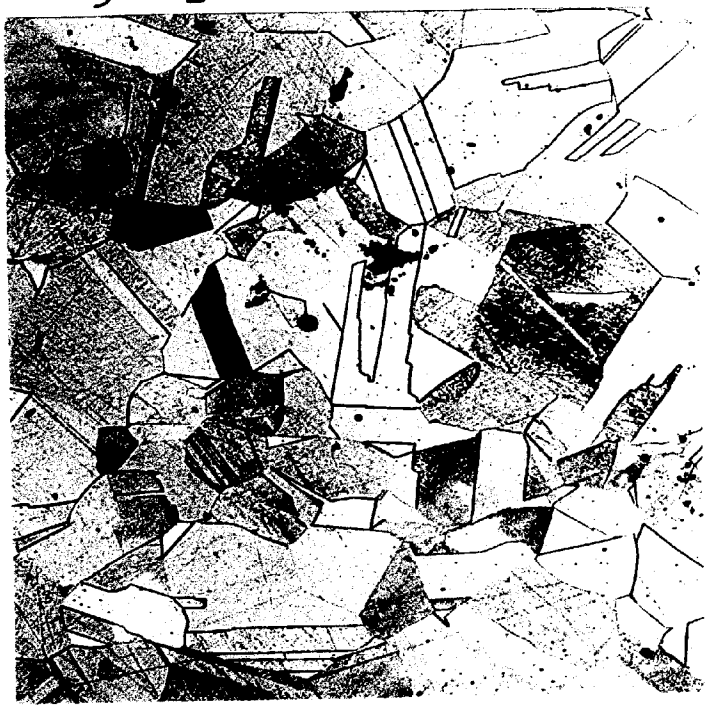

Fig. 8. Type 310 Alloy, Heat X 46063. As Received. 100x. Plane of Rolling. Etch: Electr. Chromic Acid.

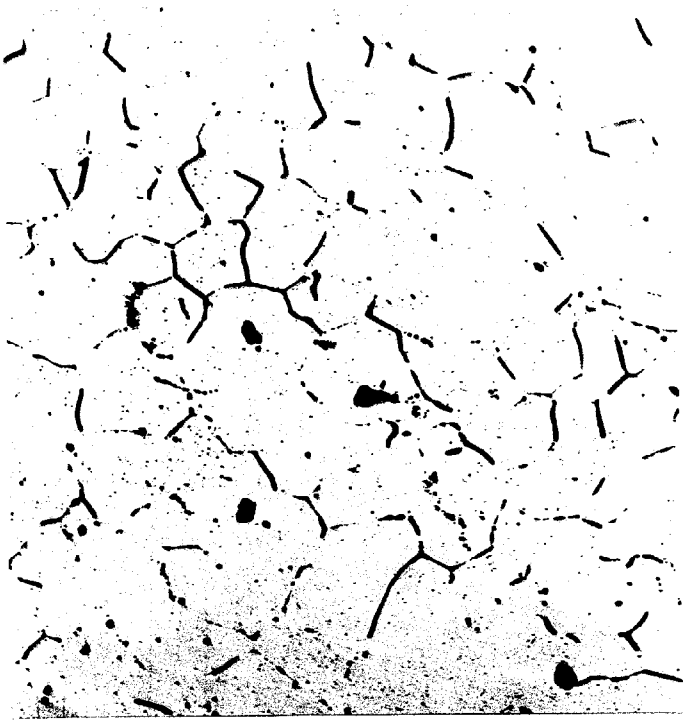

Fig. 9. Type 310 Alloy, Heat X 46572. As Received. 100x. Obl. Light. Plane of Rolling. Etch: Electr. Chromic Acid.

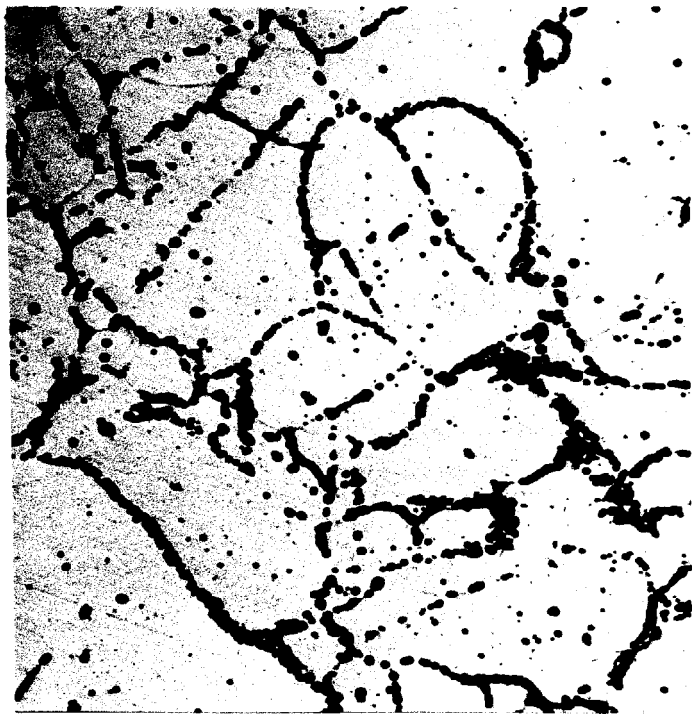

Fig. 10. Grain Boundary Network. Type 310 Alloy, Heat 64177. As Received. 1000x. Plane of Rolling. Etch: Electr. Chromic Acid.

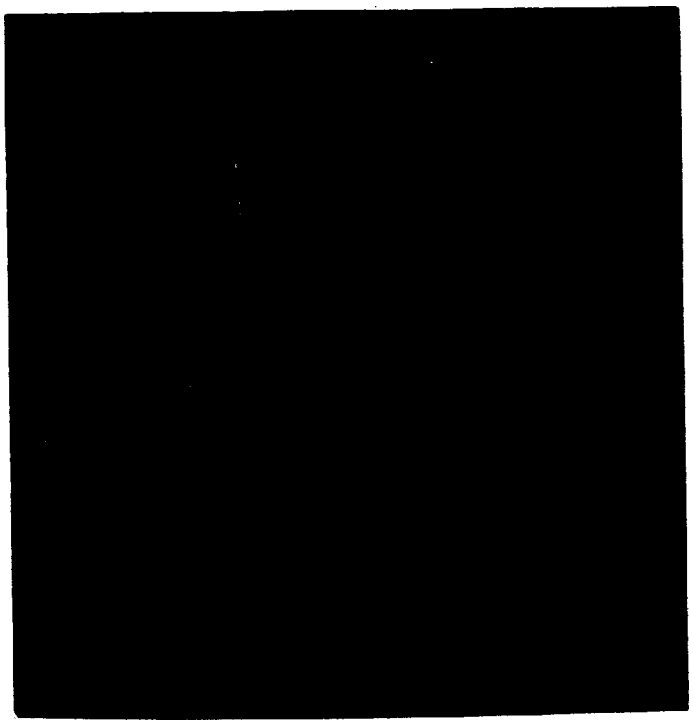

Fig. 11. Grain Boundary. Type 310 Alloy, Heat X 45558. As Received. 1000x. Obl. Light. Plane of Rolling. Etch: Electr. 1:1:1 HCl, HNO_3, H_2O.

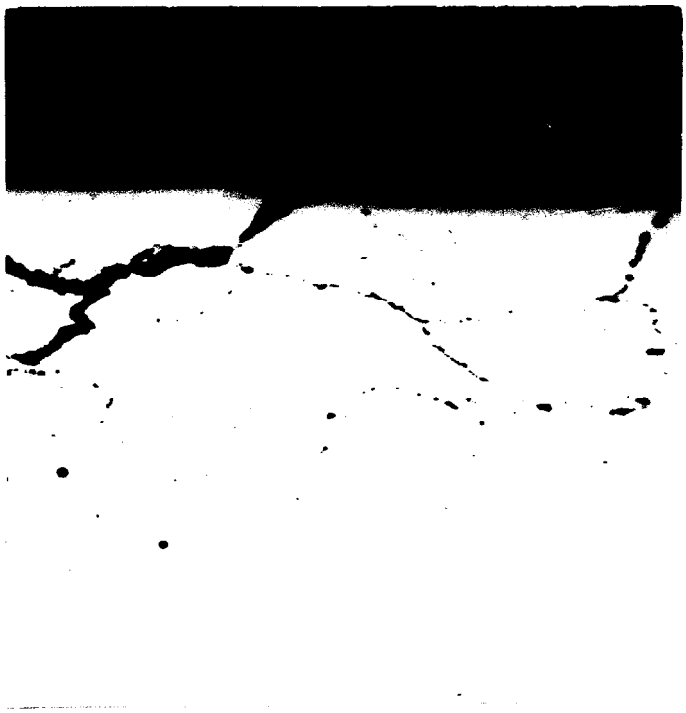

Fig. 12. Type 310 Alloy, Heat 64177. As Received. 1000x. Cross Section. Unetched.



Fig. 13. Type 310 Alloy, Heat X 11338. As Received. 1000x. Cross Section. Unetched.

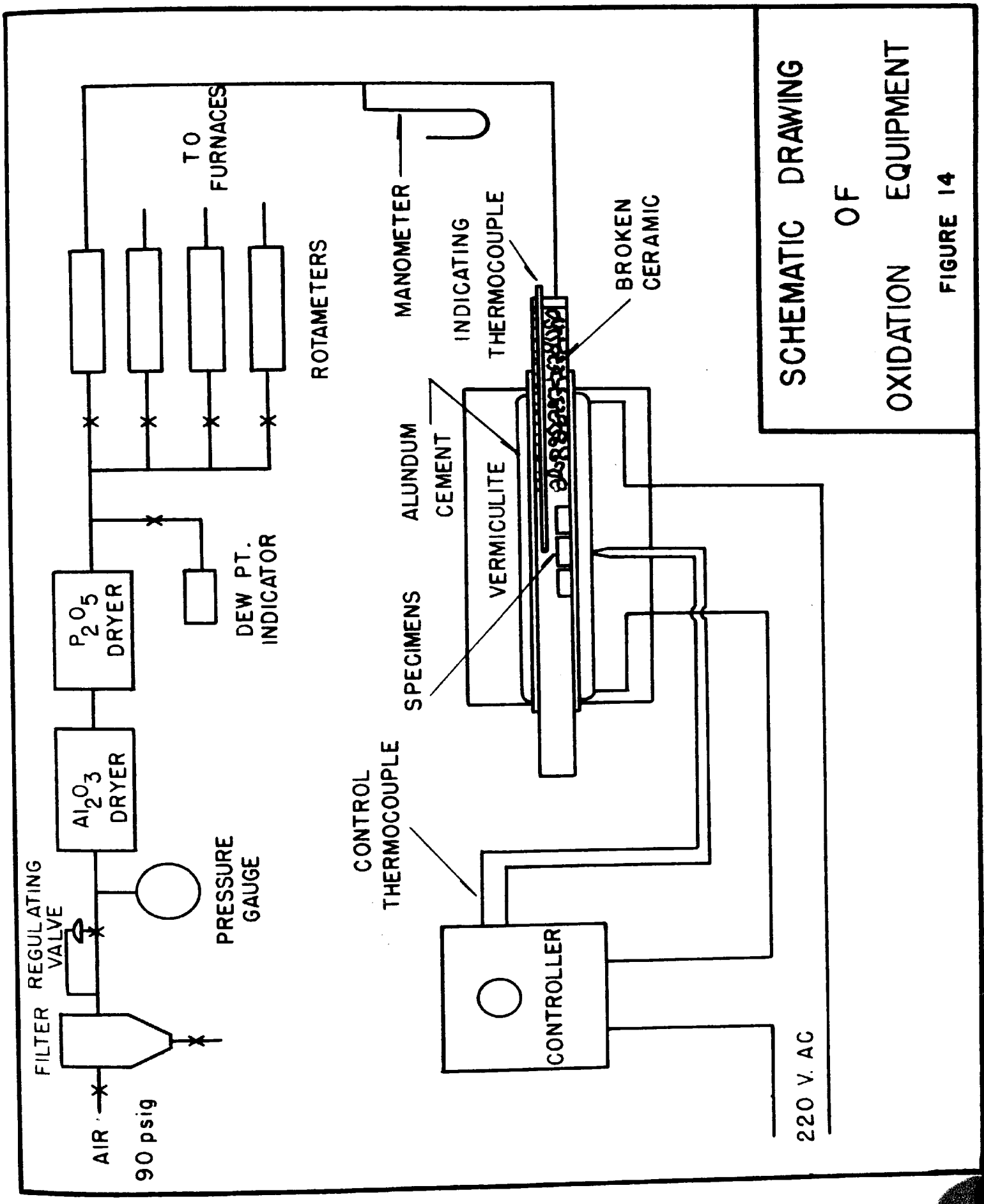

SCHEMATIC DRAWING OF OXIDATION EQUIPMENT

FIGURE 14

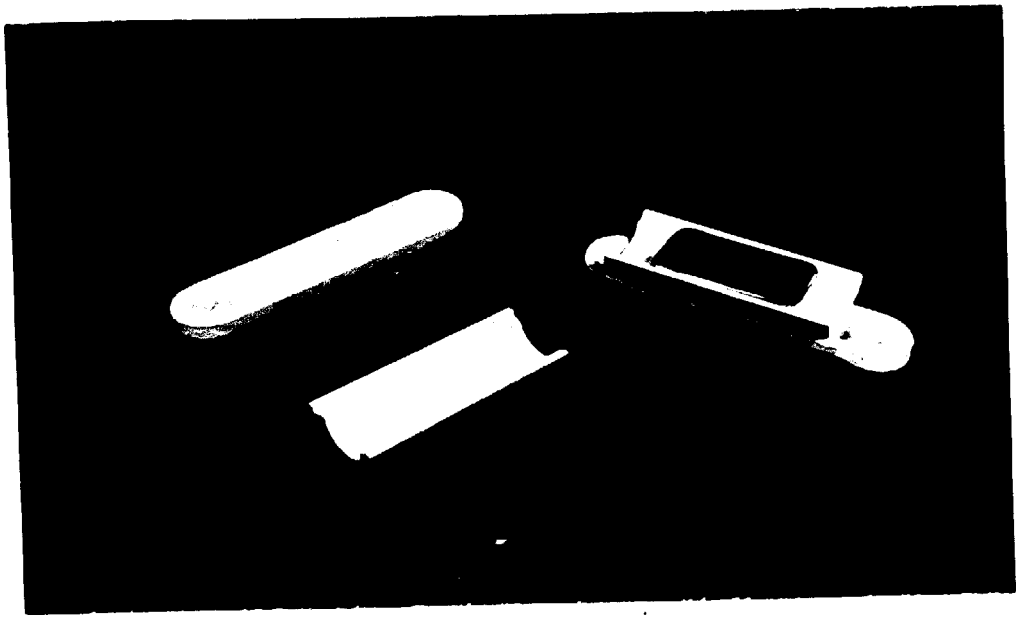

Fig. 15. Specimens and Ceramic Holders.

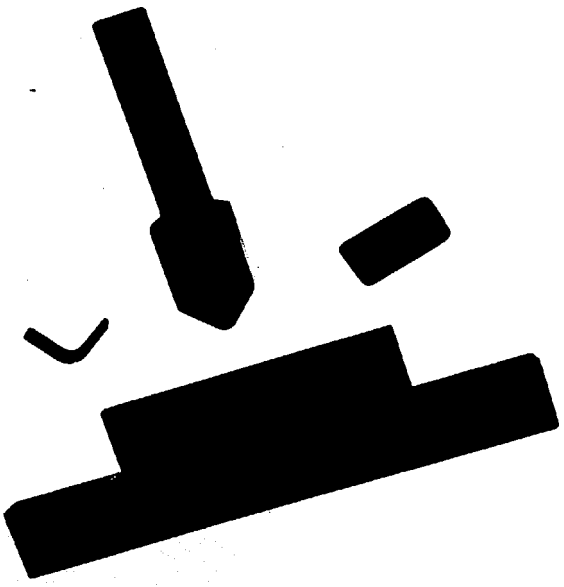

Fig. 16. Bending Die and Specimens.

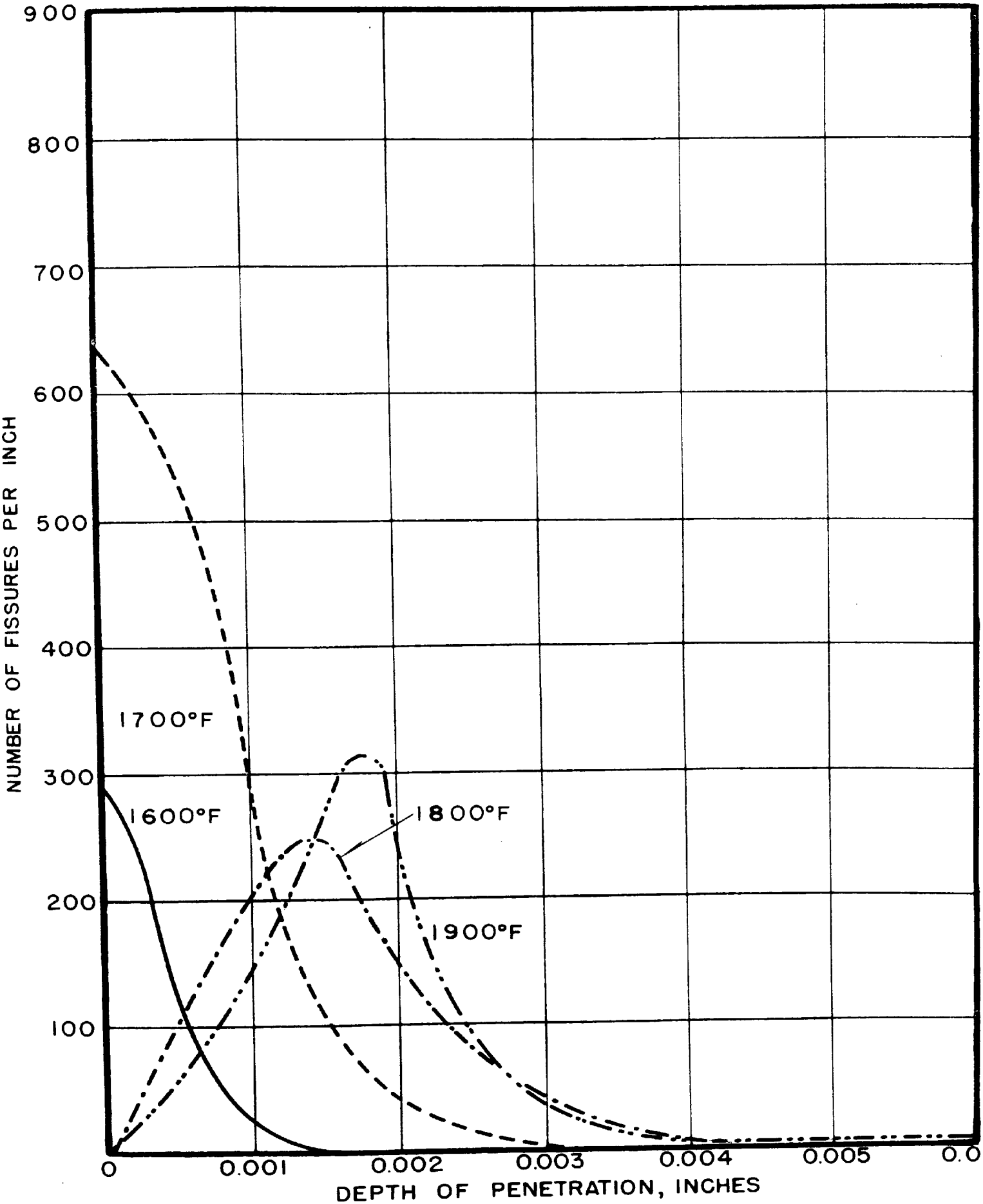

FIG. 17 – PENETRATION VS. DEPTH BELOW SURFACE.
TYPE 309+Nb ALLOY. RUN 5.

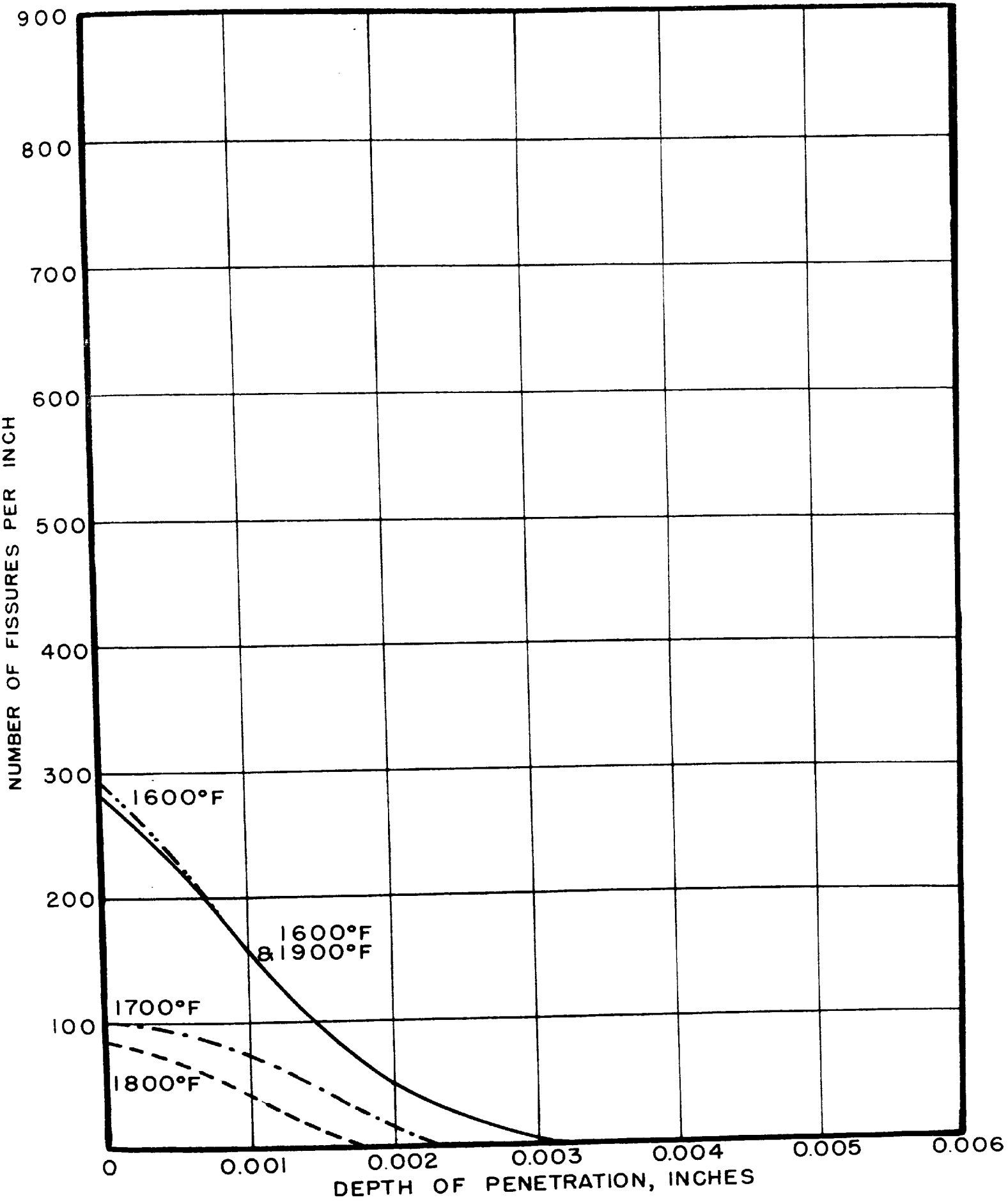

FIG. 18 – PENETRATION VS. DEPTH BELOW SURFACE.
TYPE 310 ALLOY, HEAT 64177. RUN 5.

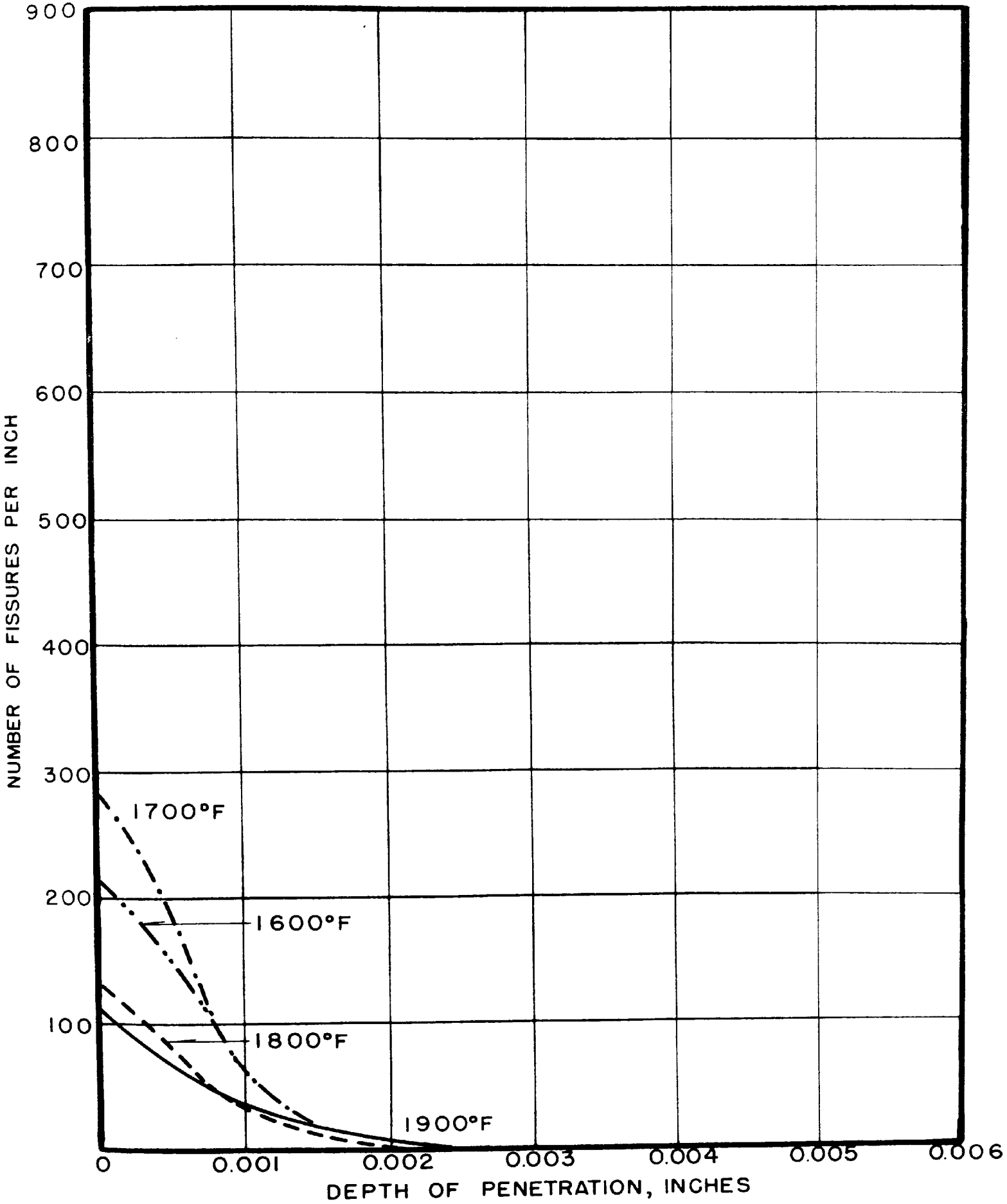

FIG. 19 – PENETRATION VS. DEPTH BELOW SURFACE.
TYPE 310 ALLOY, HEAT 64270. RUN 5.

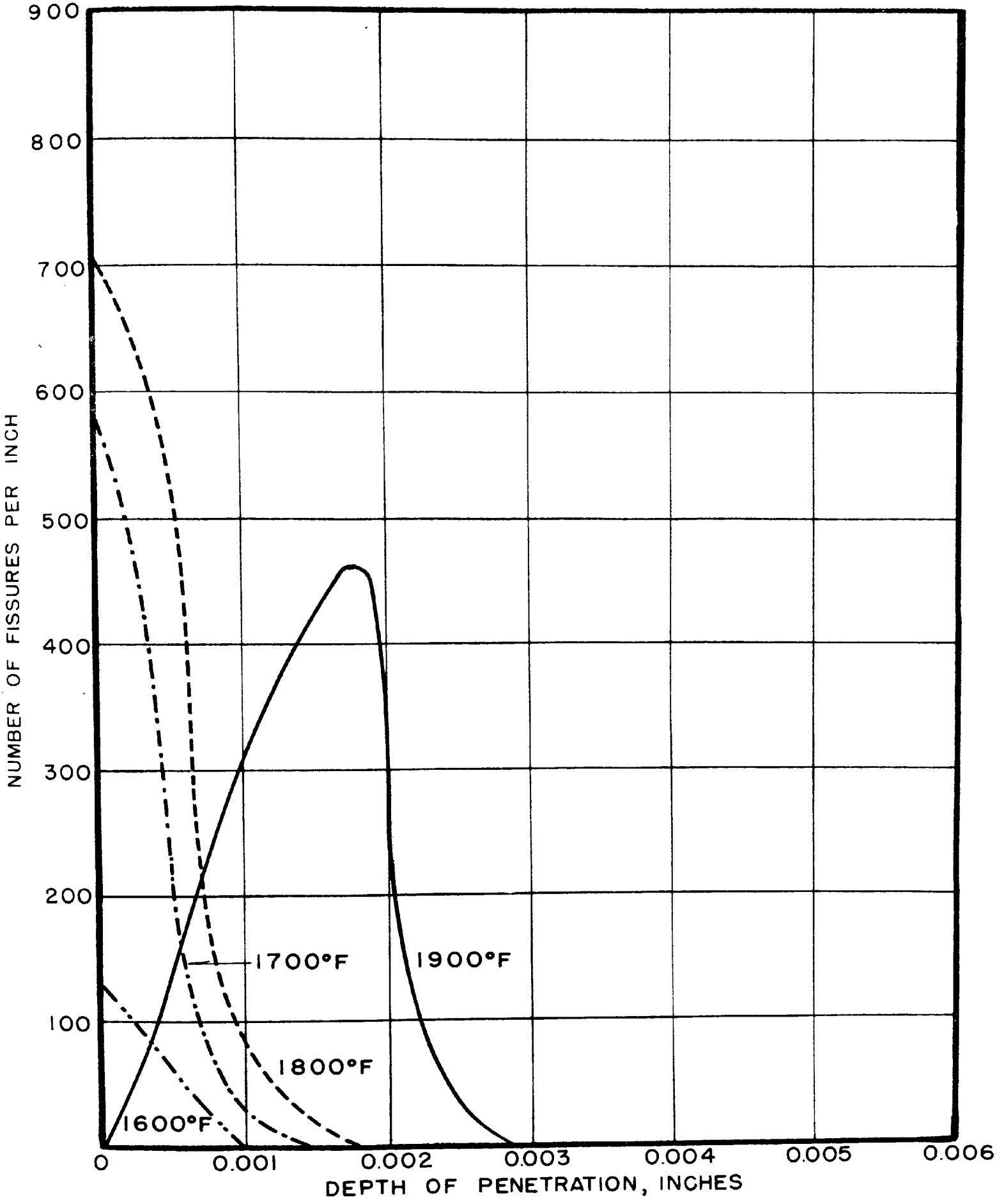

FIG. 20 - PENETRATION VS. DEPTH BELOW SURFACE.
TYPE 309 + Nb ALLOY. RUN 6.

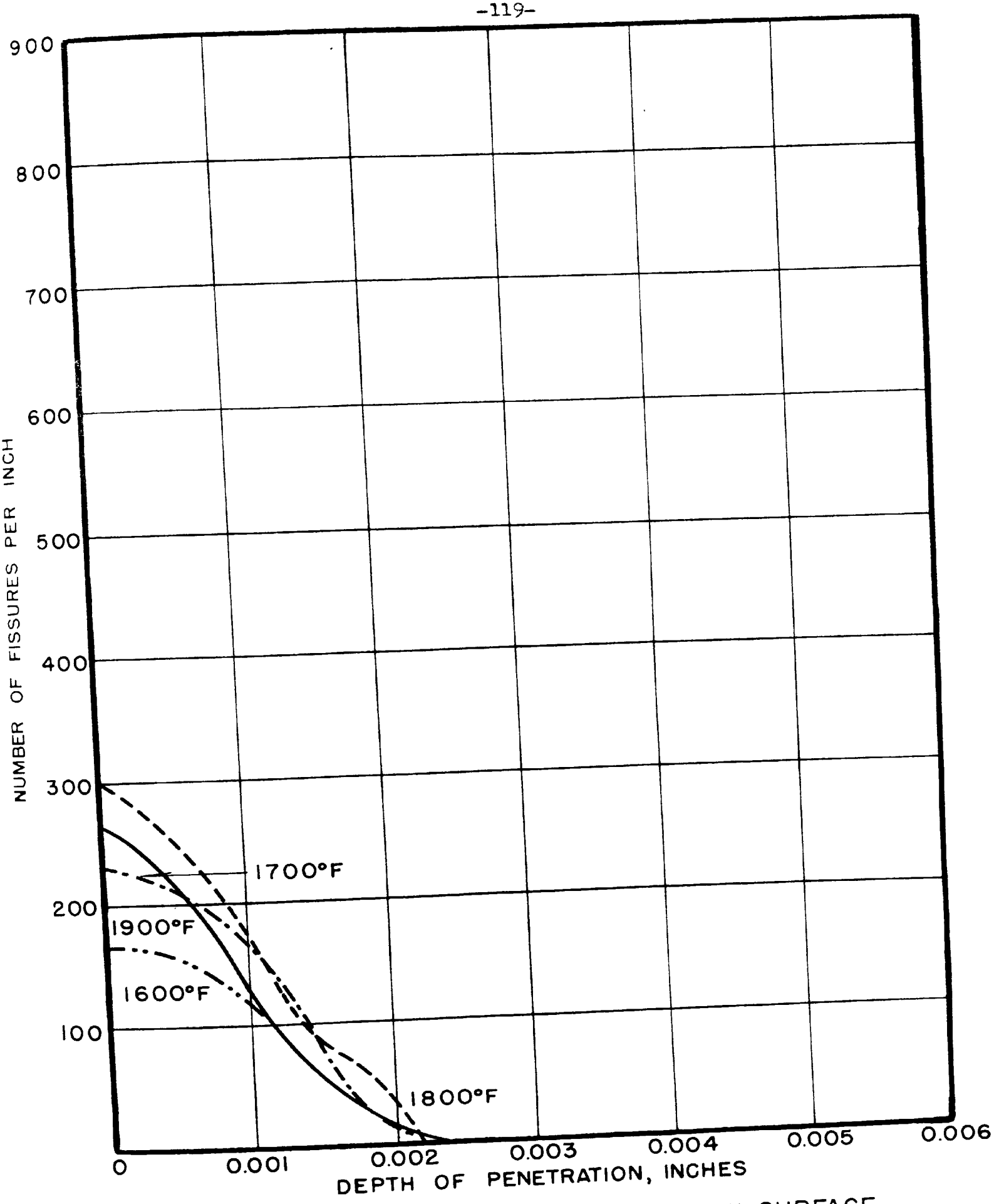

FIG. 21 - PENETRATION VS. DEPTH BELOW SURFACE.
TYPE 310 ALLOY, HEAT 64177. RUN 6.

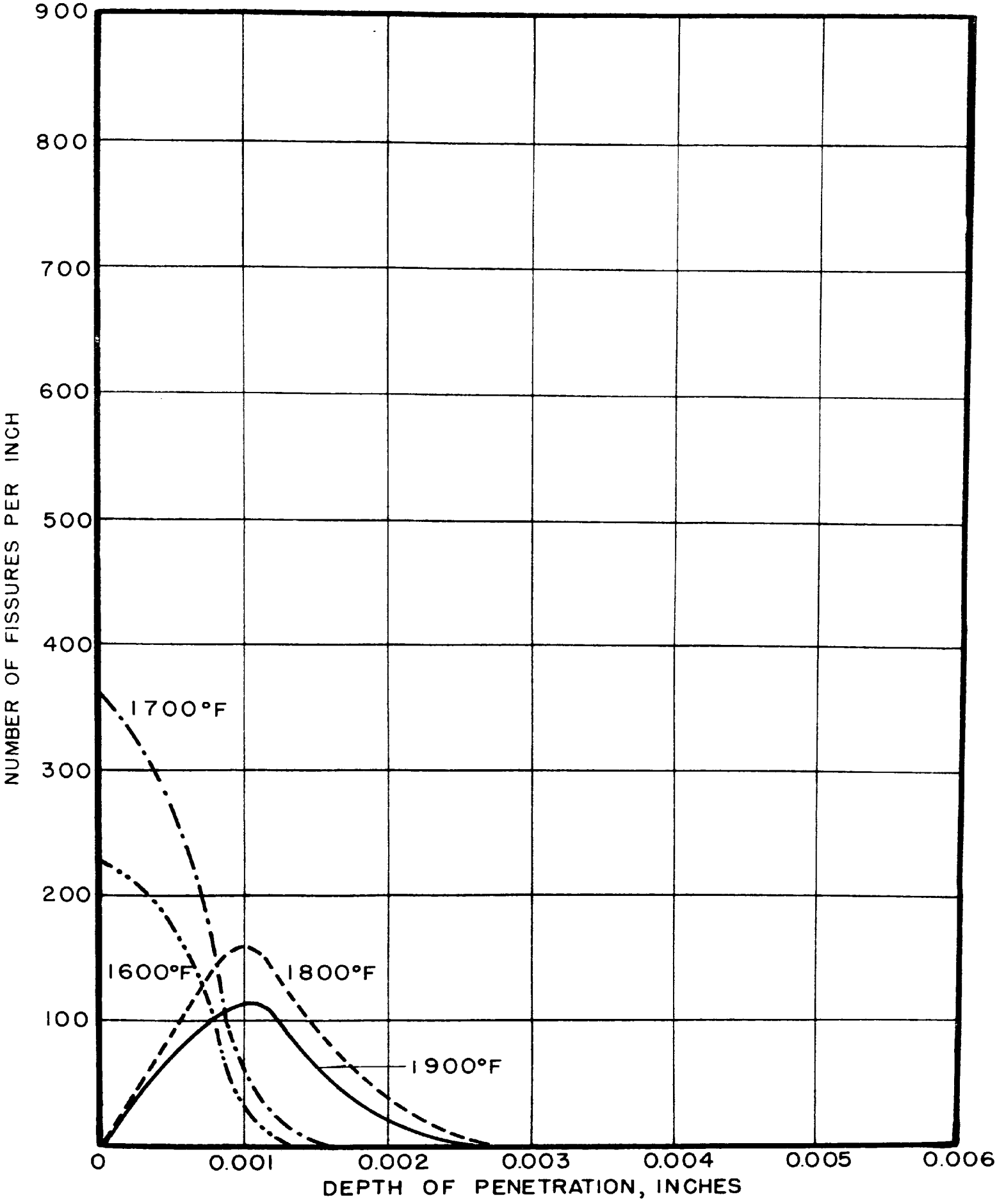

FIG. 22 – PENETRATION VS. DEPTH BELOW SURFACE.
TYPE 310 ALLOY, HEAT 64270. RUN 6.

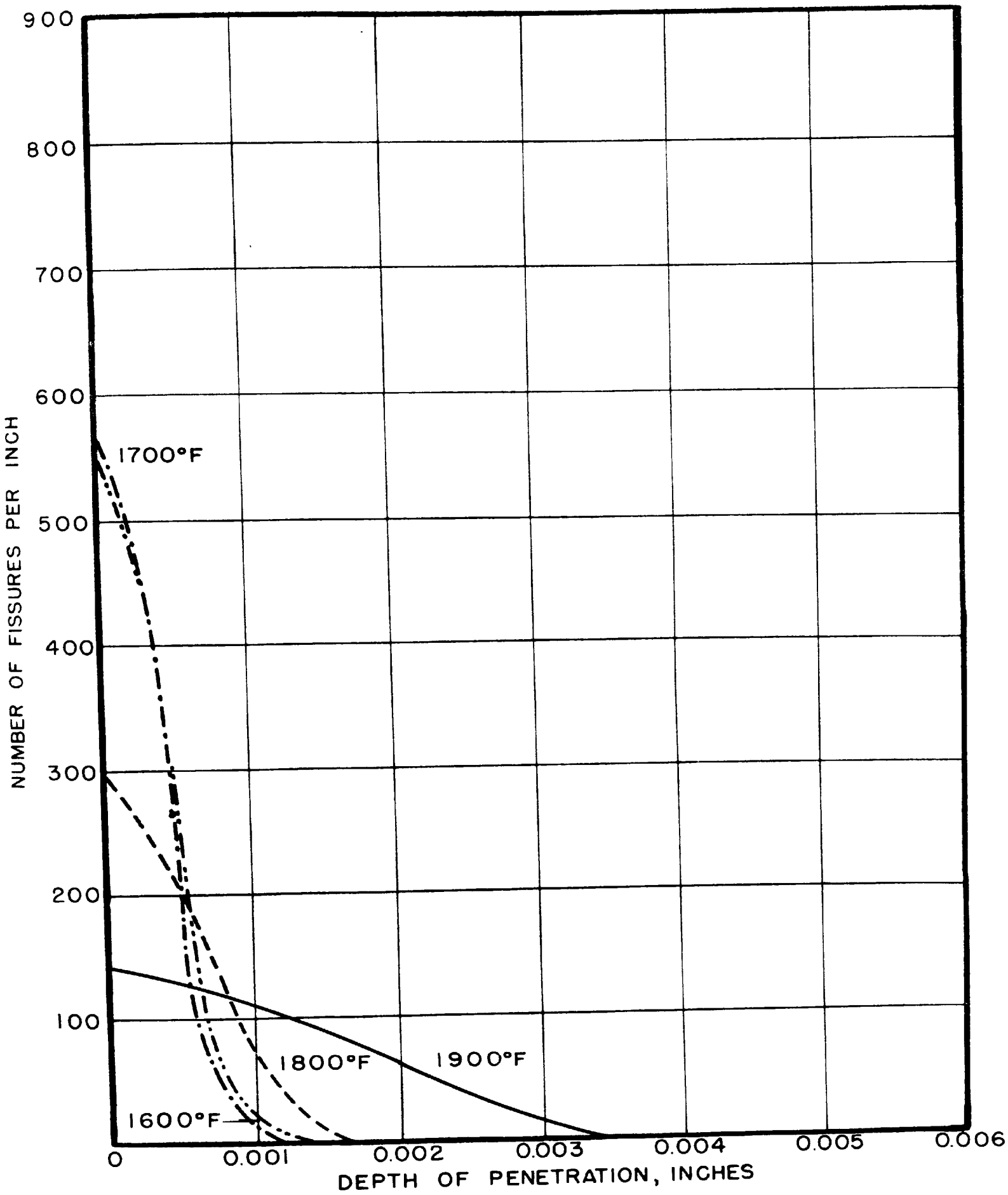

FIG. 23 - PENETRATION VS. DEPTH BELOW SURFACE. TYPE 309 + Nb ALLOY. RUN 8.

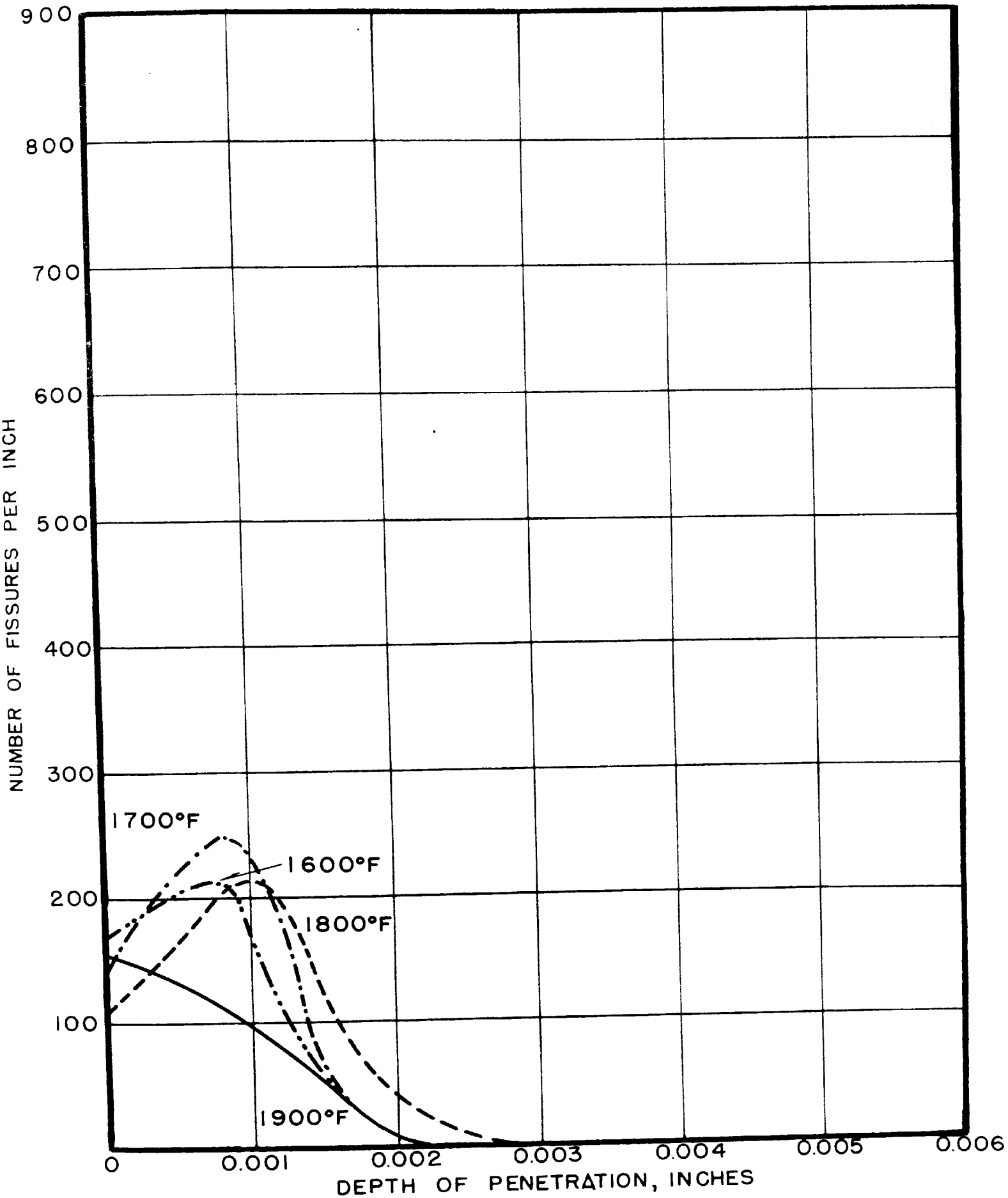

FIG. 24- PENETRATION VS. DEPTH BELOW SURFACE.
TYPE 310 ALLOY, HEAT 64177. RUN 8.

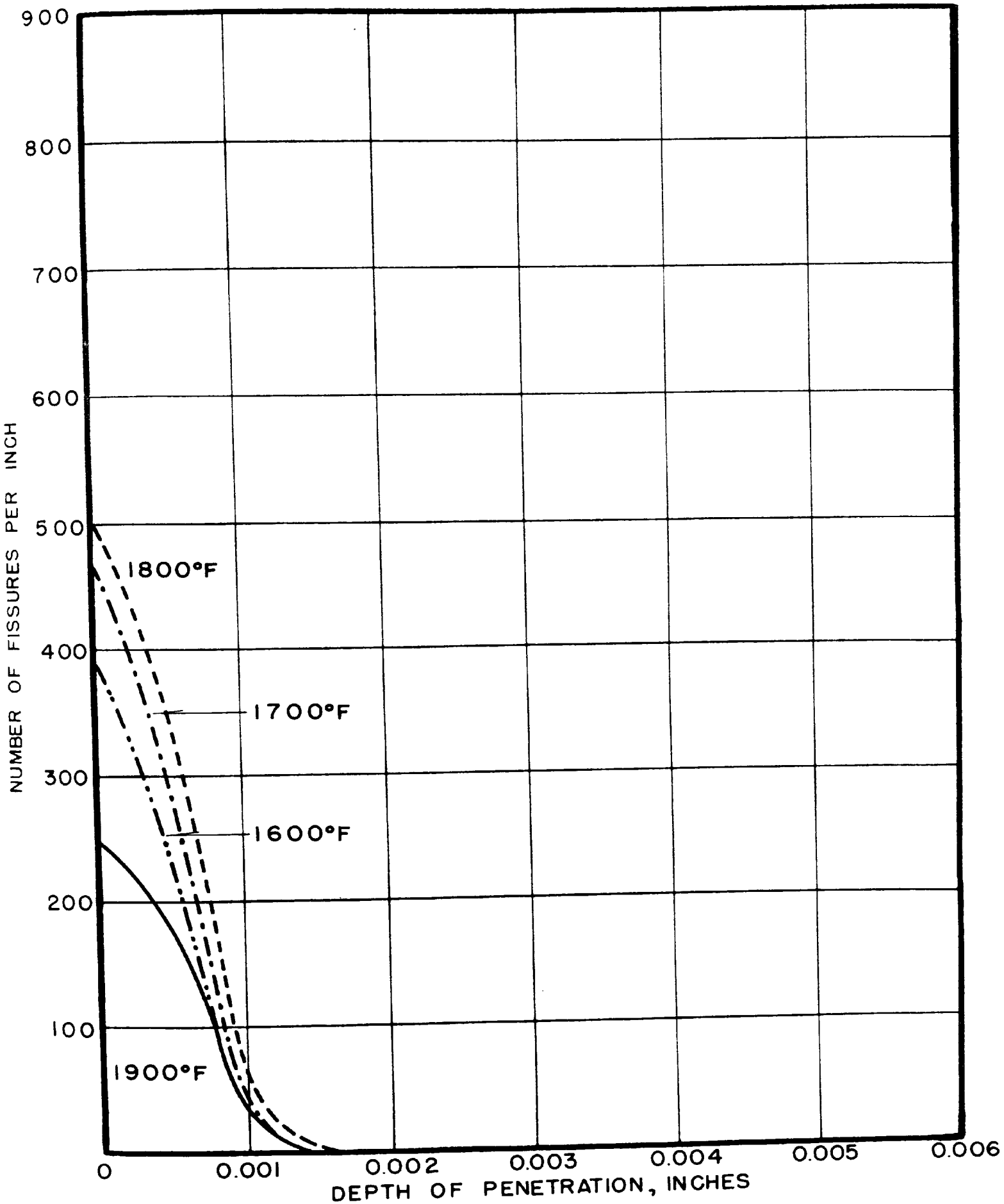

FIG. 25 - PENETRATION VS. DEPTH BELOW SURFACE.
TYPE 310 ALLOY, HEAT 64270. RUN 8.

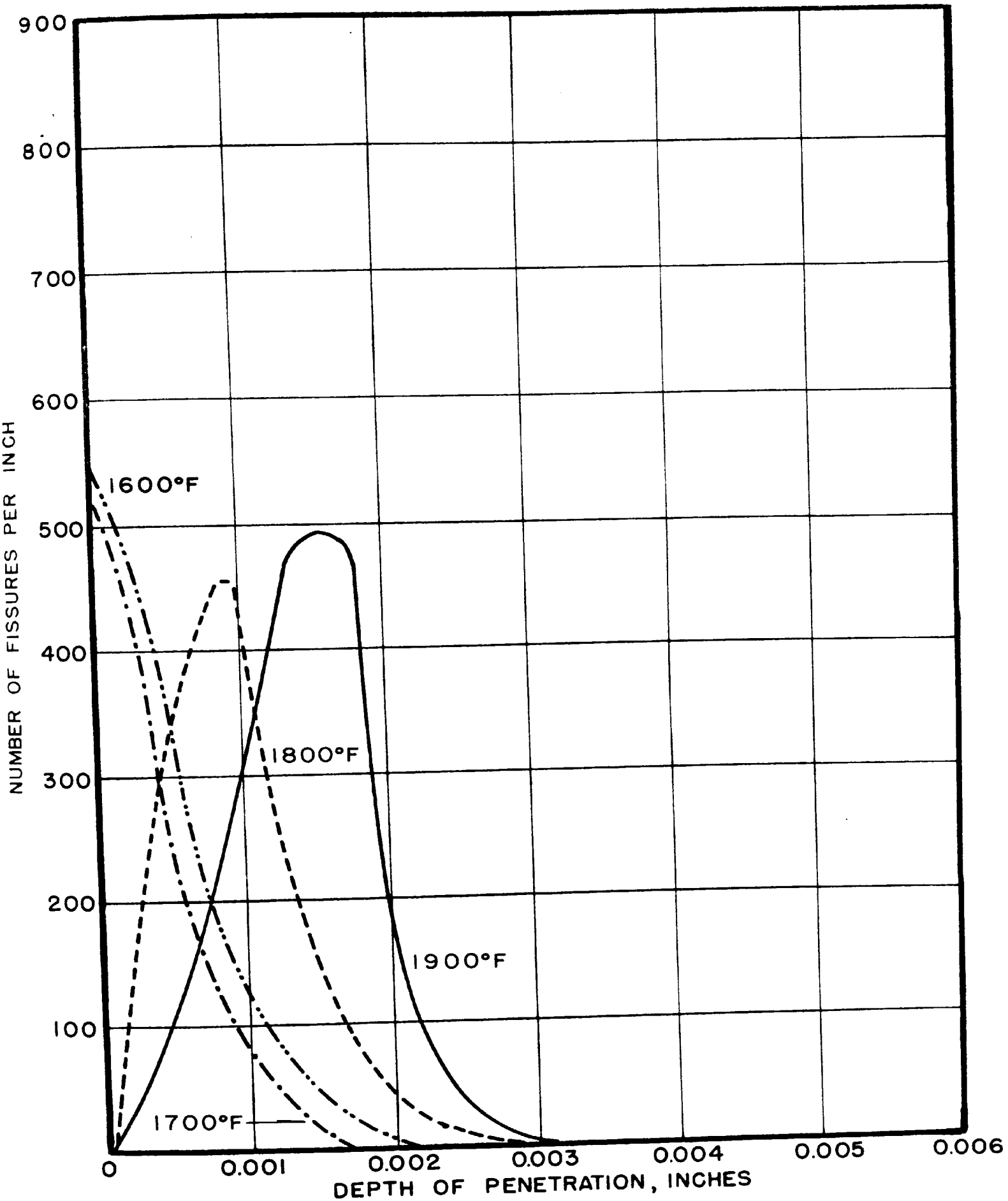

FIG. 26 - PENETRATION VS. DEPTH BELOW SURFACE.
TYPE 309 + Nb ALLOY. RUN 9.
STRAIGHT SECTION.

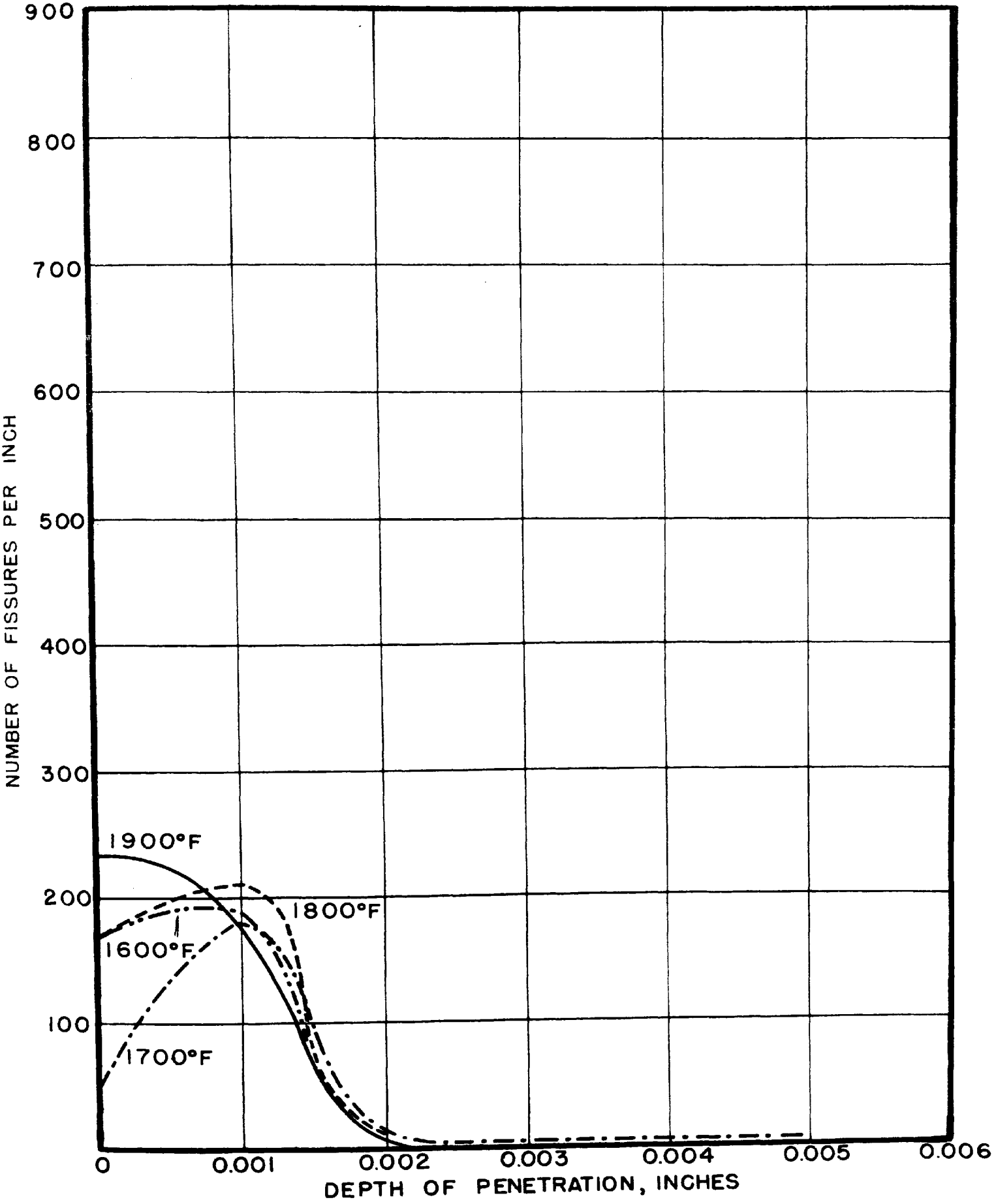

FIG. 27 - PENETRATION VS. DEPTH BELOW SURFACE. TYPE 310 ALLOY, HEAT 64177. RUN 9. STRAIGHT SECTION.

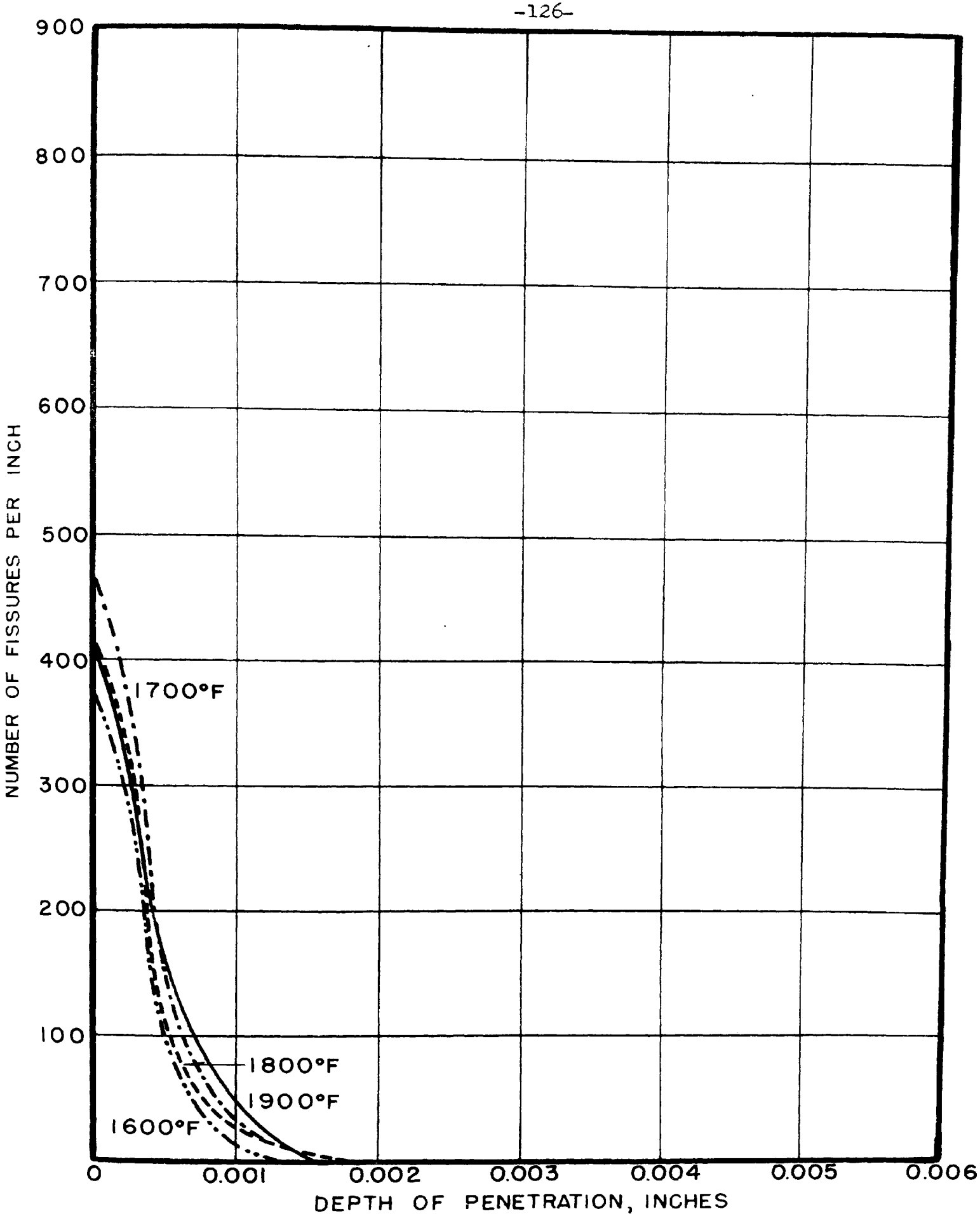

FIG. 28- PENETRATION VS. DEPTH BELOW SURFACE.
TYPE 310 ALLOY, HEAT 64270. RUN 9.
STRAIGHT SECTION.

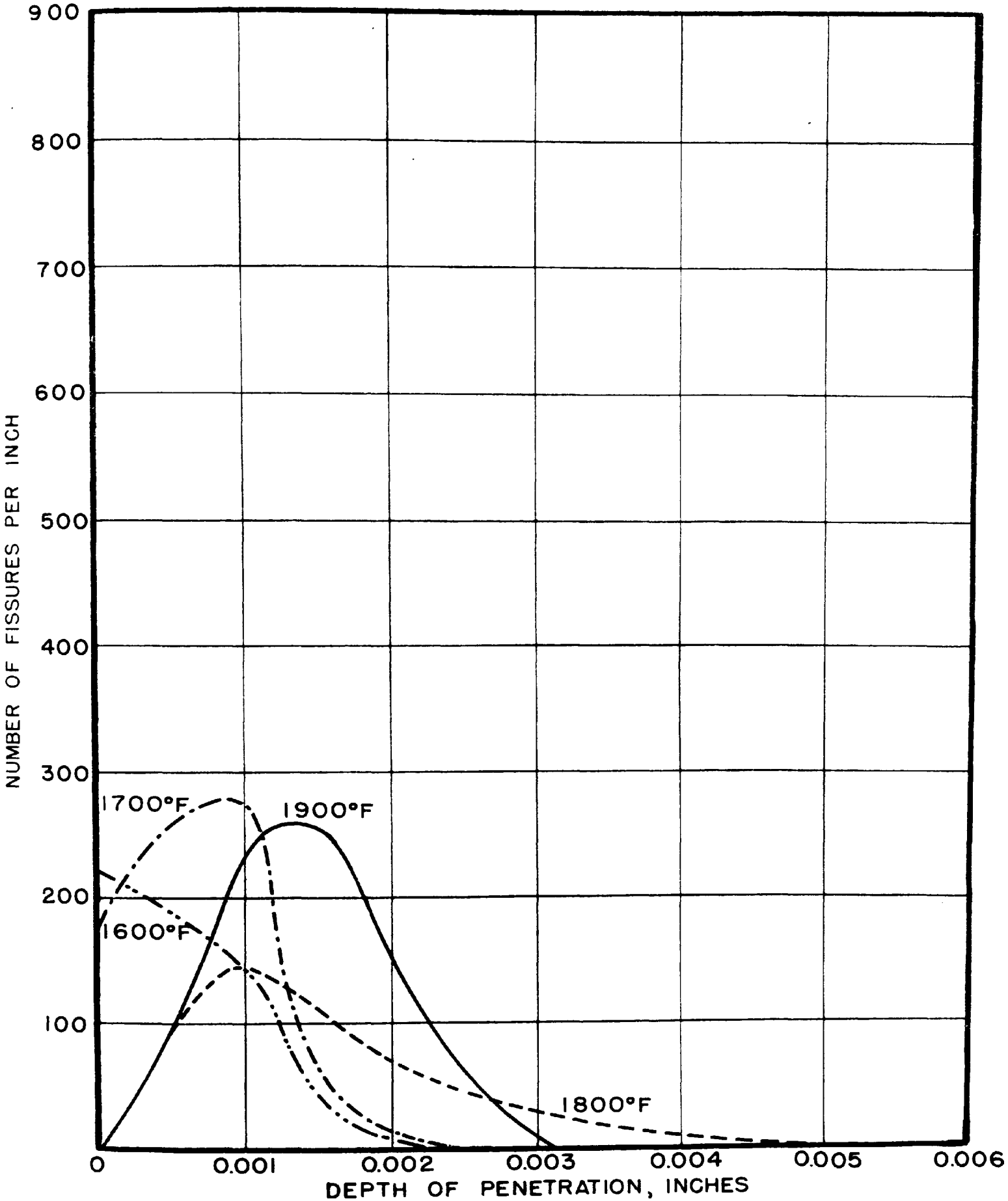

FIG. 29 - PENETRATION VS. DEPTH BELOW SURFACE.
TYPE 309 + Nb ALLOY. RUN 9.
CURVED SECTION.

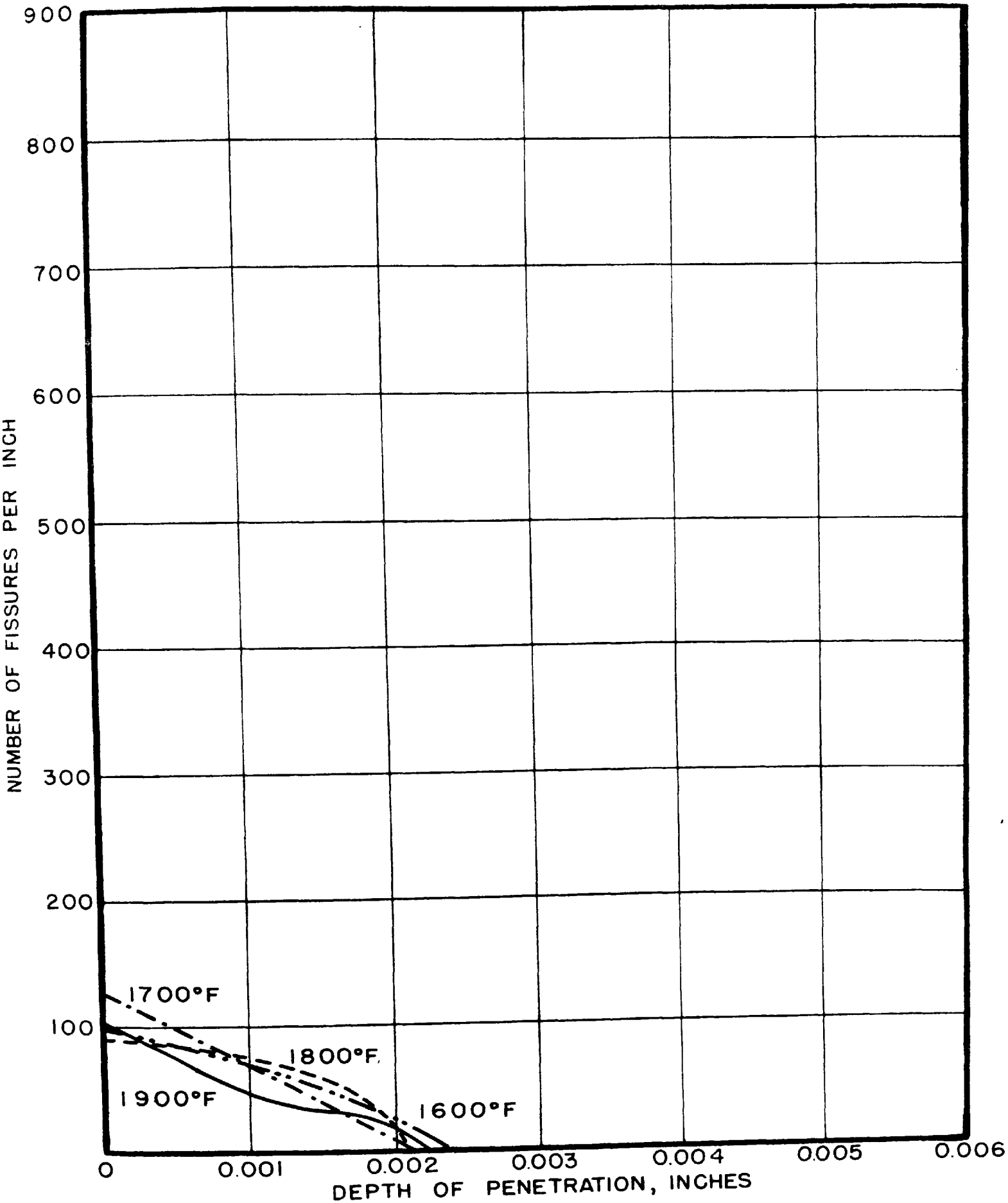

FIG. 30-PENETRATION VS. DEPTH BELOW SURFACE.
TYPE 310 ALLOY, HEAT 64177. RUN 9.
CURVED SECTION.

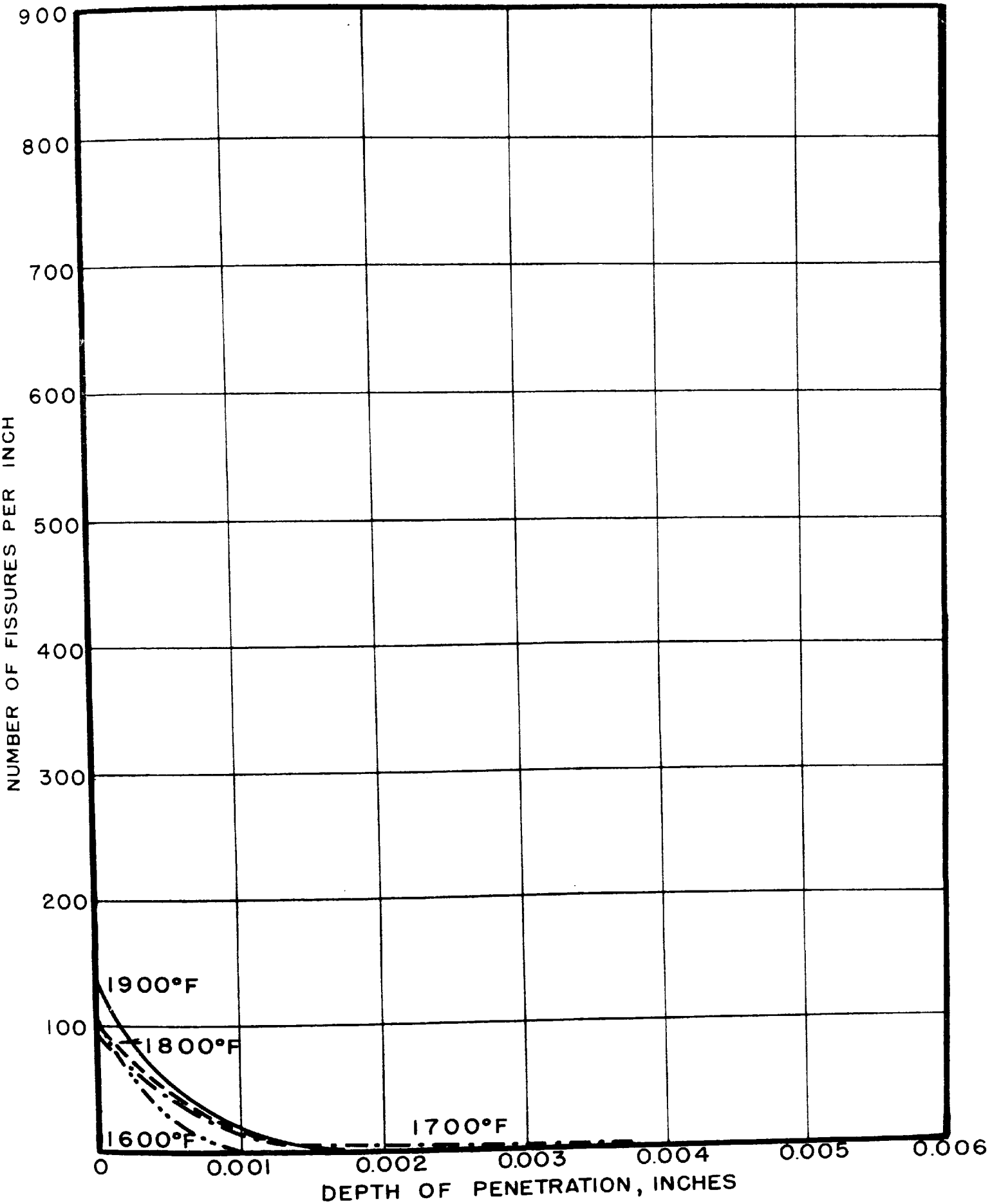

FIG. 31 - PENETRATION VS. DEPTH BELOW SURFACE. TYPE 310 ALLOY, HEAT 64270. RUN 9. CURVED SECTION.

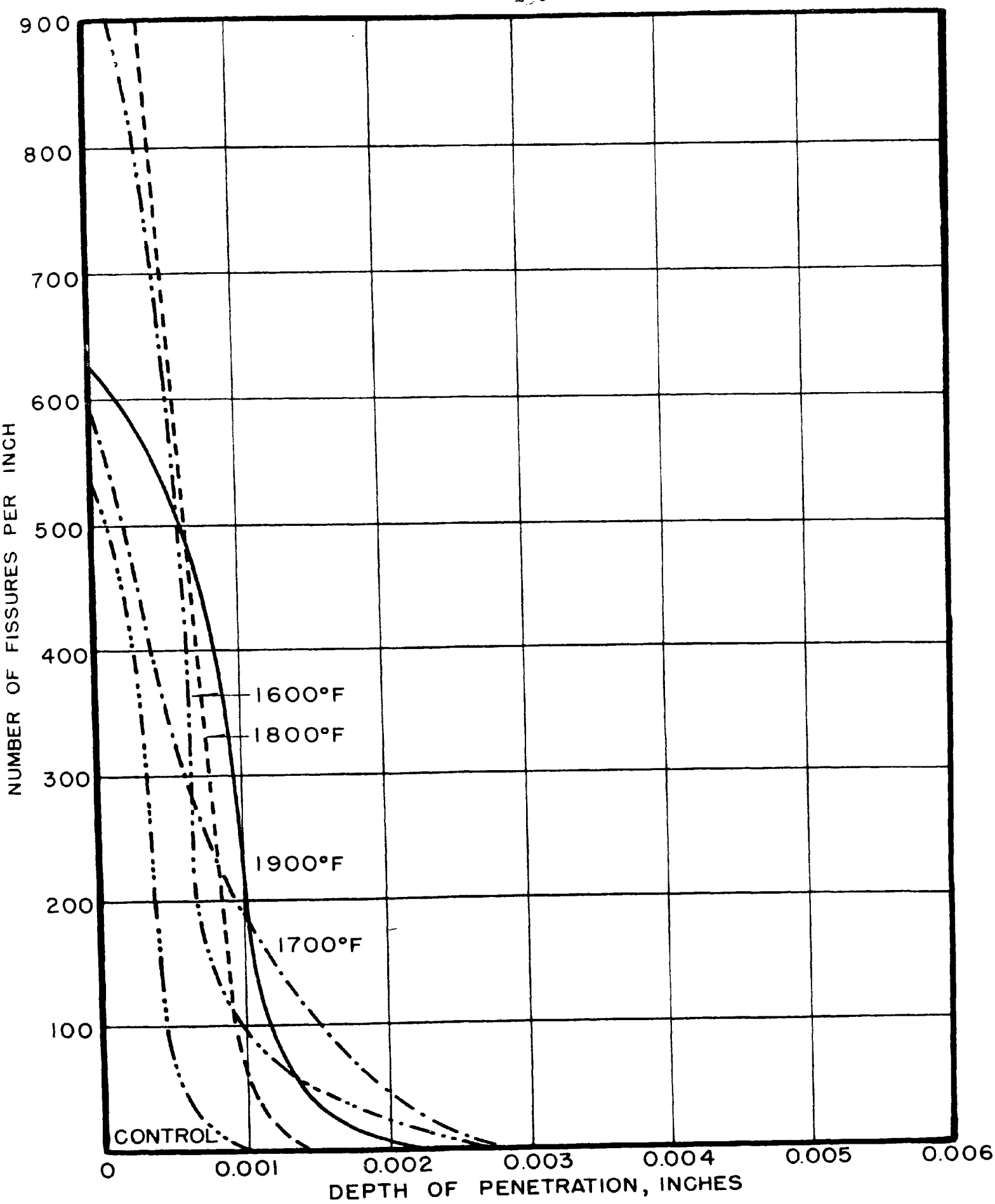

FIG. 32 - PENETRATION VS. DEPTH BELOW SURFACE.
TYPE 309+Nb ALLOY. RUN 10.

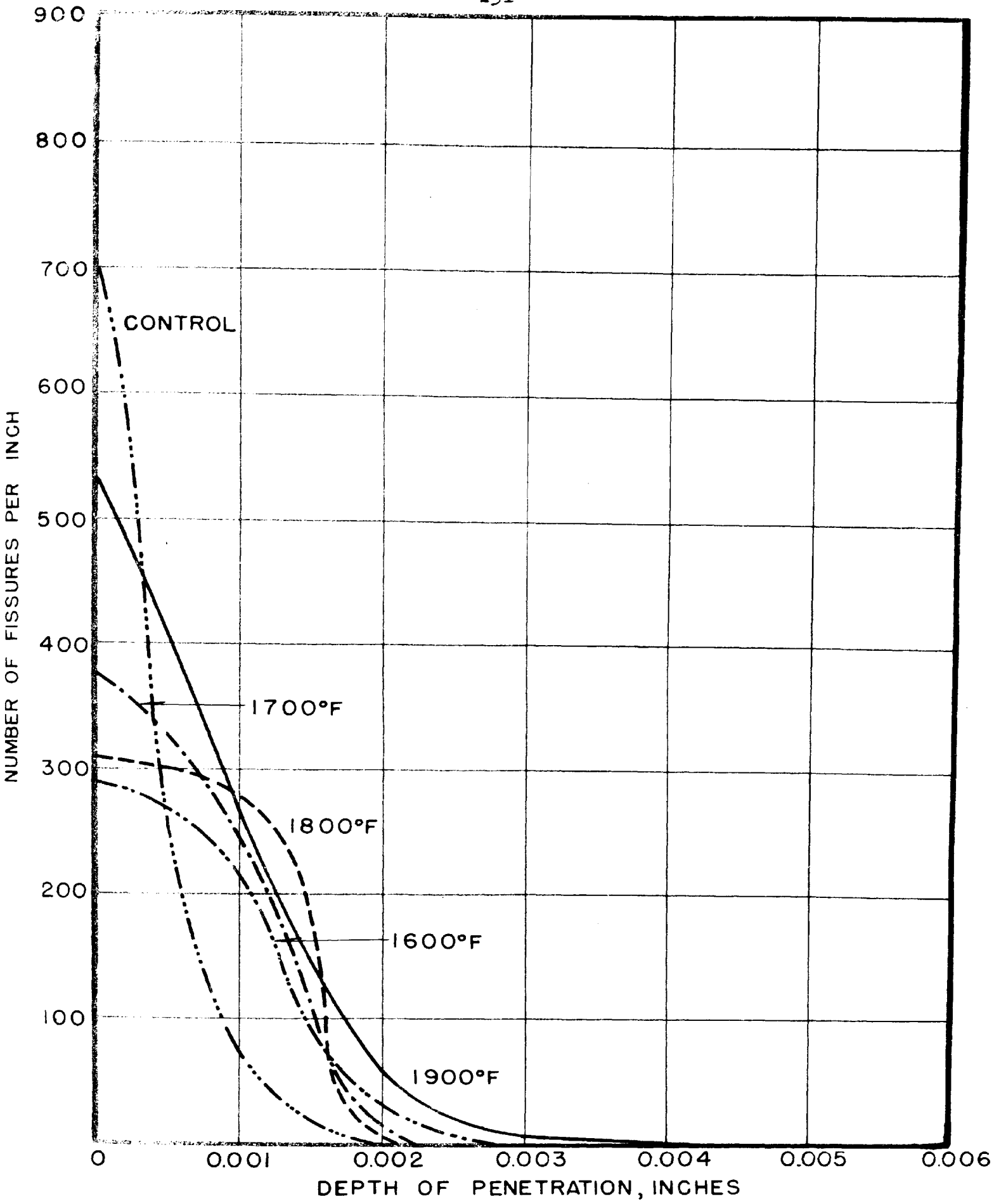

FIG. 33- PENETRATION VS. DEPTH BELOW SURFACE.
TYPE 310 ALLOY, HEAT 64177. RUN 10.

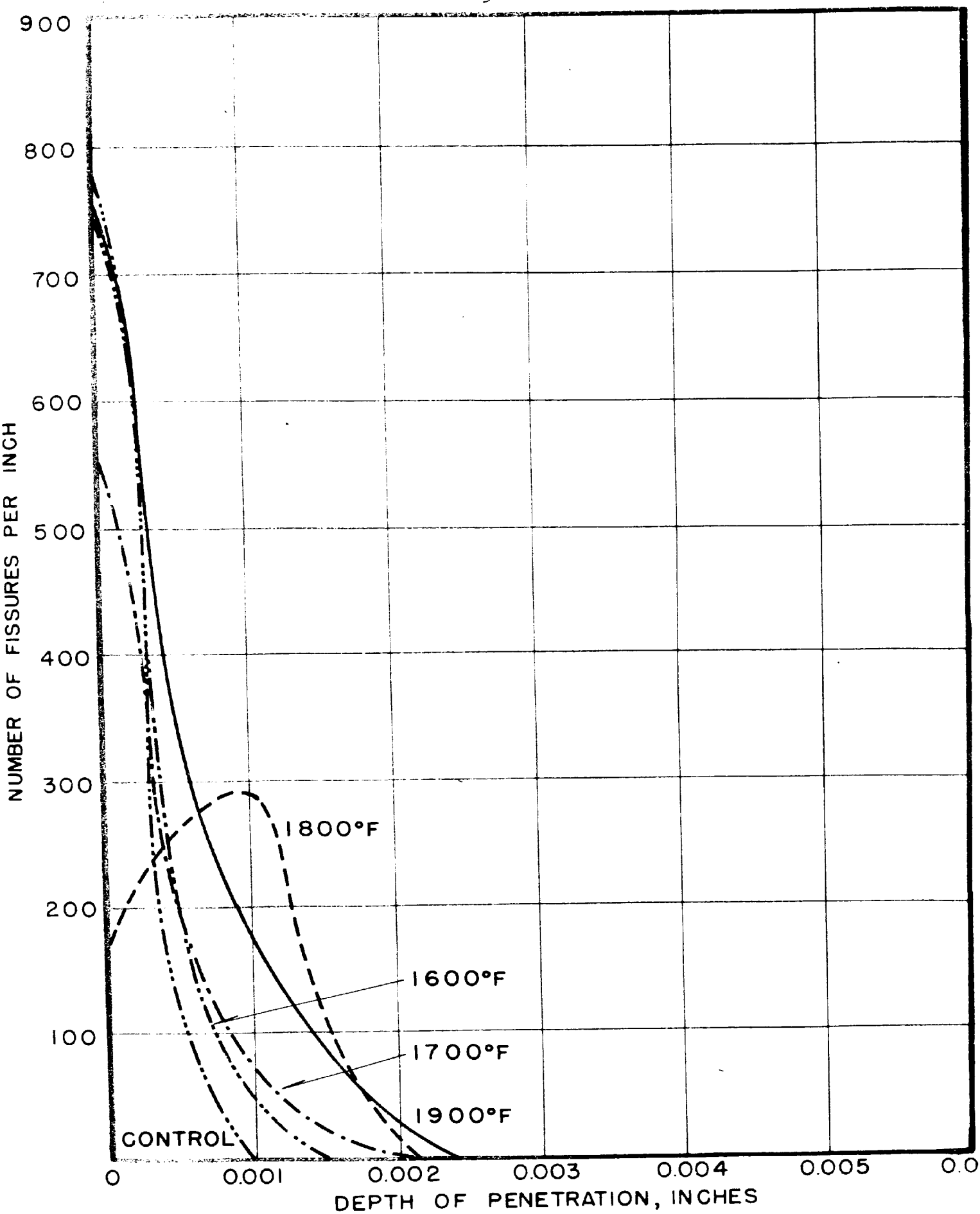

FIG. 34-PENETRATION VS. DEPTH BELOW SURFACE.
TYPE 310 ALLOY, HEAT 64270. RUN 10.

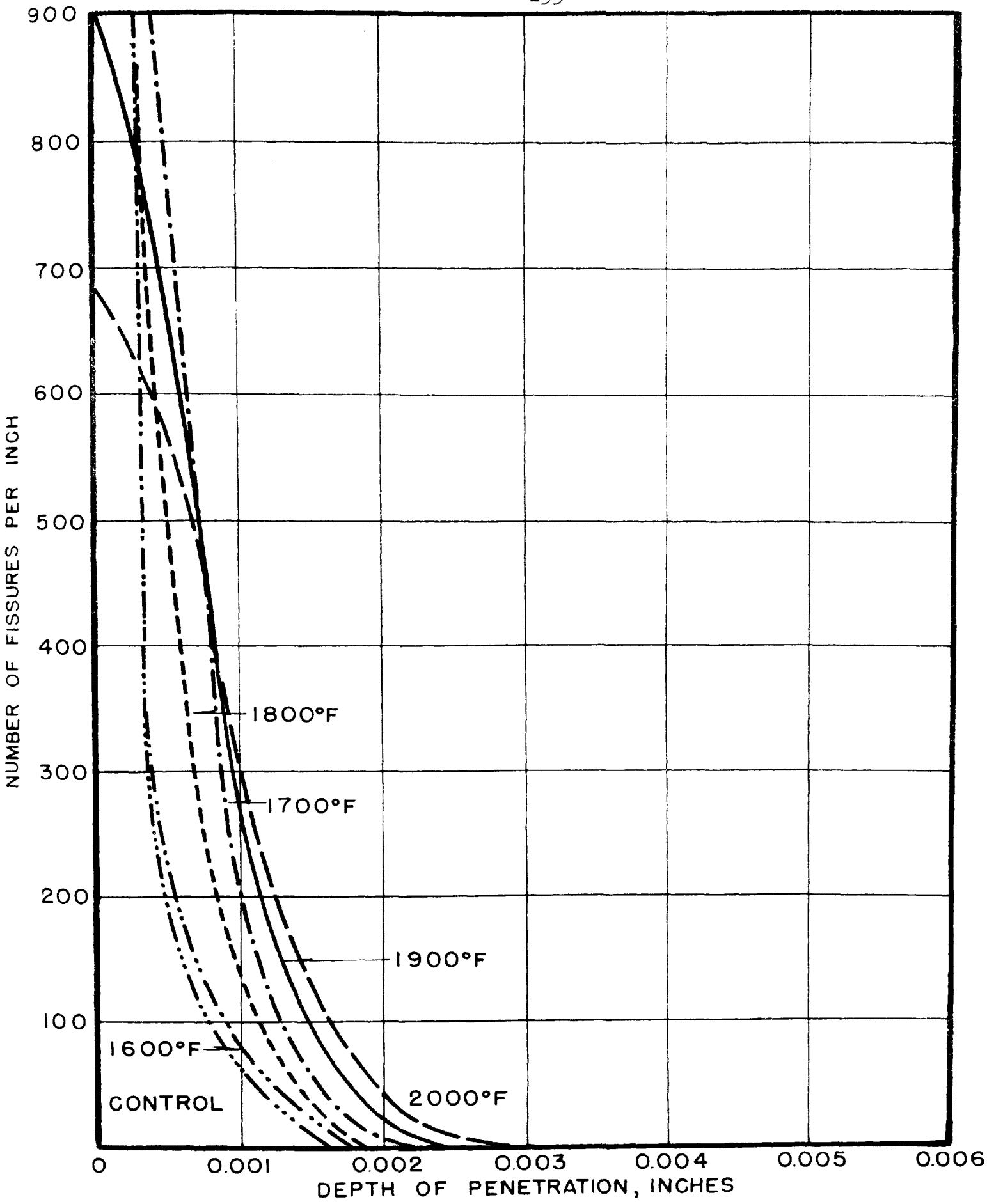

FIG. 35 – PENETRATION VS. DEPTH BELOW SURFACE.
TYPE 309 + Nb ALLOY. RUNS 11 & 27.

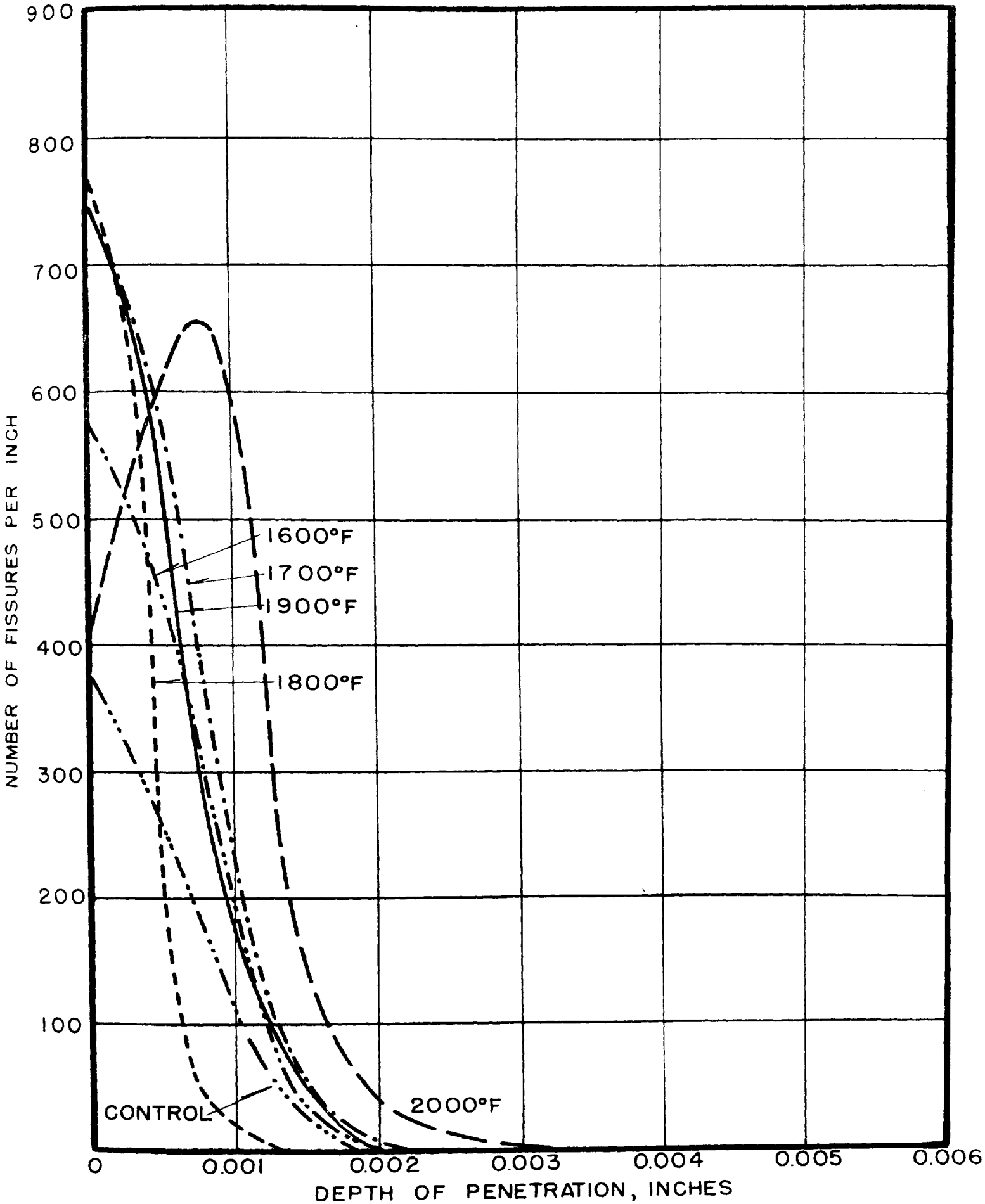

FIG. 36 - PENETRATION VS. DEPTH BELOW SURFACE.
TYPE 310 ALLOY, HEAT 64177. RUNS 11 & 27.

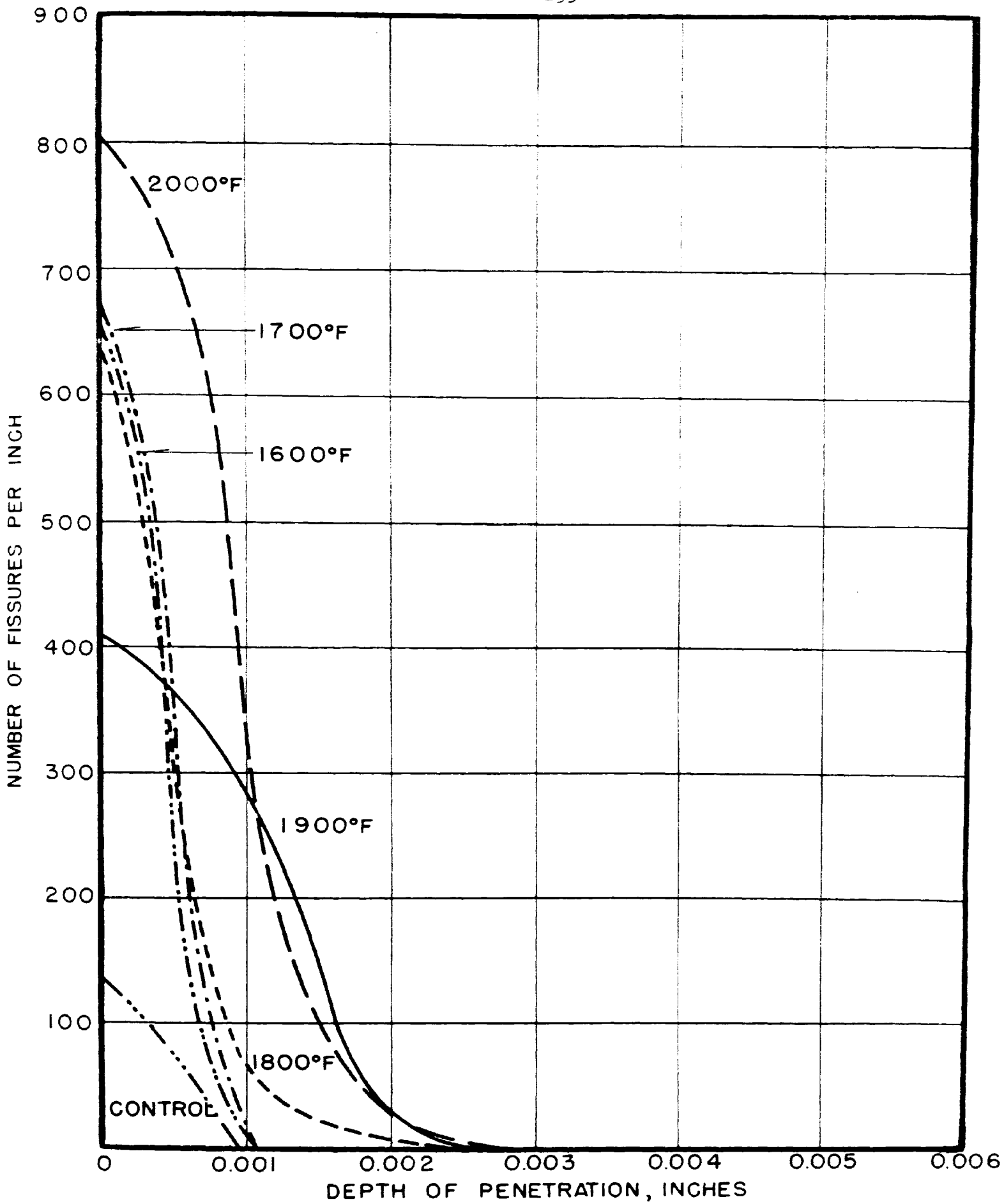

FIG. 37- PENETRATION VS. DEPTH BELOW SURFACE.
TYPE 310 ALLOY, HEAT 64270. RUNS 11 & 27.

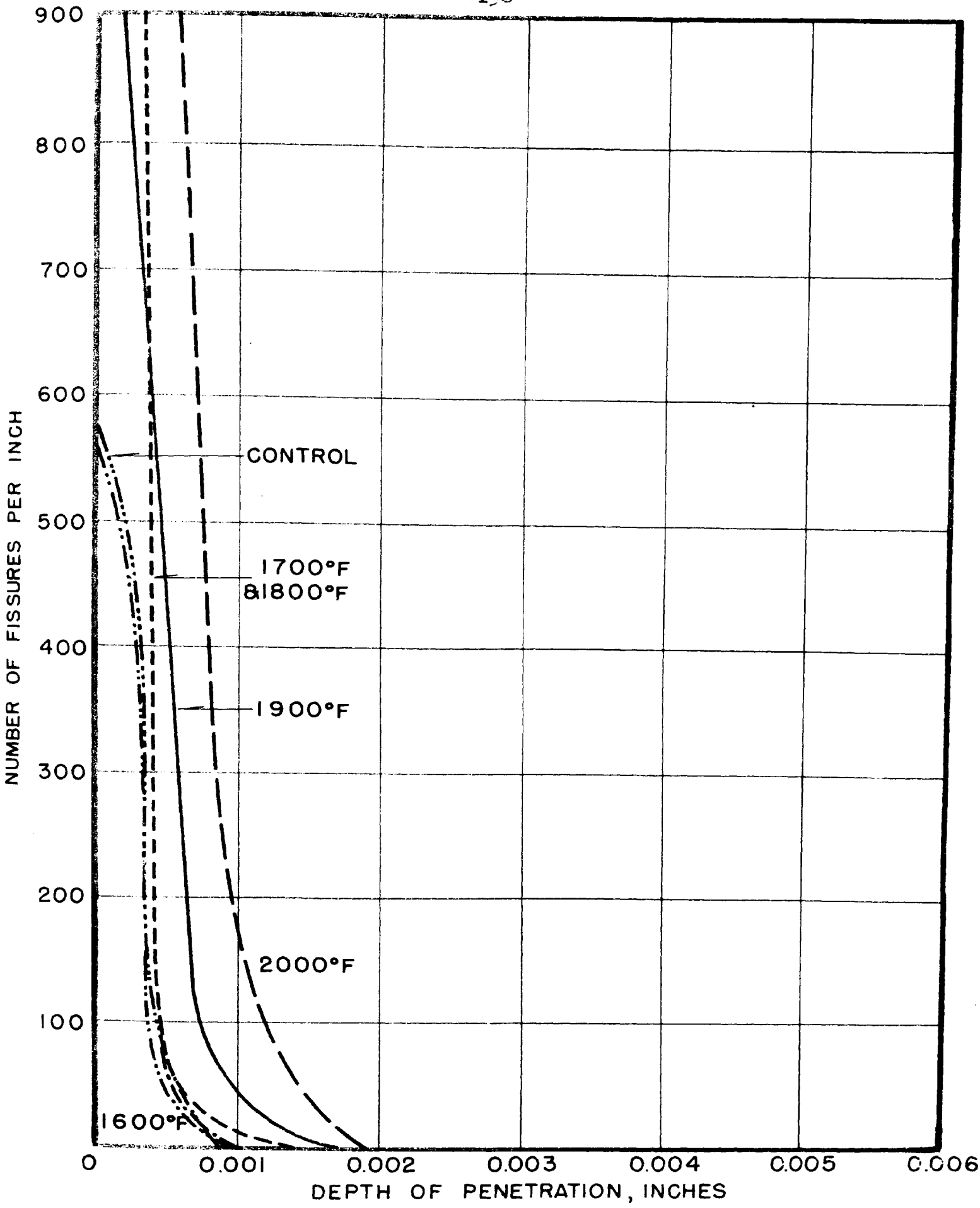

FIG. 38- PENETRATION VS. DEPTH BELOW SURFACE.
TYPE 309+Nb ALLOY. RUNS 12 & 26.

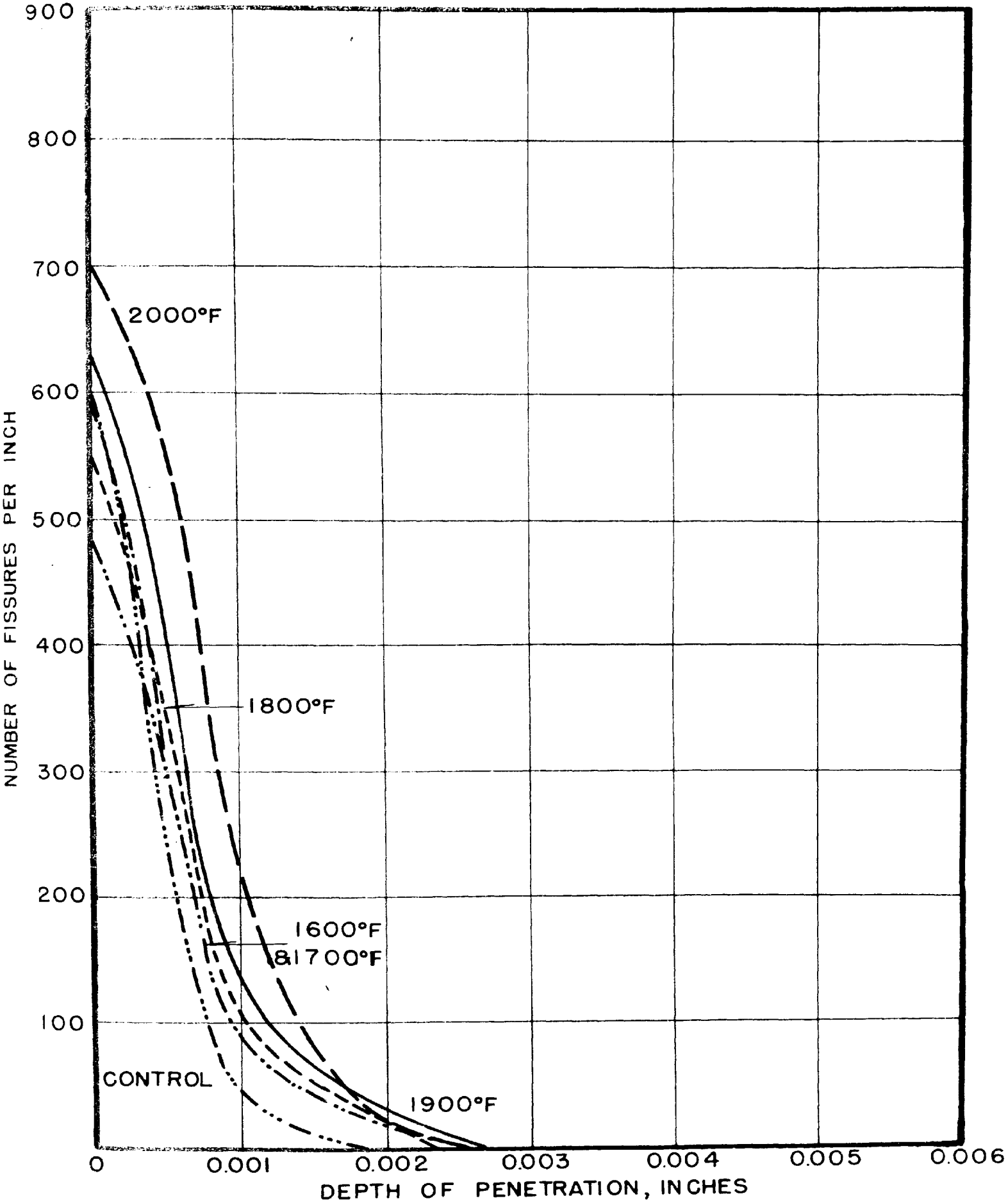

FIG. 39 - PENETRATION VS. DEPTH BELOW SURFACE.
TYPE 310 ALLOY, HEAT 64177. RUNS 12 & 26.

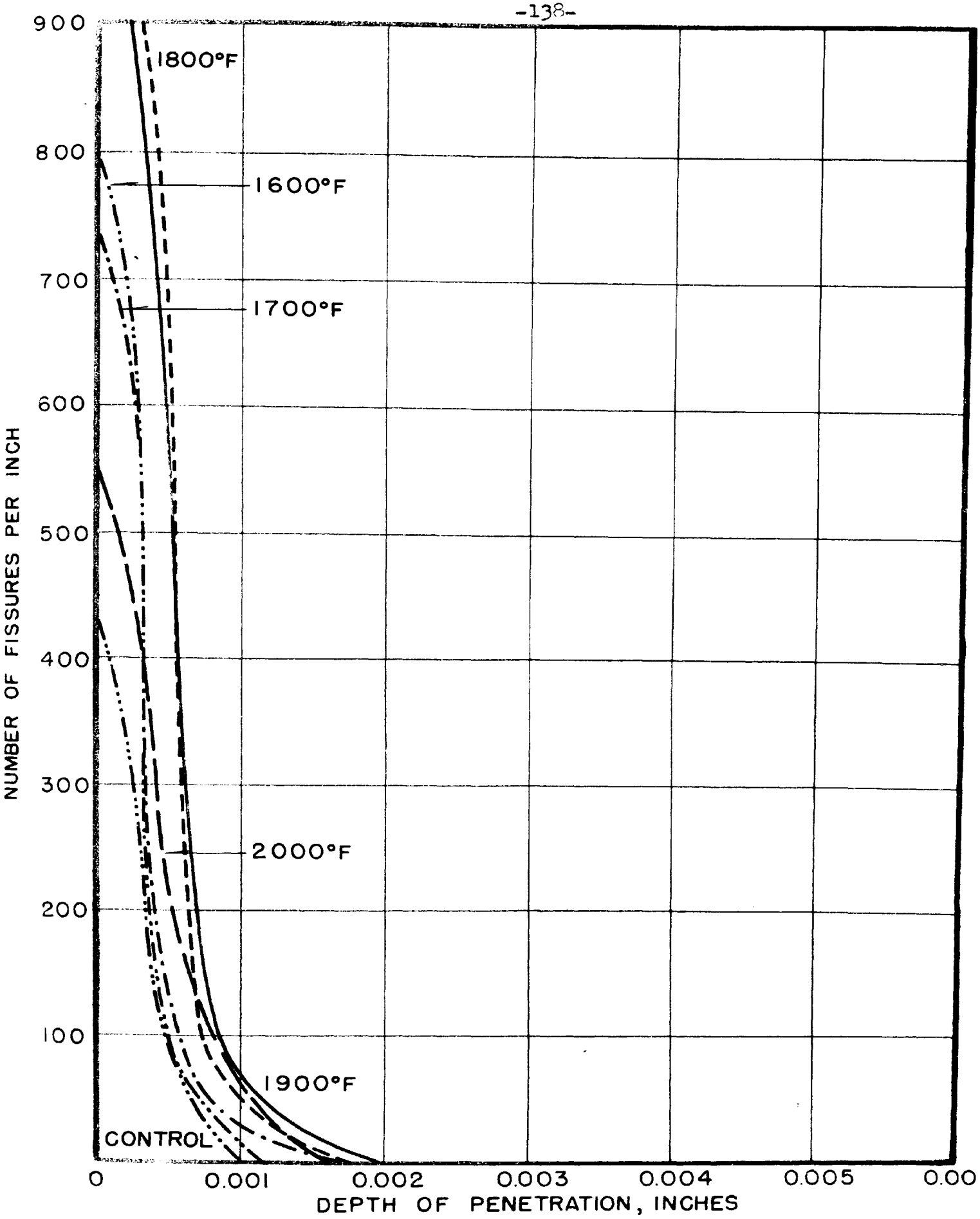

FIG. 40 - PENETRATION VS. DEPTH BELOW SURFACE.
TYPE 310 ALLOY, HEAT 64270. RUNS 12 & 26.

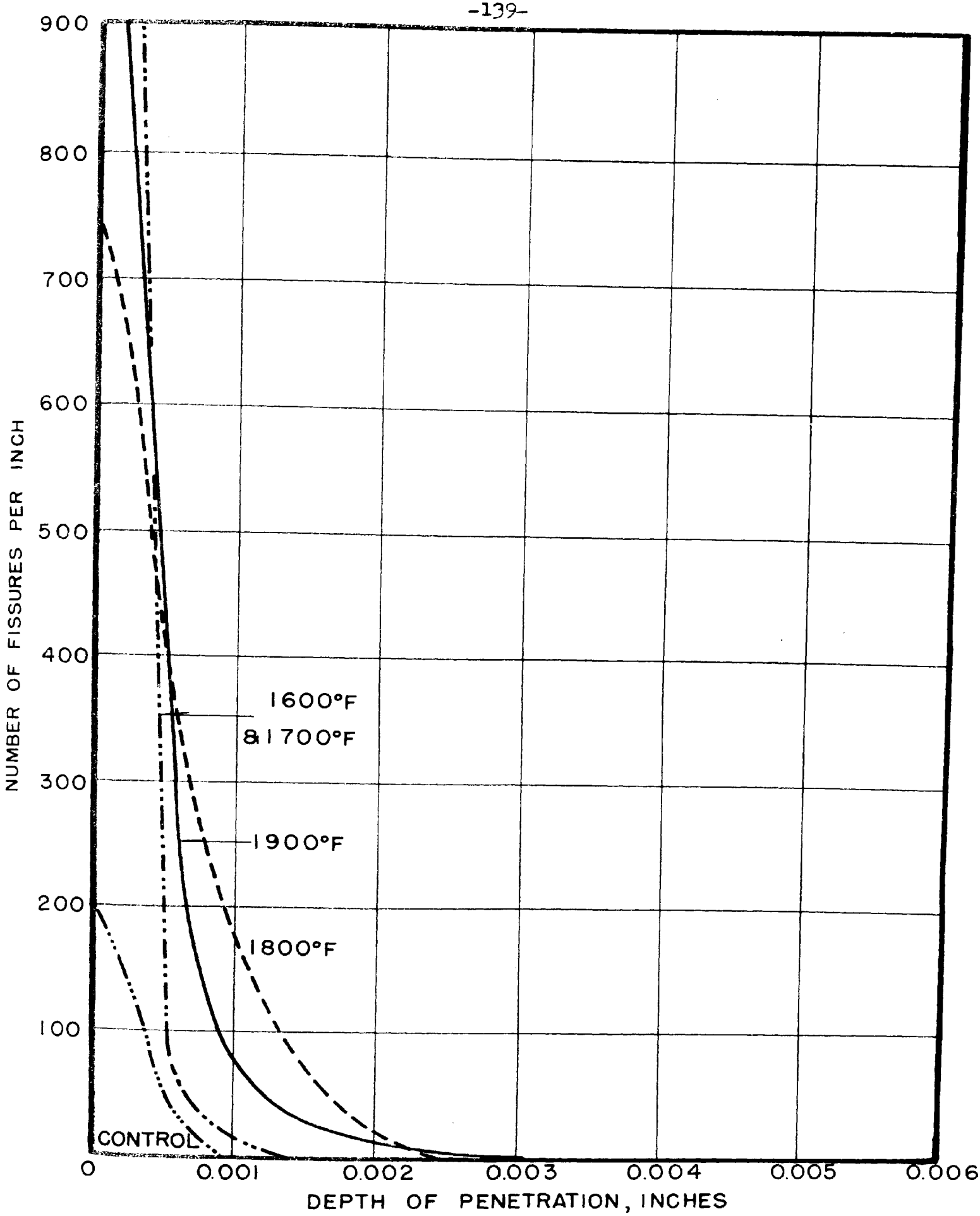

FIG. 41- PENETRATION VS. DEPTH BELOW SURFACE.
TYPE 309 + Nb ALLOY. RUN 13.

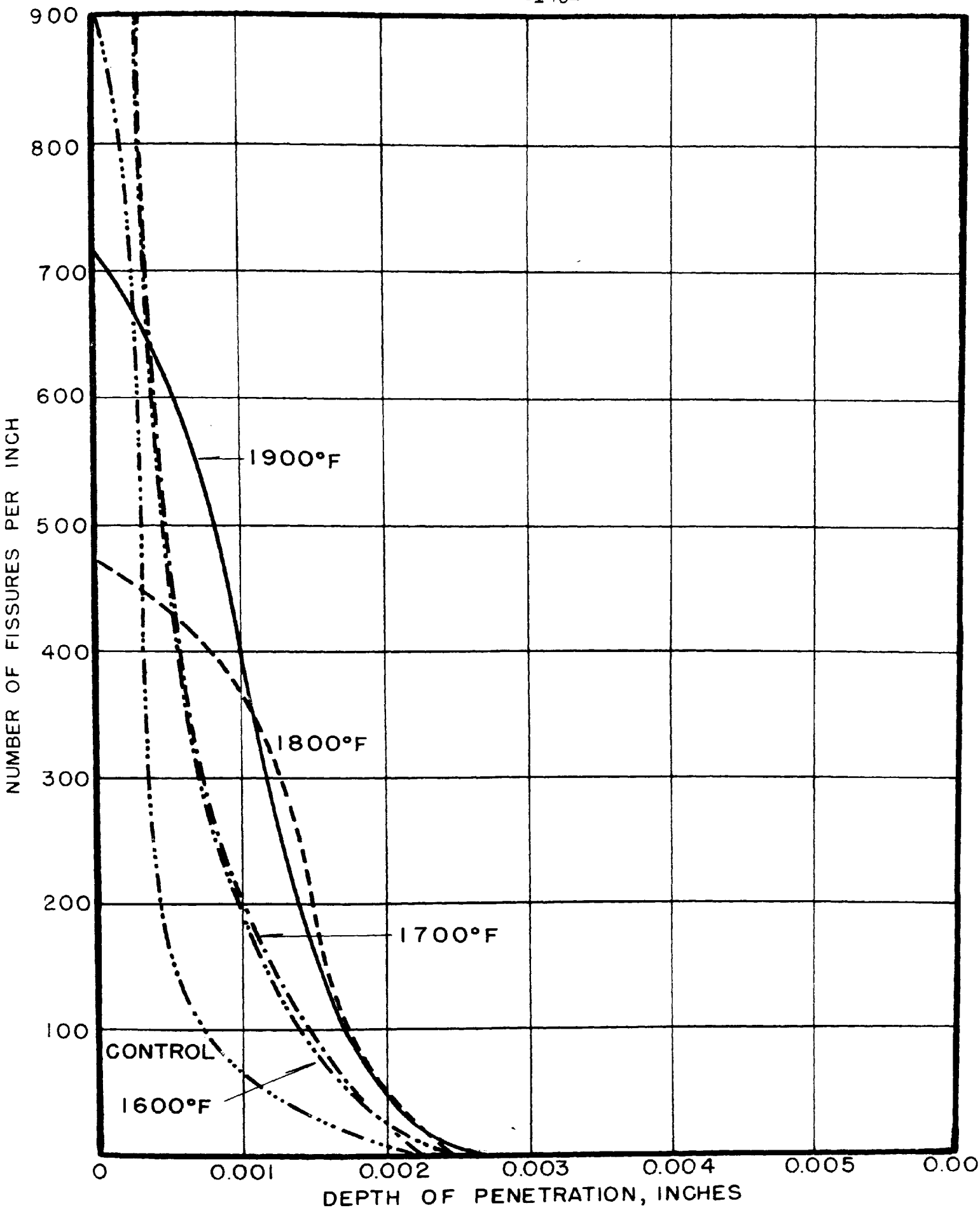

FIG. 42 - PENETRATION VS. DEPTH BELOW SURFACE.
TYPE 310 ALLOY, HEAT 64177. RUN 13.

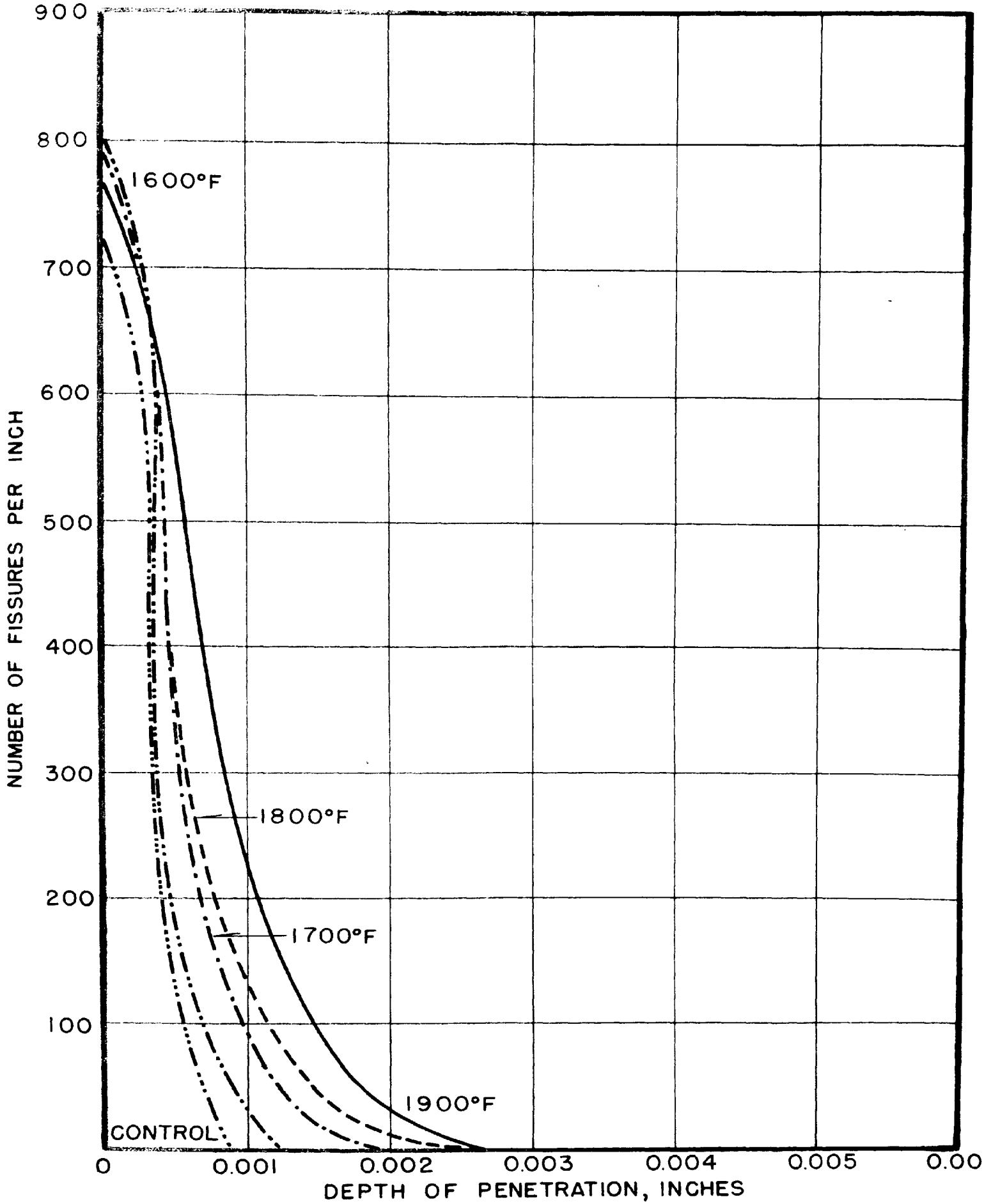

FIG. 43 - PENETRATION VS. DEPTH BELOW SURFACE.
TYPE 310 ALLOY, HEAT 64270. RUN 13.

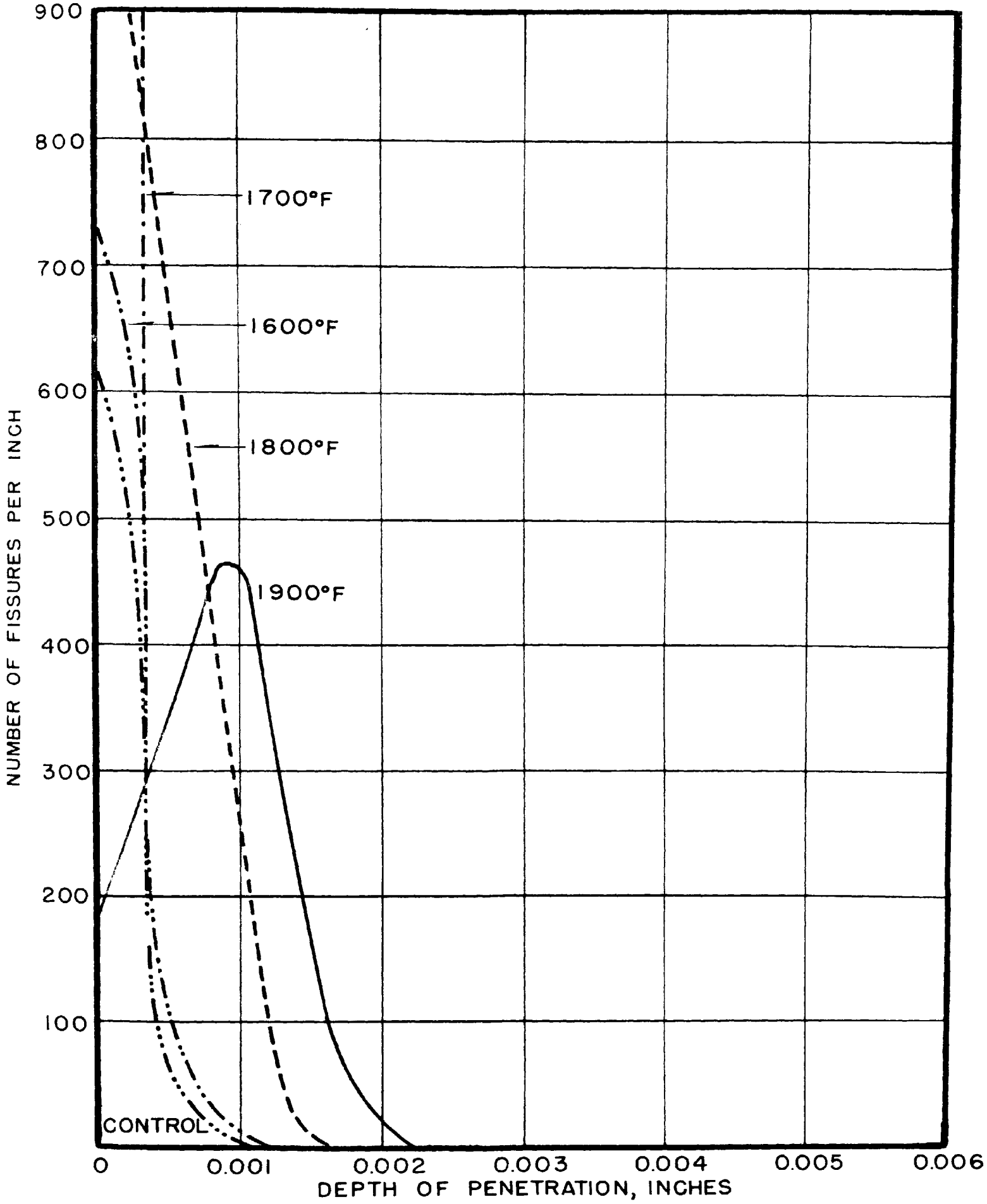

FIG. 44 - PENETRATION VS. DEPTH BELOW SURFACE.
TYPE 309 + Nb ALLOY. RUN 14.

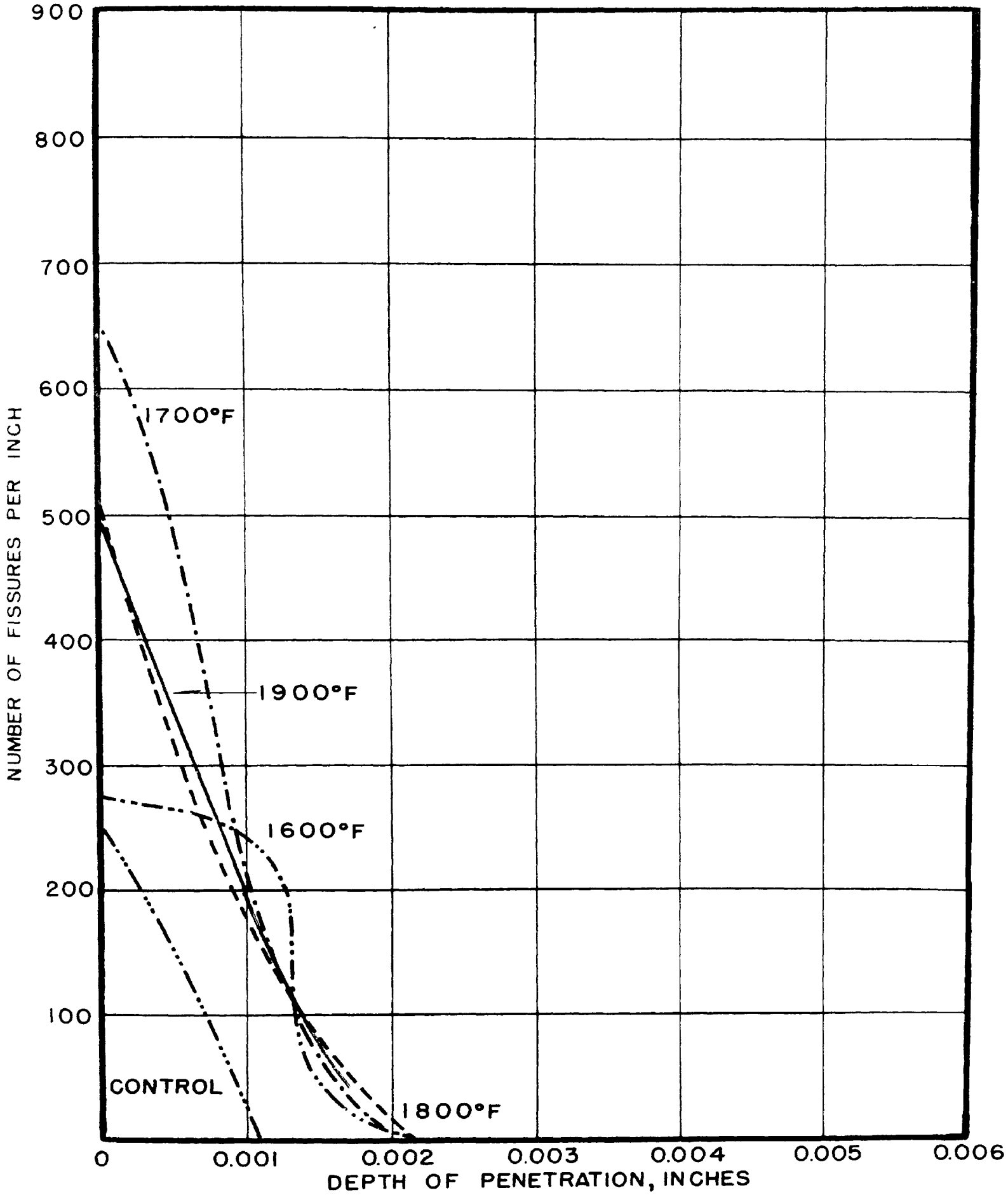

FIG. 45 - PENETRATION VS. DEPTH BELOW SURFACE.
TYPE 310 ALLOY, HEAT 64177. RUN 14.

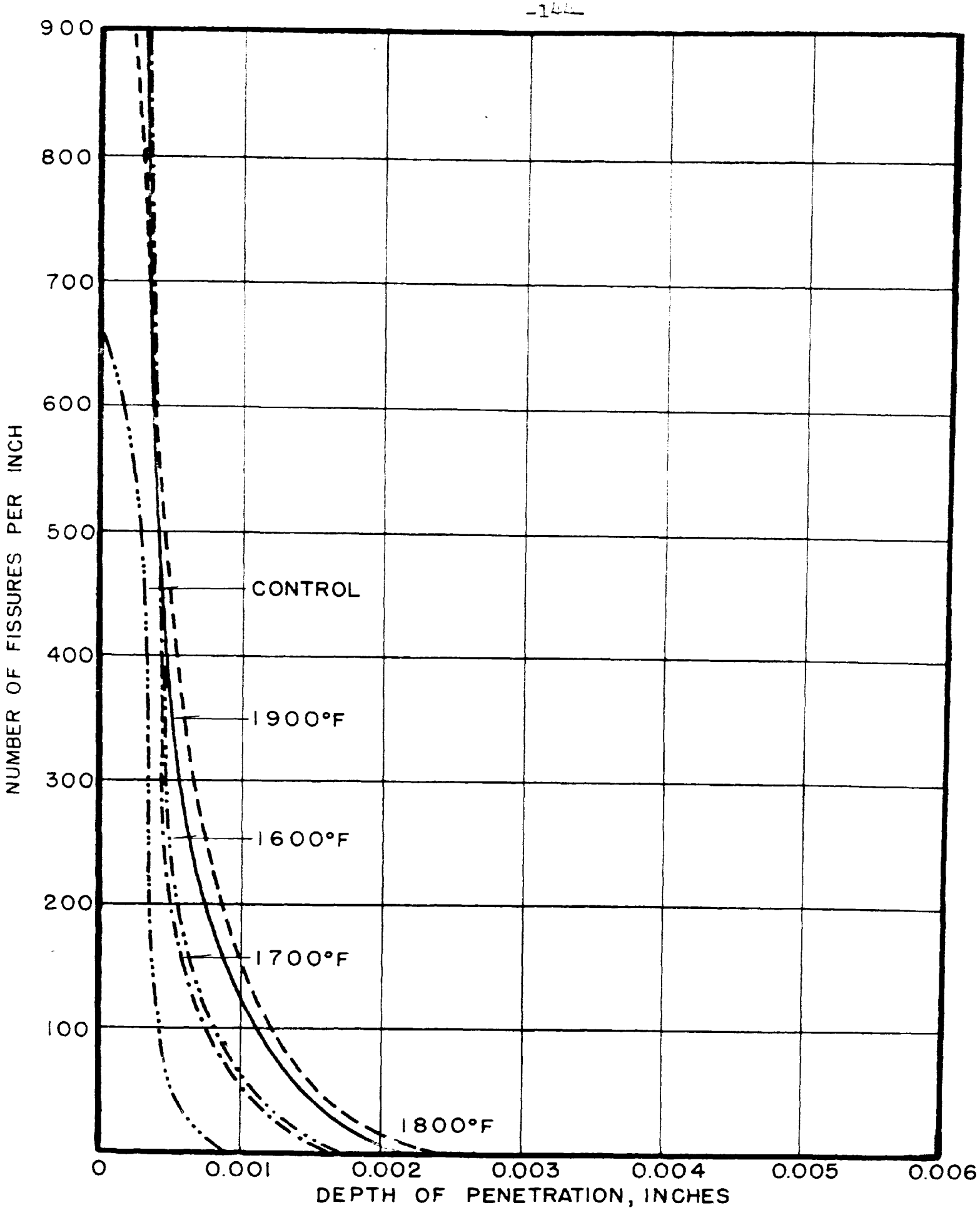

FIG. 46 - PENETRATION VS. DEPTH BELOW SURFACE.
TYPE 310 ALLOY, HEAT 64270. RUN 14.

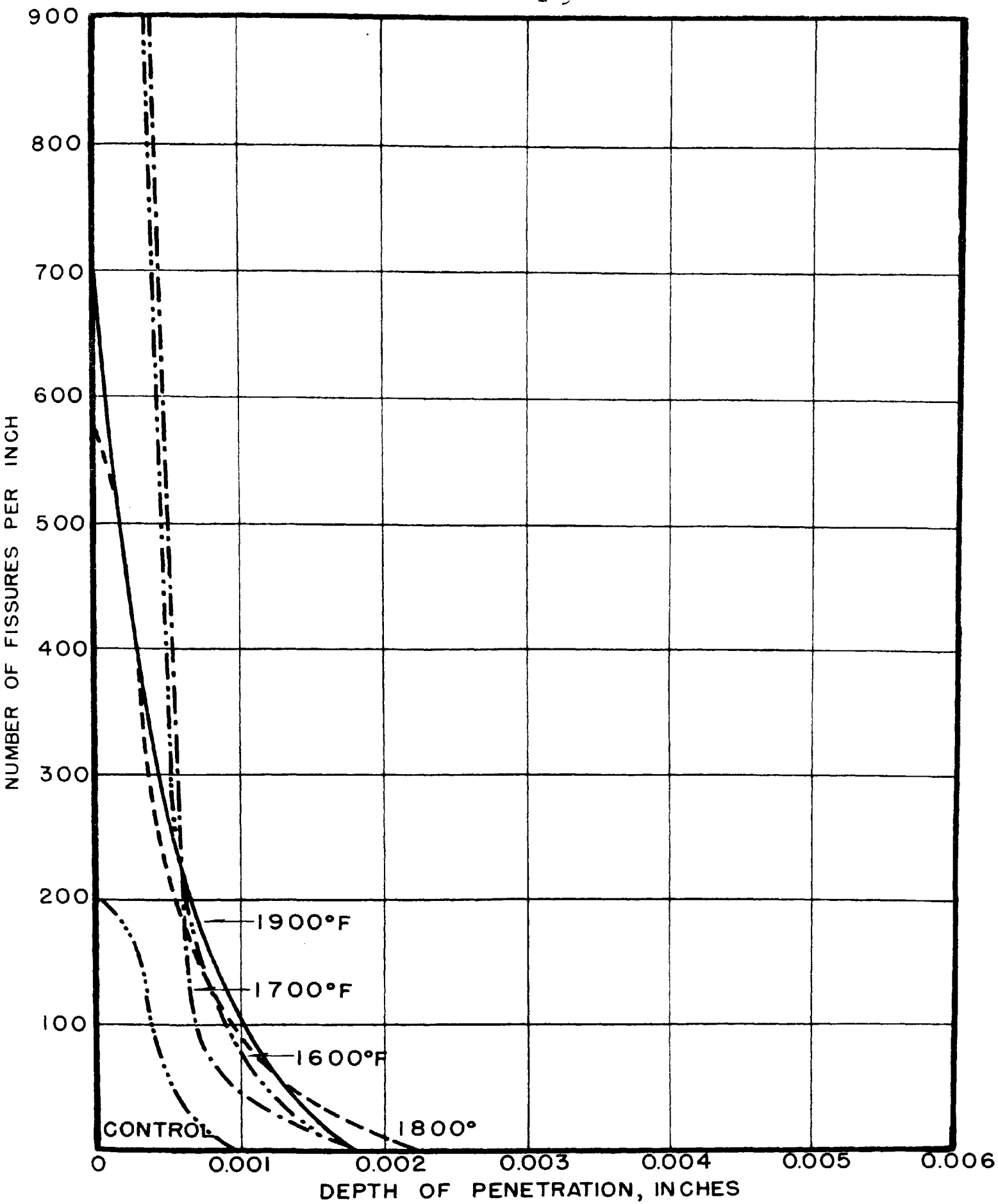

FIG. 47 - PENETRATION VS. DEPTH BELOW SURFACE.
TYPE 309 + Nb ALLOY. RUN 15.

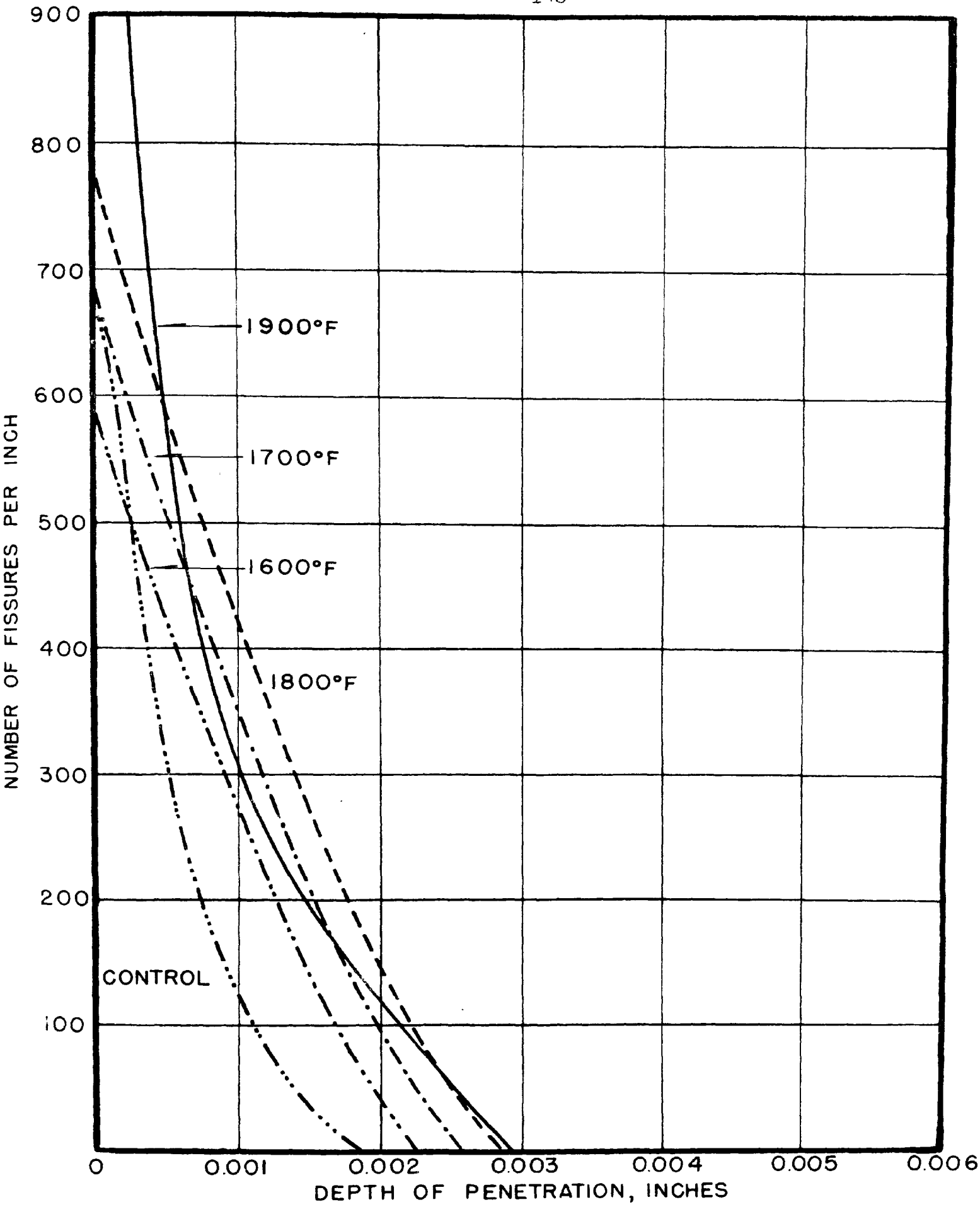

FIG. 48 - PENETRATION VS. DEPTH BELOW SURFACE.
TYPE 310 ALLOY, HEAT 64177. RUN 15.

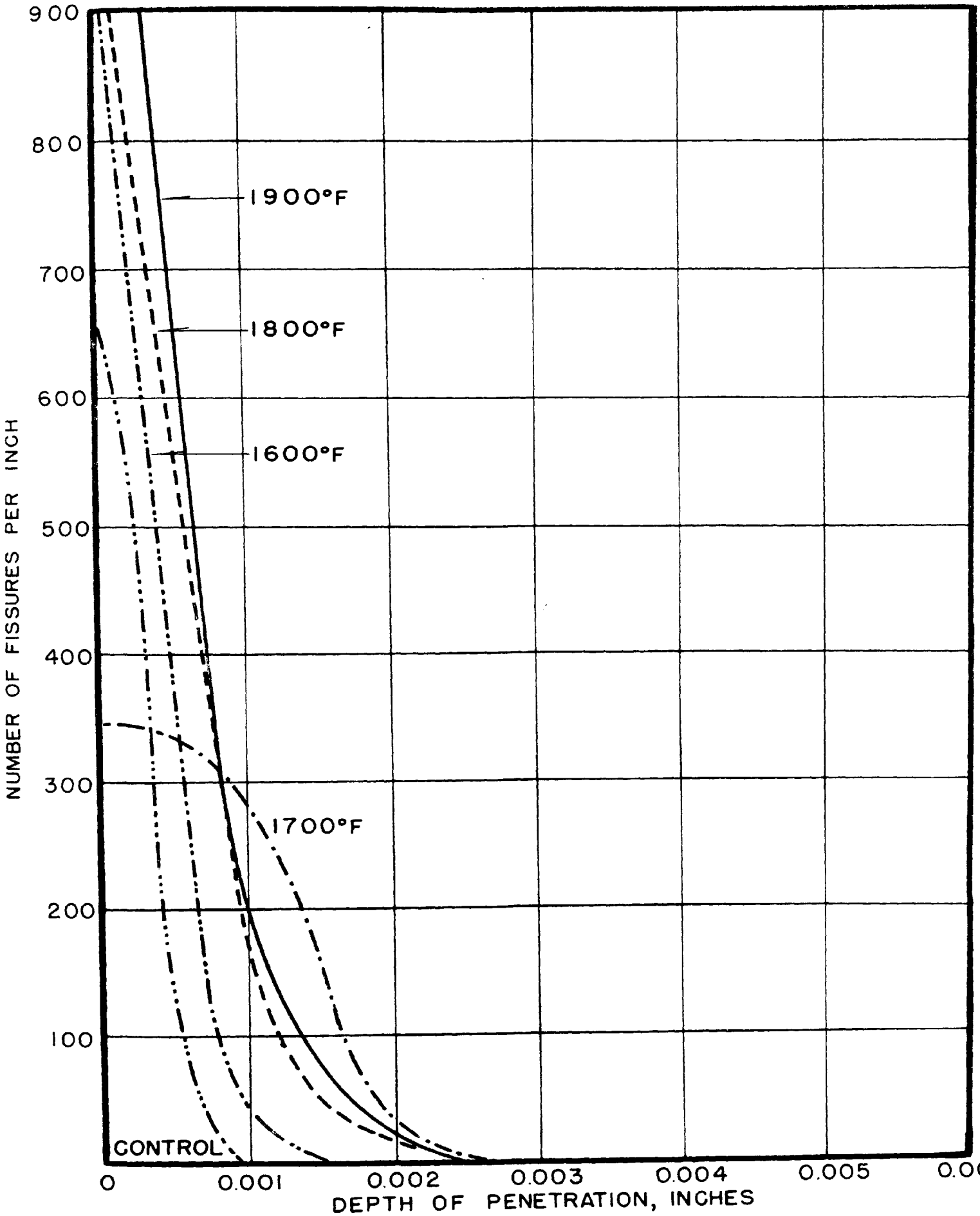

FIG. 49-PENETRATION VS. DEPTH BELOW SURFACE.
TYPE 310 ALLOY, HEAT 64270. RUN 15.

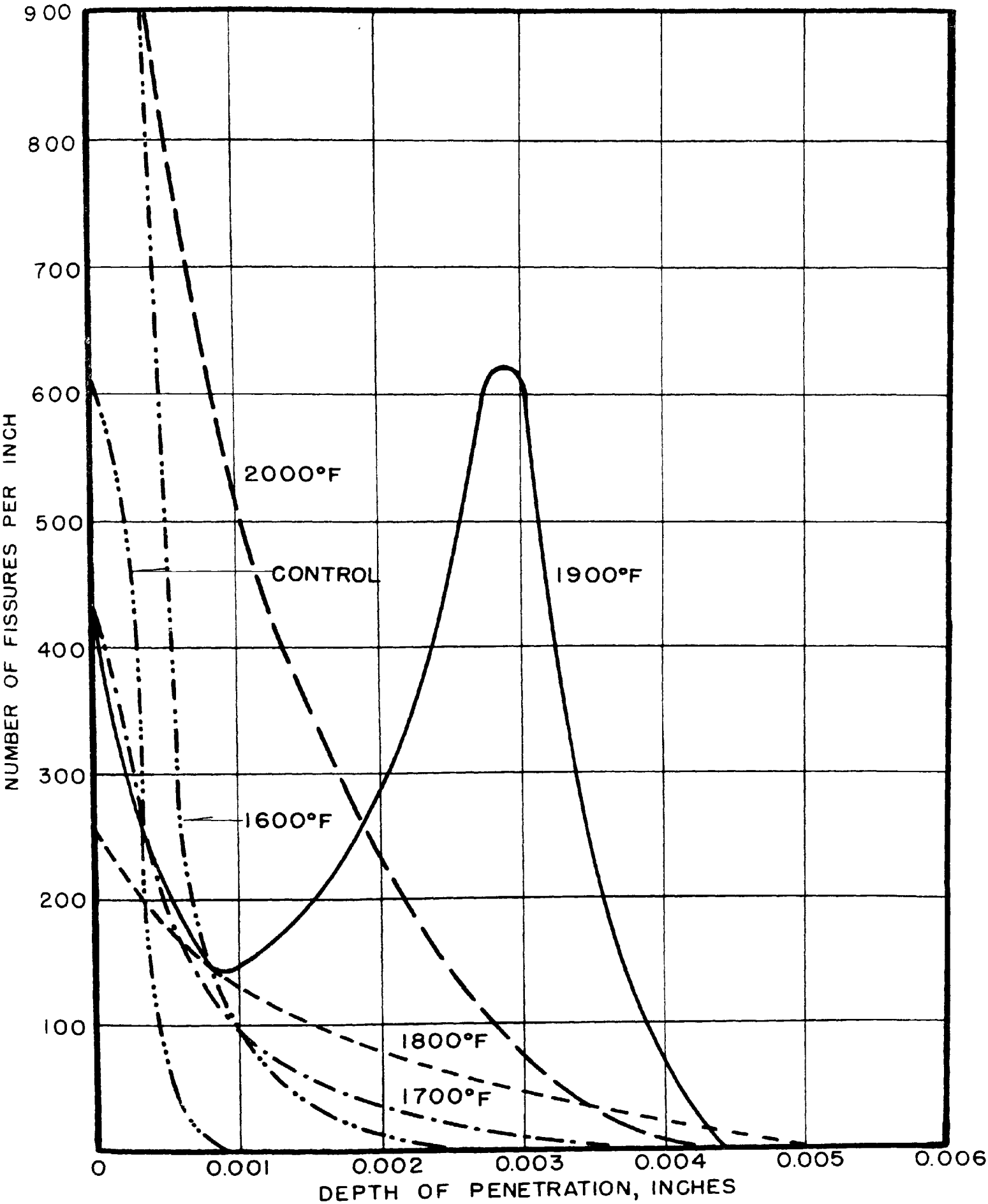

FIG.50- PENETRATION VS. DEPTH BELOW SURFACE.
TYPE 310 ALLOY, HEAT X11306. RUNS 16 & 28.

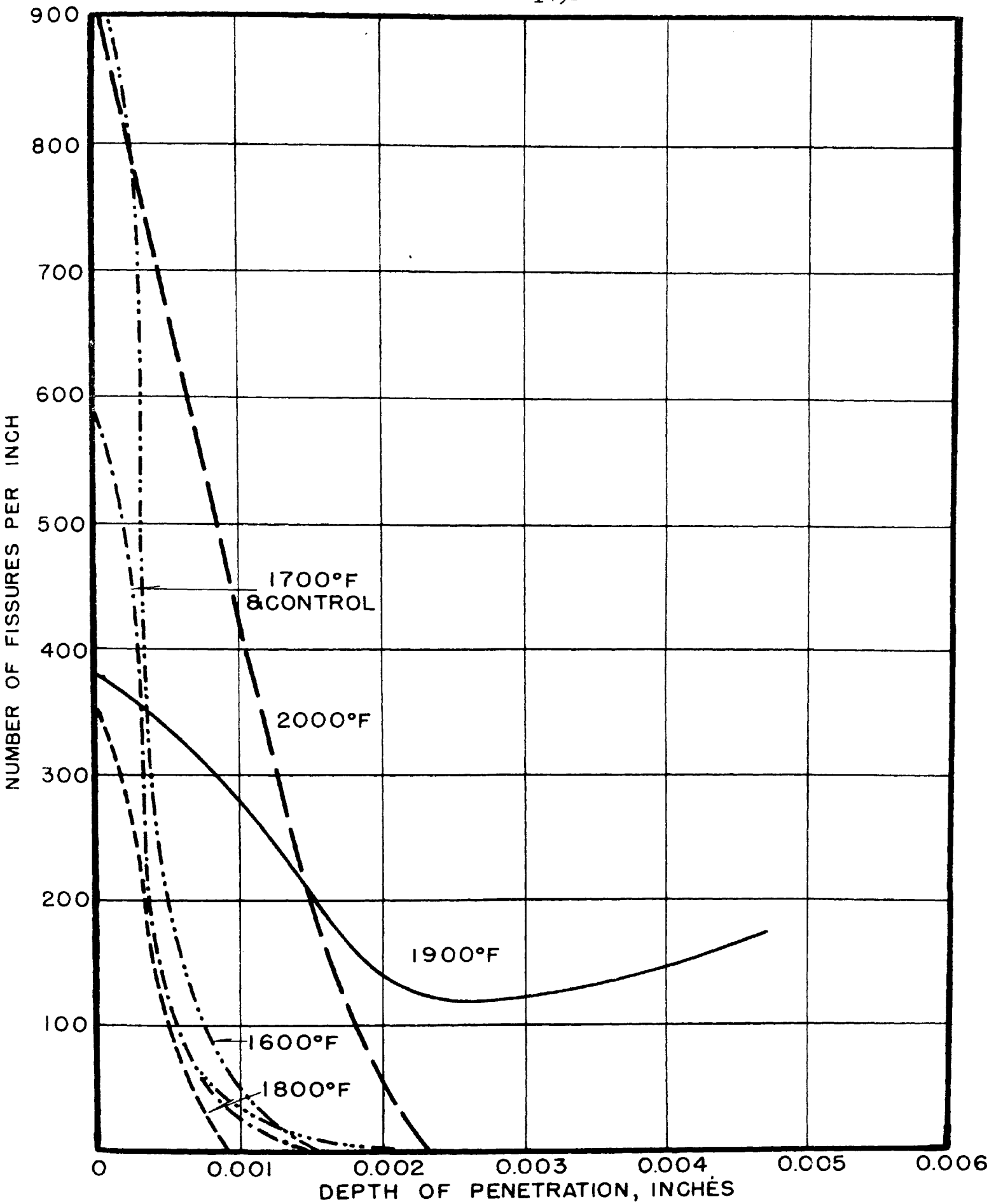

FIG. 51 - PENETRATION VS. DEPTH BELOW SURFACE.
TYPE 310 ALLOY, HEAT X11338. RUNS 16 & 28.

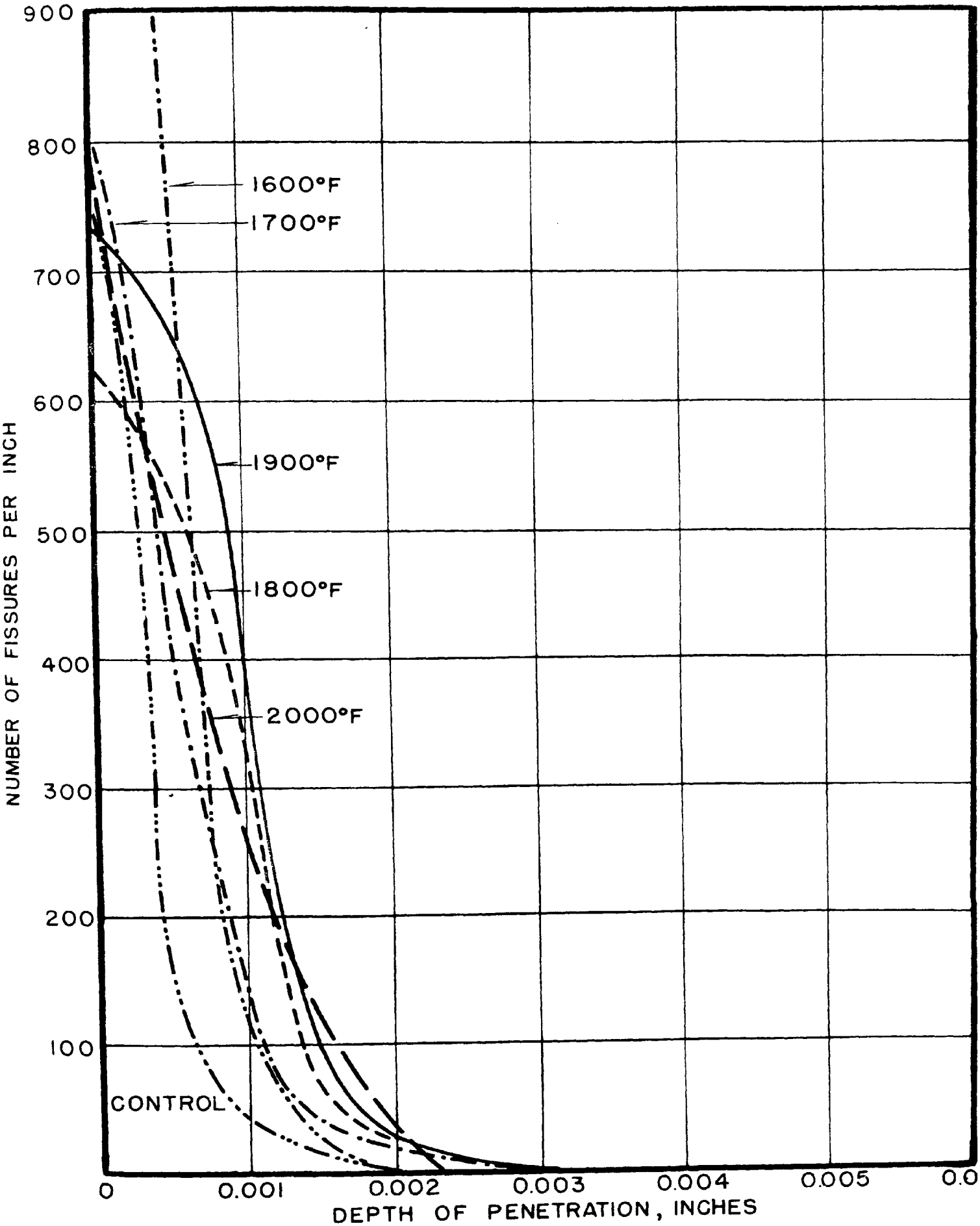

FIG. 52 - PENETRATION VS. DEPTH BELOW SURFACE.
TYPE 310 ALLOY, HEAT X27258. RUNS 16 & 28.

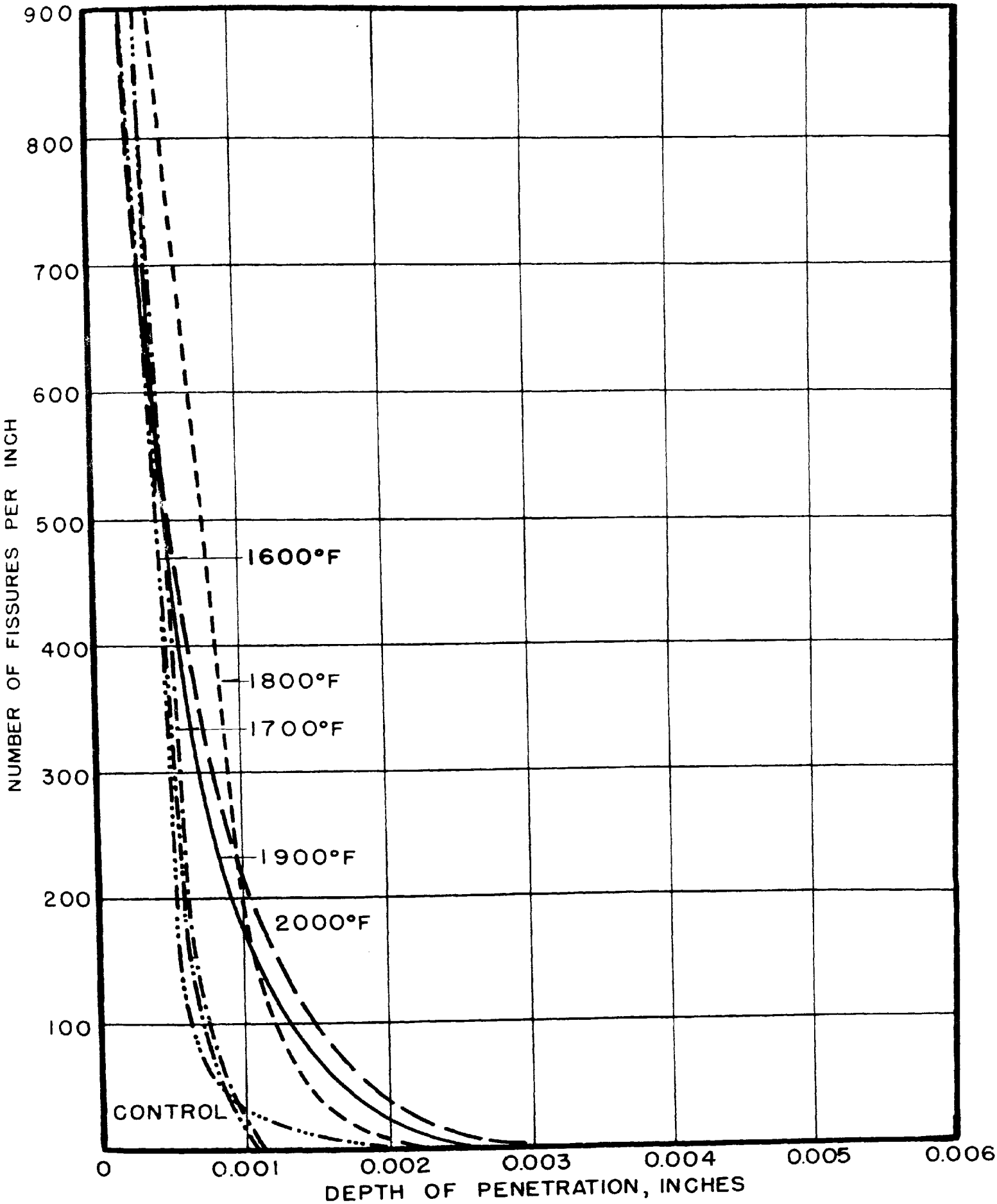

FIG.53 - PENETRATION VS. DEPTH BELOW SURFACE.
TYPE 310 ALLOY, HEAT X45558. RUNS 17 & 28.

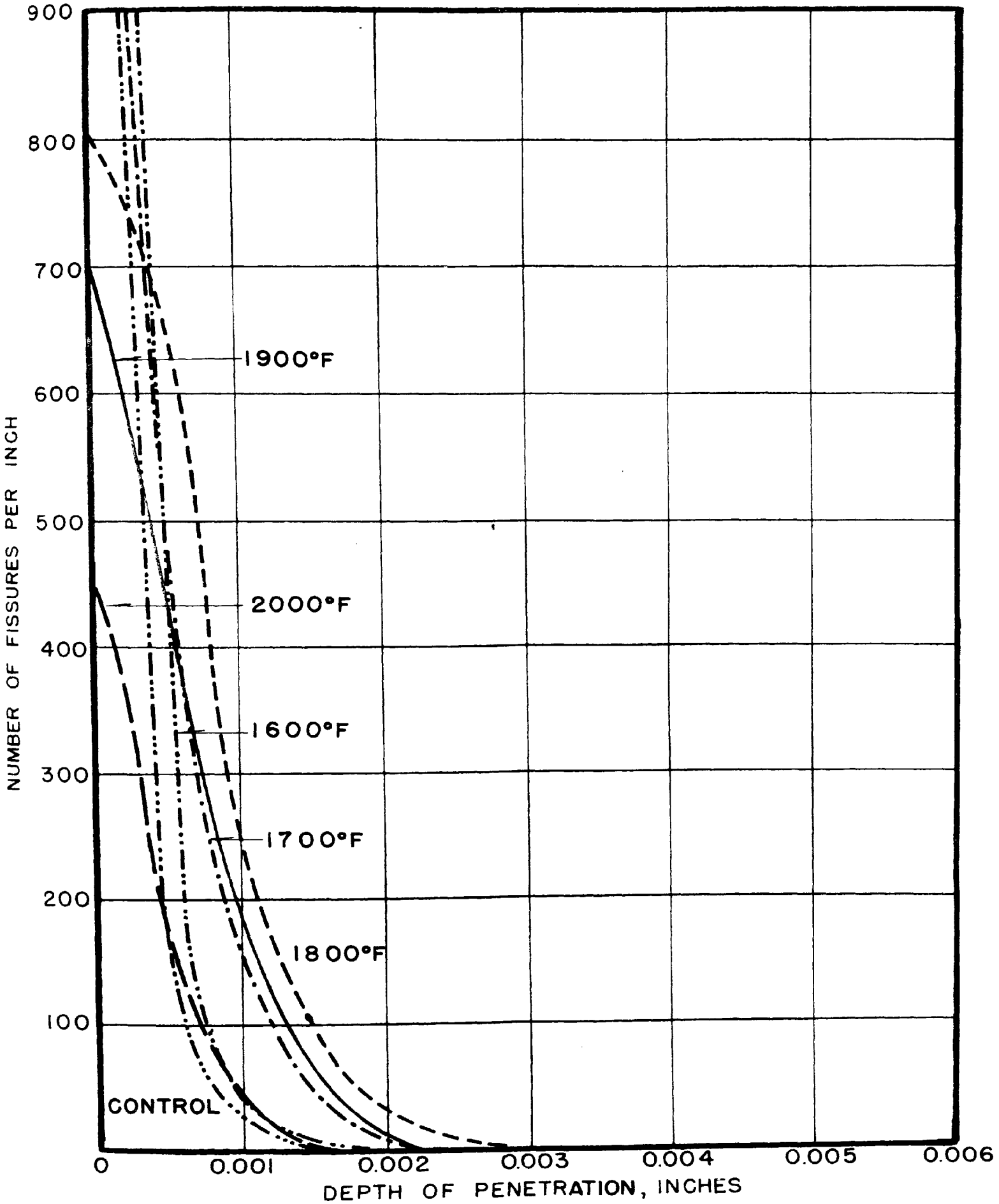

FIG. 54 - PENETRATION VS. DEPTH BELOW SURFACE.
TYPE 310 ALLOY, HEAT X46063. RUNS 17 & 28.

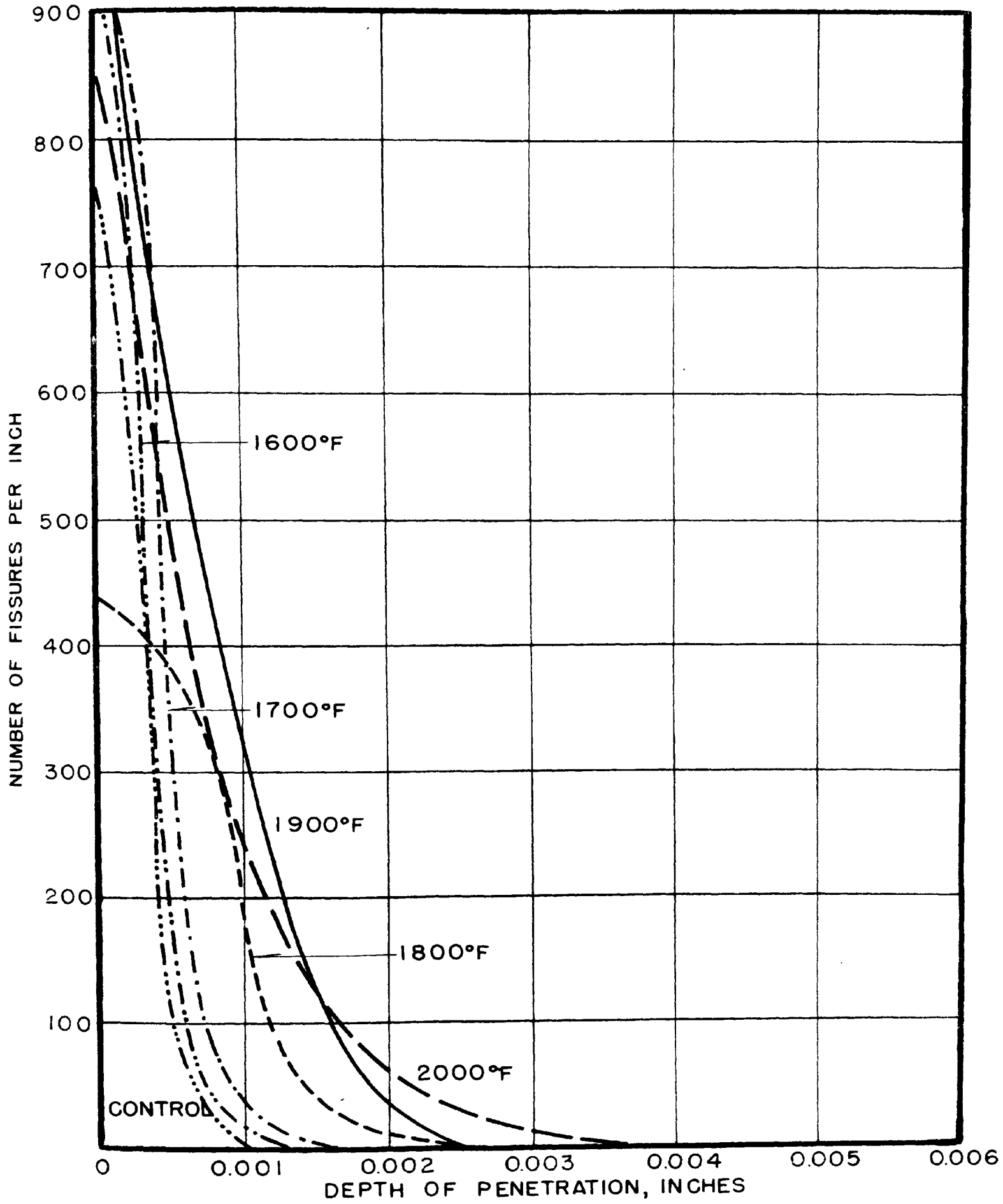

FIG. 55 - PENETRATION VS. DEPTH BELOW SURFACE.
TYPE 310 ALLOY, HEAT X46572. RUNS 17 & 28.

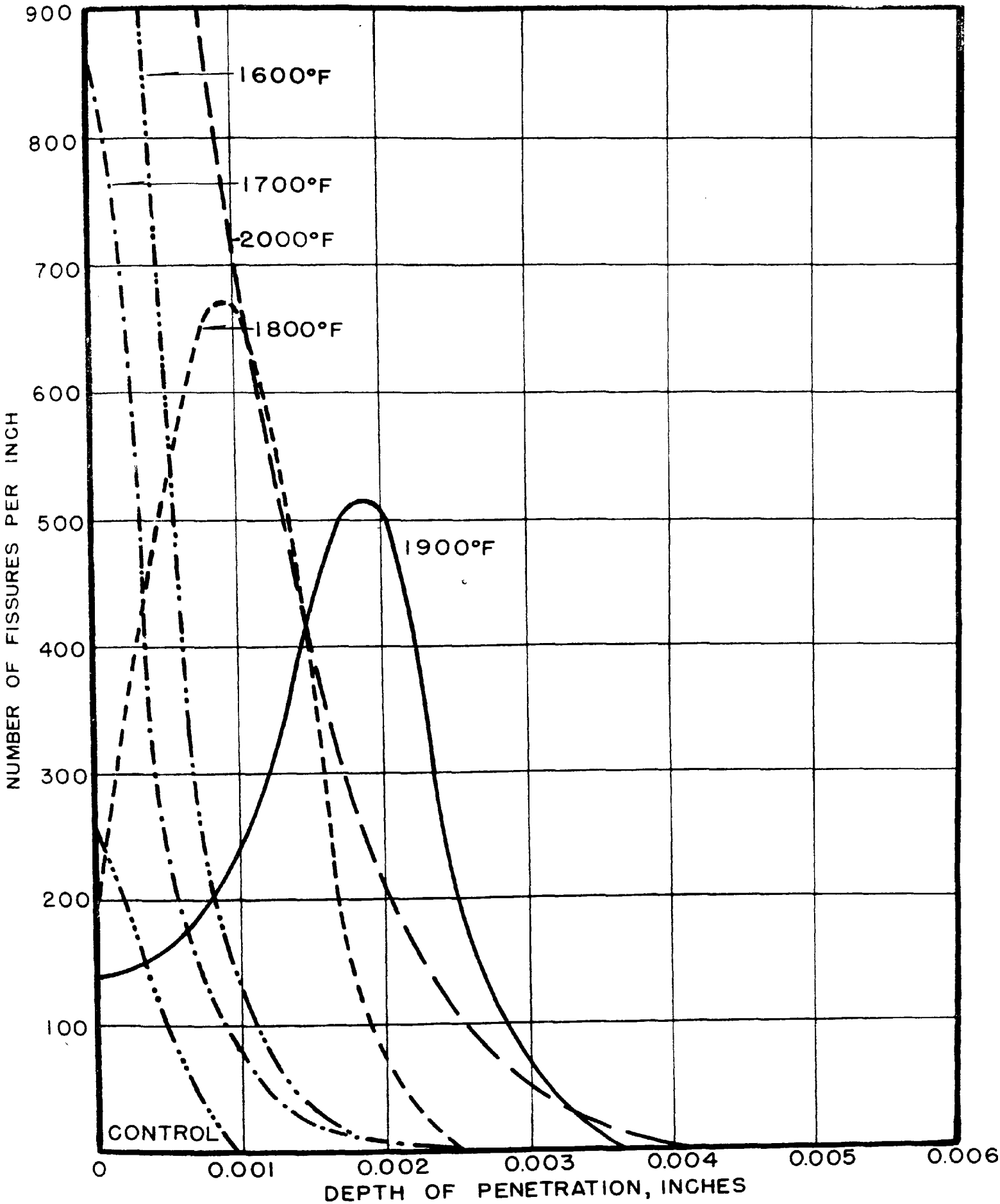

FIG. 56- PENETRATION VS. DEPTH BELOW SURFACE.
TYPE 310 ALLOY, HEAT X11306. RUNS 21 & 27.

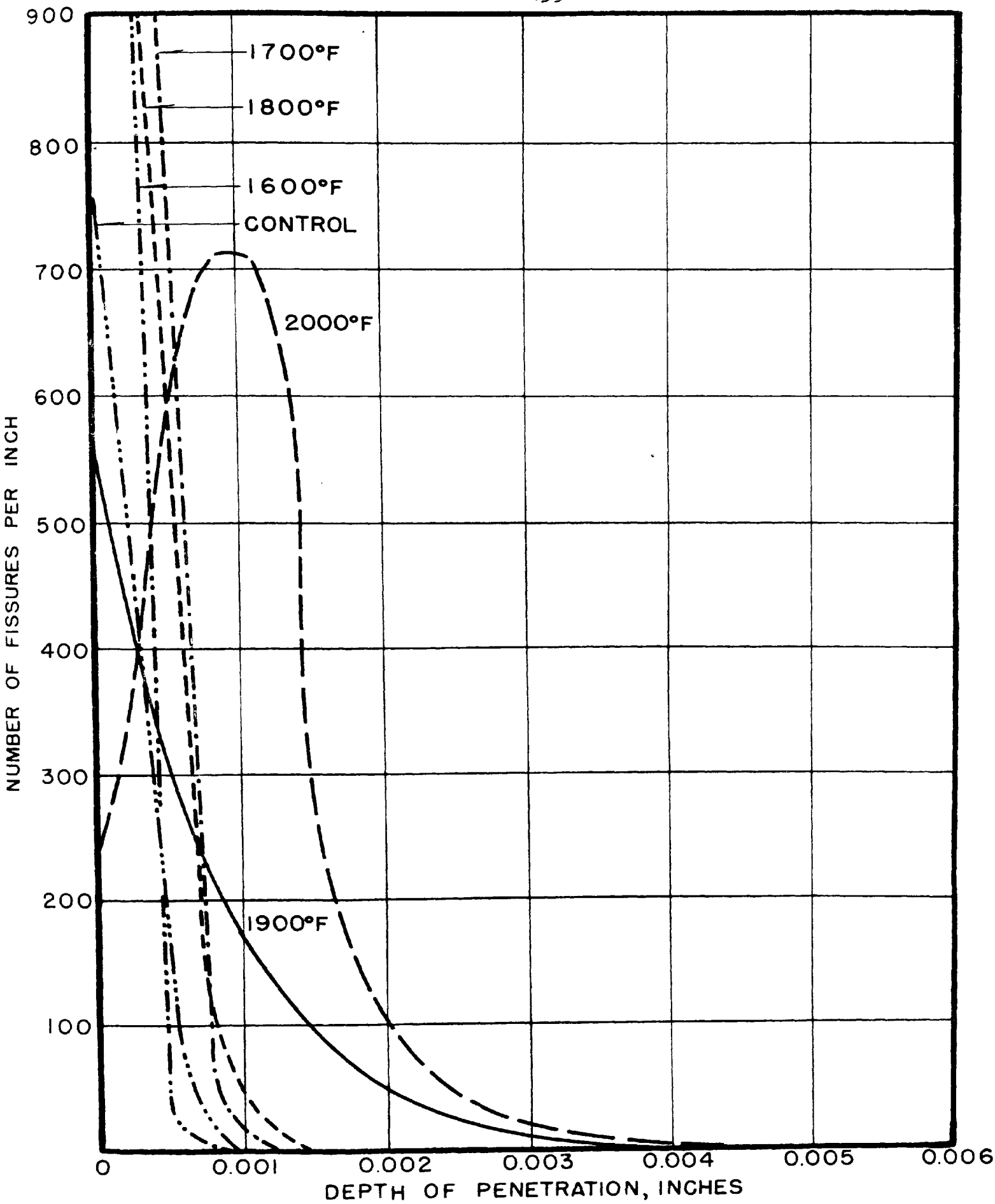

FIG. 57- PENETRATION VS. DEPTH BELOW SURFACE.
TYPE 310 ALLOY, HEAT X11338. RUNS 21 & 27.

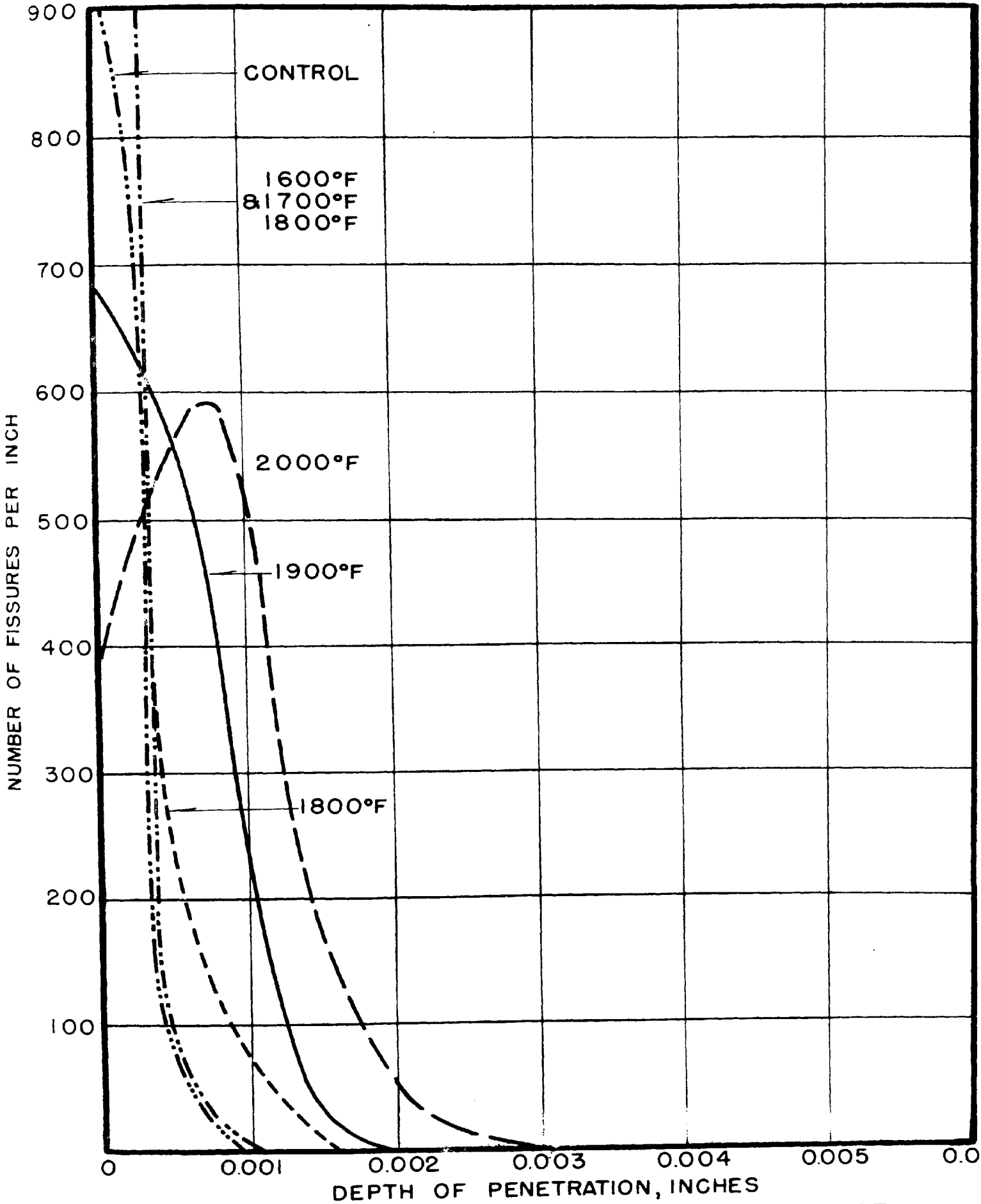

FIG. 58- PENETRATION VS. DEPTH BELOW SURFACE.
TYPE 310 ALLOY, HEAT X27258. RUNS 21 & 27.

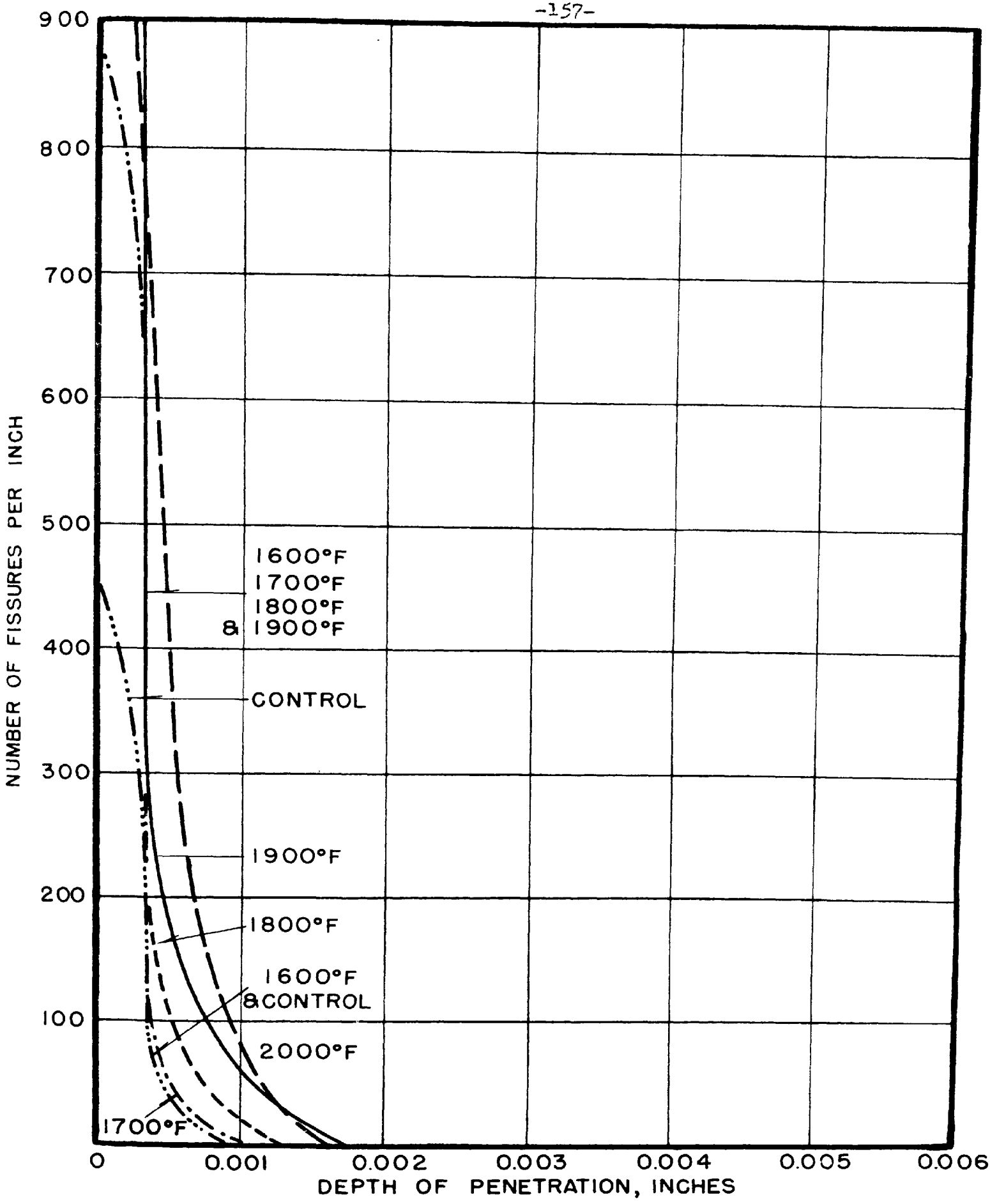

FIG. 59 - PENETRATION VS. DEPTH BELOW SURFACE.
TYPE 310 ALLOY, HEAT X 45558. RUNS 22 & 26.

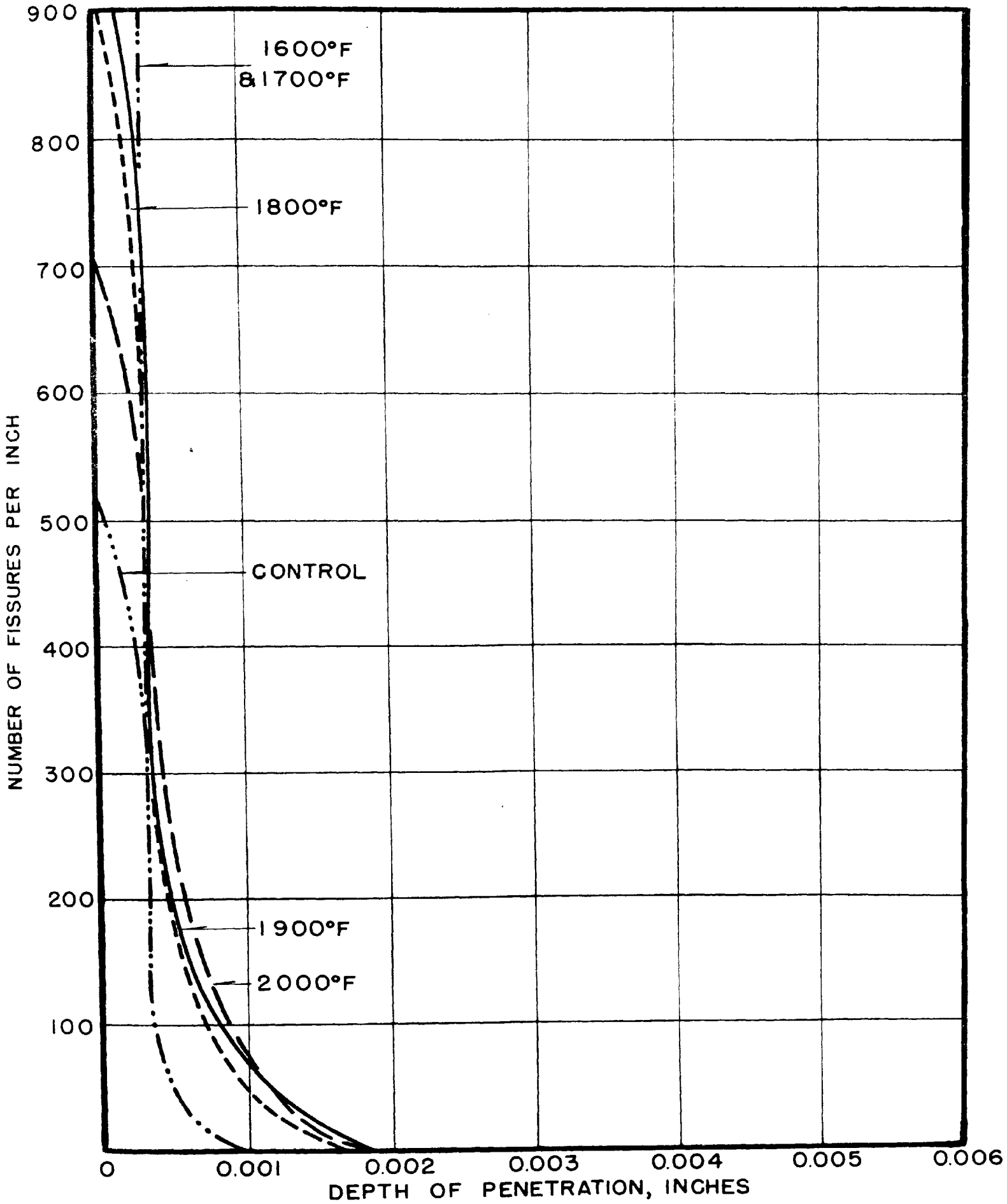

FIG. 60-PENETRATION VS. DEPTH BELOW SURFACE.
TYPE 310 ALLOY, HEAT X46063. RUNS 22 & 26.

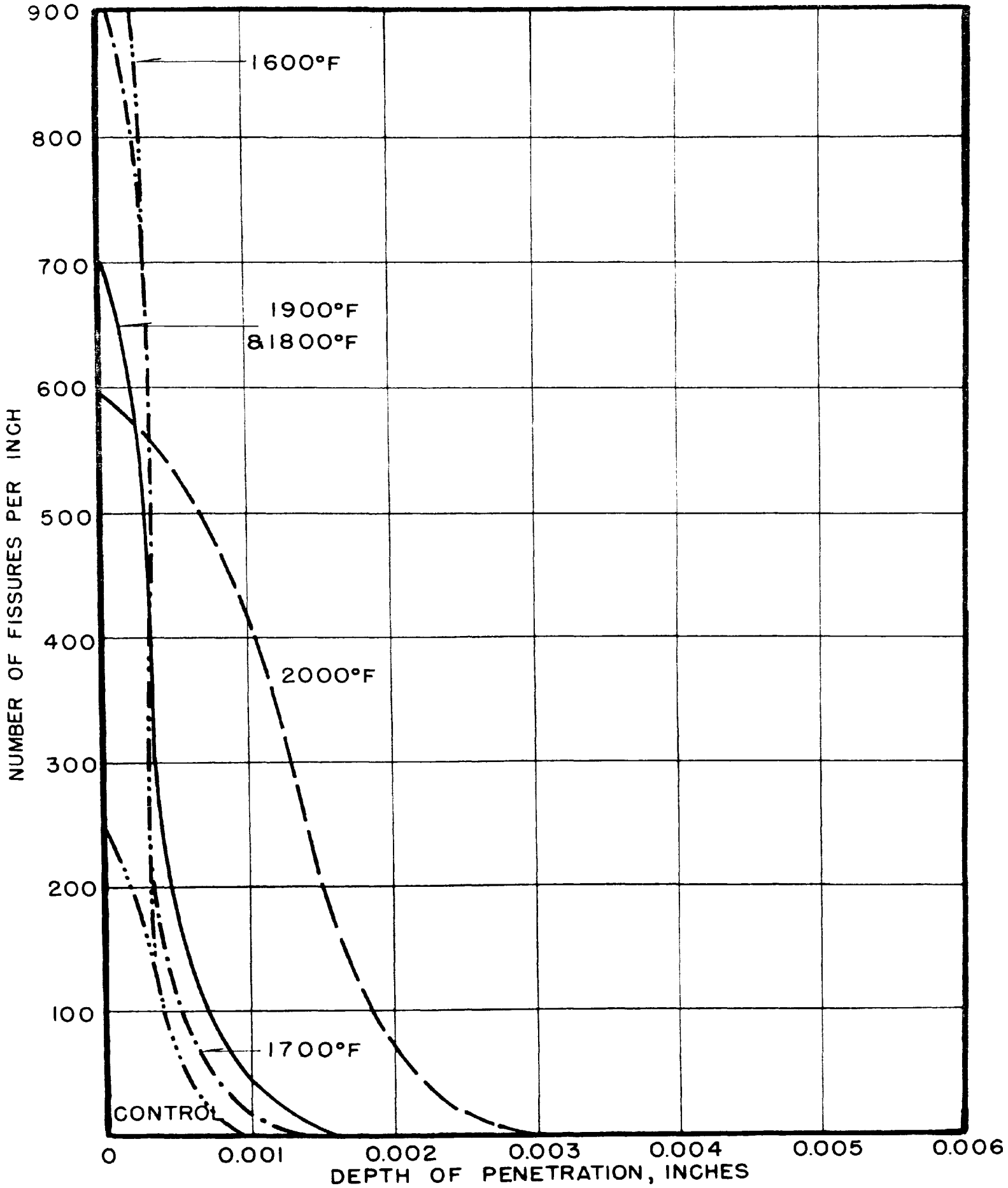

FIG. 61 – PENETRATION VS. DEPTH BELOW SURFACE.
TYPE 310 ALLOY, HEAT X46572. RUNS 22 & 26.

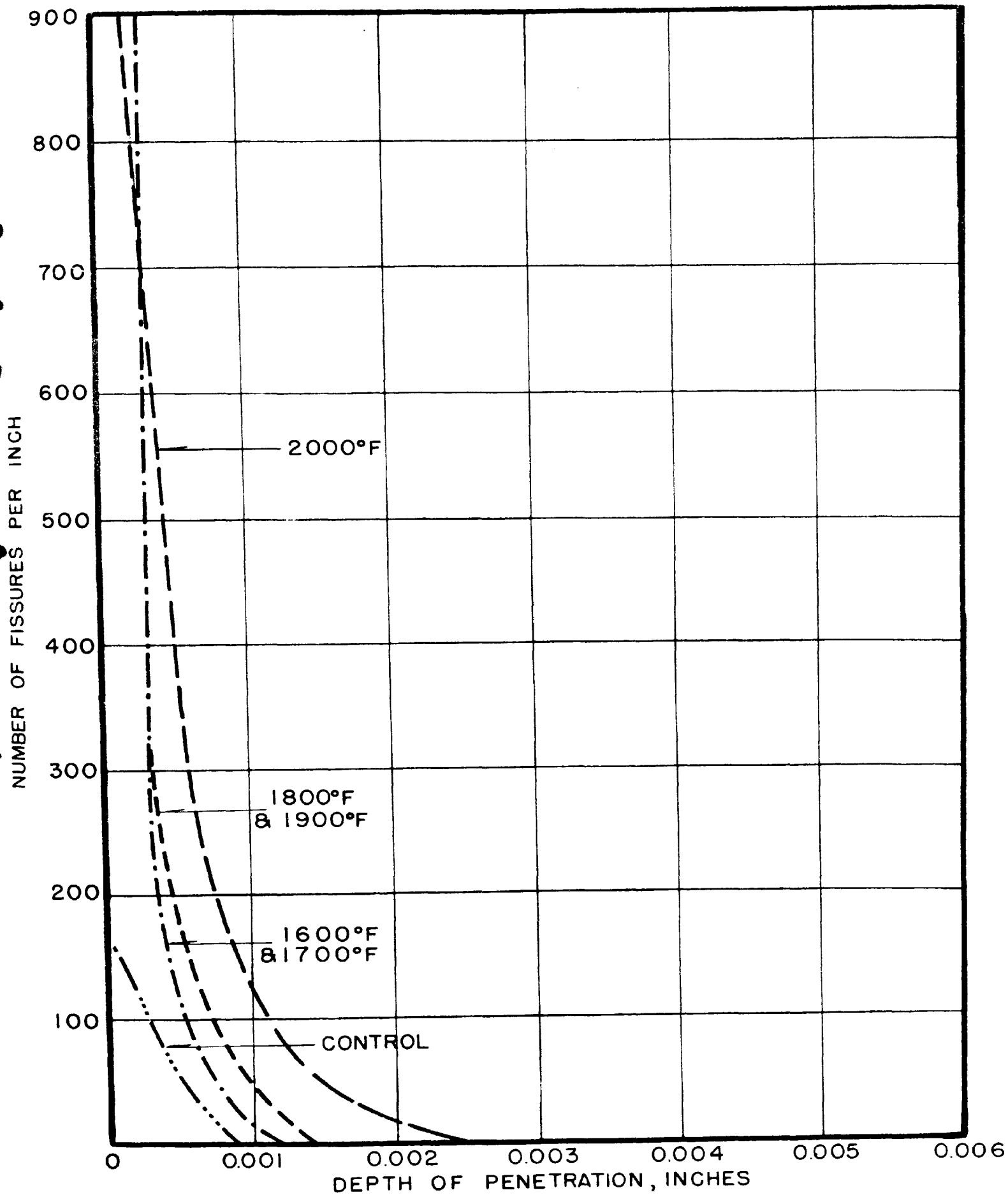

FIG. 62- PENETRATION VS. DEPTH BELOW SURFACE.
TYPE 310 ALLOY, HEAT X 45558. RUNS 23 & 27.

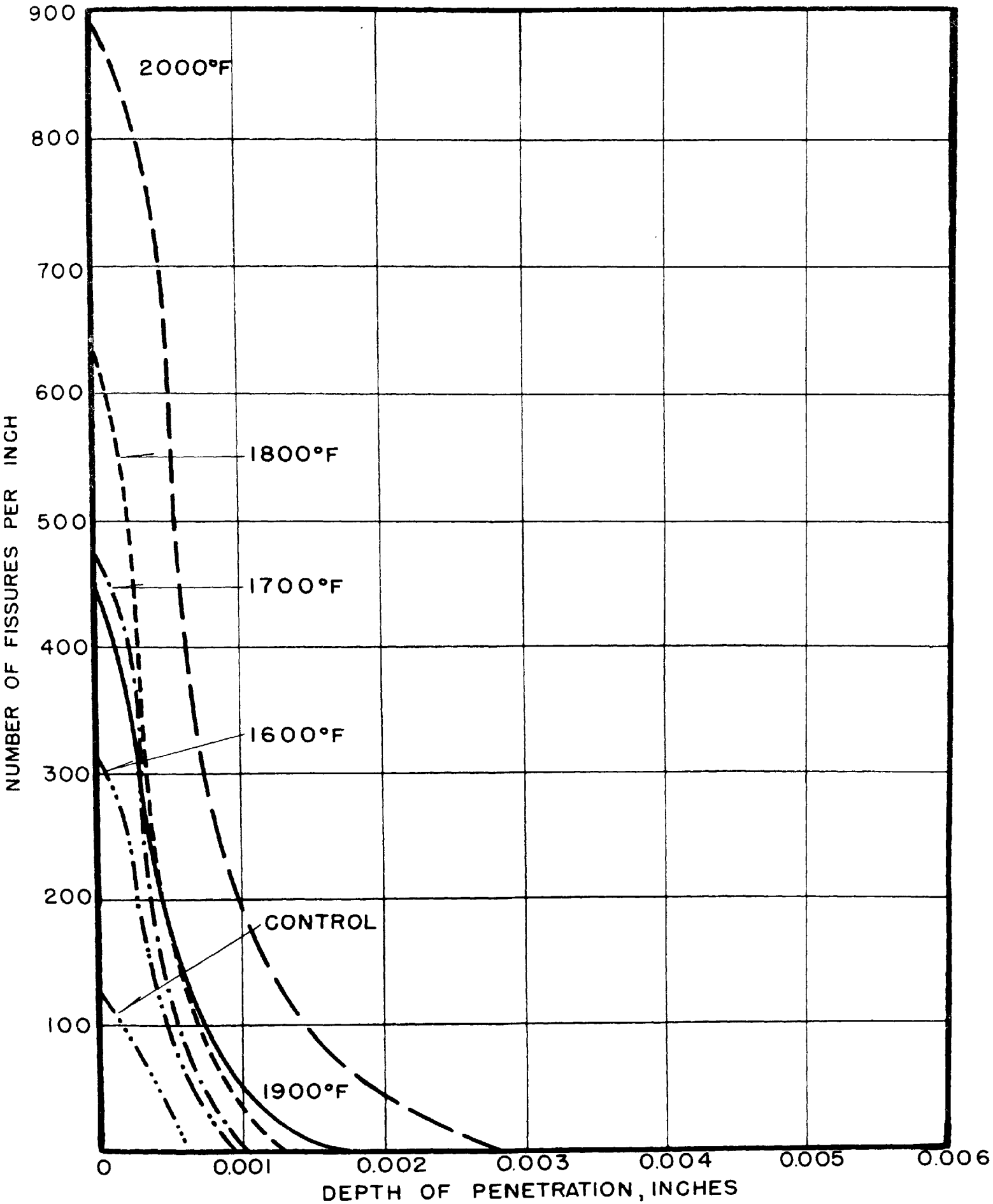

FIG. 63 - PENETRATION VS. DEPTH BELOW SURFACE.
TYPE 310 ALLOY, HEAT X46063. RUNS 23 & 27.

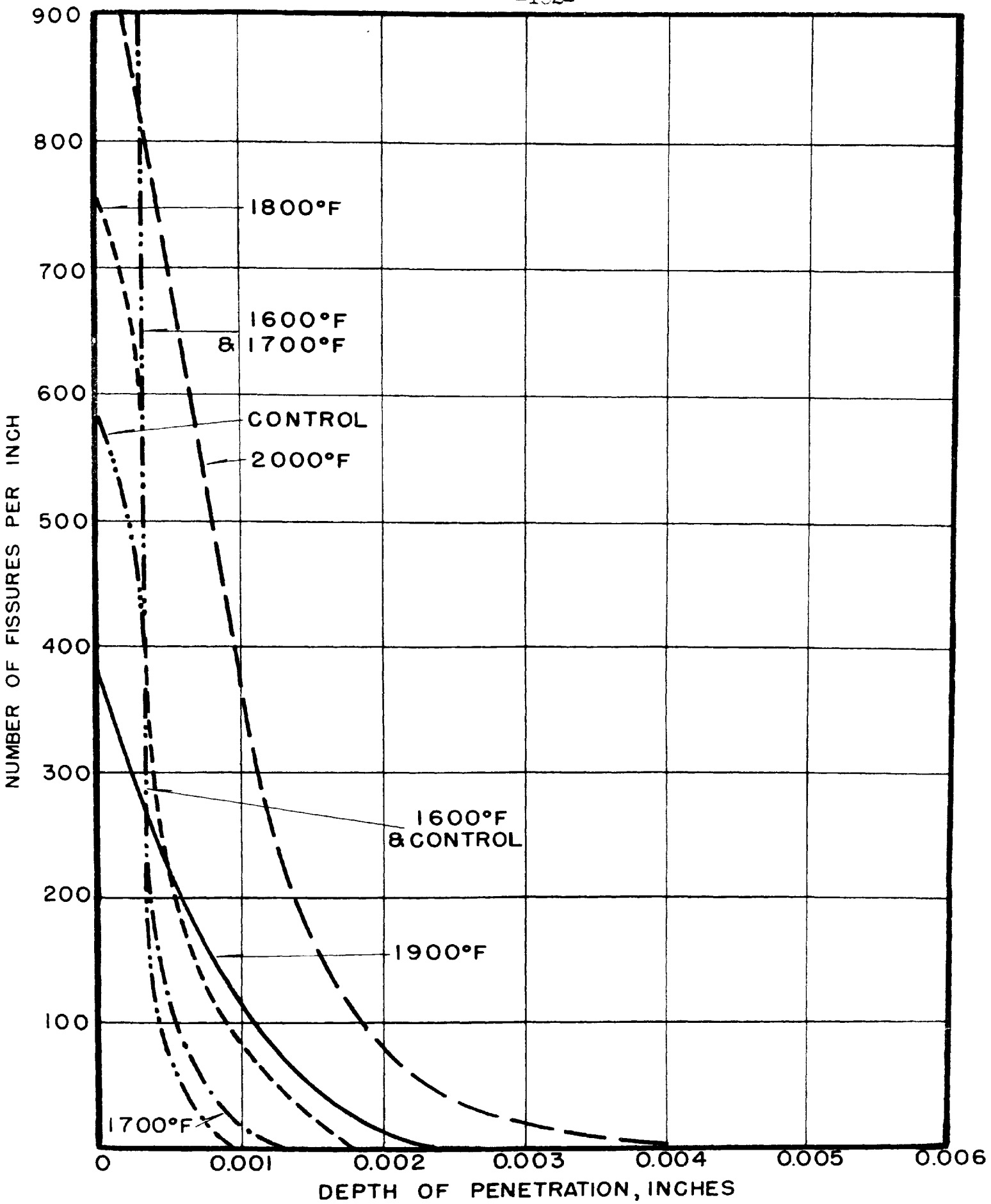

FIG. 64 - PENETRATION VS. DEPTH BELOW SURFACE.
TYPE 310 ALLOY, HEAT X46572. RUNS 23 & 27.

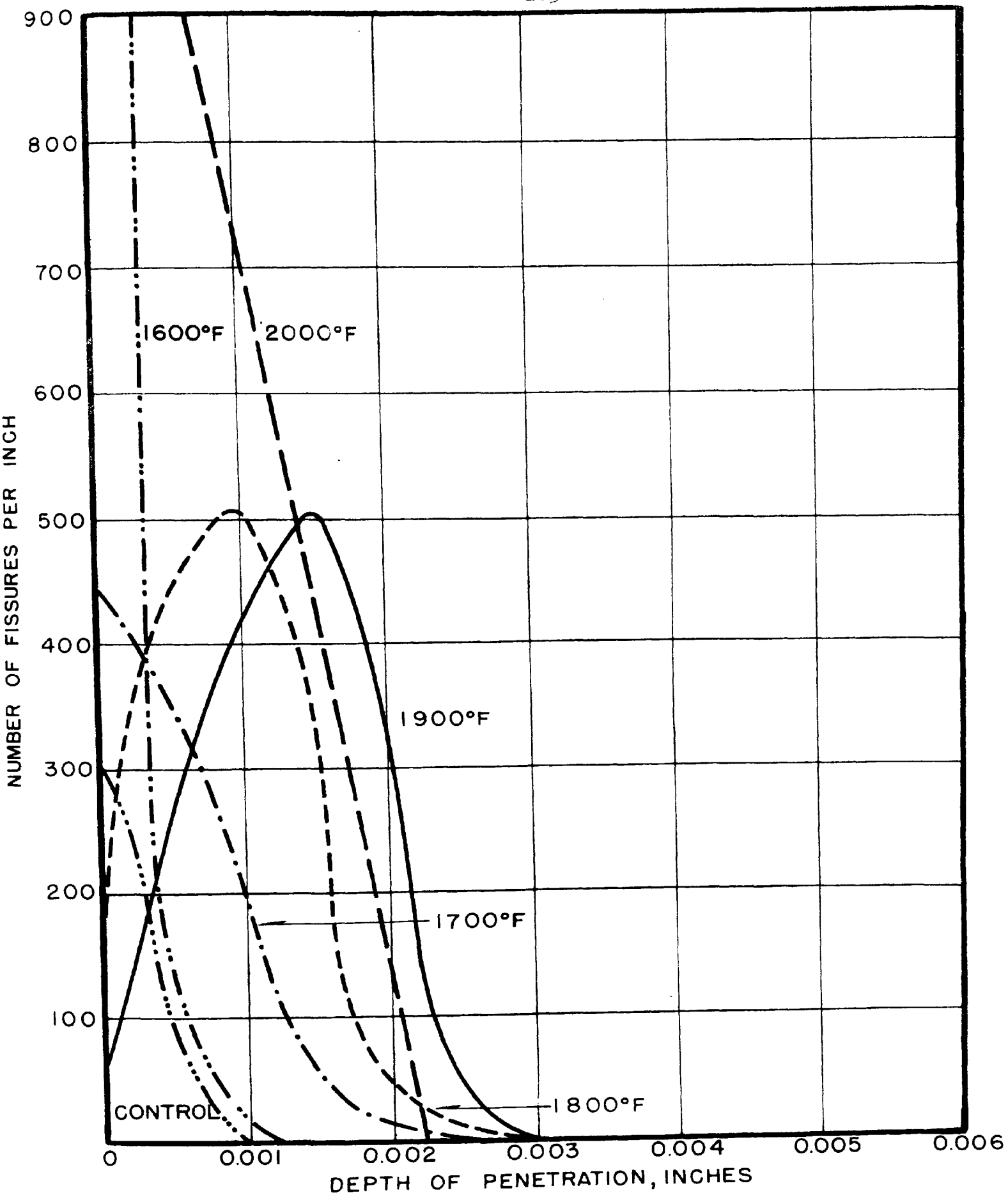

FIG. 65 - PENETRATION VS. DEPTH BELOW SURFACE.
TYPE 310 ALLOY; HEAT X 11306. RUNS 24 & 26.

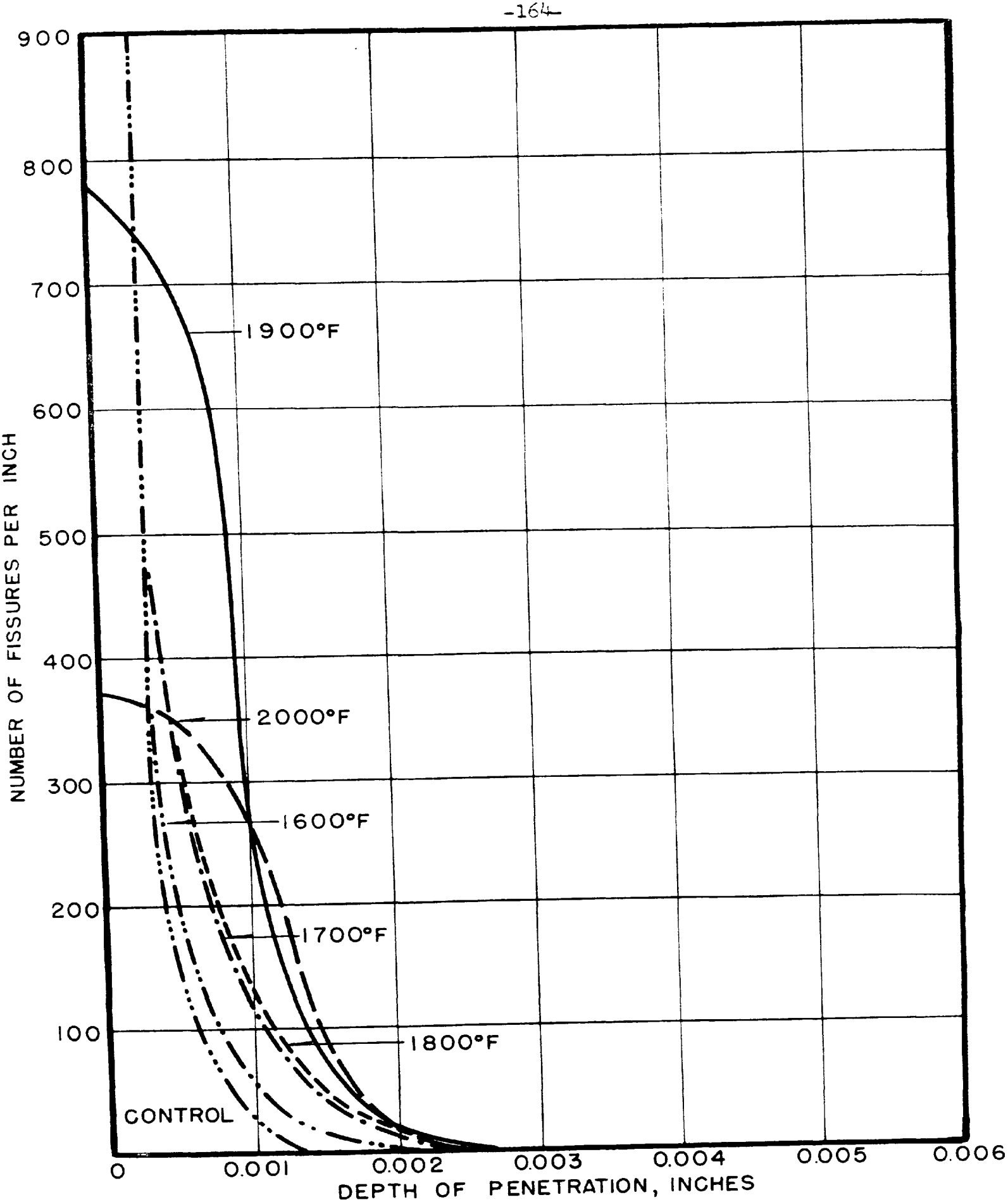

FIG. 66-PENETRATION VS. DEPTH BELOW SURFACE.
TYPE 310 ALLOY, HEAT X11338. RUNS 24 & 26.

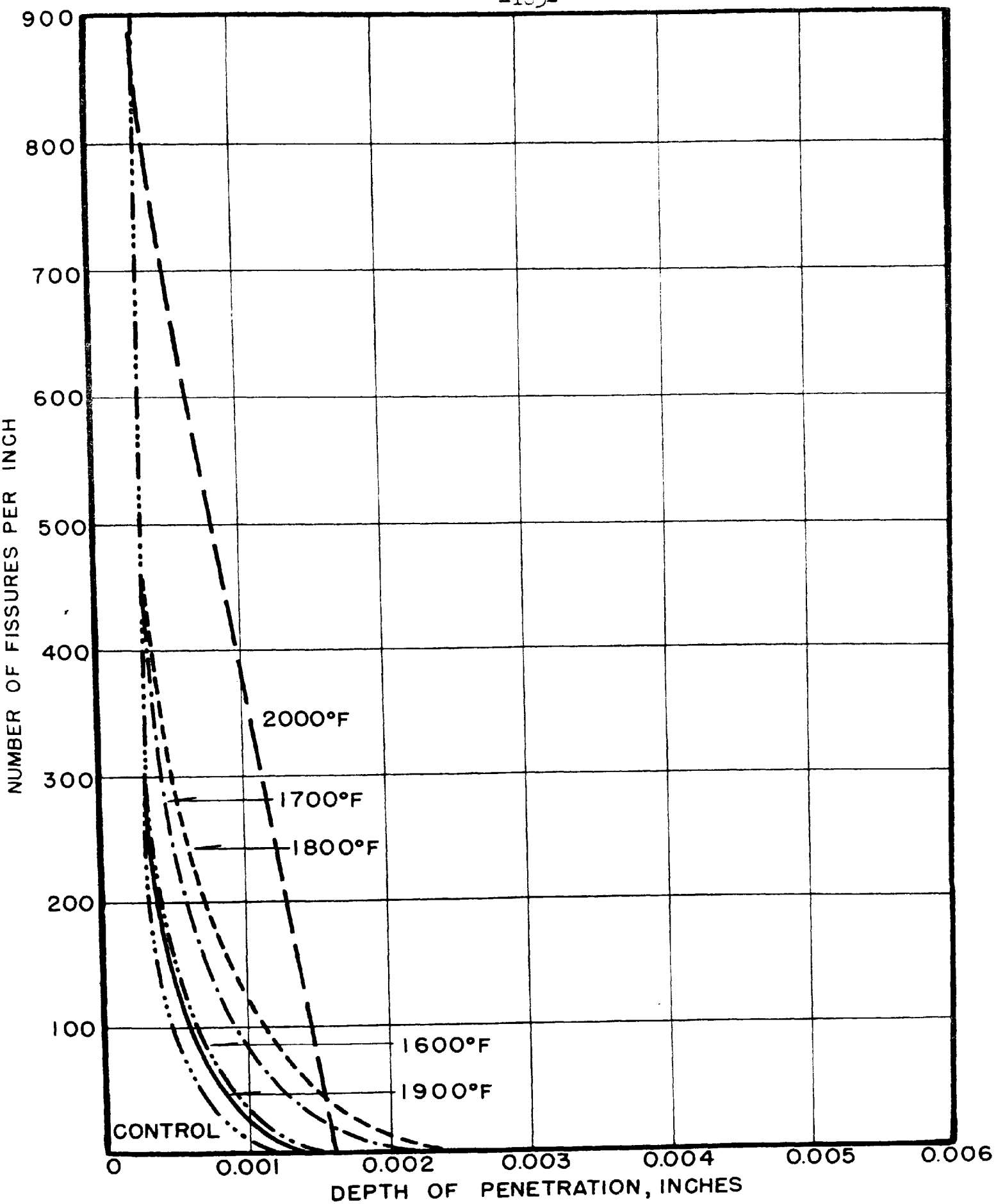

FIG. 67- PENETRATION VS. DEPTH BELOW SURFACE.
TYPE 310 ALLOY, HEAT X 27258. RUNS 24 & 26.

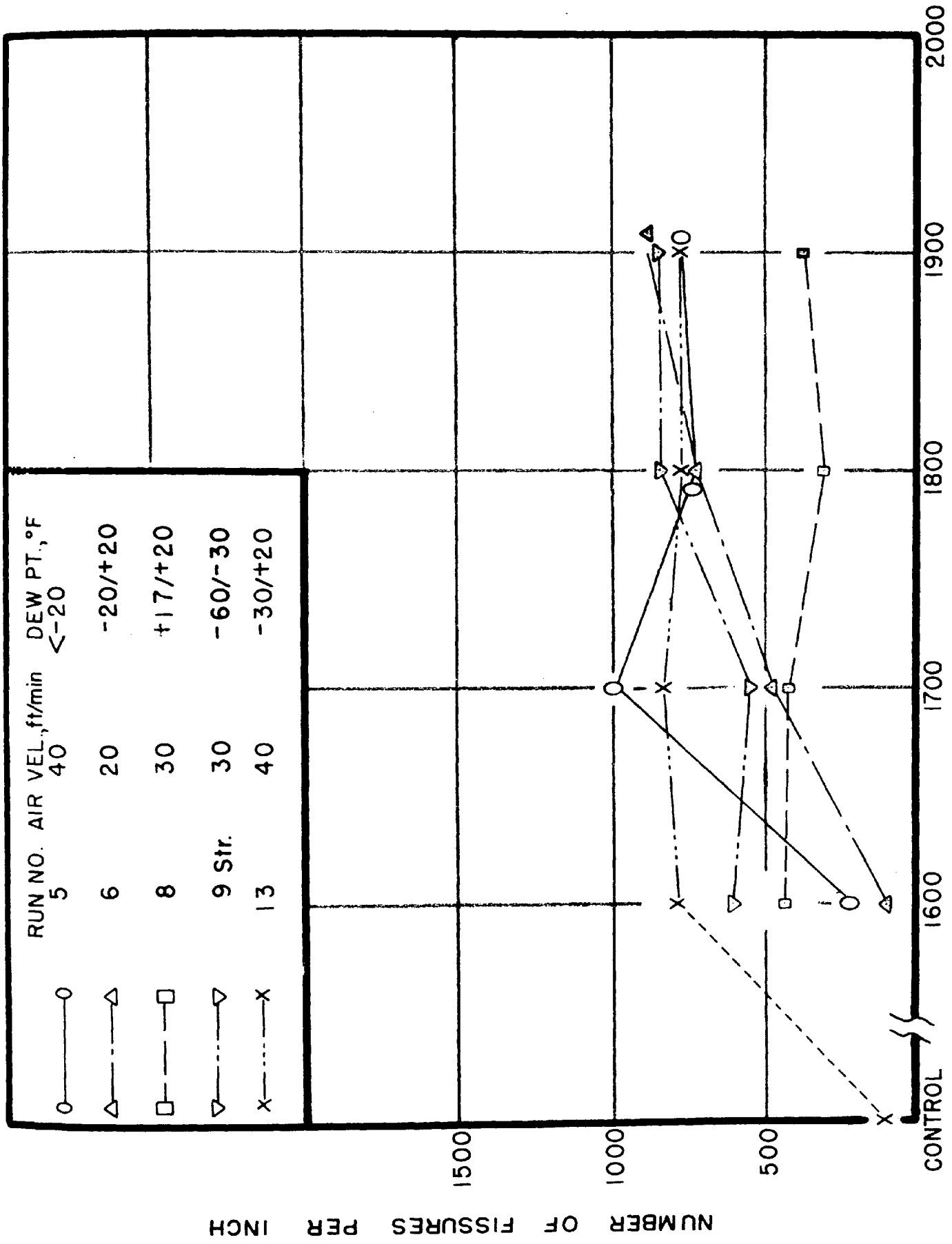

FIG.68-SUMMARY PENETRATION FREQUENCY CURVES.
TYPE 309+Nb ALLOY. 100 HOURS DURATION.
EFFECT OF AIR VELOCITY AND HUMIDITY.

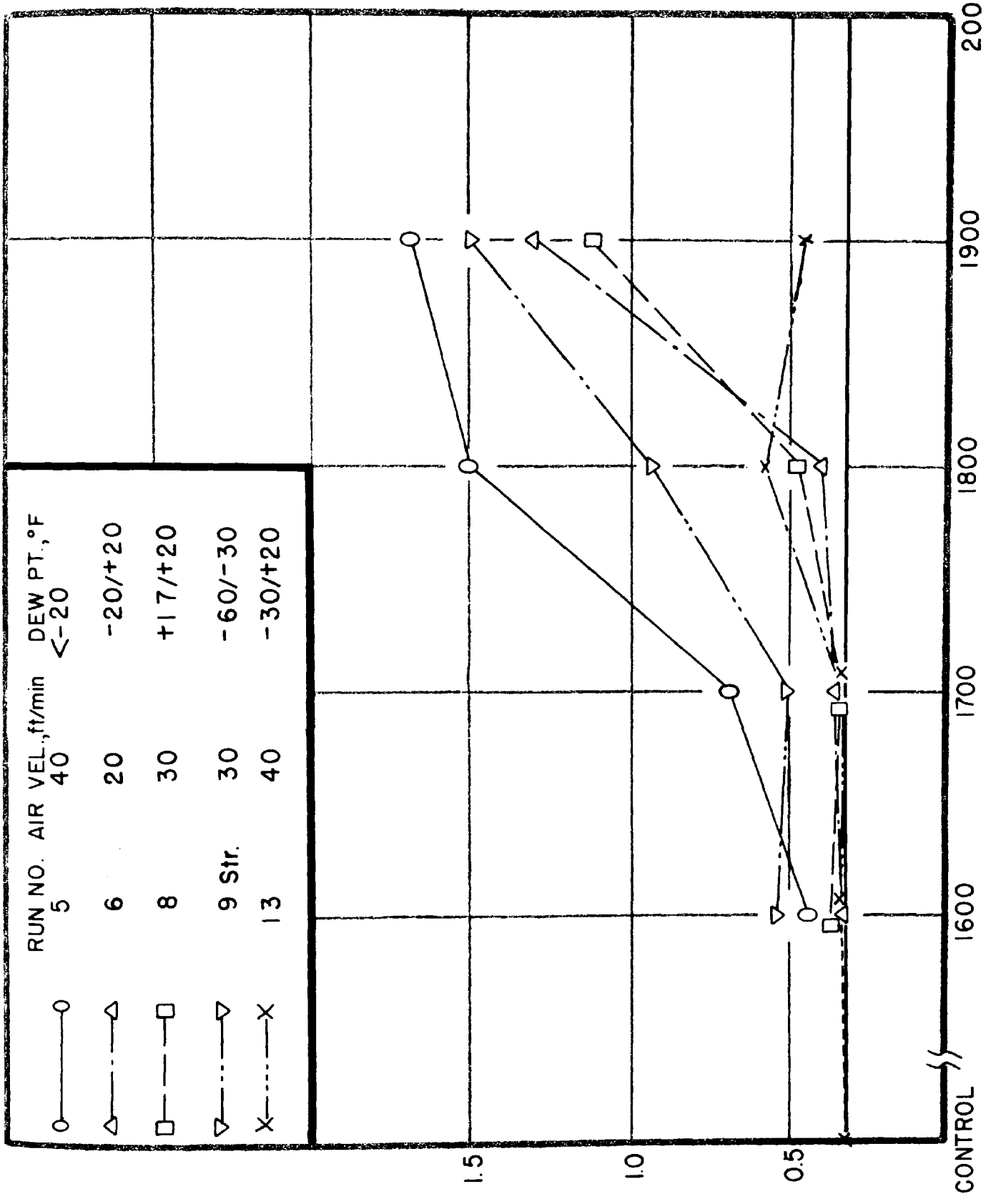

FIG.69-SUMMARY PENETRATION DEPTH CURVES.
TYPE 309+Nb ALLOY. 100 HOURS DURATION.
EFFECT OF AIR VELOCITY AND HUMIDITY.

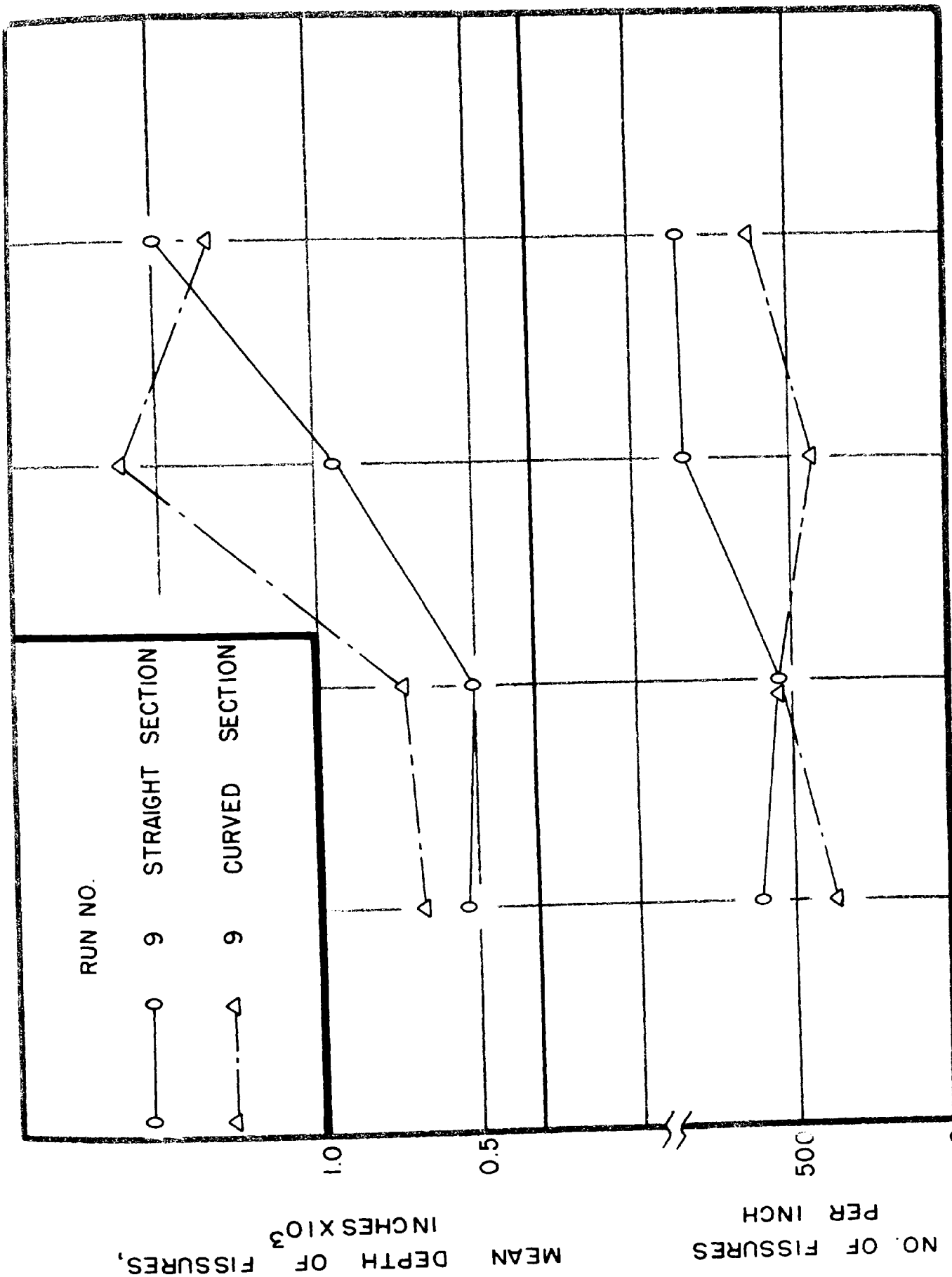

FIG. 70-SUMMARY PENETRATION FREQUENCY AND DEPTH CURVES. TYPE 309 + Nb ALLOY. EFFECT OF COLD WORK. 100 HOURS DURATION.

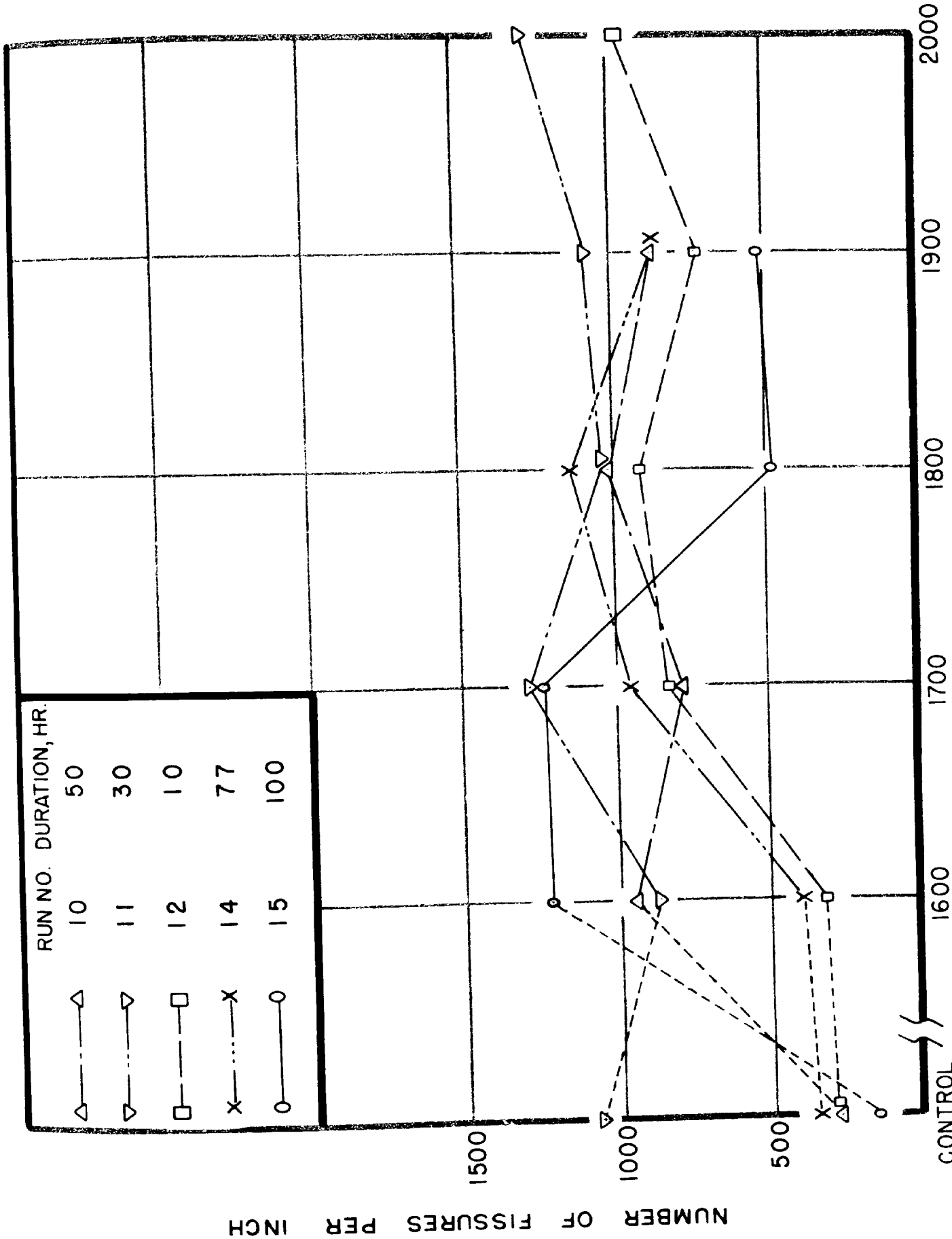

FIG. 71 – SUMMARY PENETRATION FREQUENCY CURVES.
TYPE 309+Nb ALLOY. EFFECT OF TIME.

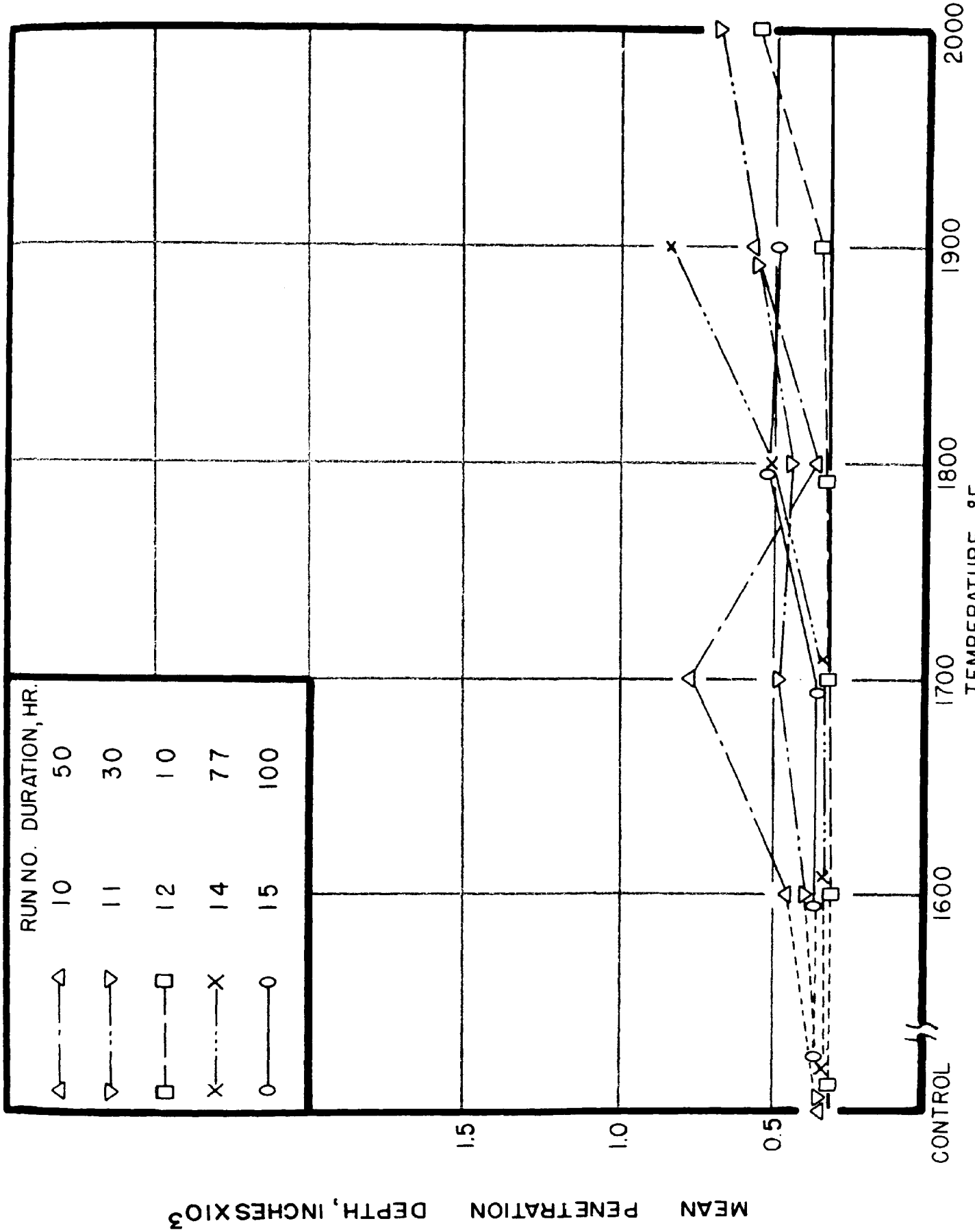

FIG. 72—SUMMARY PENETRATION DEPTH CURVES. TYPE 309+Nb ALLOY. EFFECT OF TIME.

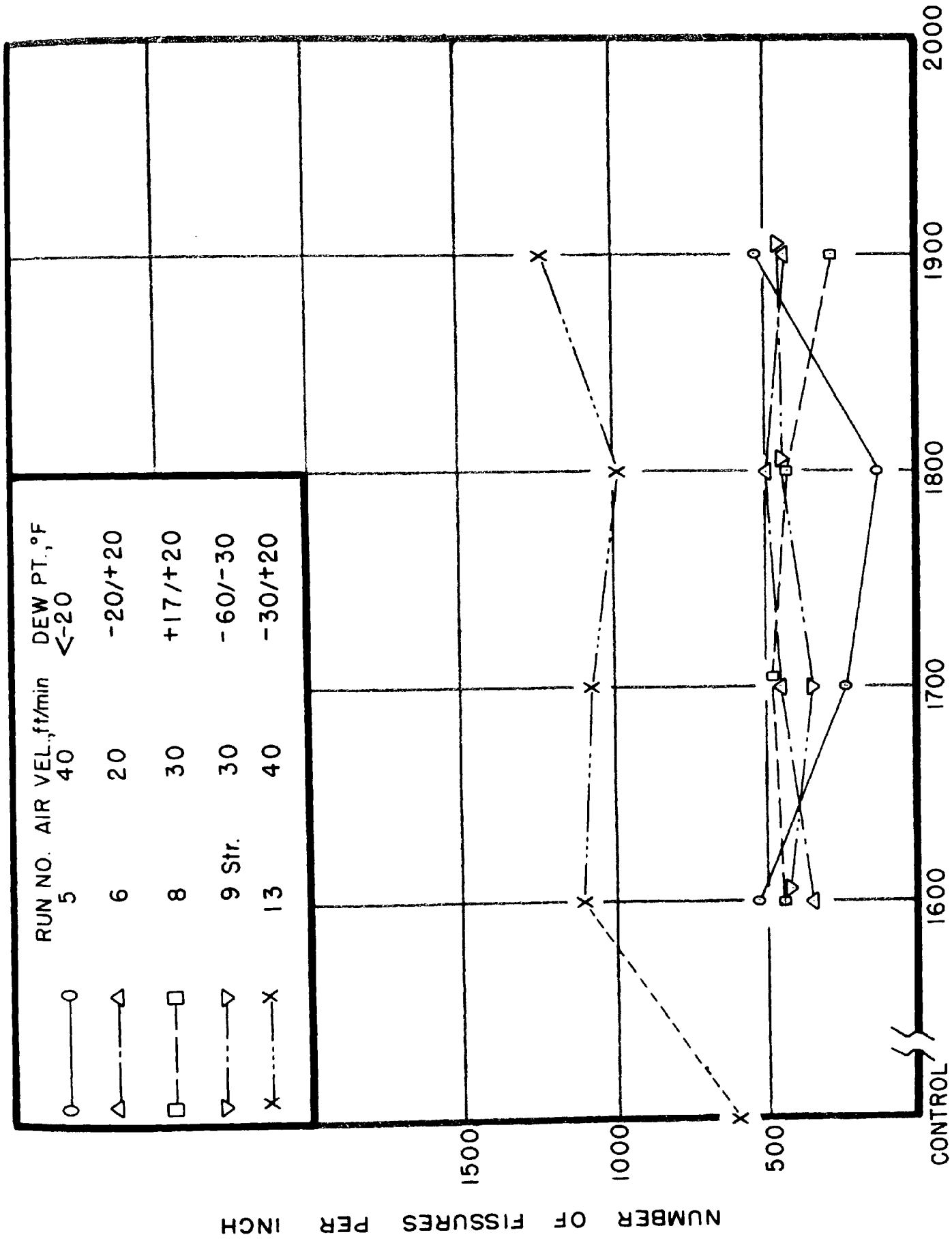

FIG. 73-SUMMARY PENETRATION FREQUENCY CURVES.
TYPE 310 ALLOY, HEAT 64177. 100 HOURS DURATION.
EFFECT OF AIR VELOCITY AND HUMIDITY.

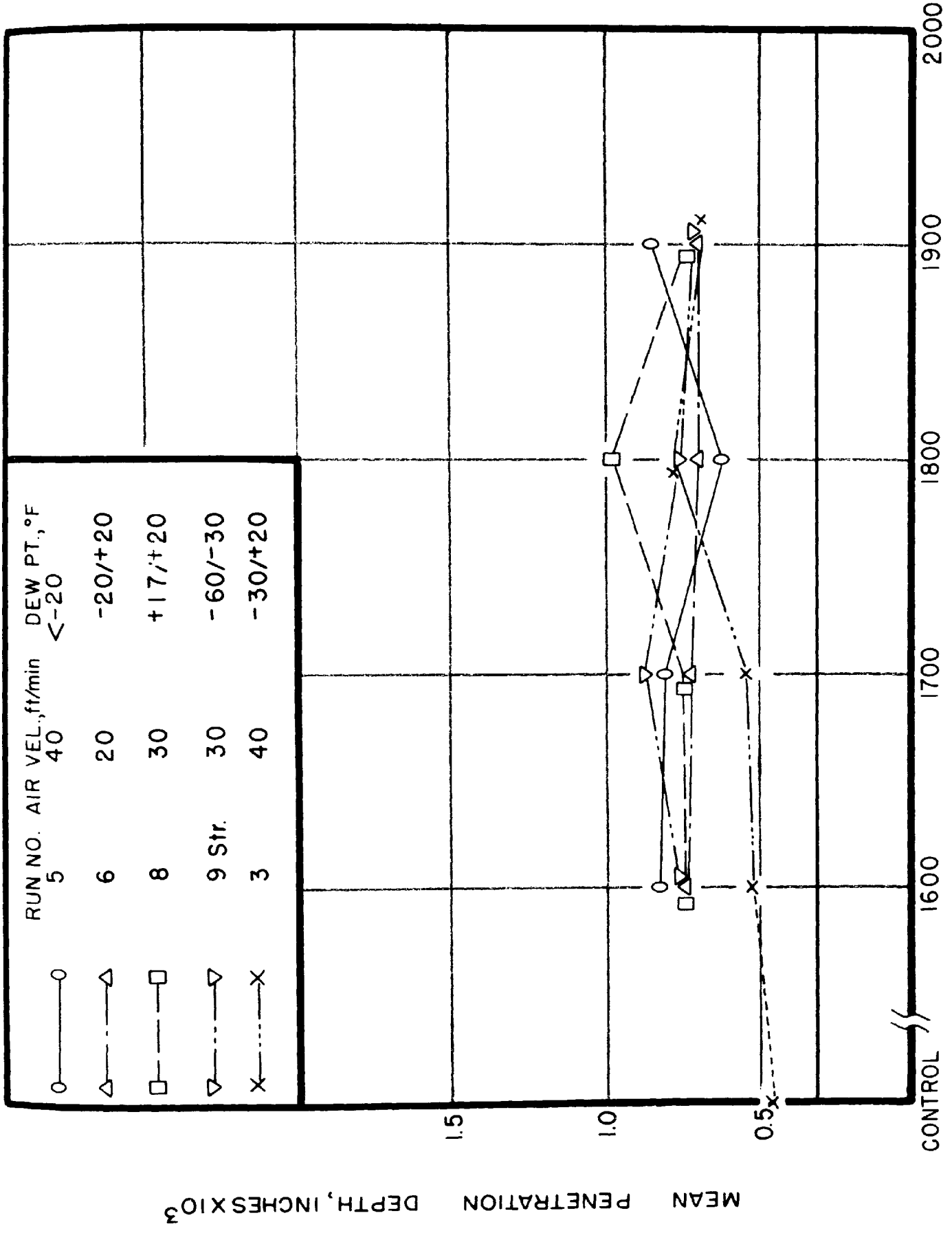

FIG. 74-SUMMARY PENETRATION DEPTH CURVES.
TYPE 310 ALLOY, HEAT 64177. 100 HOURS DURATION.
EFFECT OF AIR VELOCITY AND HUMIDITY.

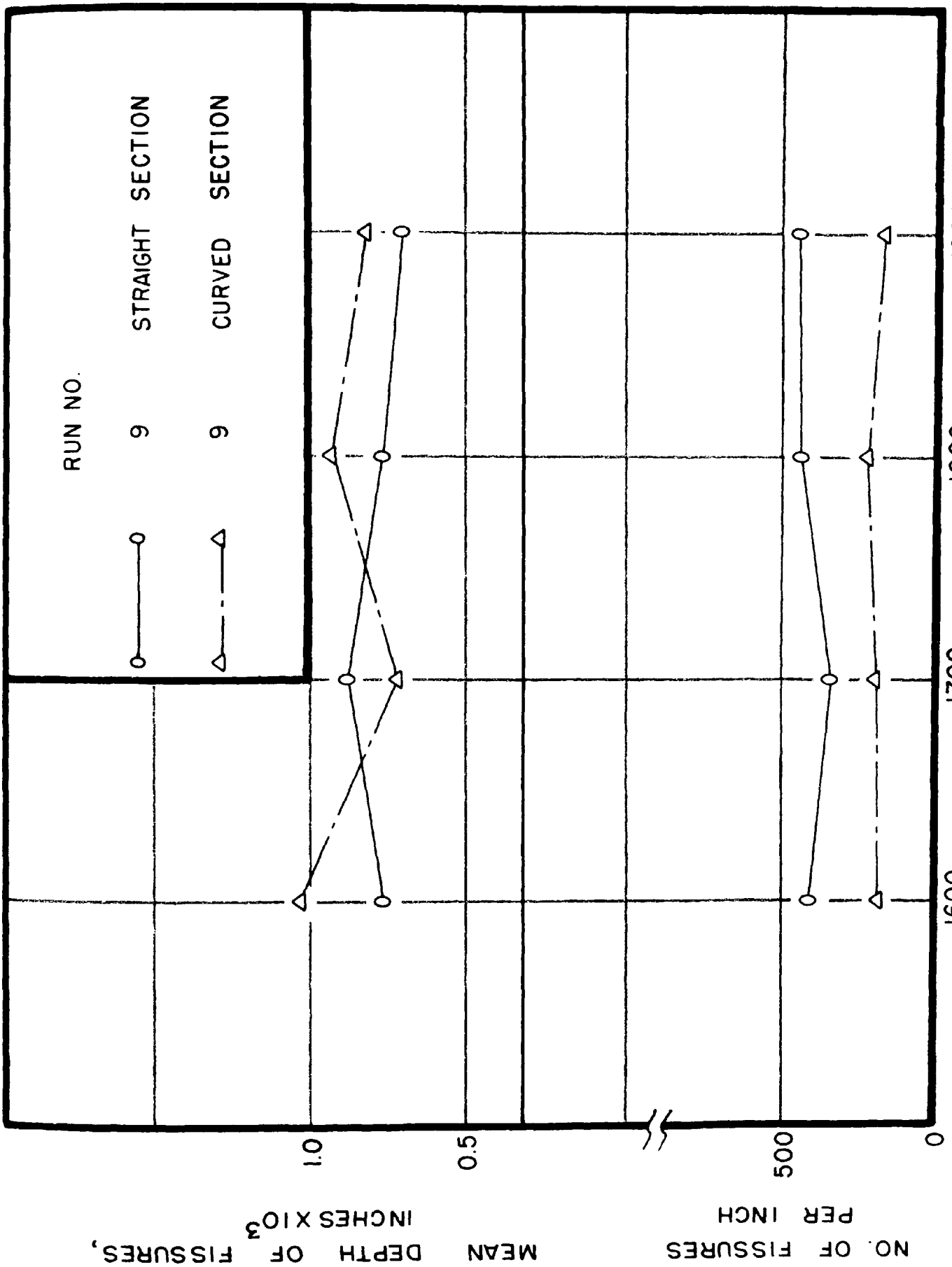

FIG.75- SUMMARY PENETRATION FREQUENCY AND DEPTH CURVES. TYPE 310 ALLOY, HEAT 64177. EFFECT OF COLD WORK. 100 HOURS DURATION.

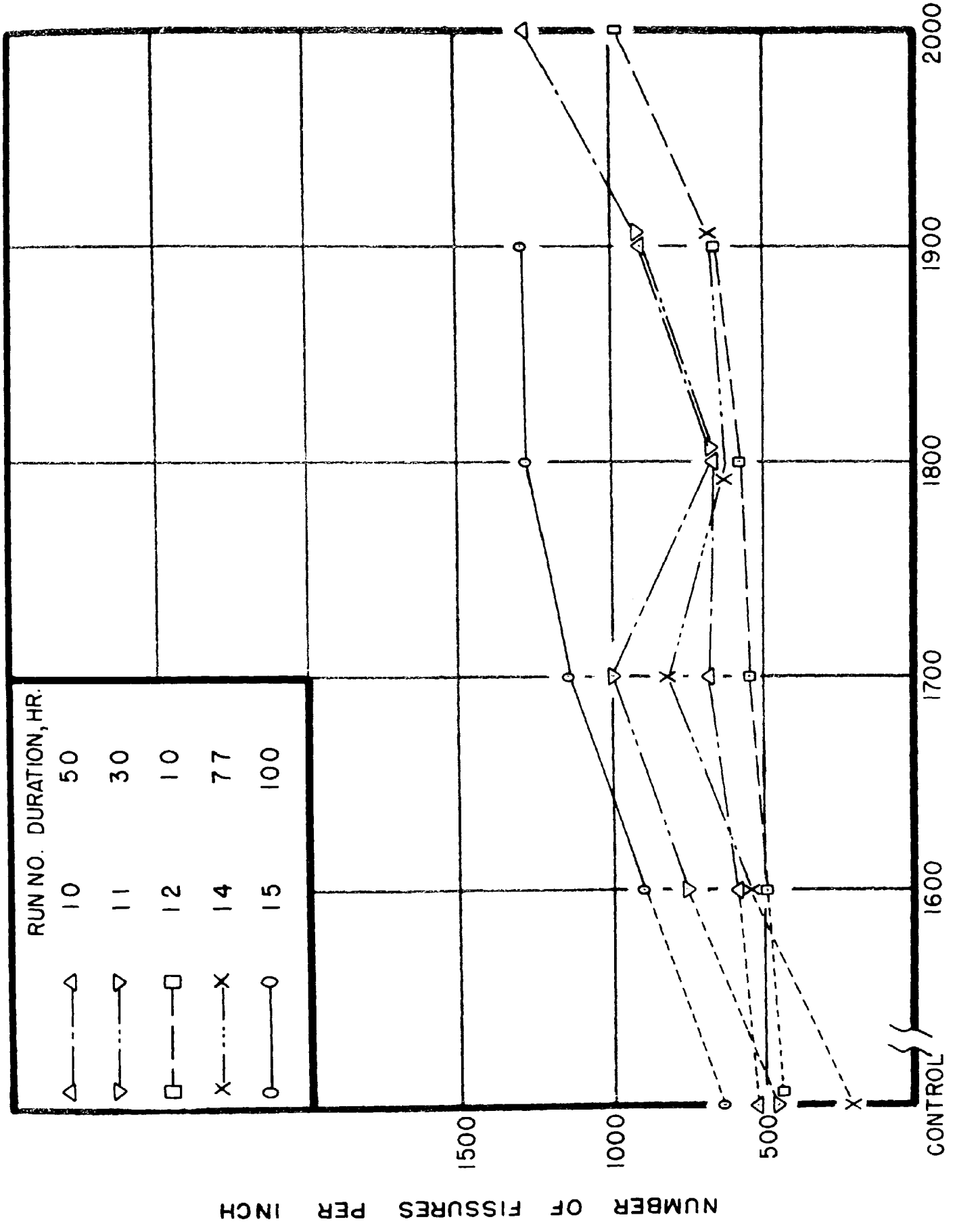

FIG. 76-SUMMARY PENETRATION FREQUENCY CURVES.
TYPE 310 ALLOY, HEAT 64177. EFFECT OF TIME.

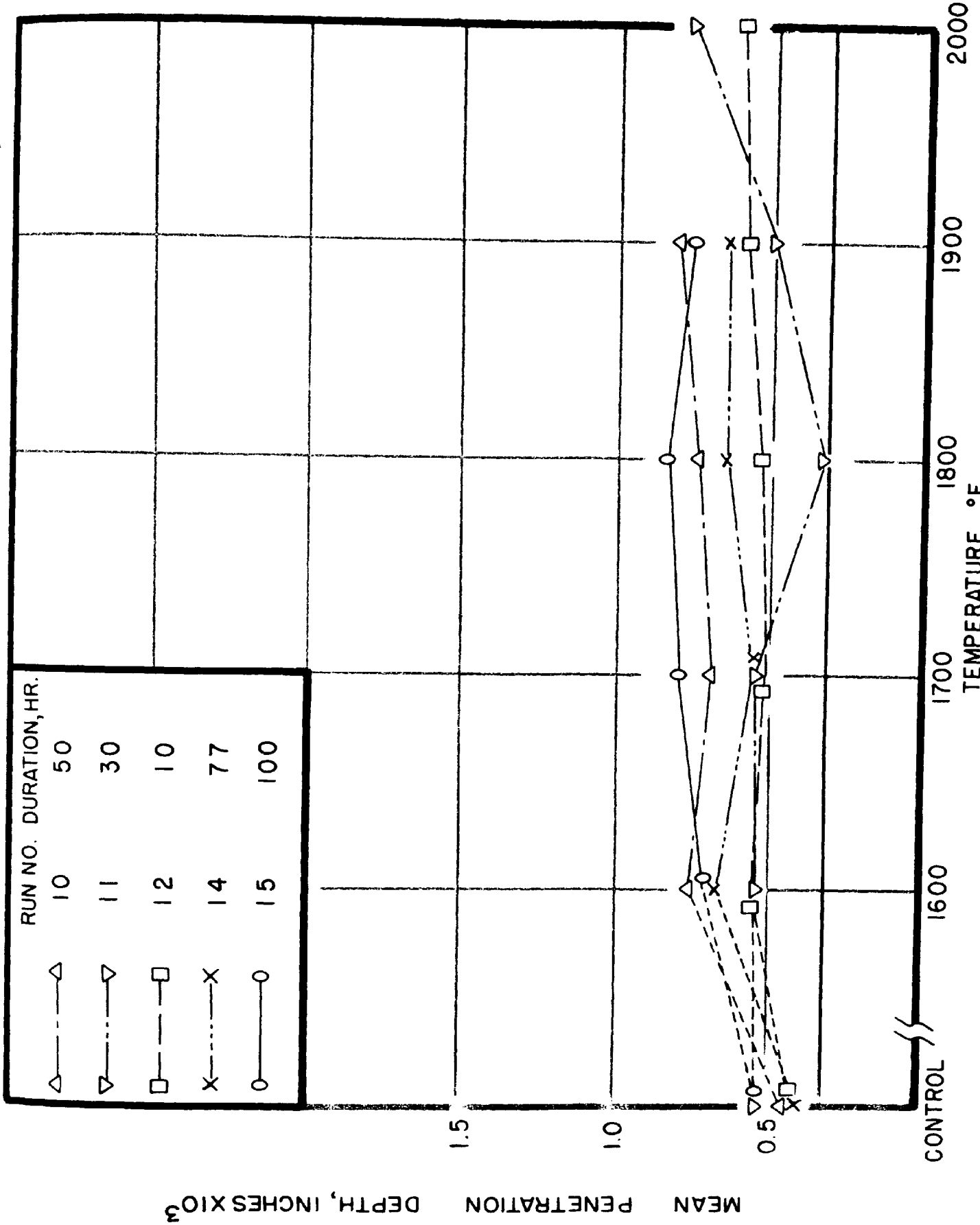

FIG. 77—SUMMARY PENETRATION DEPTH CURVES.
TYPE 310 ALLOY, HEAT 64177. EFFECT OF TIME.

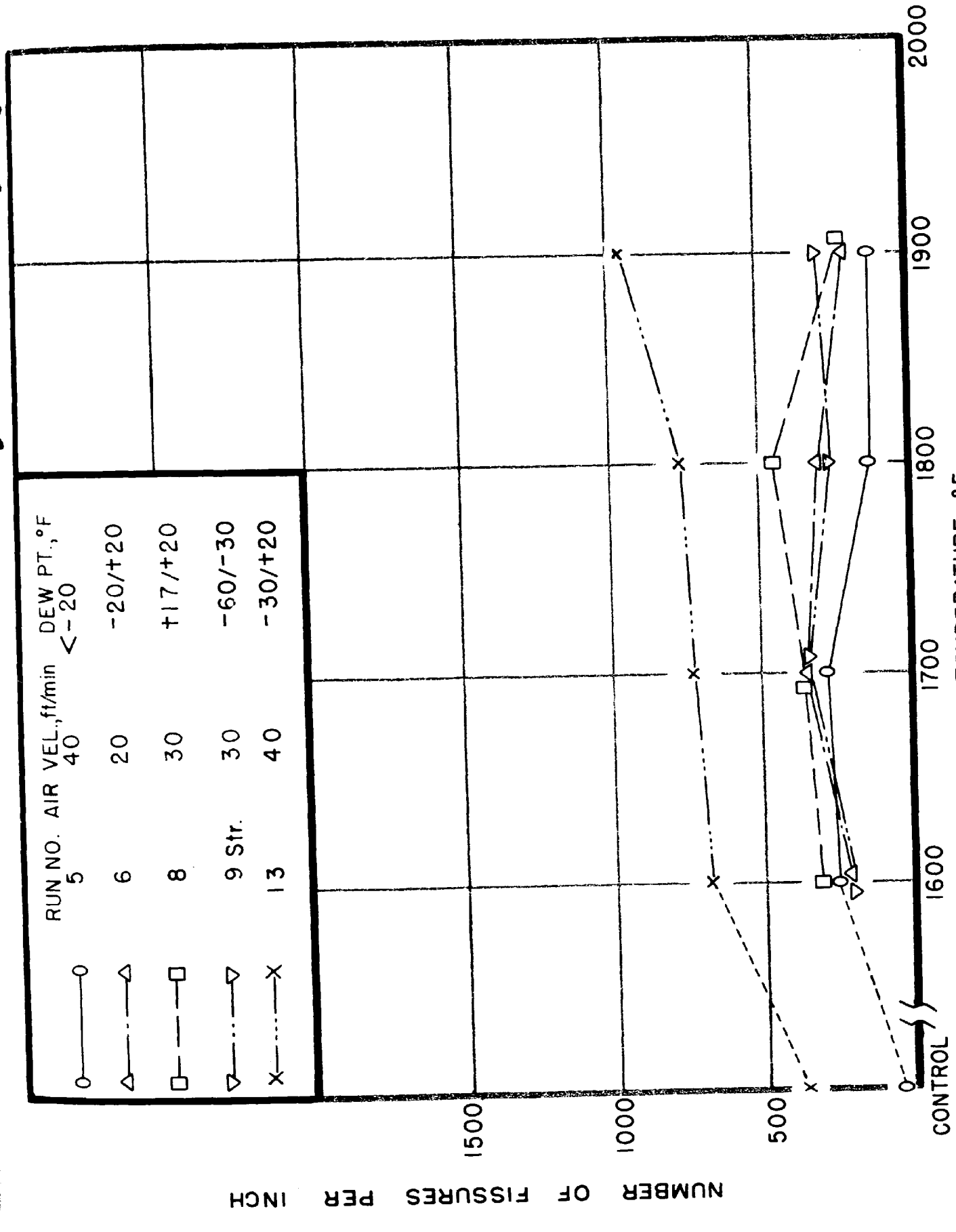

FIG. 78-SUMMARY PENETRATION FREQUENCY CURVES.
TYPE 310 ALLOY, HEAT 64270. 100 HOURS DURATION.
EFFECT OF AIR VELOCITY AND HUMIDITY.

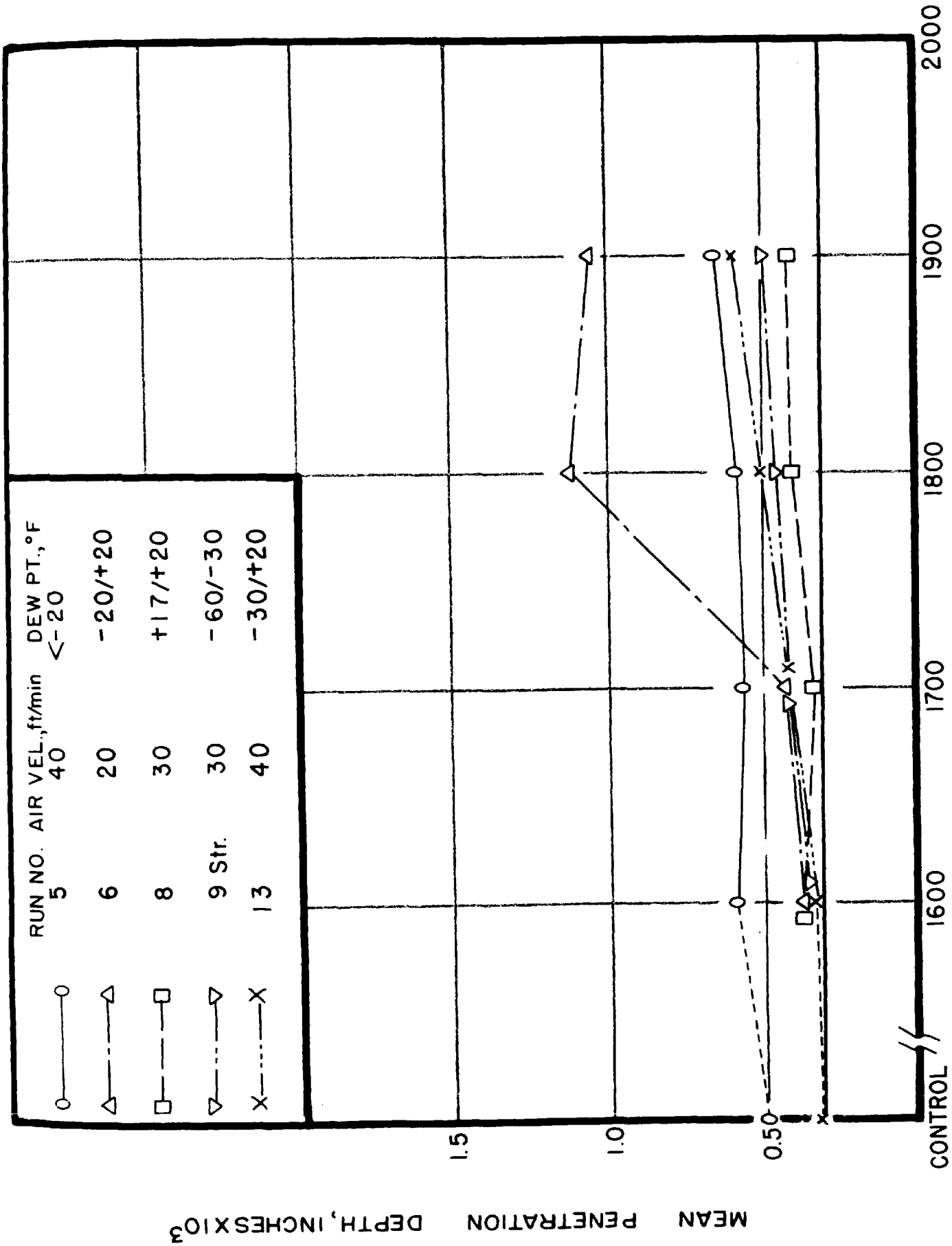

FIG. 79-SUMMARY PENETRATION DEPTH CURVES.
TYPE 310 ALLOY, HEAT 64270. 100 HOURS DURATION.
EFFECT OF AIR VELOCITY AND HUMIDITY.

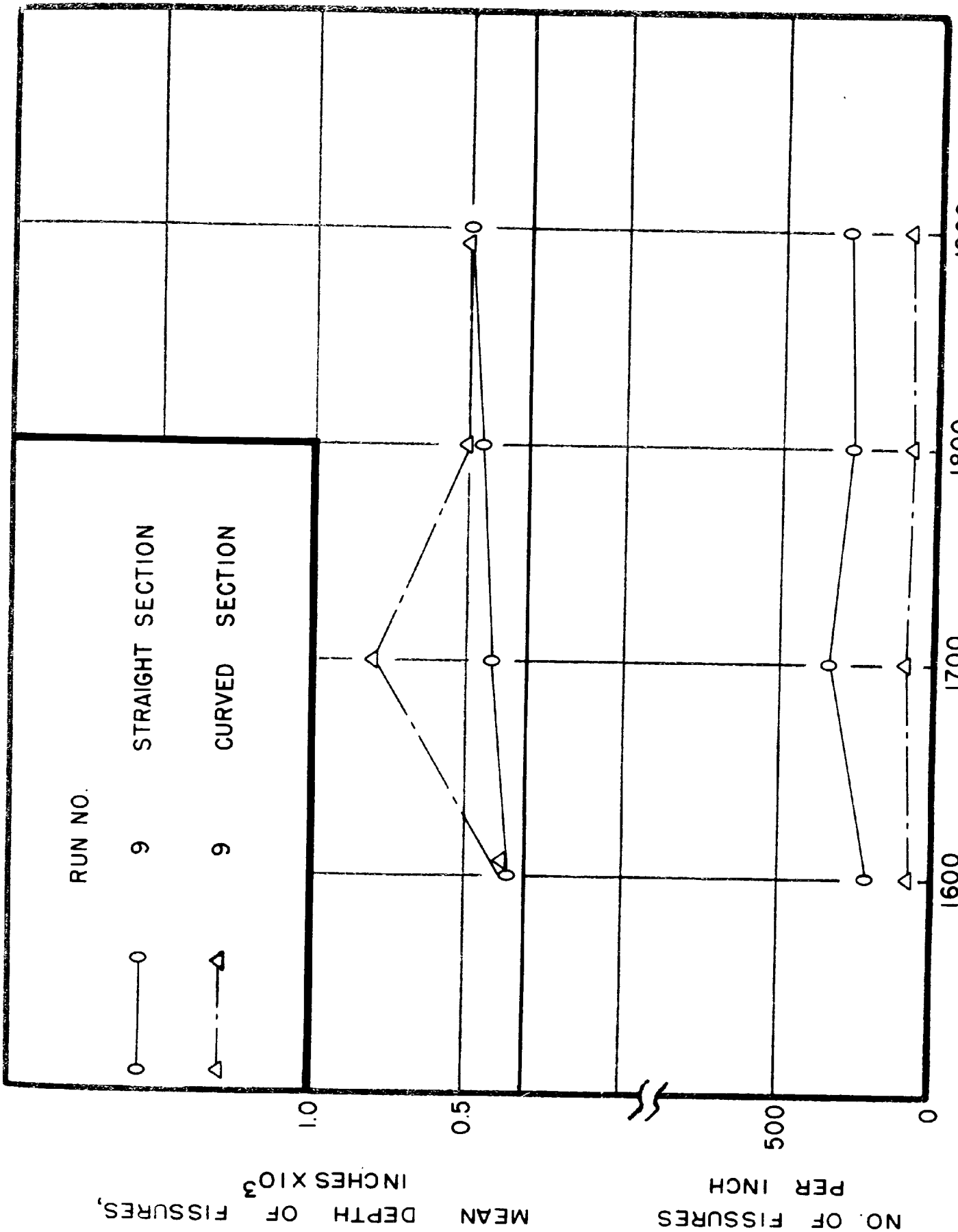

FIG.80-SUMMARY PENETRATION FREQUENCY AND DEPTH CURVES. TYPE 310 ALLOY, HEAT 64270. EFFECT OF COLD WORK. 100 HOURS DURATION.

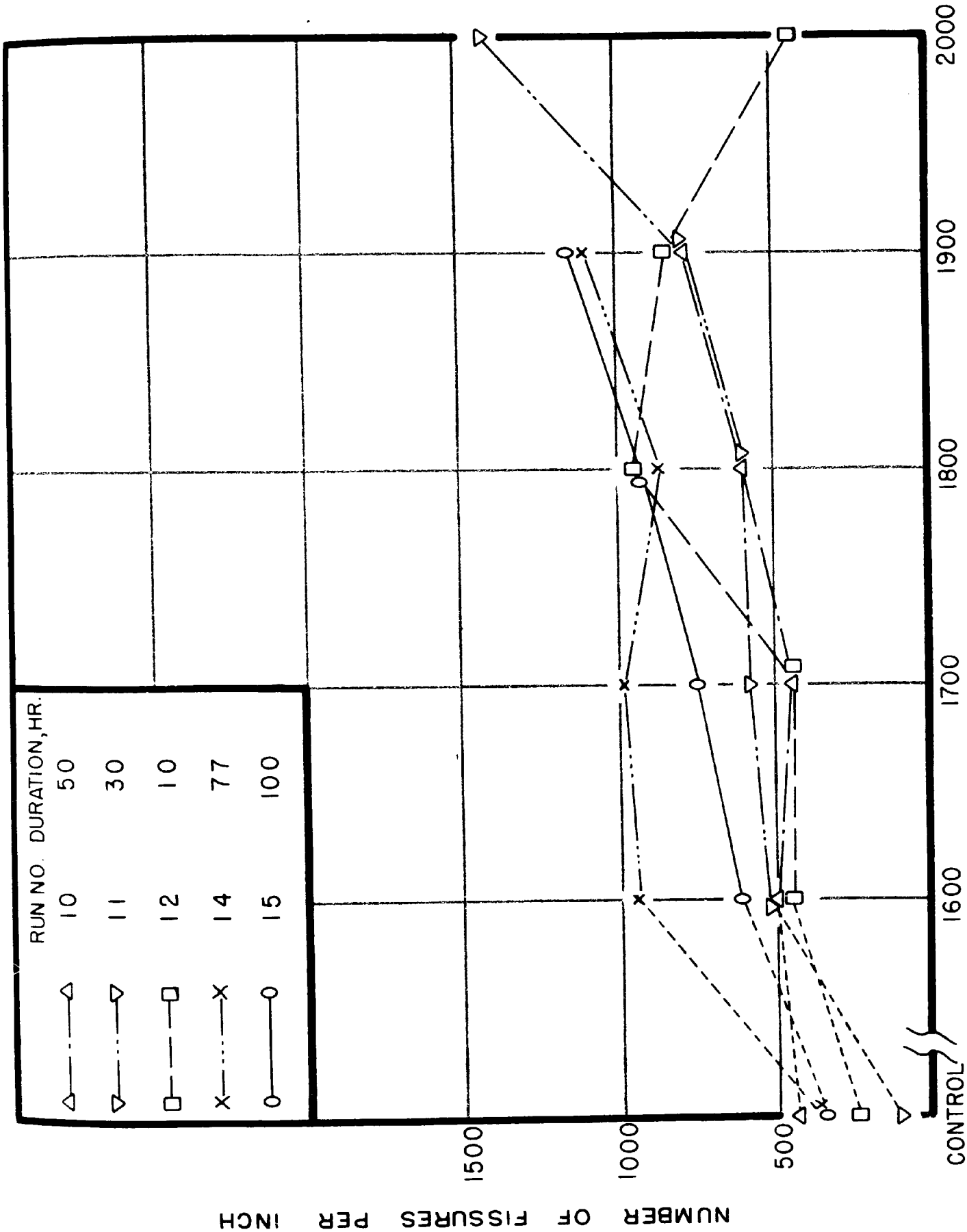

FIG.81-SUMMARY PENETRATION FREQUENCY CURVES.
TYPE 310 ALLOY, HEAT 64270. EFFECT OF TIME.

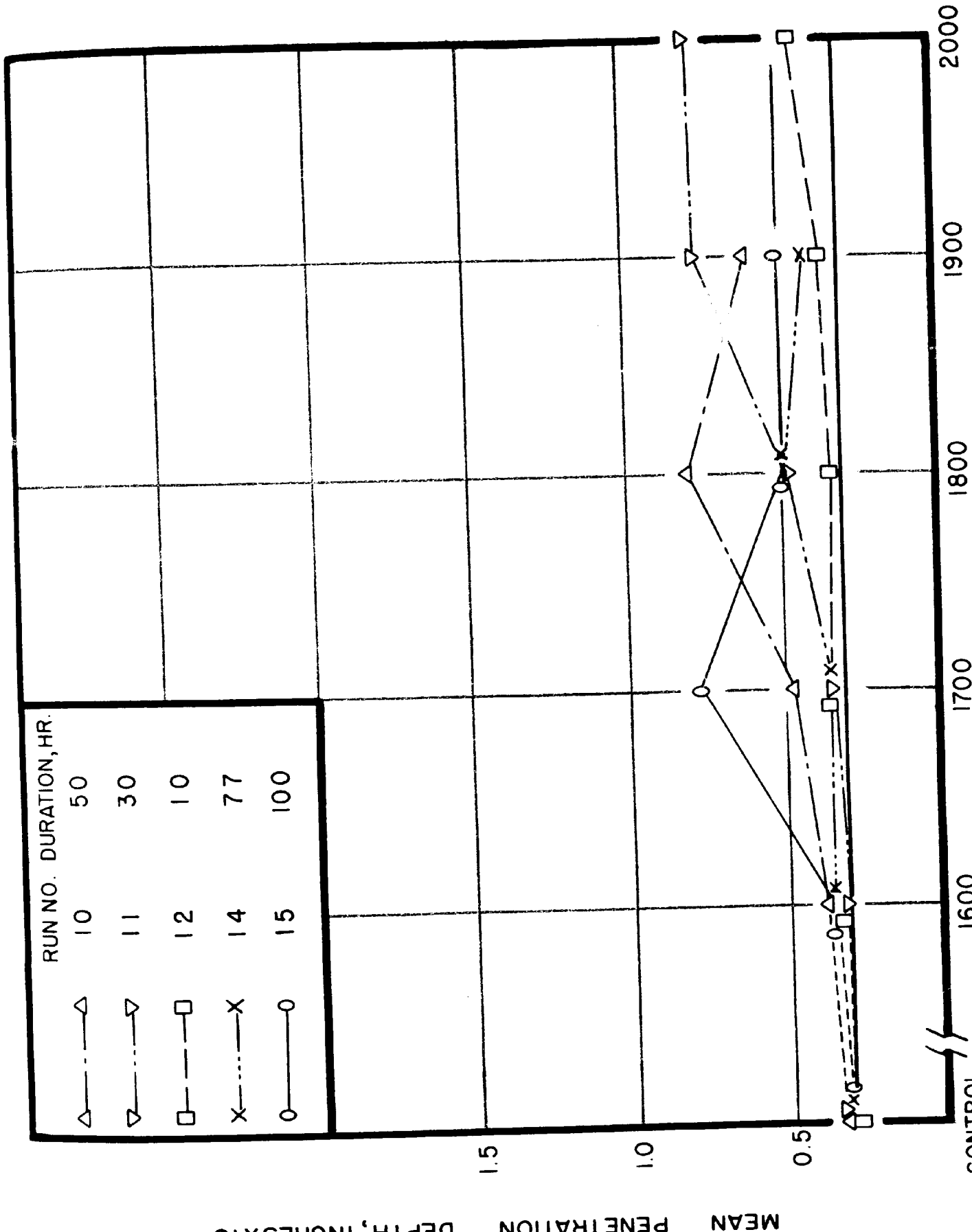

FIG. 82 - SUMMARY PENETRATION DEPTH CURVES.
TYPE 310 ALLOY, HEAT 64270. EFFECT OF TIME.

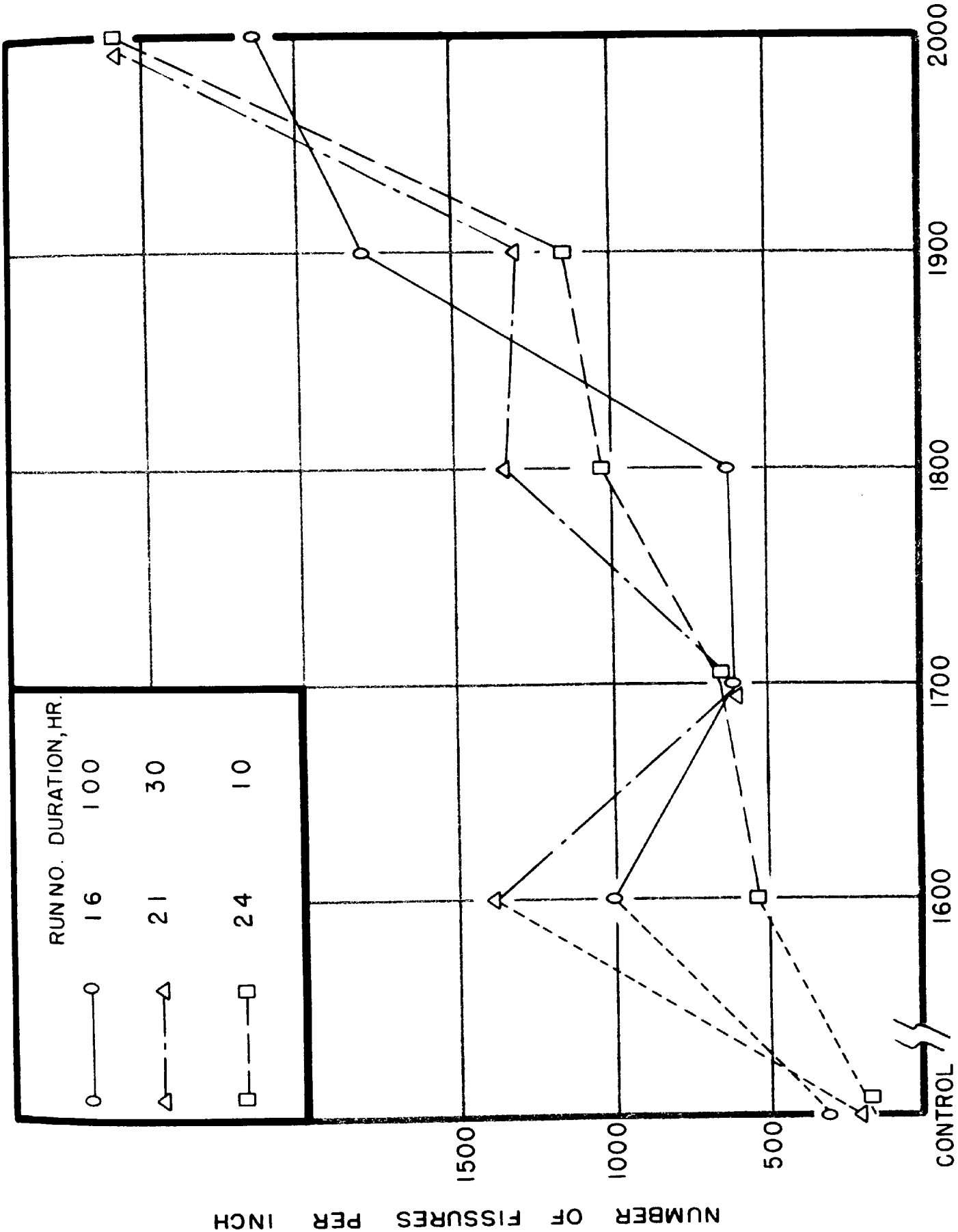

FIG.83-SUMMARY PENETRATION FREQUENCY CURVES.
TYPE 310 ALLOY, HEAT X11306. EFFECT OF TIME.

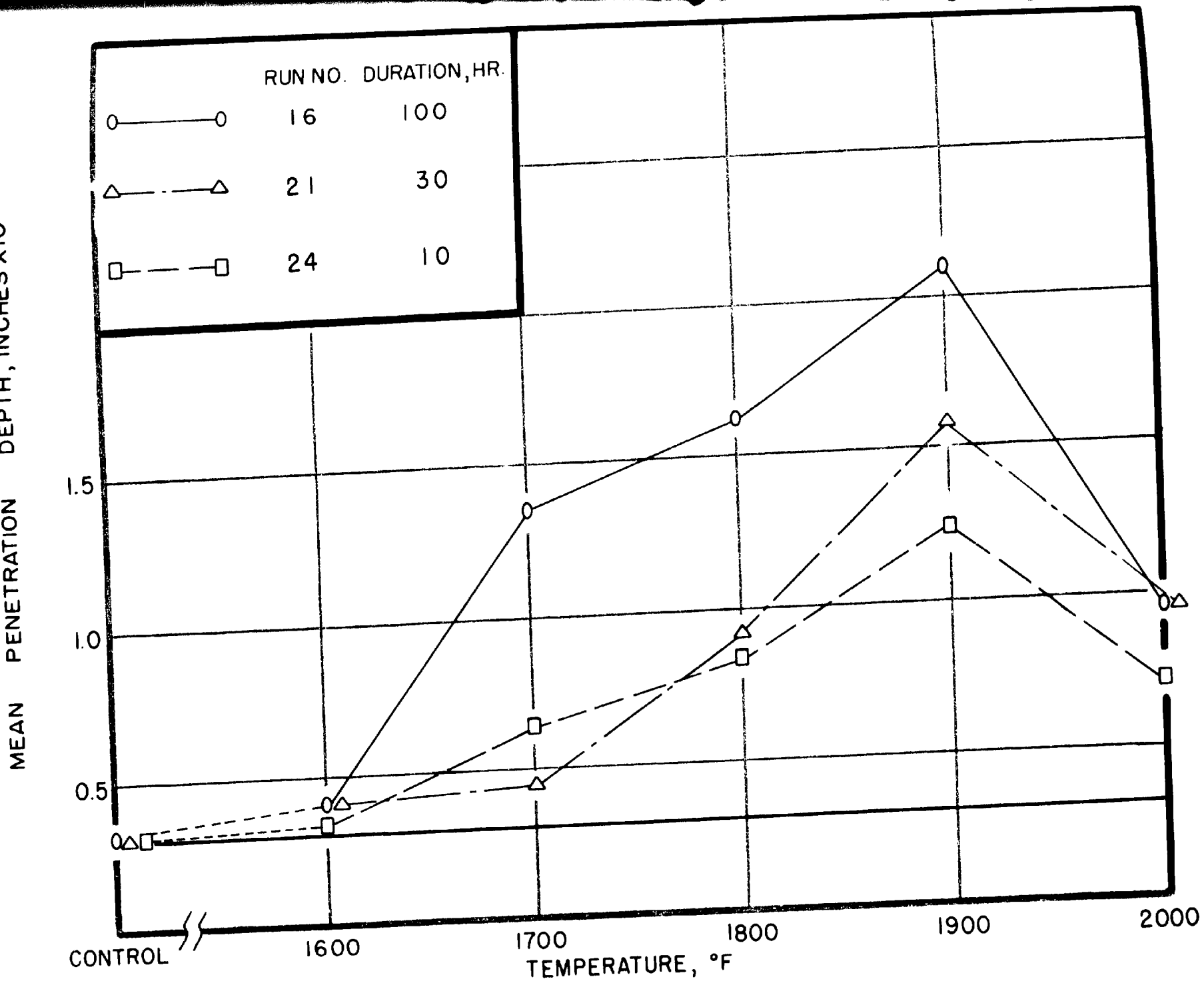

FIG.84-SUMMARY PENETRATION DEPTH CURVES.
TYPE 310 ALLOY, HEAT X11306. EFFECT OF TIME.

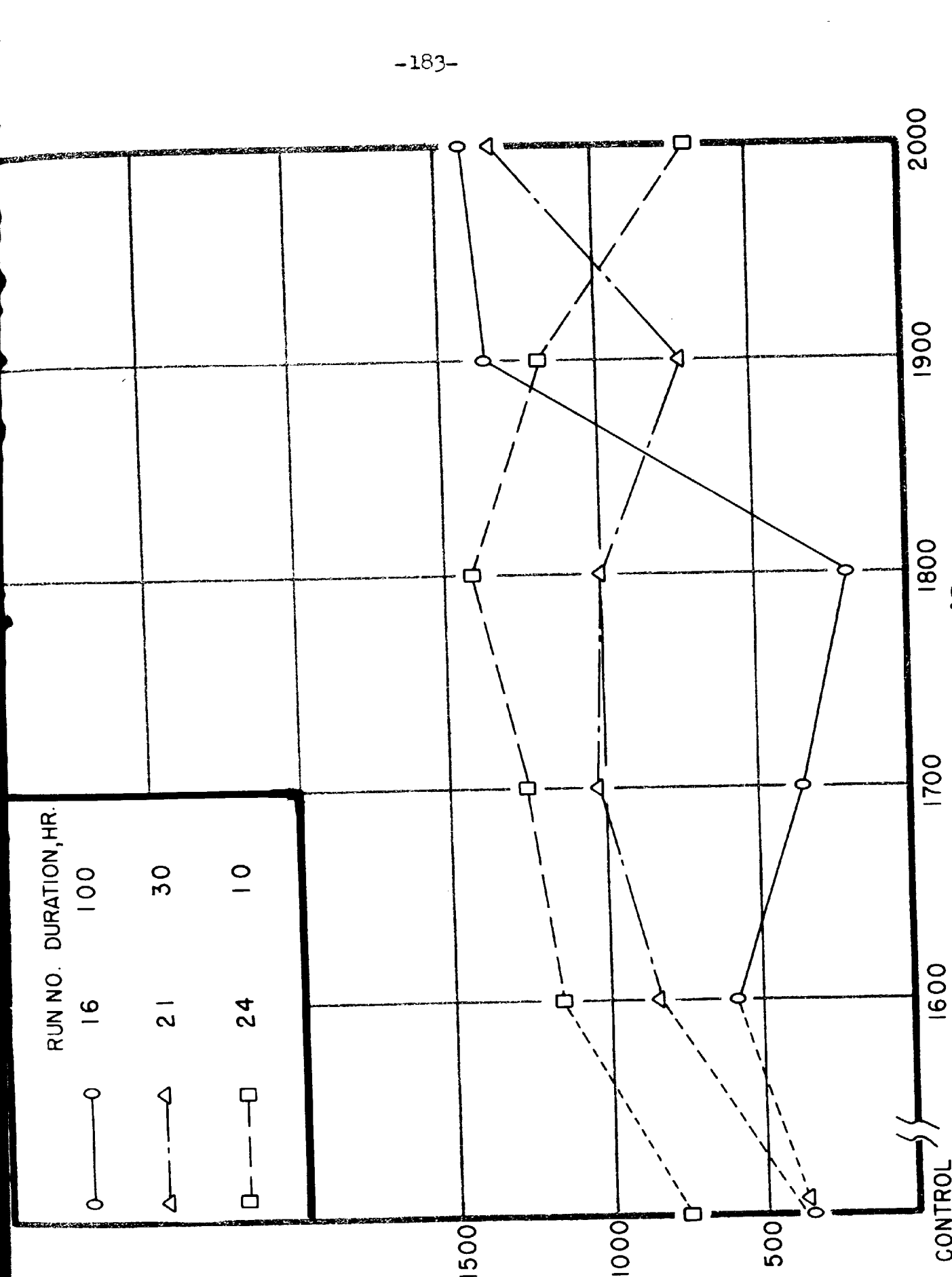

FIG.85-SUMMARY PENETRATION FREQUENCY CURVES.
TYPE 310 ALLOY, HEAT X11338. EFFECT OF TIME.

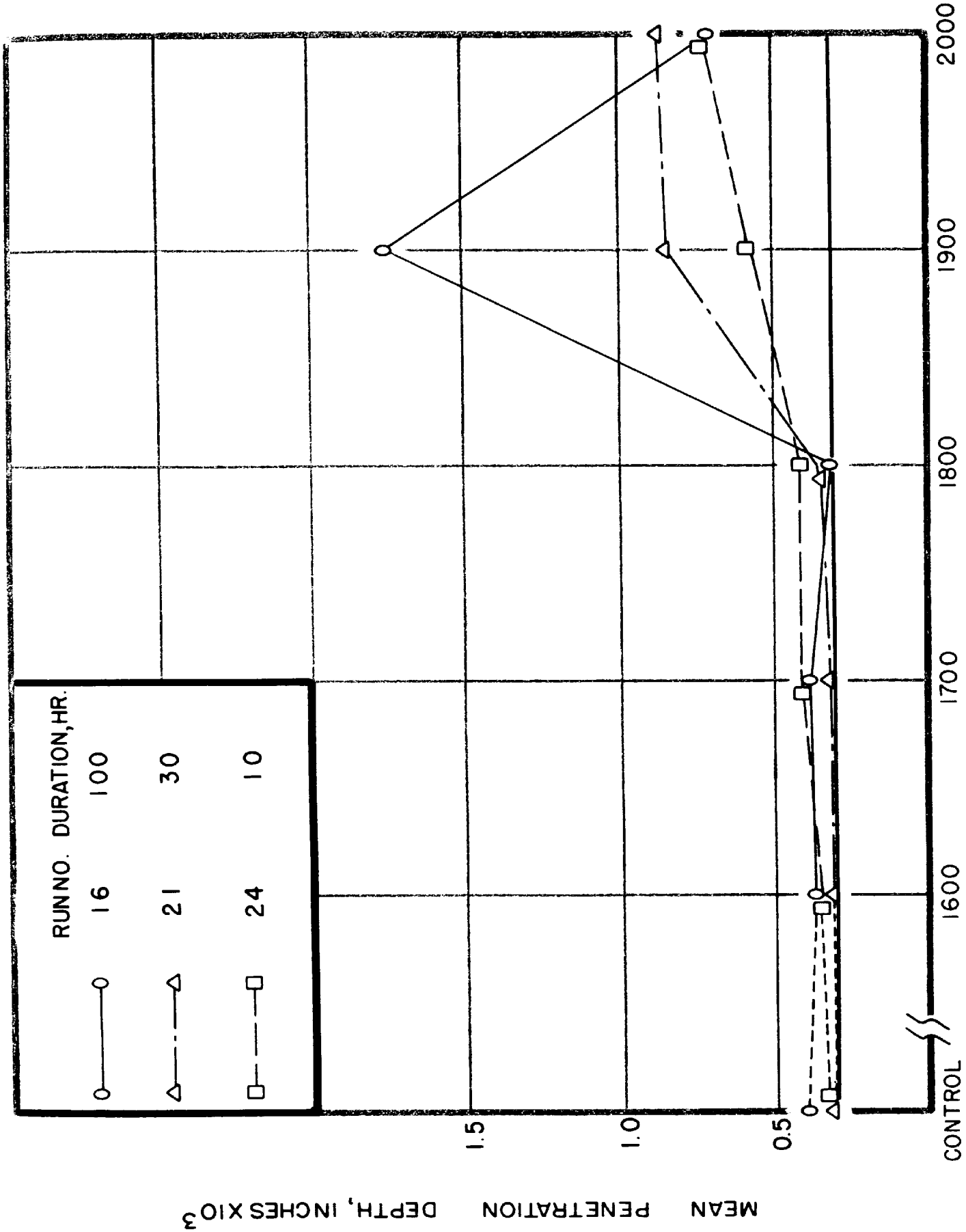

FIG.86-SUMMARY PENETRATION DEPTH CURVES.
TYPE 310 ALLOY, HEAT X11338. EFFECT OF TIME.

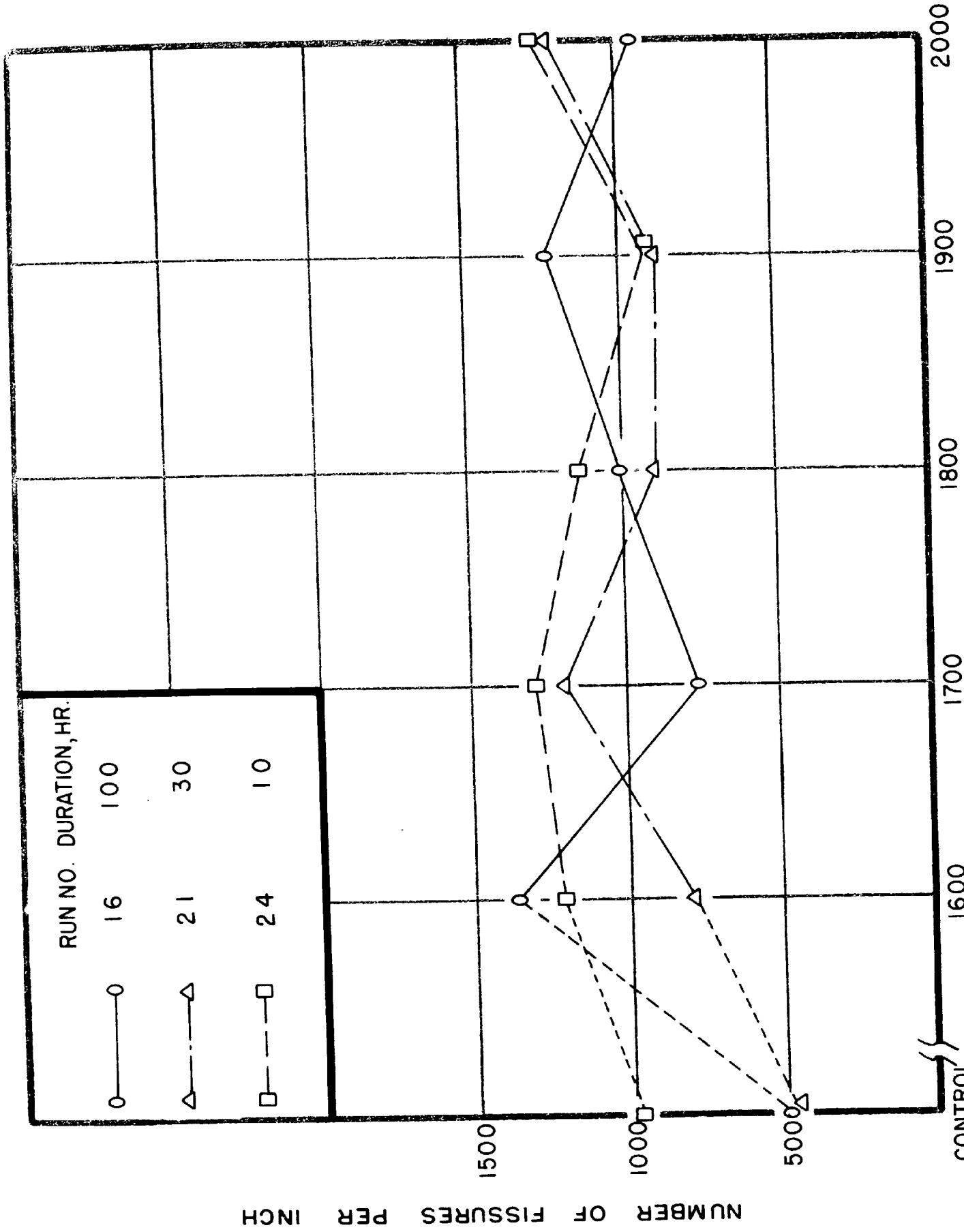

FIG. 87 - SUMMARY PENETRATION FREQUENCY CURVES.
TYPE 310 ALLOY, HEAT X27258. EFFECT OF TIME.

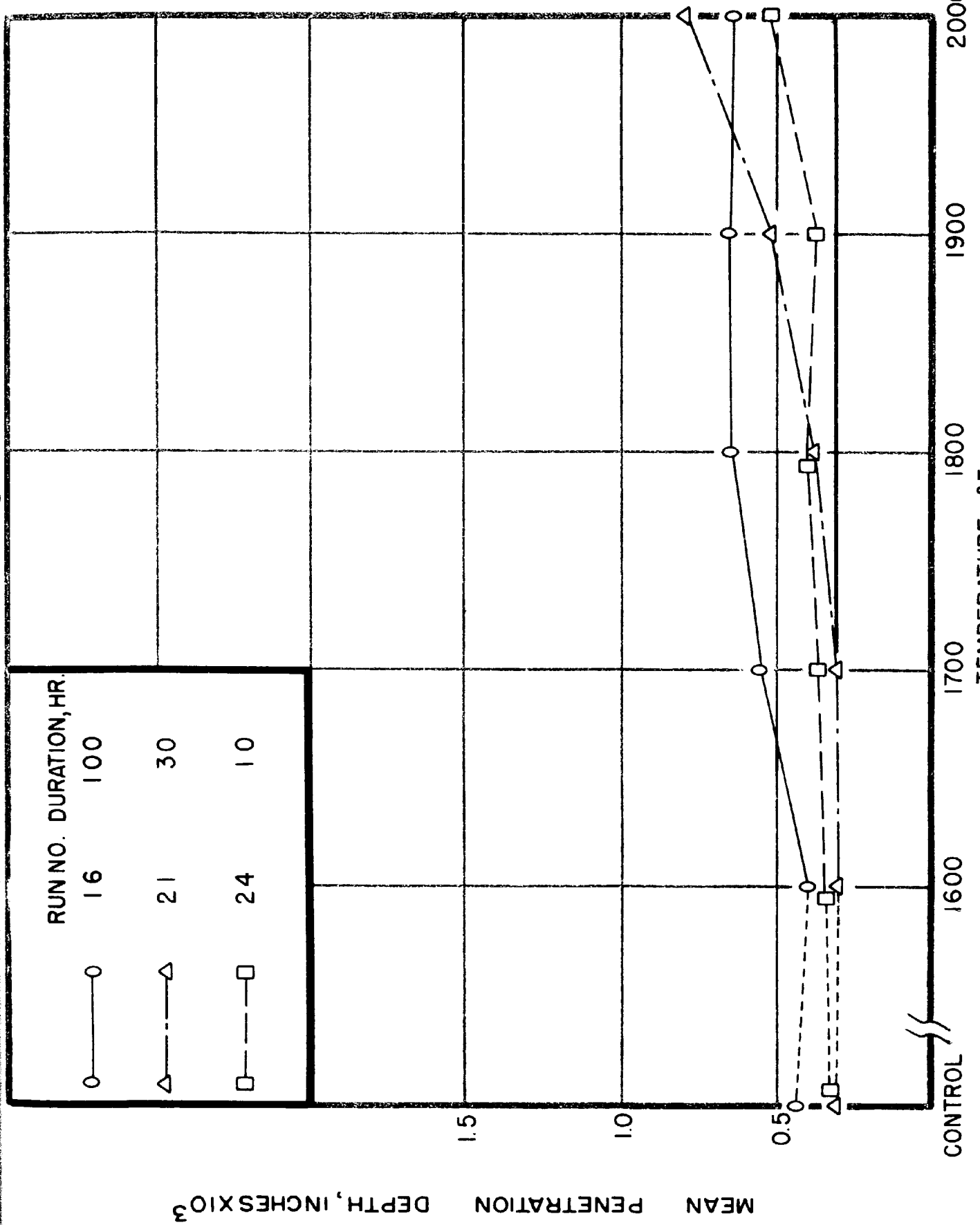

FIG.88-SUMMARY PENETRATION DEPTH CURVES.
TYPE 310 ALLOY, HEAT X27258. EFFECT OF TIME.

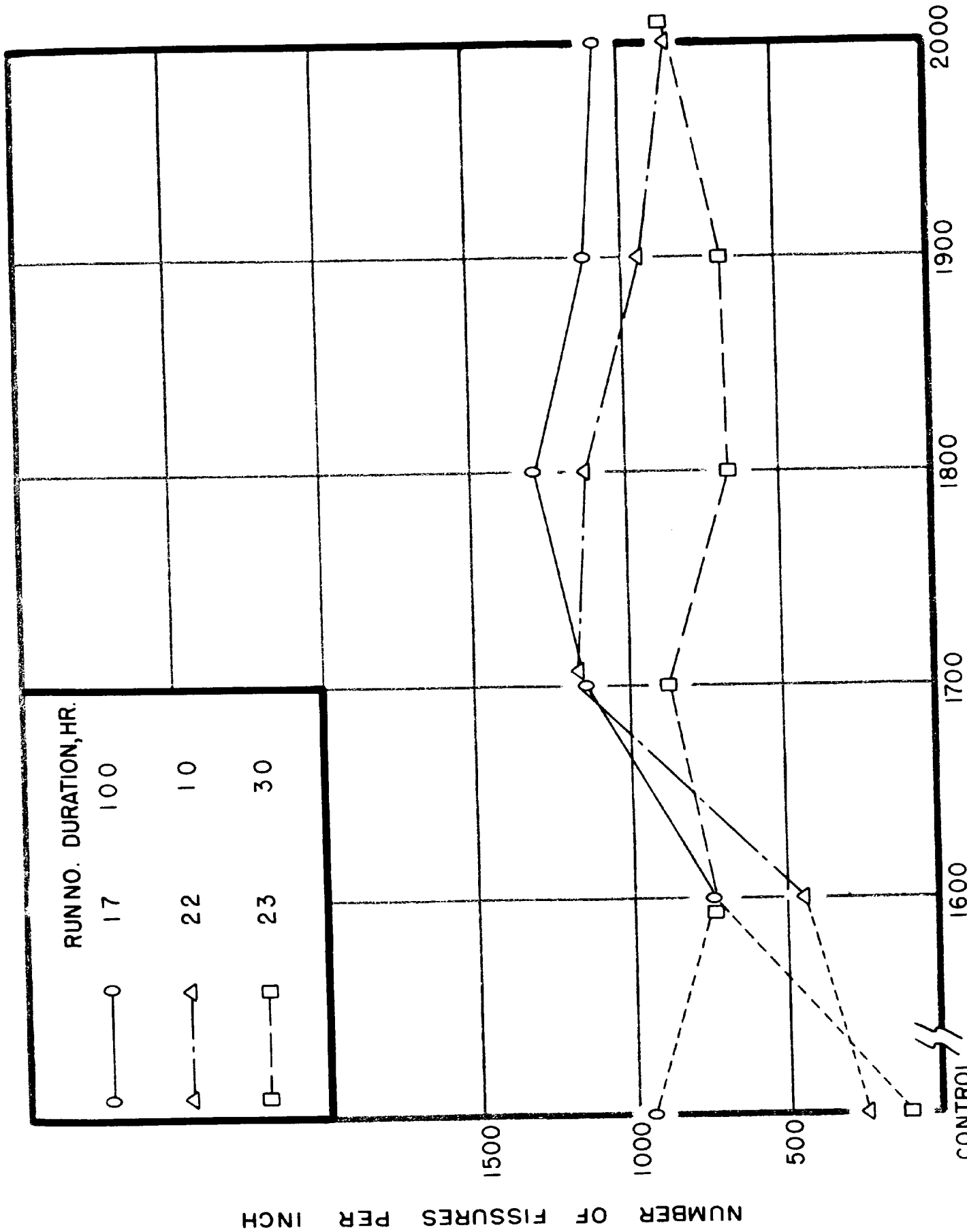

FIG.89-SUMMARY PENETRATION FREQUENCY CURVES.
TYPE 310 ALLOY, HEAT X45558. EFFECT OF TIME.

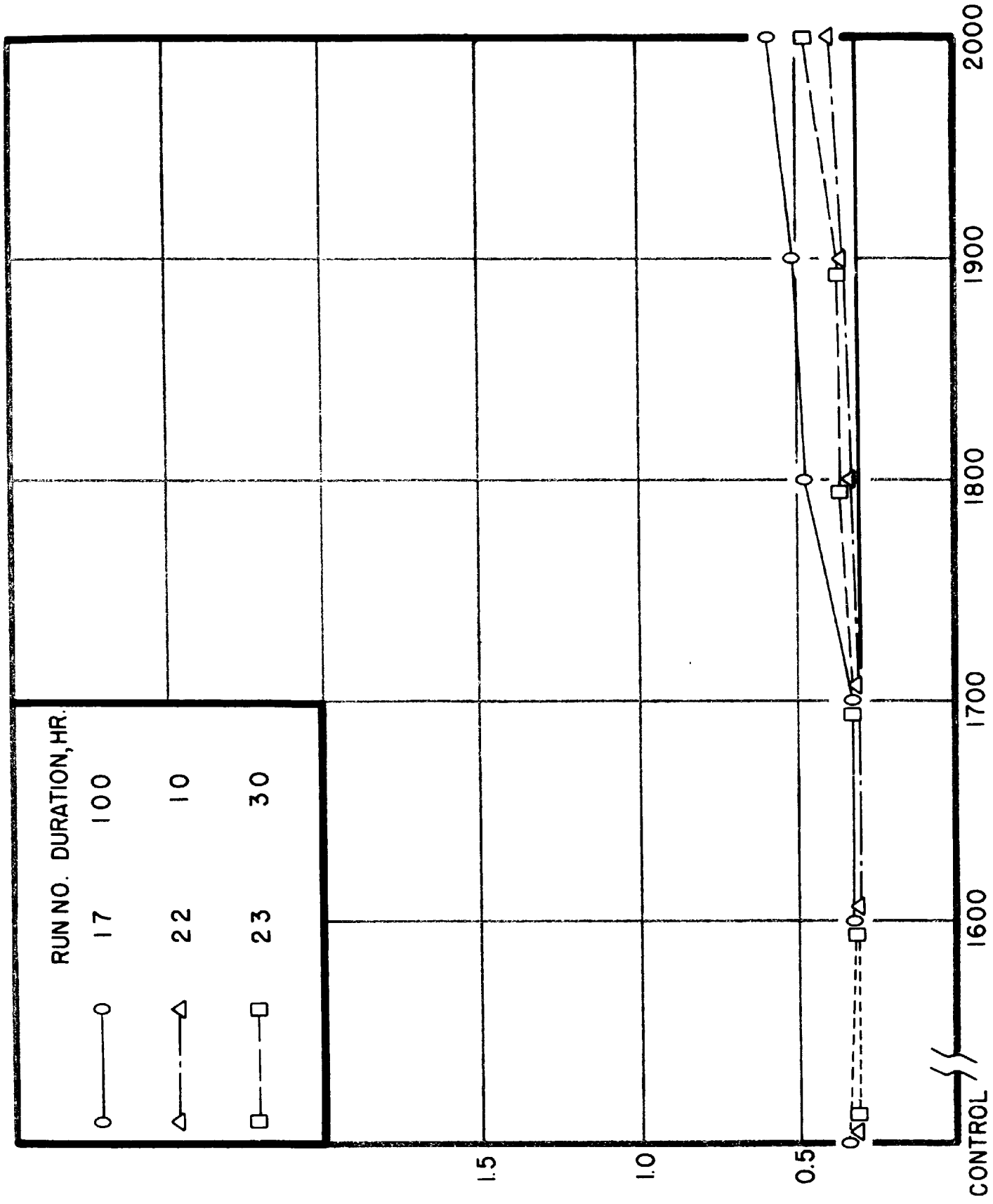

FIG. 90-SUMMARY PENETRATION DEPTH CURVES.
TYPE 310 ALLOY, HEAT X45558. EFFECT OF TIME.

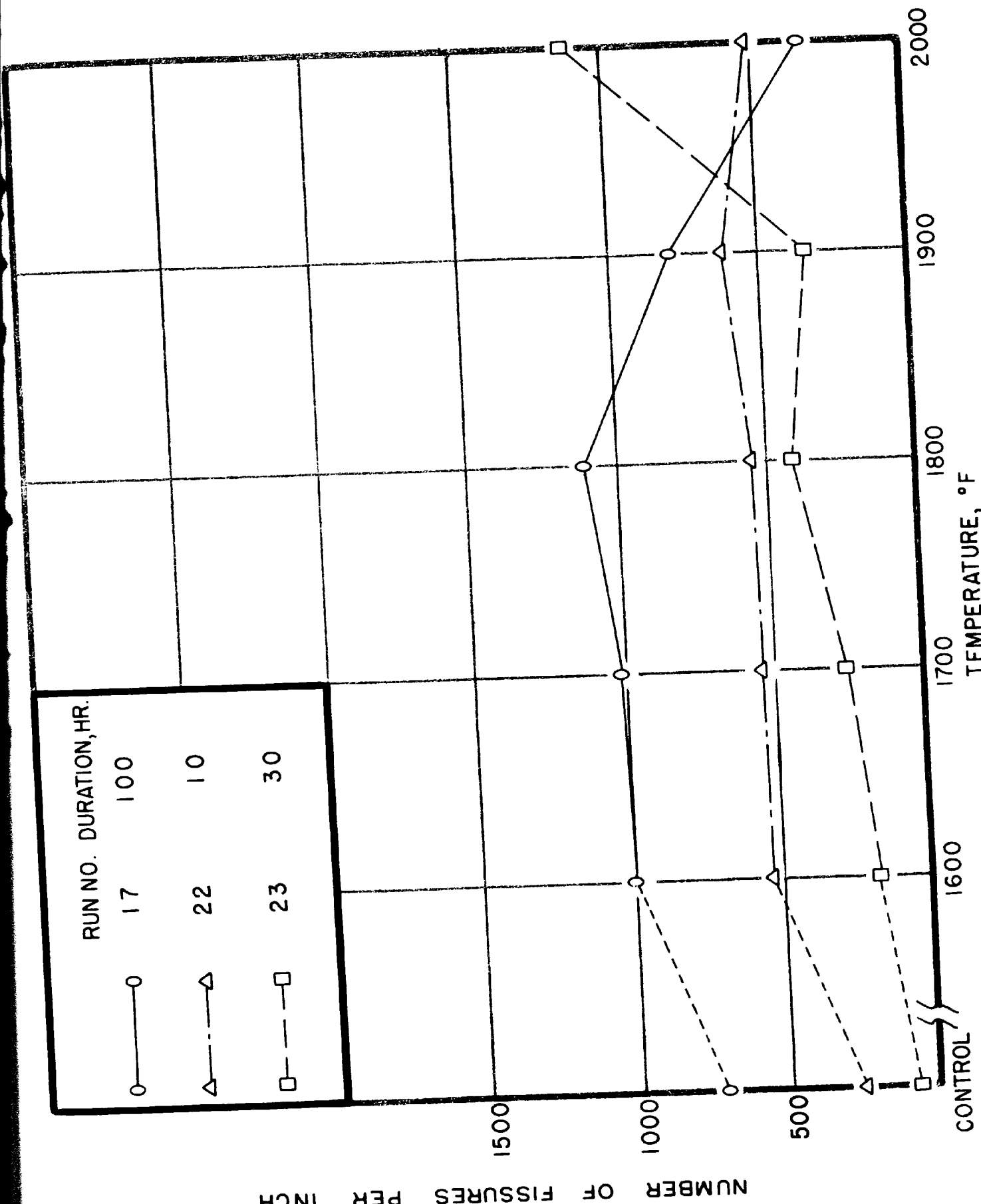

FIG. 91 - SUMMARY PENETRATION FREQUENCY CURVES.
TYPE 310 ALLOY, HEAT X46063. EFFECT OF TIME.

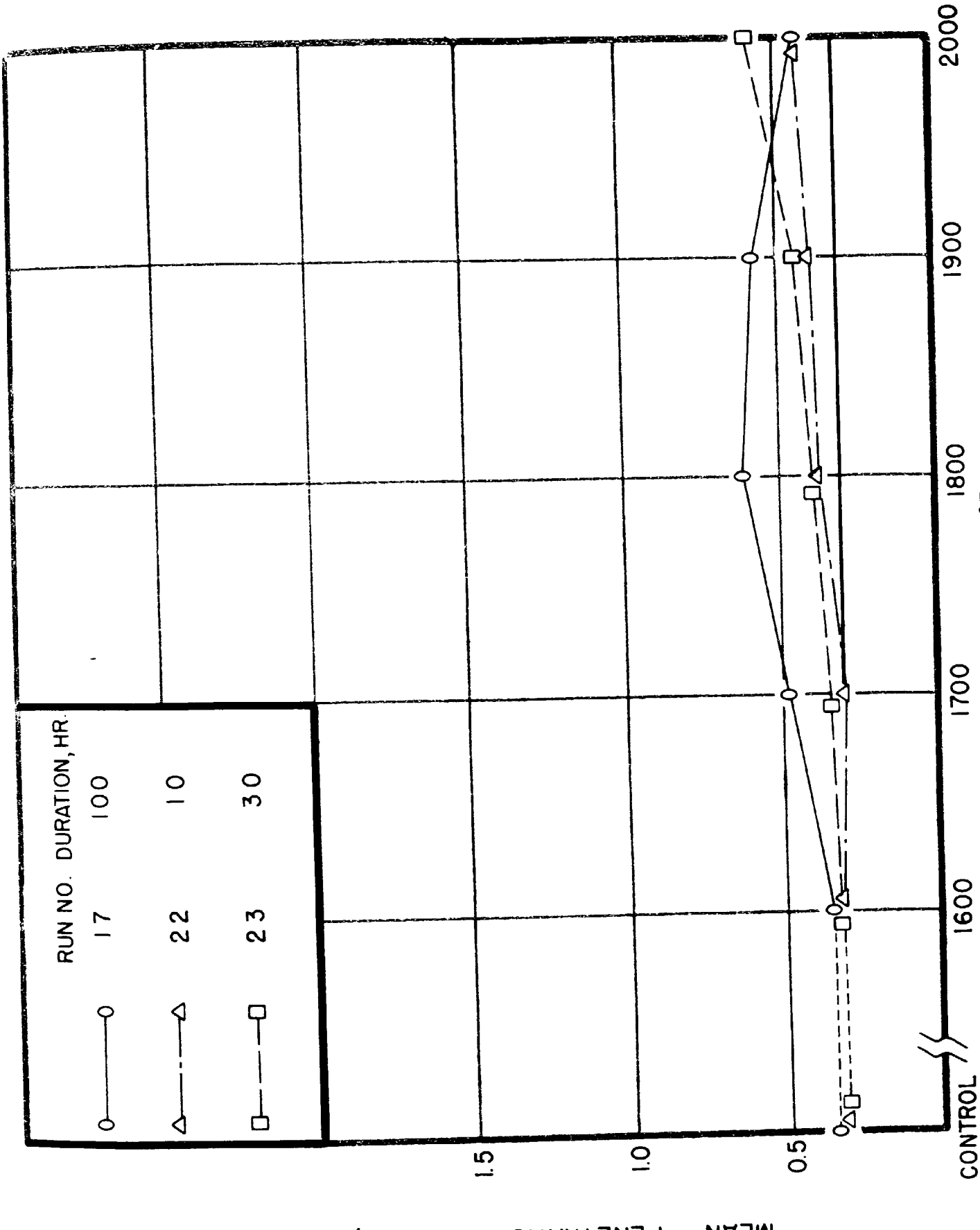

FIG. 92-SUMMARY PENETRATION DEPTH CURVES.
TYPE 310 ALLOY, HEAT X46063. EFFECT OF TIME.

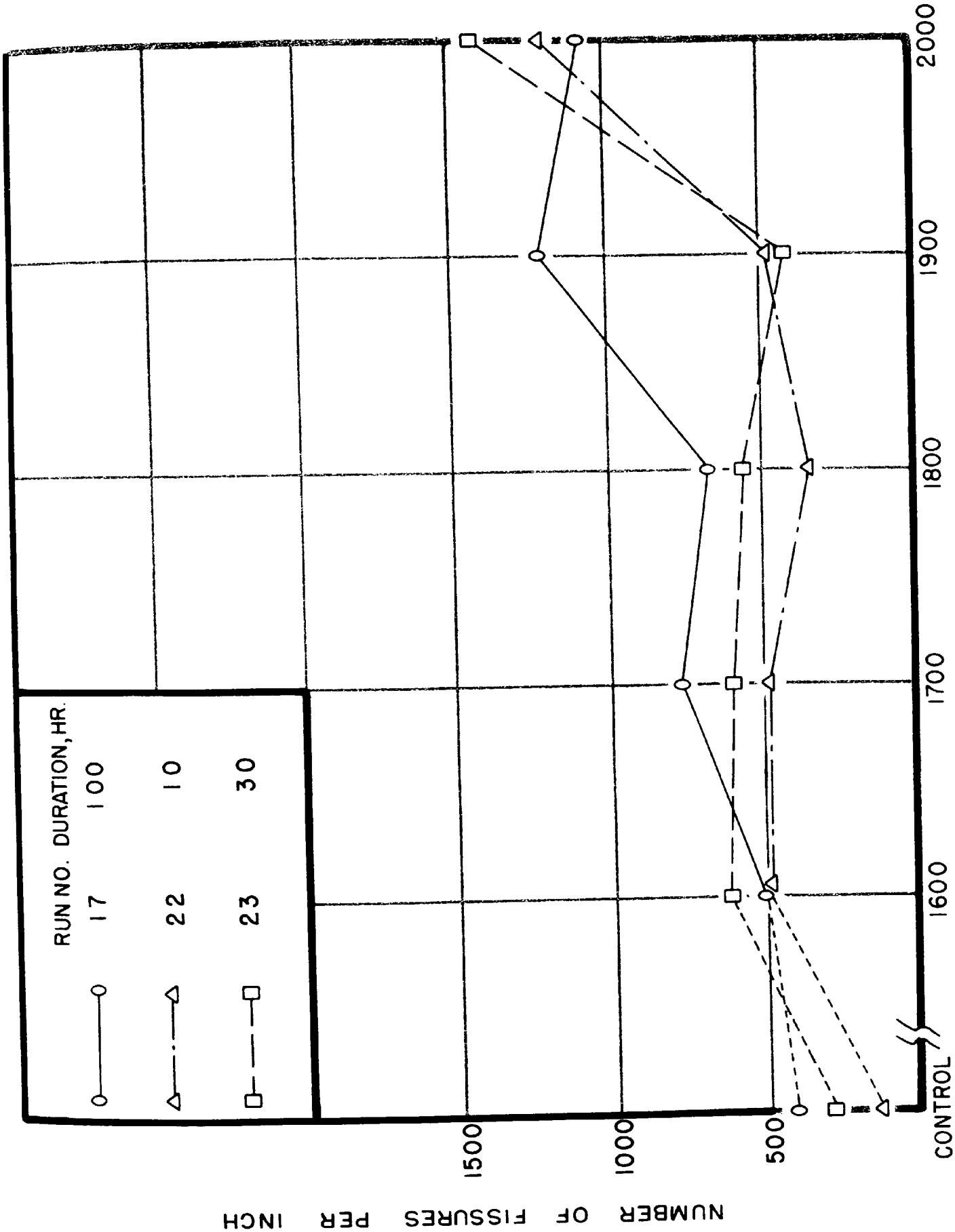

FIG.93-SUMMARY PENETRATION FREQUENCY CURVES.
TYPE 310 ALLOY, HEAT X46572. EFFECT OF TIME.

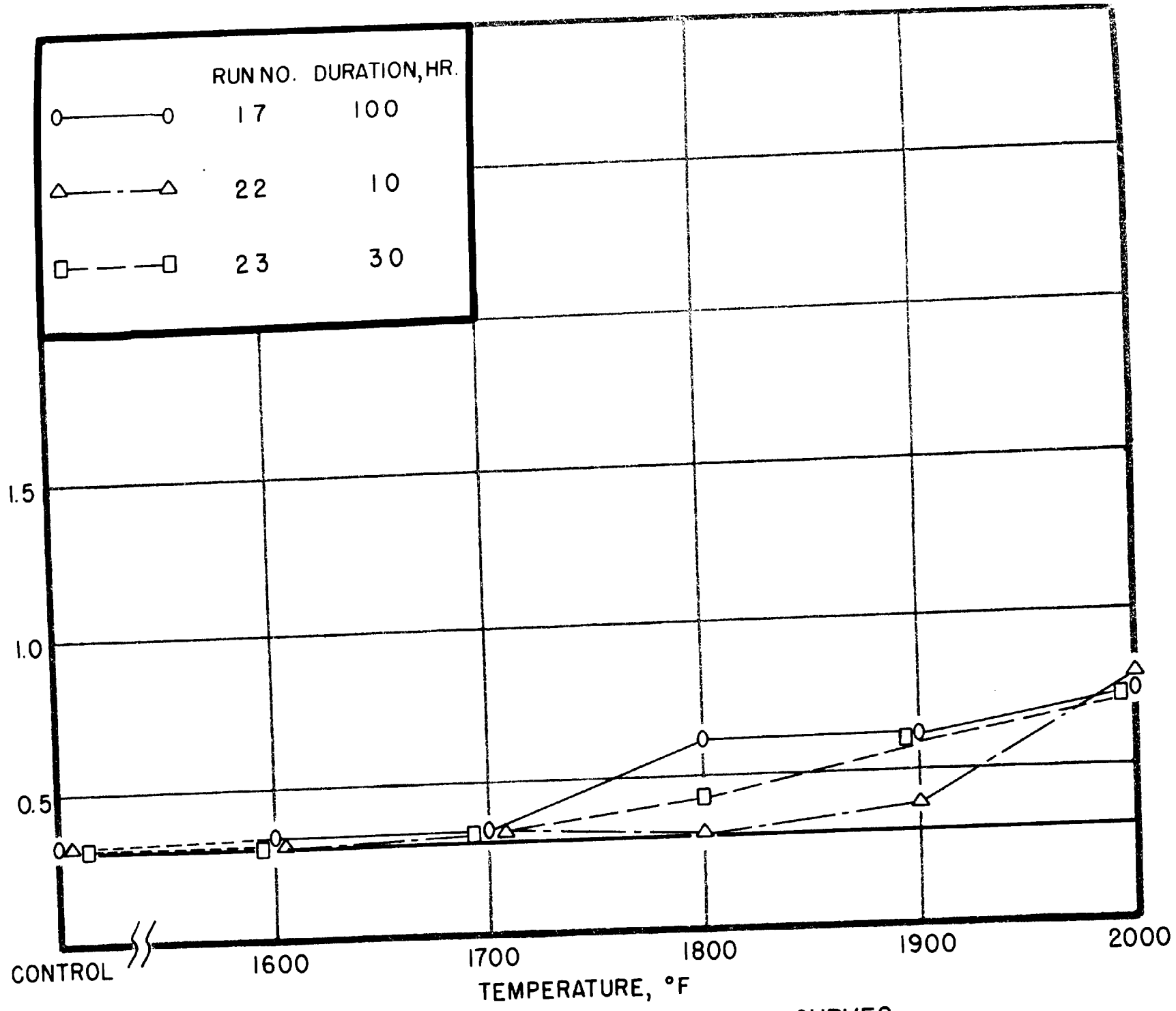

FIG. 94–SUMMARY PENETRATION DEPTH CURVES.
TYPE 310 ALLOY, HEAT X46572. EFFECT OF TIME.

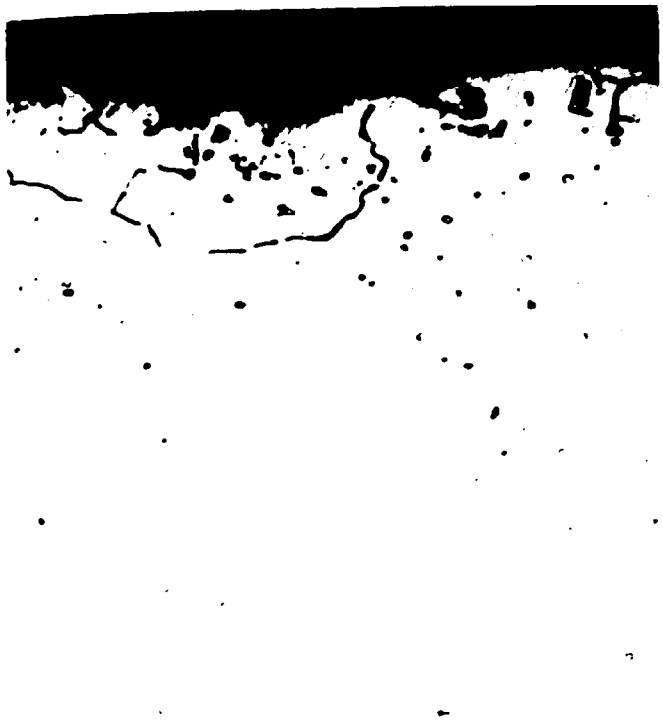

Fig. 95. Type I Penetration. Web from Surface. Type 309 + Nb Alloy. 1900°F and 100 hr. 750x. Cross Section. Unetched.



Fig. 96. Type II Penetration. Web from Pits. Type 310 Alloy, Heat 64270. 1800°F and 100 hr. 750x. Cross Section. Unetched.



Fig. 97. Type III Penetration. Rough Web. Type 310 Alloy, Heat 64177. 1900°F and 100 hr. 750x. Cross Section. Unetched.

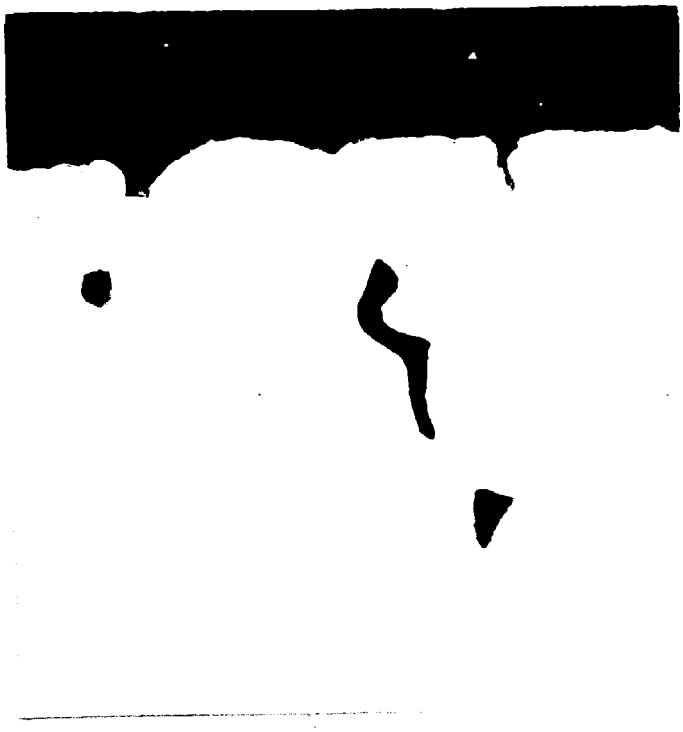

Fig. 98. Type IV Penetration. Smooth Fissures. Type 310 Alloy, Heat X 11338. 1800°F and 100 hr. 750x. Cross Section. Unetched.



Fig. 99. Type V Penetration. Developed Web. Type 310 Alloy, Heat X 11338. 1900°F and 100 hr. 750x. Cross Section. Unetched.



Fig. 100. Type VI Penetration. Coalesced Web. Type 310 Alloy, Heat X 11338. 2000°F and 100 hr. 750x. Cross Section. Unetched.

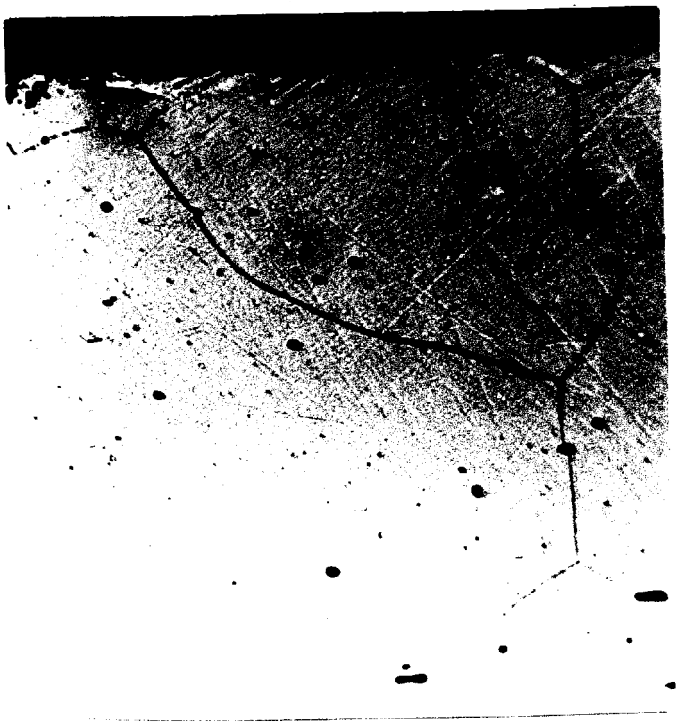

Fig. 101. Grain Boundaries before Testing. Type 310 Alloy, Heat 64270. As Received. 750x. Cross Section. Etch: Electr. Chromic Acid.



Fig. 102. Penetration and Grain Structure. Type 310 Alloy, Heat 64270. 1700°F and 100 hr. 750x. Cross Section. Etch: Electr. Chromic Acid.

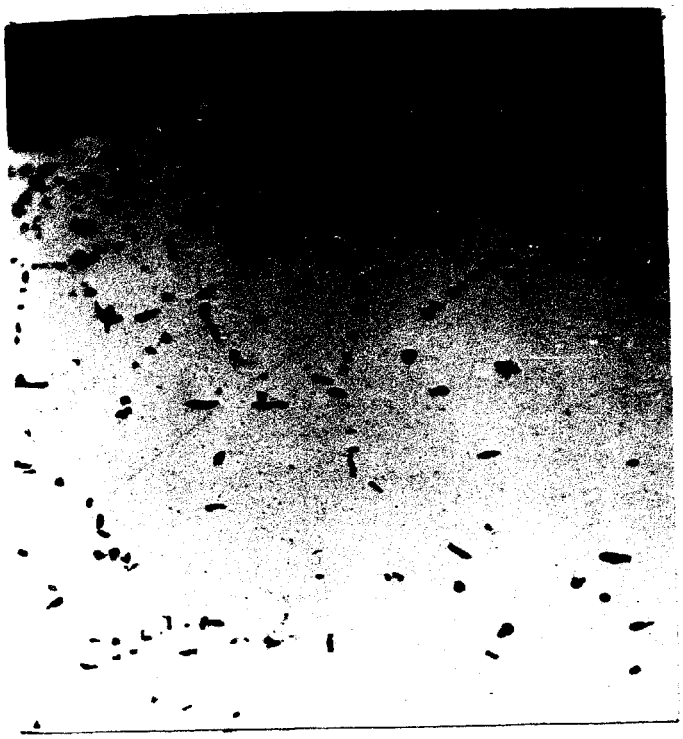

Fig. 103. Penetration and Precipitation. Type 310 Alloy, Heat X 11306. 1600°F and 100 hr. 750x. Cross Section. Unetched.



Fig. 104. Penetration and Precipitation. Type 310 Alloy, Heat X 11306. 1900°F and 100 hr. 750x. Cross Section. Unetched.



Fig. 105. Penetration and Precipitation. Type 310 Alloy, Heat X 11306. 2000°F and 100 hr. 750x. Cross Section. Unetched.

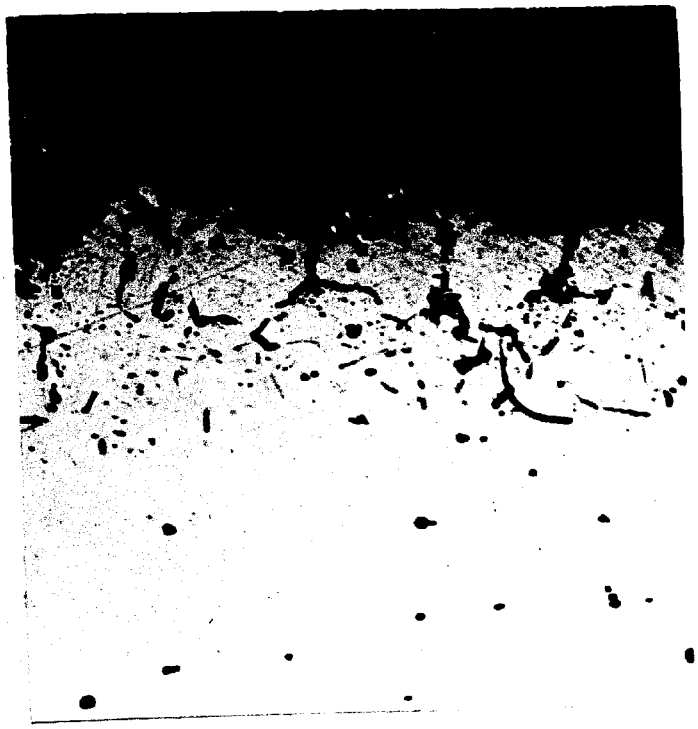

Fig. 106. Penetration and Precipitation. Type 310 Alloy, Heat X 11306. 2000°F and 10 hr. 750x. Cross Section. Unetched.



Fig. 107. Developed Web Penetration. Type 310 Alloy, Heat X 11338. 1900°F and 100 hr. 750x. Cross Section. Etch: Electr. Chromic Acid.



Fig. 108. Developed Web Penetration. Type 310 Alloy, Heat X 11338. 1900°F and 100 hr. 500x. Cross Section. Unetched.



Fig. 109. Oxide-filled Pits. Type 310 Alloy, Heat X 45558. 2000°F and 100 hr. 750x. Cross Section. Unetched.

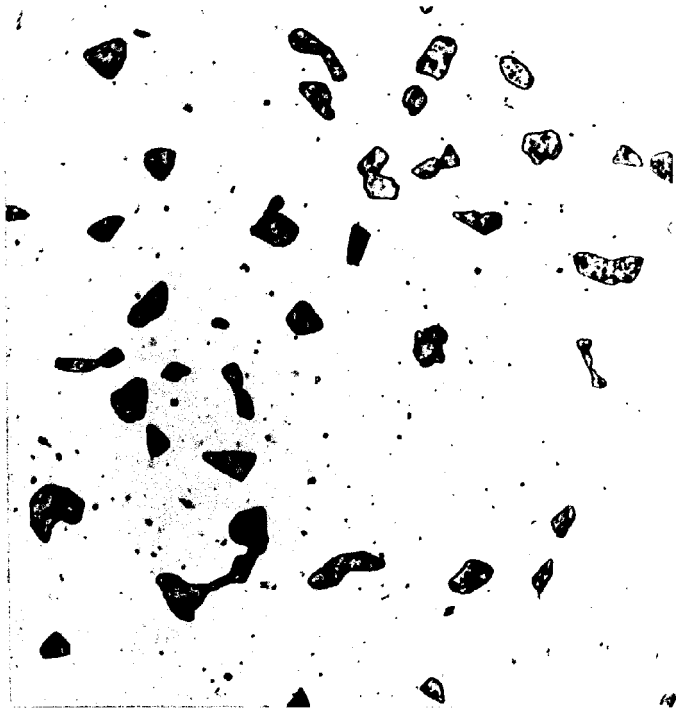

Fig. 110. Delta Ferrite. Type 309+ Nb Alloy. 1700°F and 100 hr. 1000x. Cross Section. Etch: Murakami's Reagent.

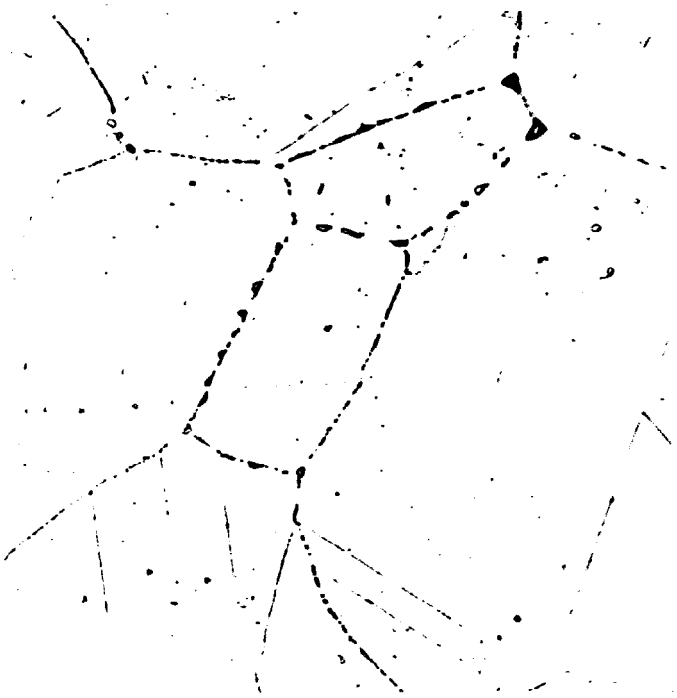

Fig. 111. Sigma Phase or Chromium Nitrides. Type 310 Alloy, Heat X 27258. 1600°F and 100 hr. 1000x. Cross Section. Etch: Murakami's Reagent.



Fig. 112. Delta Ferrite near Edge. Type 309 + Nb Alloy. 1700°F and 100 hr. 1000x. Cross Section. Etch: Murakami's Reagent.



Fig. 113. Sigma or Chromium Nitrides near Edge. Type 310 Alloy, Heat X 27258. 1600°F and 100 hr. 1000x. Cross section. Etch: Murakami's Reagent.

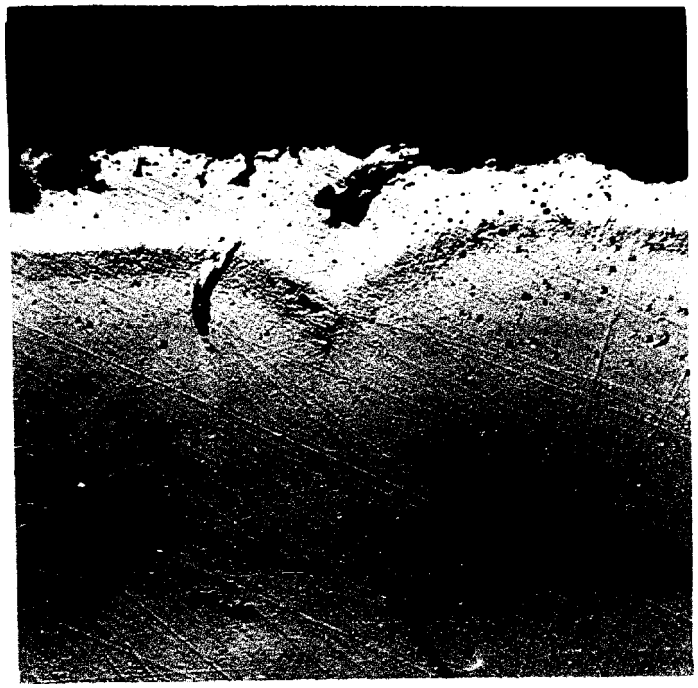

Fig. 114. Surface Layer. Type 310 Alloy, Heat X 27258. 1900°F and 10 hr. 1000x. Cross Section. Oblique Light. Etch: Electr. Chromic Acid.



Fig. 115. Concentration Gradients. Type 310 Alloy, Heat X 45558. As Received. 1000x. Cross Section. Oblique Light. Etch: Electr. Chromic Acid.

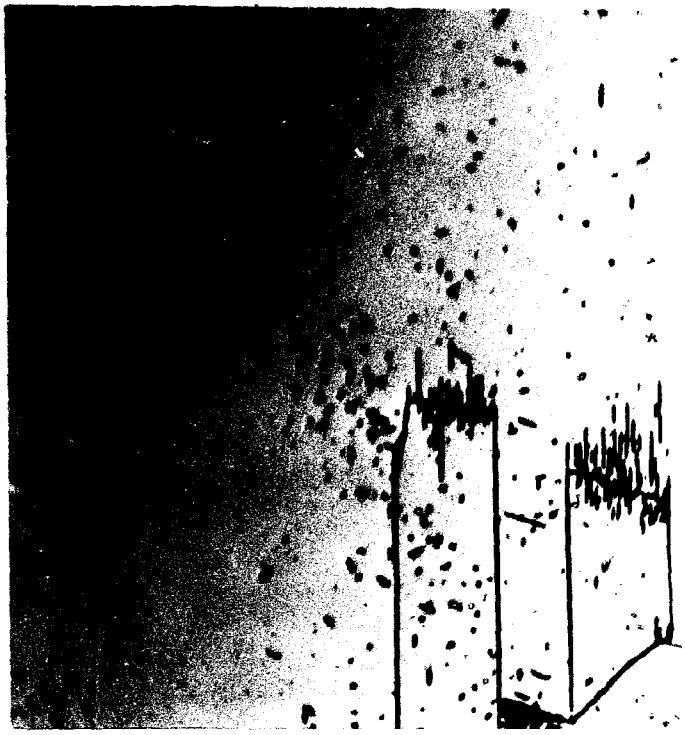

Fig. 116. Carbide Precipitation Bands. Type 310 Alloy, Heat X 45558. 1600°F and 10 hr. 1000x. Cross Section. Etch: Electr. Chromic Acid.

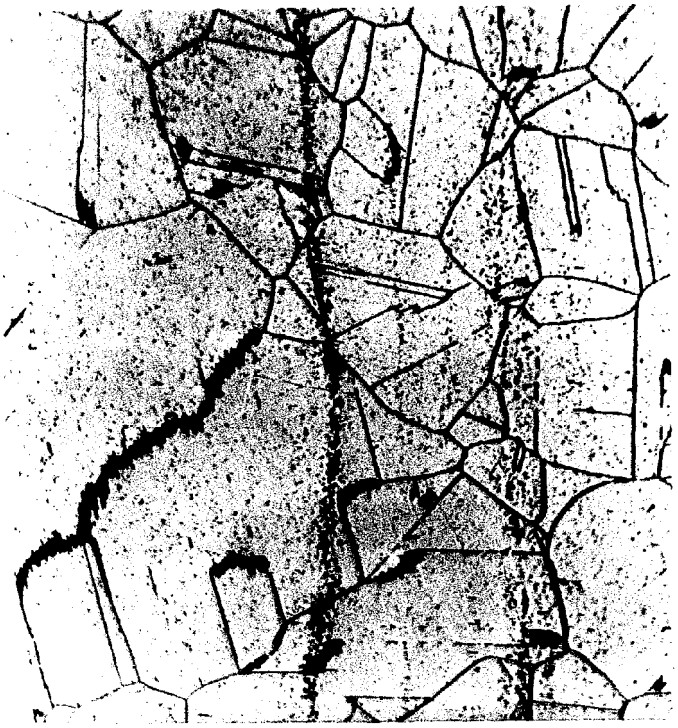

Fig. 117. Carbide Precipitation Bands. Type 310 Alloy, Heat X 45558. 1600°F and 10 hr. 250x. Cross Section. Etch: Electr. Chromic Acid.



Fig. 118. Carbide Bands and Grain Refinement. Type 310 Alloy Heat X 45558. 1600°F and 100 hr. 250x. Cross Section. Etch: Electr. Chromic Acid.

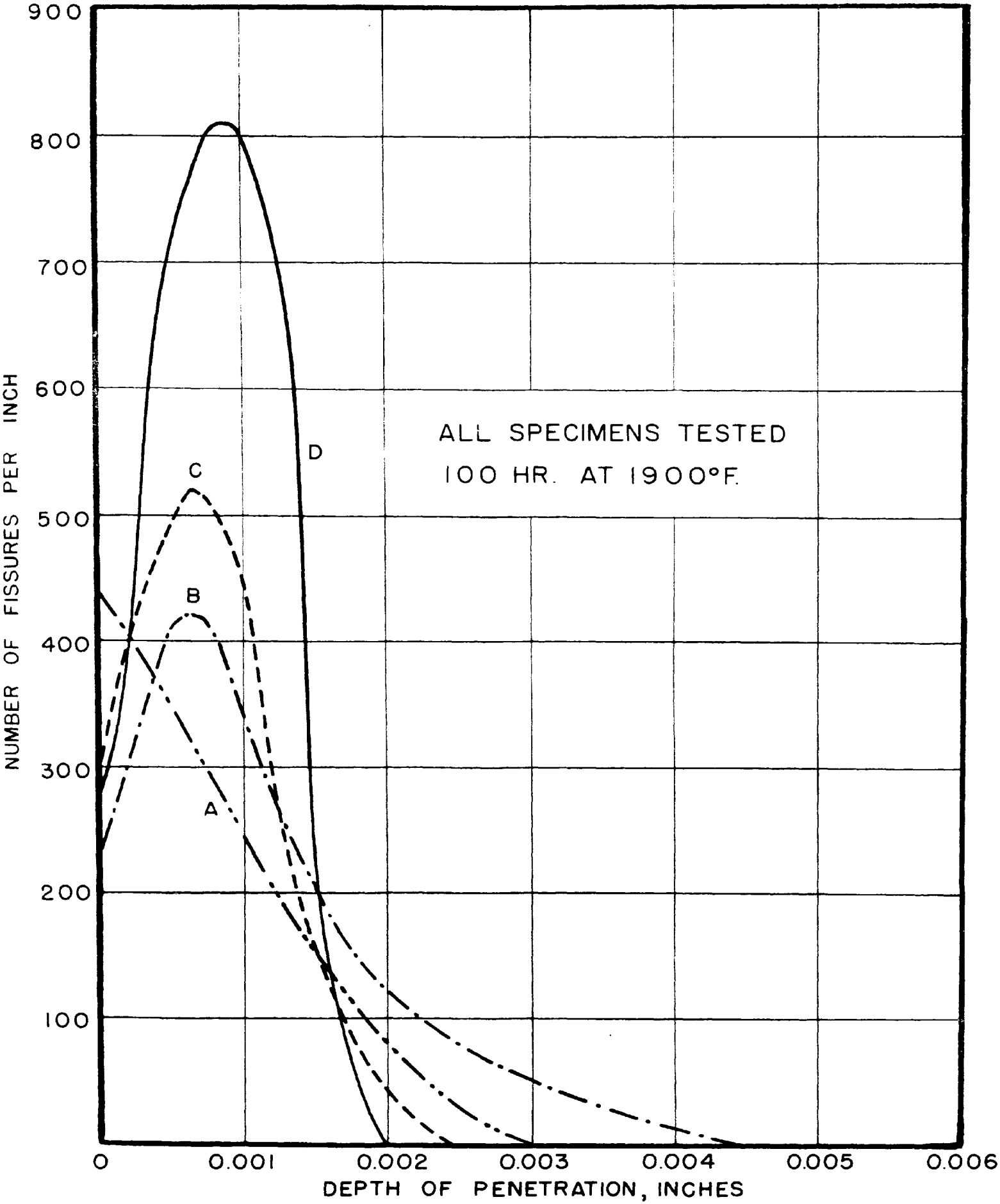

FIG. 119 - PENETRATION VS. DEPTH BELOW SURFACE. TYPE 310 ALLOY, HEAT X11338. VARIABILITY.

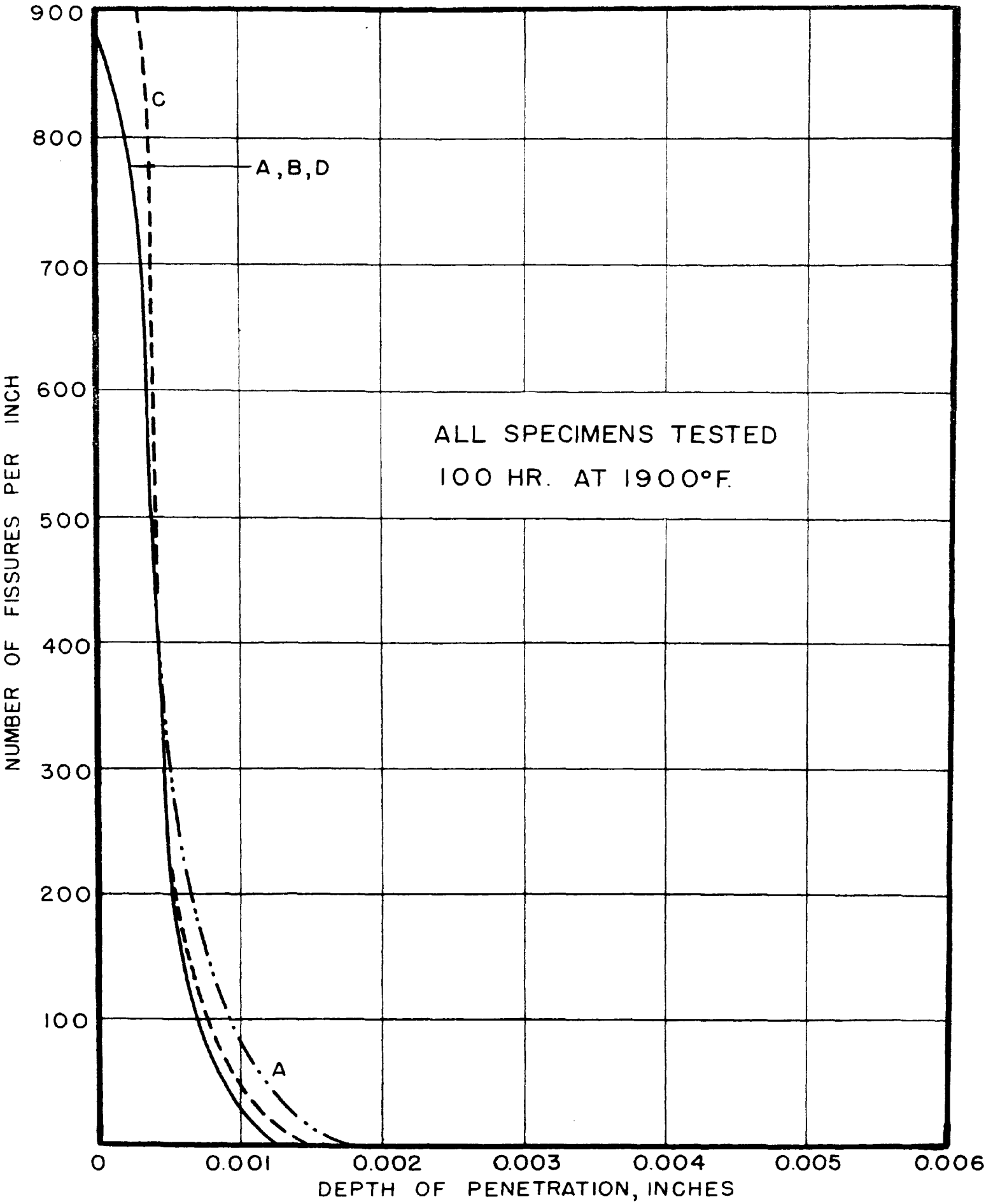

FIG. 120 - PENETRATION VS. DEPTH BELOW SURFACE. TYPE 310 ALLOY, HEAT X 45558. VARIABILITY.

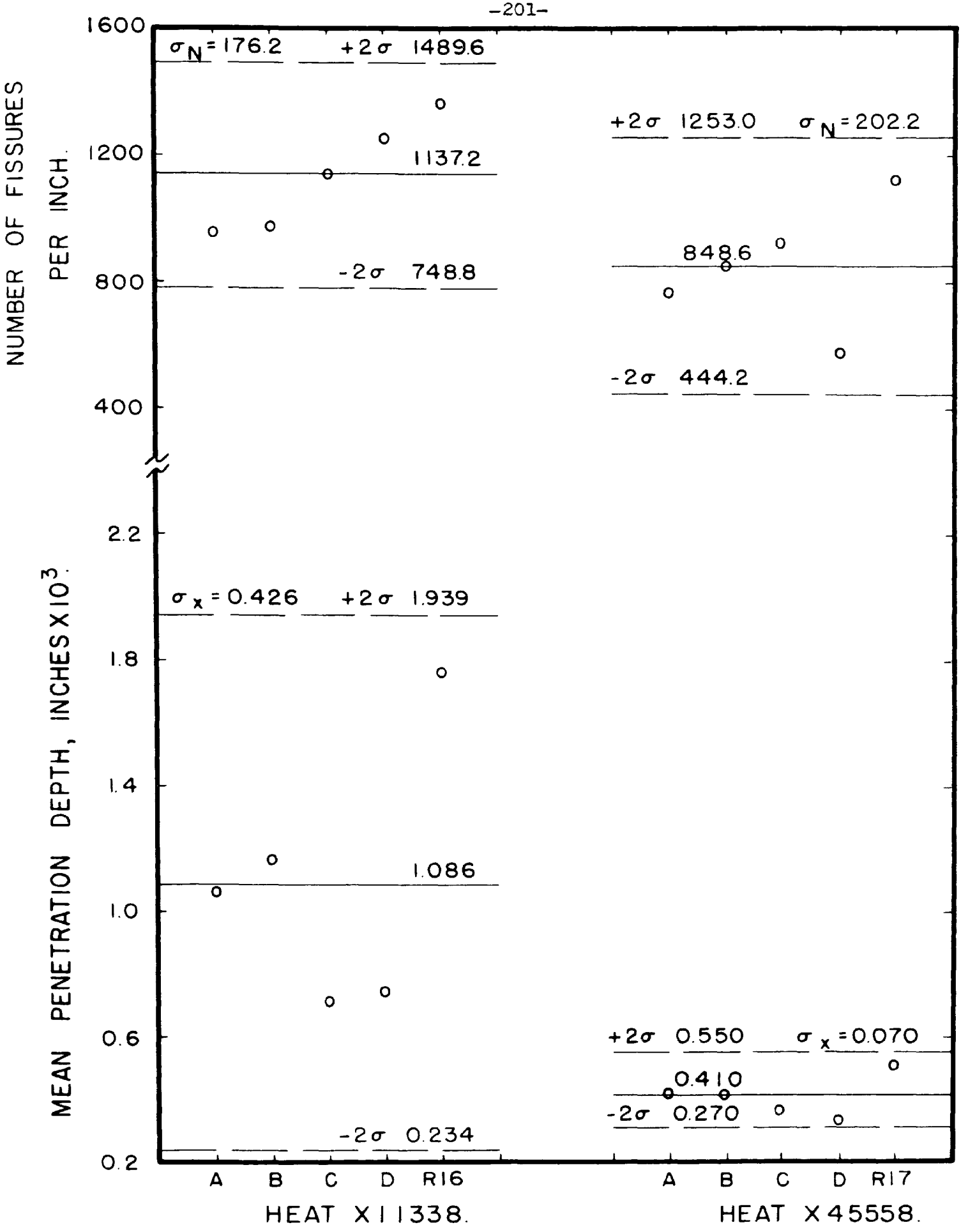

FIG. 121 - VARIABILITY OF MEAN PENETRATION FREQUENCY AND DEPTH.

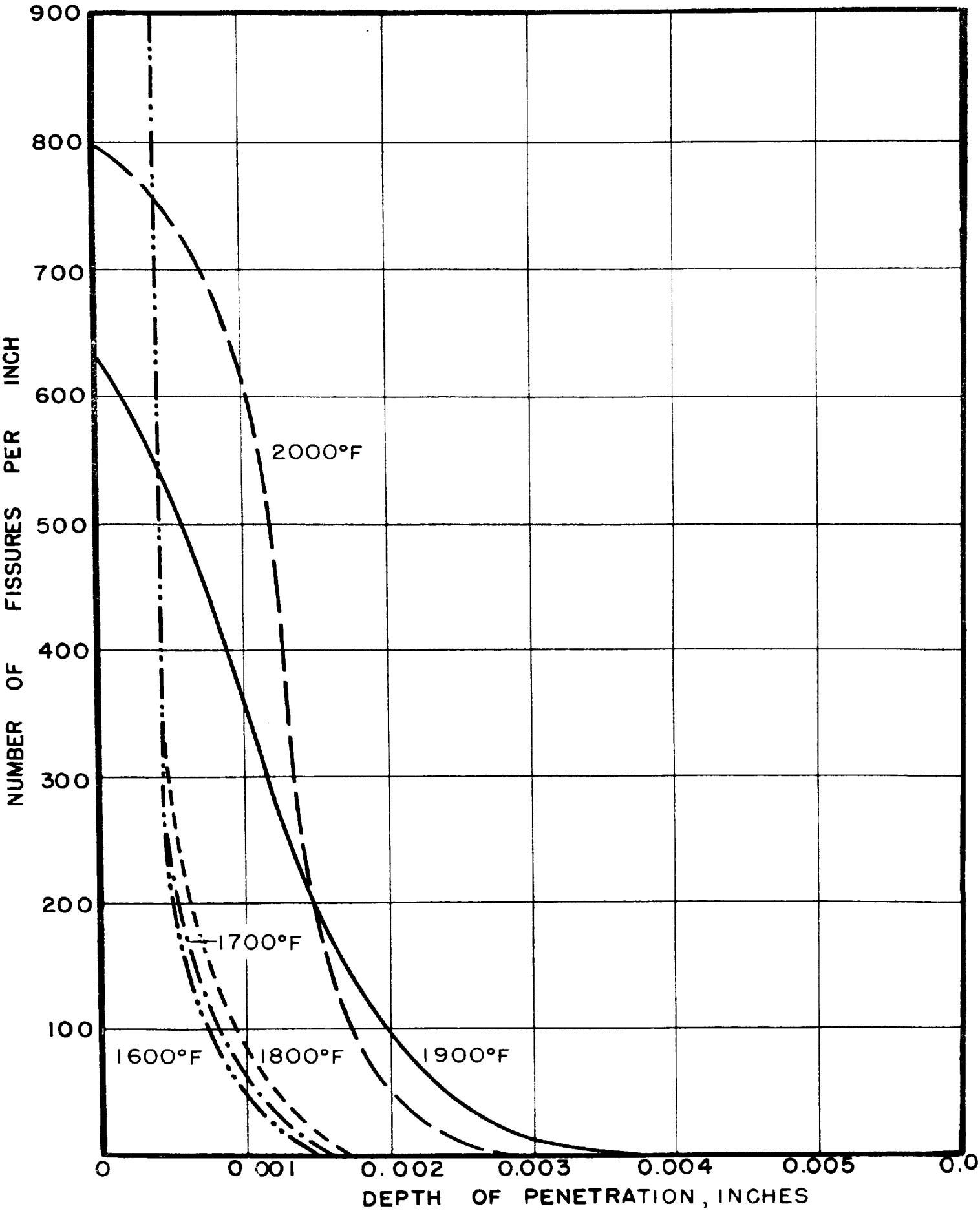

FIG. 122 - PENETRATION VS. DEPTH BELOW SURFACE.
TYPE 310 ALLOY, HEAT 31372.
AS RECEIVED. RUN 33.

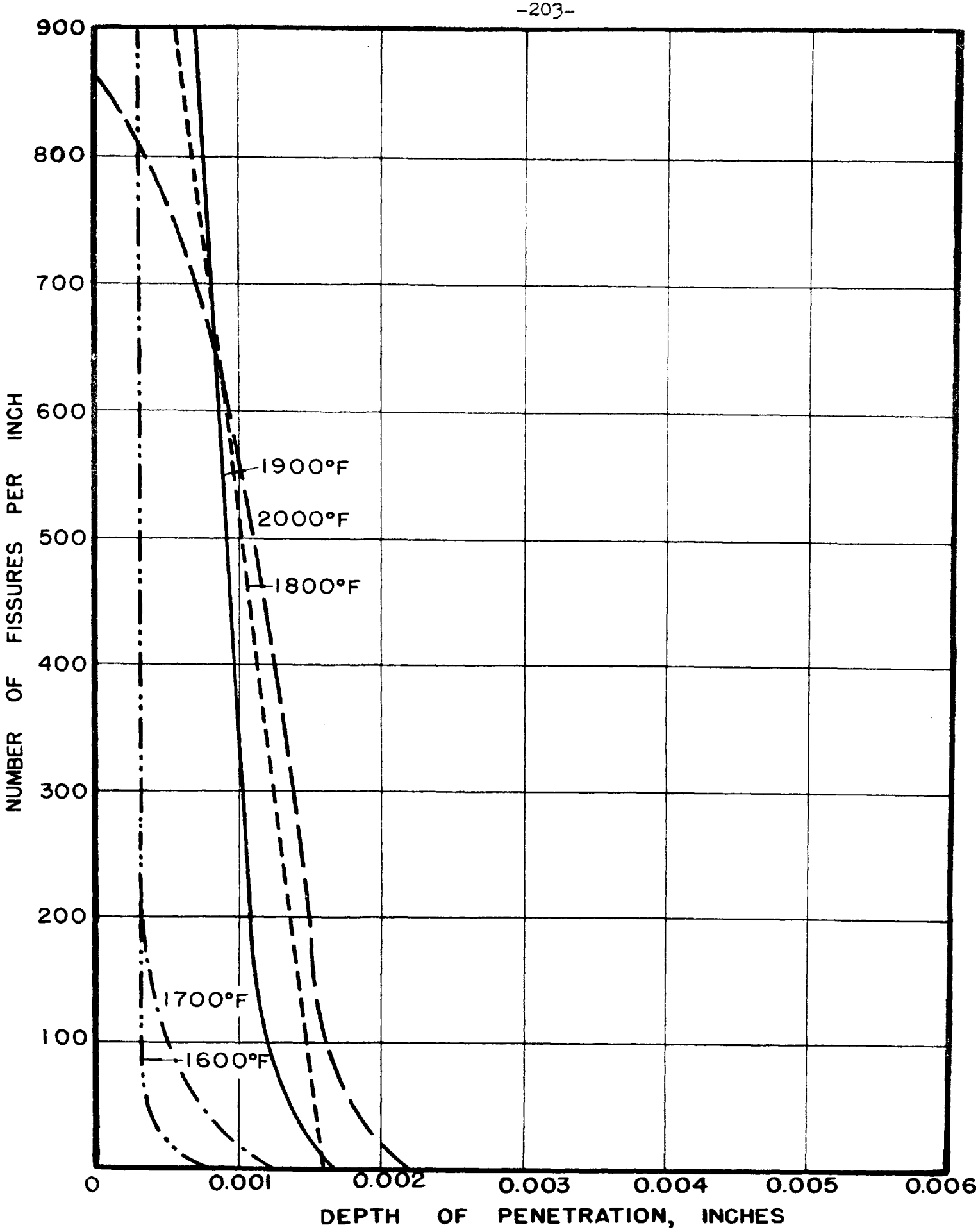

FIG. 123 – PENETRATION VS. DEPTH BELOW SURFACE.
TYPE 310 ALLOY, HEAT 31372.
REDUCED 97% & ANNEALED. RUN 33.

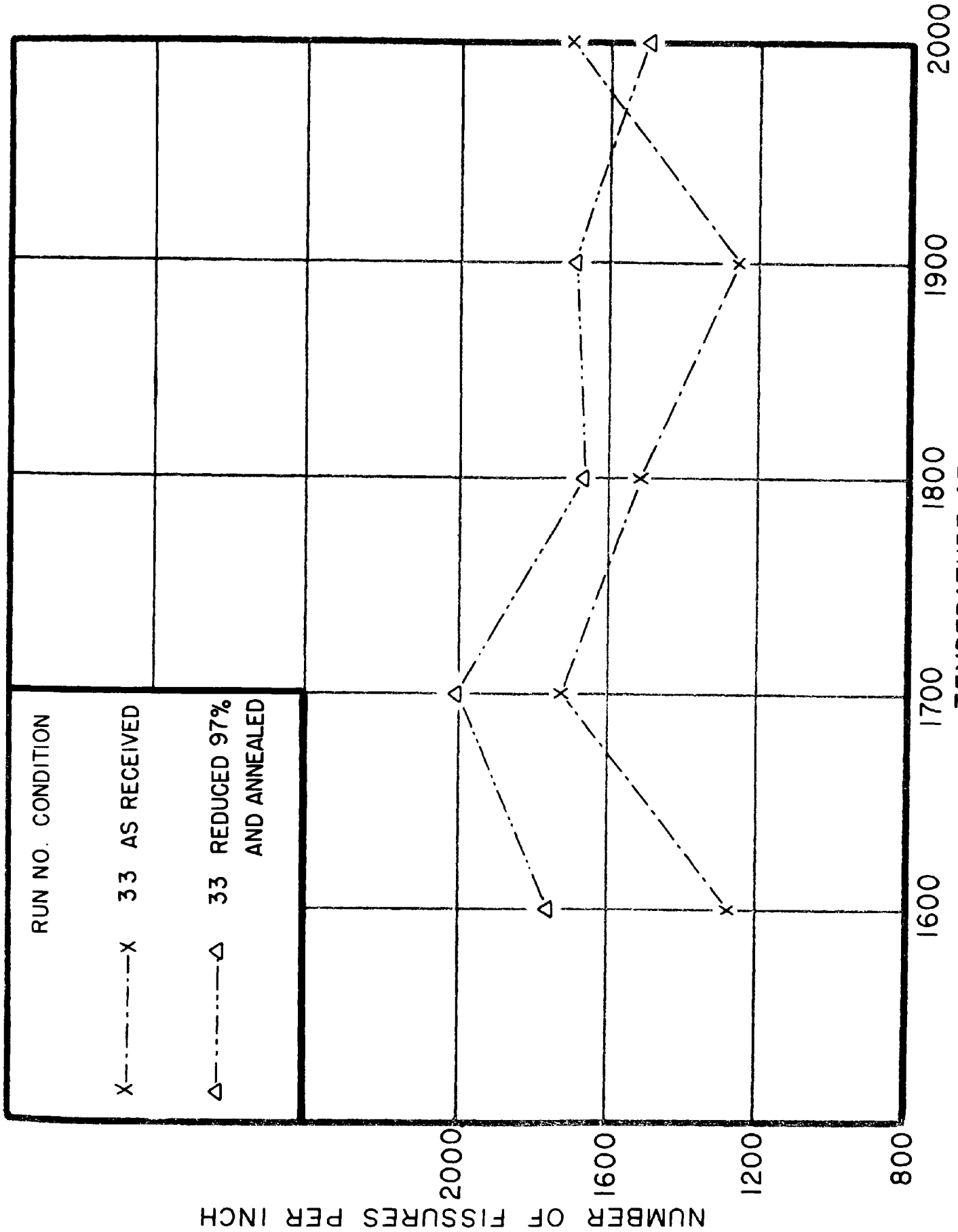

FIG. 124 - SUMMARY PENETRATION FREQUENCY CURVES.
TYPE 310 ALLOY, HEAT 31372. 100 HOURS DURATION.
EFFECT OF PREFERRED ORIENTATION.

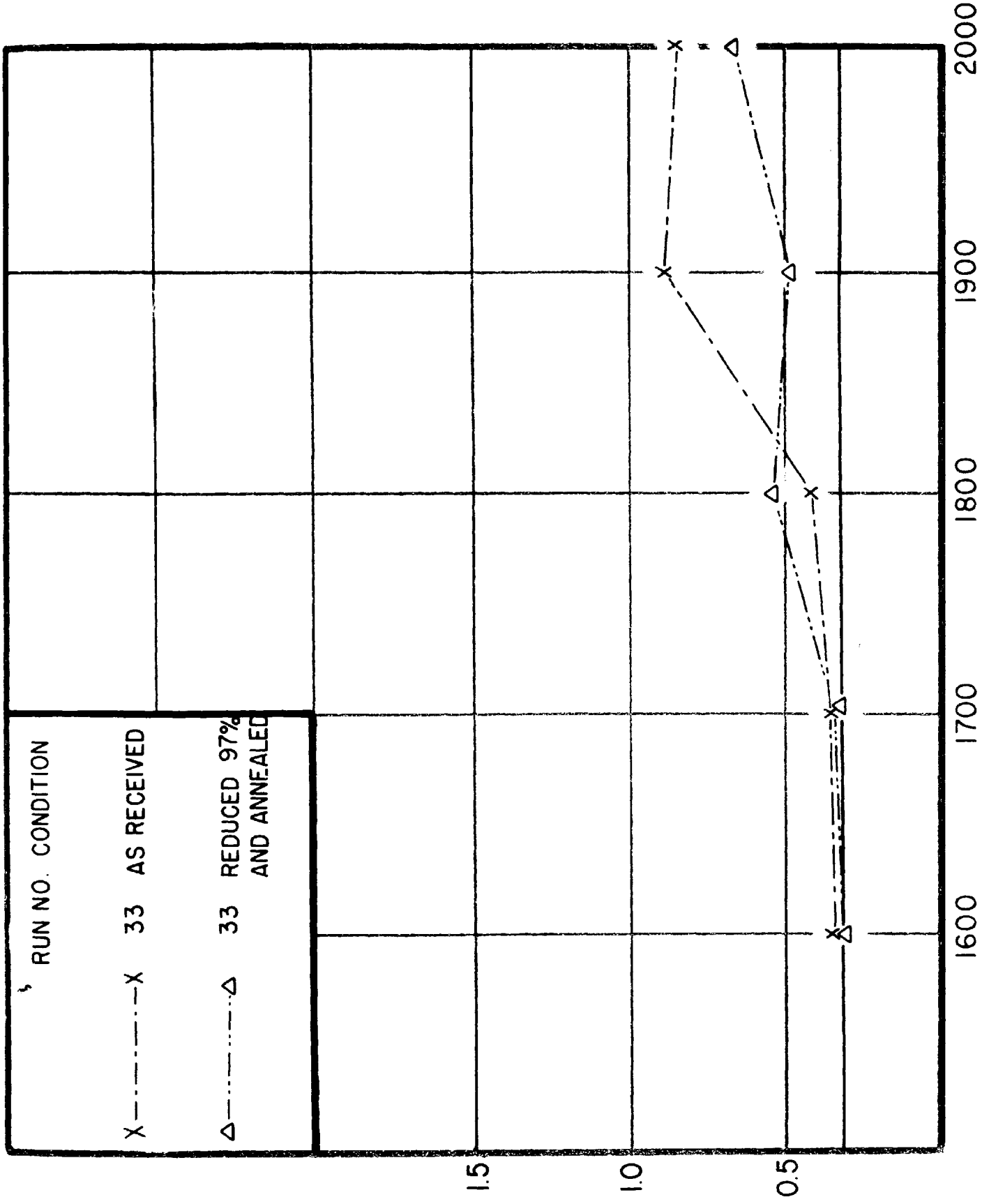

FIG. 125 – SUMMARY PENETRATION DEPTH CURVES.
TYPE 310 ALLOY, HEAT 31372. 100 HOURS DURATION.
EFFECT OF PREFERRED ORIENTATION.



Fig. 126. X-Ray Transmission Pattern. Type 310 Alloy, Heat 31372. Cold-reduced 97% in Thickness.

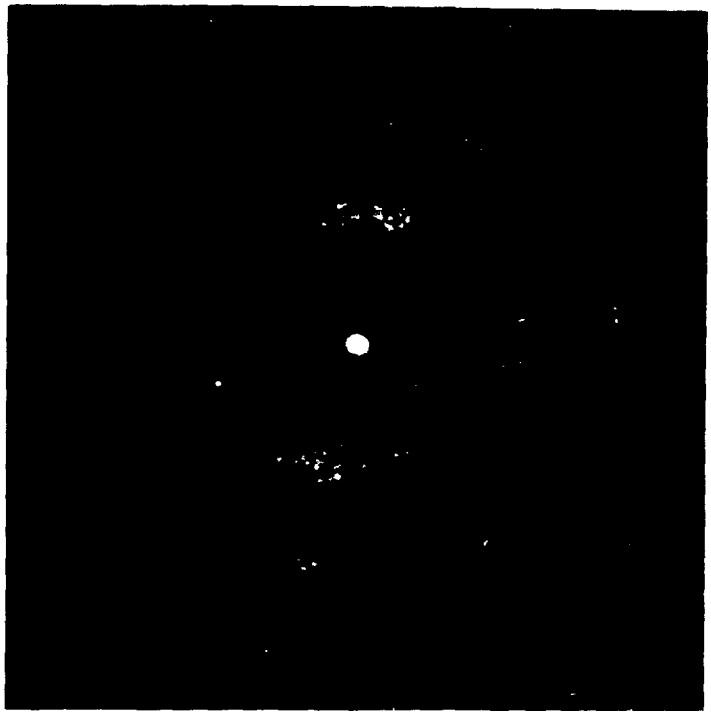

Fig. 127. X-Ray Transmission Pattern. Type 310 Alloy, Heat 31372. Cold-reduced 97% in Thickness and Annealed in Argon at 2000°F for 5-1/2 hr.

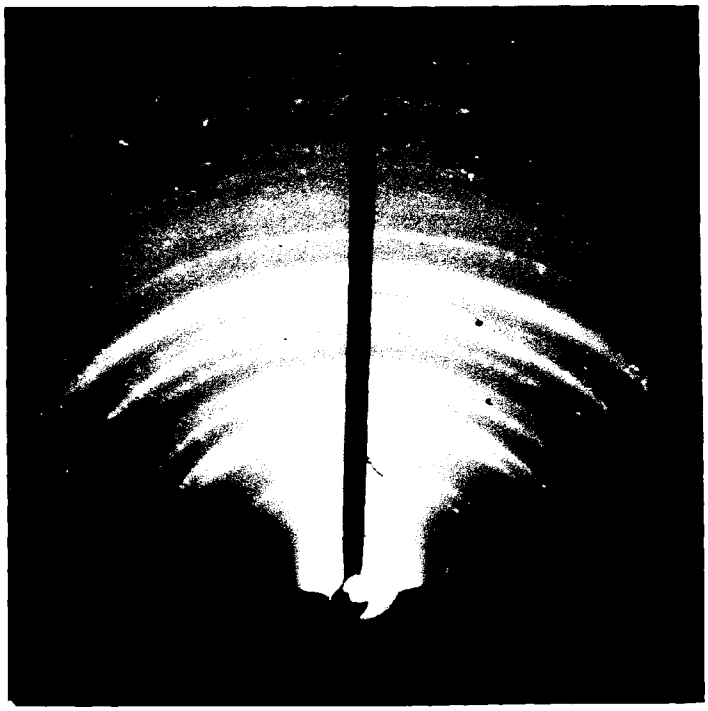

Fig. 128. Typical Electron Diffraction Pattern of Rhombohedral Phase.



Fig. 129. Typical Electron Diffraction Pattern of Spinel Phase. Some Rhombohedral Phase also present.

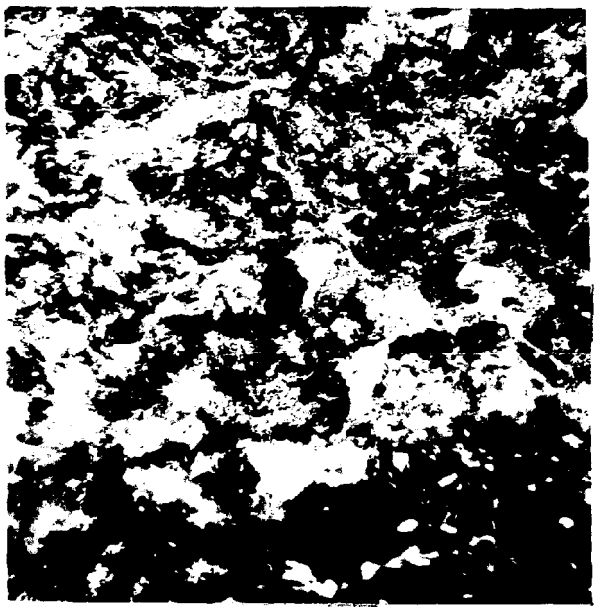

Fig. 130. Metallographic Appearance of Typical Oxidized Specimen Surface. Unetched 250 x Oblique Light.

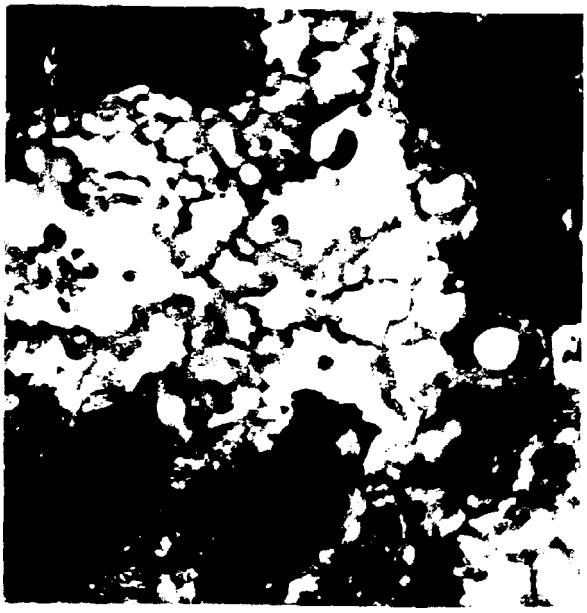

Fig. 131. Metallographic Appearance of Typical Oxidized Specimen Surface After 4 Min. Electr. Etch in 90% Glacial Acetic Acid - 10% Perchloric Acid. 0.0004 in. Removed. 250 x, Oblique Light.

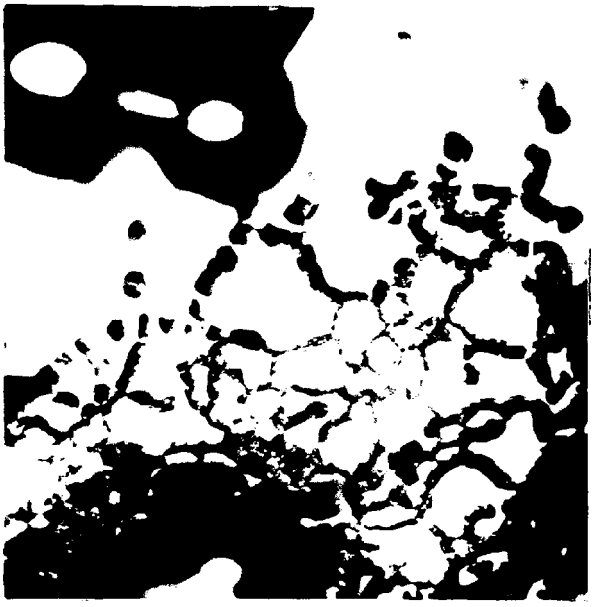

Fig. 132. Metallographic Appearance of Typical Oxidized Specimen Surface after 10 min. Electr. Etch in 90% Glacial Acetic Acid - 10% Perchloric Acid. 0.0004 in. Removed. 250x Oblique Light.



Fig. 133. Metallographic Appearance of Typical Oxidized Specimen Surface after 12 min. Electr. Etch in 90% Glacial Acetic Acid - 10% Perchloric Acid. 0.0011 in. Removed. 250x Oblique Light.

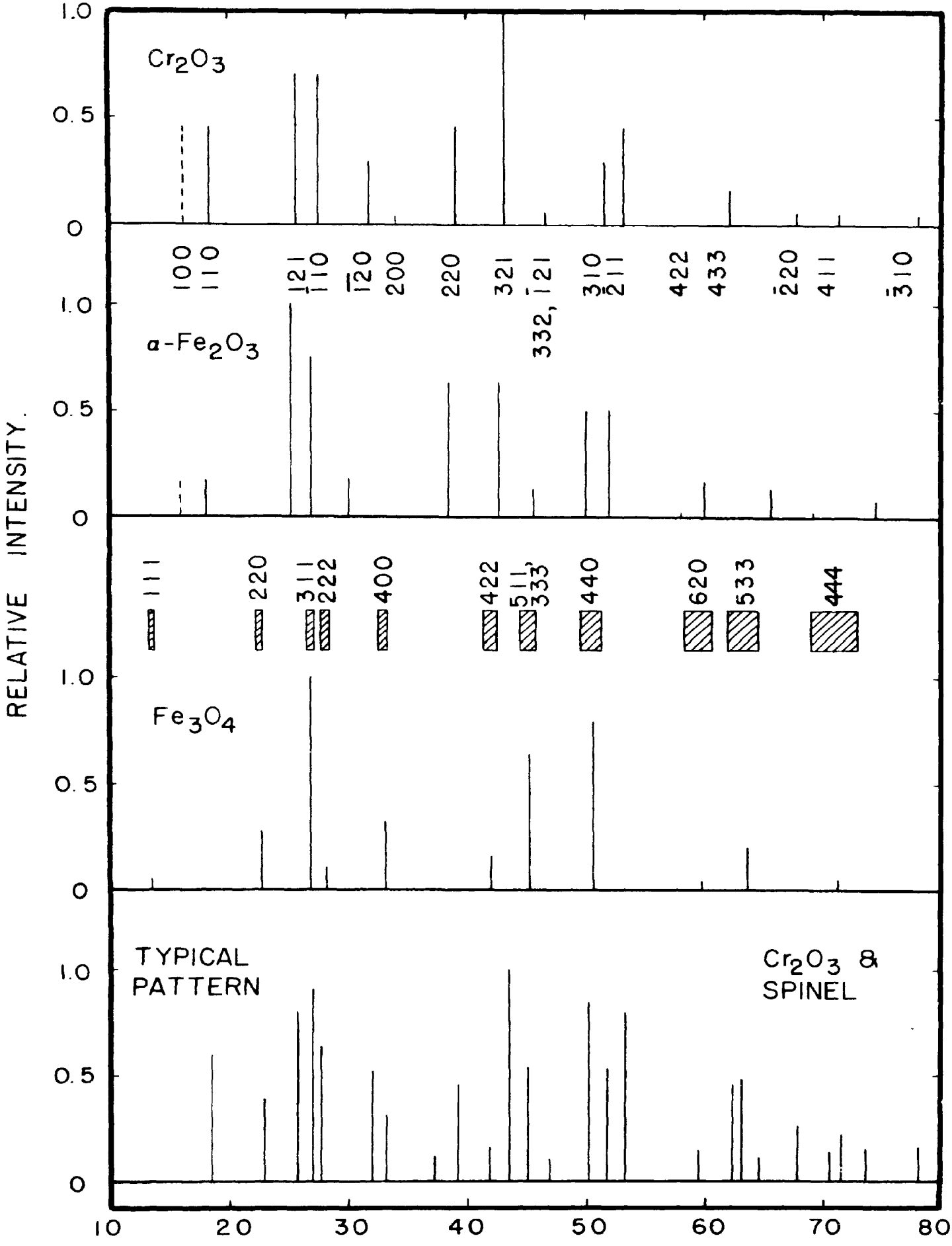

FIG. 134 - X-RAY DIFFRACTION PATTERNS OF TYPICAL SCALE COMPONENTS. CR RADIATION